3D Time-of-flight distance measurement with custom solid-state image sensors in CMOS/CCD-technology

Robert Lange

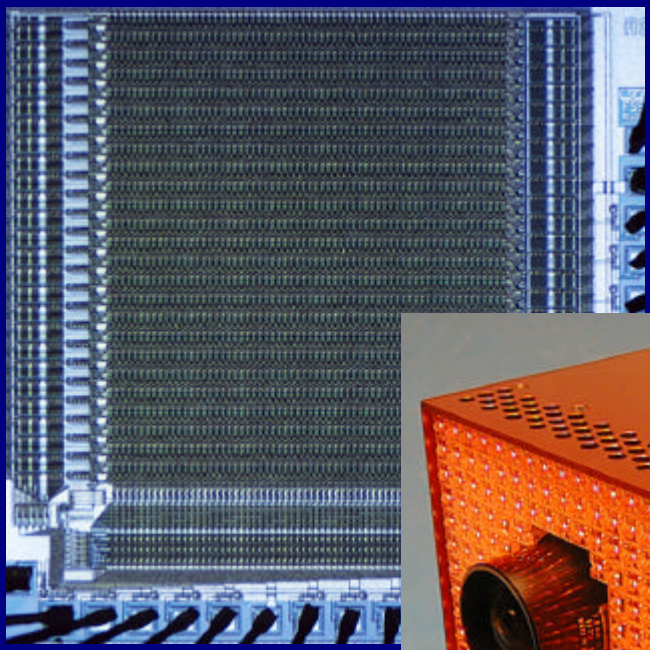

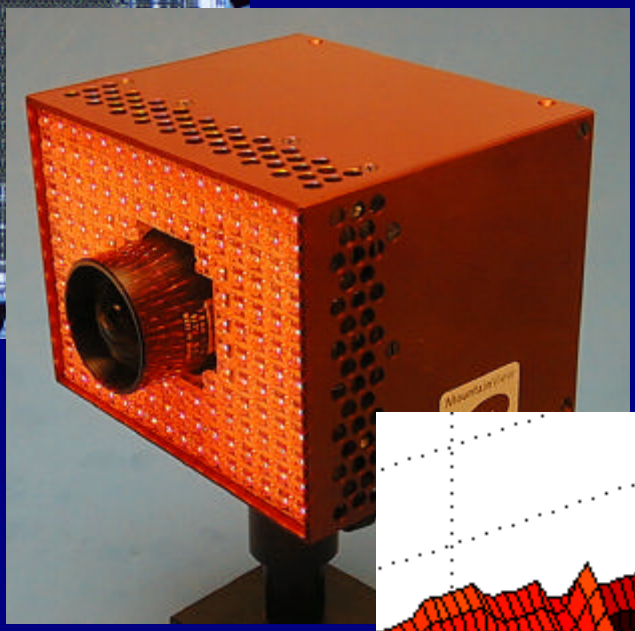

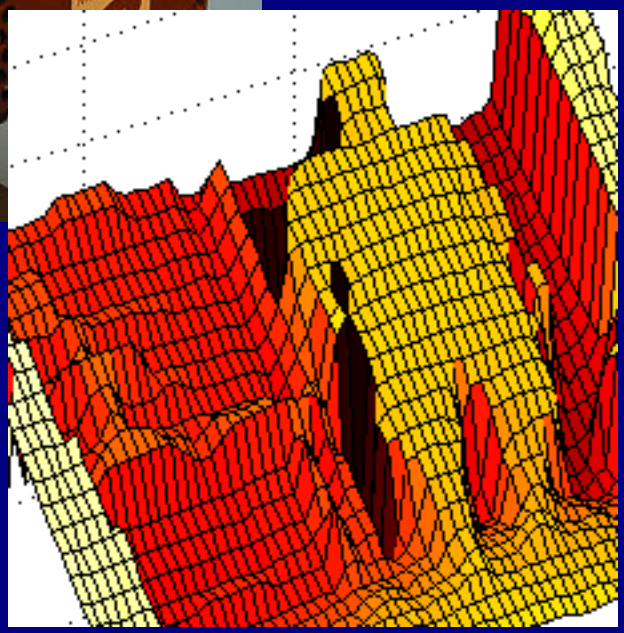

3D Time-of-Flight Distance Measurement with Custom Solid-State Image Sensors in CMOS/CCD-Technology

A dissertation submitted to the

DEPARTMENT OF ELECTRICAL ENGINEERING AND COMPUTER SCIENCE AT UNIVERSITY OF SIEGEN

for the degree of

DOCTOR OF TECHNICAL SCIENCES

presented by
Dipl.-Ing. Robert Lange

born March 20, 1972

accepted on the recommendation of

Prof. Dr. R. Schwarte, examiner
Prof. Dr. P. Seitz, co-examiner

Submission date: June 28, 2000
Date of oral examination: September 8, 2000

To my parents

3D Distanzmessung nach dem „Time-of-Flight“- Verfahren mit kundenspezifischen Halbleiterbildsensoren in CMOS/CCD Technologie

VOM FACHBEREICH ELEKTROTECHNIK UND INFORMATIK
DER UNIVERSITÄT-GESAMTHOCHSCHULE SIEGEN

zur Erlangung des akademischen Grades

DOKTOR DER INGENIEURWISSENSCHAFTEN
(DR.-ING.)

genehmigte Dissertation
vorgelegt von
Dipl.-Ing. Robert Lange
geboren am 20. März 1972

1. Gutachter: Prof. Dr.-Ing. R. Schwarte
2. Gutachter: Prof. Dr. P. Seitz
Vorsitzender der Prüfungskommission: Prof. Dr.-Ing H. Roth

Tag der Abgabe: 28. Juni 2000
Tag der mündlichen Prüfung: 8. September 2000

Meinen Eltern

Contents

Abstract

Since we are living in a three-dimensional world, an adequate description of our environment for many applications includes the relative position and motion of the different objects in a scene. Nature has satisfied this need for spatial perception by providing most animals with at least two eyes. This stereo vision ability is the basis that allows the brain to calculate qualitative depth information of the observed scene. Another important parameter in the complex human depth perception is our experience and memory. Although it is far more difficult, a human being is even able to recognize depth information without stereo vision. For example, we can qualitatively deduce the 3D scene from most photos, assuming that the photos contain known objects [COR].

The acquisition, storage, processing and comparison of such a huge amount of information requires enormous computational power - with which nature fortunately provides us. Therefore, for a technical implementation, one should resort to other simpler measurement principles. Additionally, the qualitative distance estimates of such knowledge-based passive vision systems can be replaced by accurate range measurements.

Imaging 3D measurement with useful distance resolution has mainly been realized so far with triangulation systems, either passive triangulation (stereo vision) or active triangulation (e.g. projected fringe methods). These triangulation systems have to deal with shadowing effects and ambiguity problems (projected fringe), which often restrict the range of application areas. Moreover, stereo vision cannot be used to measure a contrastless scene. This is because the basic principle of stereo vision is the extraction of characteristic contrast-related features within the observed scene and the comparison of their position within the two images. Also, extracting the 3D information from the measured data requires an enormous time-consuming computational effort. High resolution can only be achieved with a relatively large triangulation base and hence large camera systems.

A smarter range measurement method is the TOF (Time-Of-Flight) principle, an optical analogy to a bat's ultrasonic system rather than human's stereo vision. So far TOF systems are only available as 1D systems (point measurement), requiring laser scanners to acquire 3D images. Such TOF scanners are expensive, bulky, slow, vibration sensitive and therefore only suited for restricted application fields.

In this dissertation an imaging, i.e. non-scanning TOF-camera is introduced, based on an array of demodulation pixels, where each pixel can measure both the background intensity and the individual arrival time of an RF-modulated (20 MHz) scene illumination with an accuracy of a few hundreds of picoseconds ($300 \cdot 10^{-12}$ s). The pixel's working concept is based on the CCD principle (Charge Coupled Device), allowing the transportation, storage and accumulation of optically generated charge carriers to defined local sites within the imaging device. This process is extremely fast and essentially loss-free. We call our new, powerful high-functionality pixels *demodulation pixels* because they extract the target's distance and reflectivity from the received optical signal. This extracted information is modulated into the active optical signal during the time of propagation of the light (or time of flight) through the observed scene. Each pixel works like an individual high-precision stopwatch, and since its realization is mainly based on CMOS technology this new technique will benefit from the ongoing technology developments in terms of improved time- and hence distance resolution. Thanks to the use of CMOS, all commonly known CMOS APS (Active Pixel Sensor) features (Regions Of Interest addressing: ROI, AD conversion, etc.) can be implemented monolithically in the future.

The imaging devices have been fabricated in a 2 µm CMOS/CCD process, a slightly modified CMOS process which is available as an inexpensive prototyping service (Multi Project Wafer: MPW). This process offers the freedom to implement CCDs with sufficiently good performance for our application, although the performance is inferior to dedicated CCD technologies. We have realized and characterized several different pixel structures and will present these results here. The demodulation pixel with the best fill-factor and demodulation performance has been implemented (1) as a line sensor with 108 pixels and (2) as an image sensor with 64 x 25 pixels. Both devices have been integrated in separate range cameras working with modulated LED illumination and covering a distance range of 7.5 up to 15 meters. For non-cooperative diffusely reflecting targets these cameras achieve

centimeter accuracy. With the single exception of the demodulation pixel array itself, only standard electronic and optical components have been used in these range cameras. For a resolution of 5 centimeters, an optical power of 600 fW per pixel is sufficient, assuming an integration time of 50 ms (20 Hz frame rate of 3D images). This low optical power implies that only 0.06 electrons are generated per modulation period (T_{mod}=50 ns at 20 MHz modulation frequency).

Furthermore, we present an in-depth analysis of the influences of non-linearities in the electronics, aliasing effects, integration time and modulation functions. Also, an optical power budget and a prediction for the range accuracy is derived as a function of the ratio of active illumination to background illumination. The validity of this equation is confirmed by both computer simulations and experimental measurements with real devices. Thus, we are able to predict the range accuracy for given integration time, optical power, target distance and reflectance.

With this work we demonstrate the first successful realization of an all-solid-state 3D TOF range-camera without moving parts that is based on a dedicated customized PhotoASIC. The measured performance is very close to the theoretical limits. We clearly demonstrate that optical 3D-TOF is an excellent, cost-effective tool for all modern vision problems, where the relative position or motion of objects need to be monitored.

Kurzfassung

Da wir in einer dreidimensionalen Welt leben, erfordert eine geeignete Beschreibung unserer Umwelt für viele Anwendungen Kenntnis über die relative Position und Bewegung der verschiedenen Objekte innerhalb einer Szene. Die daraus resultierende Anforderung räumlicher Wahrnehmung ist in der Natur dadurch gelöst, daß die meisten Tiere mindestens zwei Augen haben. Diese Fähigkeit des Stereosehens bildet die Basis dafür, daß unser Gehirn qualitative Tiefeninformationen berechnen kann. Ein anderer wichtiger Parameter innerhalb des komplexen menschlichen 3D-Sehens ist unser Erinnerungsvermögen und unsere Erfahrung. Der Mensch ist sogar in der Lage auch ohne Stereosehen Tiefeninformation zu erkennen. Beispielsweise können wir von den meisten Photos, vorausgesetzt sie bilden Objekte ab, die wir bereits kennen, die 3D Information im Kopf rekonstruieren [COR].

Die Aufnahme, Speicherung, Weiterverarbeitung und der Vergleich dieser riesigen Datenmengen erfordert eine enorme Rechenleistung. Glücklicherweise stellt uns die Natur diese Rechenleistung zur Verfügung. Für eine technische Realisierung sollten wir aber nach einfacheren und genaueren Meßprinzipien suchen.

Bildgebende 3D Meßmethoden mit einer brauchbaren Distanzauflösung sind bisher nur in Form von passiven (z.B. Stereosehen) oder aktiven (z.B. Streifenprojektionsverfahren) Triangulationssystemen realisiert worden. Solche Triangulationssysteme bringen vor allem die Nachteile der Abschattungsproblematik und der Mehrdeutigkeit (Streifenprojektion) mit sich. Somit sind oftmals die möglichen Einsatzgebiete eingeschränkt. Außerdem erfordert Stereosehen kontrastreiche Szenen, denn sein Grundprinzip besteht in der Extrahierung bestimmter signifikanter (kontrastreicher) Merkmale innerhalb der Szenen und dem Positionsvergleich dieser Merkmale in den beiden Bildern. Überdies erfordert die Gewinnung der 3D Information einen hohen Rechenaufwand. Hohe Meßauflösung hingegen kann man nur mit einer großen Triangulationsbasis gewährleisten, welche wiederum zu großen Kamerasystemen führt.

Eine elegantere Methode zur Entfernungsmessung ist das „Time-of-Flight (TOF)“-Verfahren (Fluglaufzeitverfahren), ein optisches Analogon zum Ultraschall Navigationssystem der Fledermaus. Bisher wird das TOF- Verfahren nur eindimensional eingesetzt, also für die Distanzbestimmung zwischen zwei Punkten. Um mit solchen 1D Meßsystemen die 3D Information der Szene zu erlangen, benutzt man Laserscanner. Diese sind aber teuer, groß, verhältnismäßig langsam und empfindlich gegen Erschütterungen und Vibrationen. Scannende TOF- Systeme sind daher nur für eine eingeschränkte Anzahl von Applikationen geeignet.

In dieser Dissertation stellen wir erstmals eine nicht scannende bildgebende 3D-Kamera vor, die nach dem TOF- Prinzip arbeitet und auf einem Array von sogenannten Demodulationspixeln beruht. Jedes dieser Pixel ermöglicht sowohl die Messung der Hintergrundintensität als auch die individuelle Ankunftszeit einer HF-modulierten Szenenbeleuchtung mit einer Genauigkeit von wenigen hundert Pikosekunden. Das Funktionsprinzip der Pixel basiert auf dem CCD Prinzip (Charge Coupled Device), welches den Transport, die Speicherung und die Akkumulation optisch generierter Ladungsträger in definierten örtlich begrenzten Gebieten auf dem Bildsensor erlaubt. Ladungstransport und -addition können von CCDs enorm schnell und beinahe verlustfrei durchgeführt werden. Wir bezeichnen diese neuartigen, hochfunktionalen und leistungsstarken Pixel als *Demodulations-pixel*, weil man mit jedem von ihnen die Entfernungs- und Reflektivitätsinformation des zu vermessenden Ziels aus dem empfangenen optischen Signal extrahieren kann. Die gesuchte Information wird dem aktiven optischen Signal während der Ausbreitung des Lichts durch die Szene (Time of Flight) aufmoduliert. Jedes Pixel arbeitet wie eine individuelle Hochpräzisions- Stoppuhr. Da die Realisierung im wesentlichen auf CMOS- Technologie basiert, wird diese neue Technik von den stetig fortschreitenden Technologieentwicklungen und -verbesserungen profitieren und zwar in Form von besserer Zeitauflösung und damit höherer Distanzgenauigkeit. Dank der Benutzung einer CMOS- Technologie können zukünftig sehr leicht auch alle bekannten CMOS-APS- Eigenschaften (Active Pixel Sensor) monolithisch implementiert werden (z.B. Definition und Auslese von Bildsegmenten: *regions of interest*, A/D Wandlung auf dem Sensor, …).

Die neuen Bildsensoren sind in einem 2 µm CMOS/CCD Prozess hergestellt worden, einem leicht modifizierten CMOS Prozess, der zur kostengünstigen Prototypenfertigung zur Verfügung steht (sogenannte MPWs, Multi Project Wafer).

Dieser Prozess bietet die Möglichkeit, CCD Strukturen zu realisieren. Obwohl diese CCDs nicht die Qualität spezieller CCD- Prozesse erreichen, genügen sie den Anforderungen unserer Anwendung vollkommen. Wir haben verschiedene Pixelstrukturen realisiert und charakterisiert und präsentieren in dieser Arbeit die Ergebnisse. Das Demodulationspixel mit dem besten Füllfaktor und den effizientesten Demodulationseigenschaften wurde als Zeilensensor mit 108 Pixeln und als Bildsensor mit 64 x 25 Pixeln fabriziert. Beide Sensoren sind in separaten Entfernungskameras implementiert, die jeweils modulierte LEDs als Lichtquelle benutzen und einen Entfernungsbereich von 7.5 Metern oder sogar 15 Metern abdecken. Für nicht kooperative diffus reflektierende Ziele erreichen beide Kameras eine Auflösung von wenigen Zentimetern. Mit Ausnahme der Bildsensoren werden in den Distanzkameras ausschließlich optische und elektrische Standardkomponenten eingesetzt. Bei einer Integrationszeit von 50 ms (20 Hz 3D-Bild-Wiederholrate) genügt für eine Distanzauflösung von 5 Zentimetern eine optische Leistung von 600 Femtowatt pro Pixel (Wellenlänge des Lichts: 630 nm). Bei dieser niedrigen optischen Leistung werden statistisch lediglich 0.06 Elektronen innerhalb einer Modulationsperiode von 50 ns akkumuliert (20 MHz Modulationsfrequenz), also nur ein Elektron in jeder 16ten Periode.

Wir führen eine ausführliche Analyse der Einflüsse von Nichtlinearitäten innerhalb der Elektronik, von Aliasing Effekten, von der Integrationszeit und von den Modulationssignalen durch. Außerdem stellen wir eine optische Leistungsbilanz auf und präsentieren eine Formel zur Voraussage der Distanzauflösung als Funktion des Verhältnisses der Hintergrundhelligkeit zur Intensität des aktiven optischen Signals sowie weiteren Kamera- und Szenenparametern. Die Gültigkeit dieser Formel wird durch Simulationen und echte Messungen verifiziert, so daß wir in der Lage sind, für eine vorgegebene Integrationszeit, optische Leistung und Zieldistanz und -reflektivität die Meßgenauigkeit des Systems vorherzusagen.

Wir demonstrieren die ersten erfolgreichen Realisierungen bildgebender, rein elektronischer 3D-Entfernungskameras nach dem Laufzeitprinzip ohne bewegte Teile, welche auf kundenspezifischen PhotoASICS beruhen. Die erzielten Meßresultate dieser Kameras sind beinahe ausschließlich vom natürlichen Quantenrauschen das Lichts limitiert. Wir zeigen, daß das optische 3D TOF- Verfahren ein exzellentes kostengünstiges Werkzeug für alle modernen berührungslosen optischen Meßaufgaben zur Überwachung relativer Objektpositionen oder -bewegungen ist.

1. Introduction

One can find time-of-flight measurement systems in nature's navigation solutions for dolphins and bats, which use this sensor system for both navigation and object tracking (hunting). Moreover, humans have also used TOF techniques since a long time, for example by dropping rocks down deep holes and waiting for the echo or by trying to estimate the distance of a lightning discharge by evaluating the time delay between the lightning and the associated thunder. These TOF methods are based on the propagation time of sound [STR].

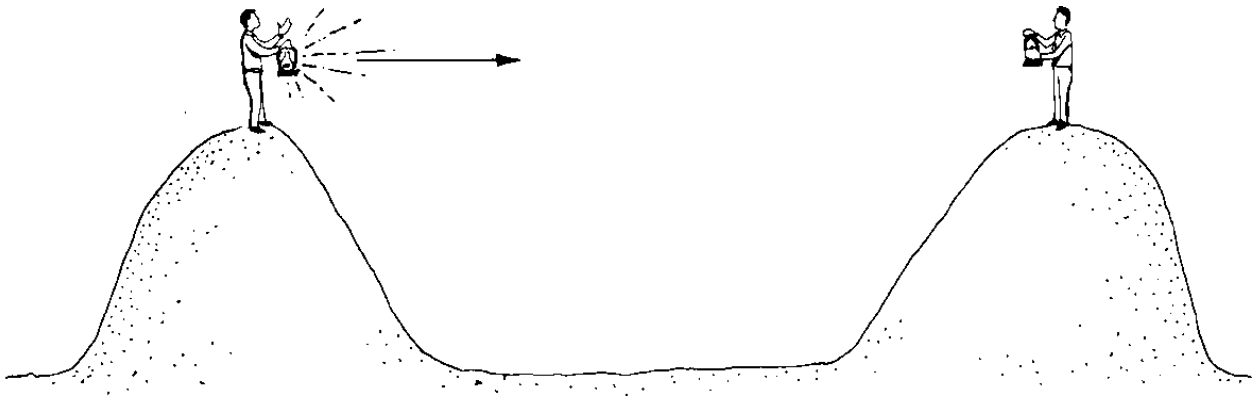

Figure 1.1 *Galileo Galilei's experiment of the early 17th century to prove that light travels through free space rather than existing instantaneously [HOF].*

The actual pioneer in optical time-of-flight measurement was Galileo Galilei, who was probably the first to imagine light as a kind of active event, something that travels through free space rather than existing instantaneously. He also tried to prove his idea by a simple experiment, described in one of his "Discorsi" that he wrote under house arrest in the early 17th century. In the dark of night he placed two men (A and B) onto two neighboring hills, about 1 kilometer away from each other. Each of them carried a lantern, covered by their hands, so that one could not see the other's lantern light initially. The experiment started with person A uncovering his lantern and waiting for B to uncover his lantern as well, as soon as he saw the

first lantern's light (c.f. **Figure 1.1**). That way Galilei hoped to measure the propagation time that the light needed to travel from person A to person B and back to A, a hopeless attempt from today's point of view, since we know that the light only needs 6.6 microseconds to travel the distance of 2 kilometers. So much more remarkable is Galilei's conclusion from this experience. We know that Galilei was an excellent engineer: Before carrying out his experiment, he trained the experimenters to react quickly and measured their reaction times. He found that the measured speed of light was of the same order of magnitude as the reaction times that he had previously measured. Therefore, he concluded that either light exists instantaneously, as physics has taught previously, or that it propagates so incredibly quickly that it was not possible to measure its speed with the proposed experiment. A little later, in 1676 it was Roemer who succeeded in measuring the speed of light by using the departures from predicted eclipse times of a Jupiter moon, strictly speaking also a TOF experiment.

It was only 200 years later, in1849, that Fizeau was more successful in measuring the time of flight on earth. He built a more precise, more mature and complicated experimental setup (illustrated in **Figure 1.2**) in the suburbs of Paris. Fizeau used a rotating cogwheel as a mechanical shutter for a focused light beam. This pulsed beam was projected onto a mirror, located 8633 m away. For an appropriate rotation speed of the cogwheel the complete light packet, which had been transmitted by a gap in the wheel was obstructed by a tooth after being reflected by the distant mirror, so that it could not be seen behind the cogwheel. As the distance and the shutter rate (rotation period divided by the number of teeth) were known, Fizeau could calculate the speed of light. With this early TOF experiment he obtained an astonishingly precise result of $3.153 \cdot 10^8$ m/s.

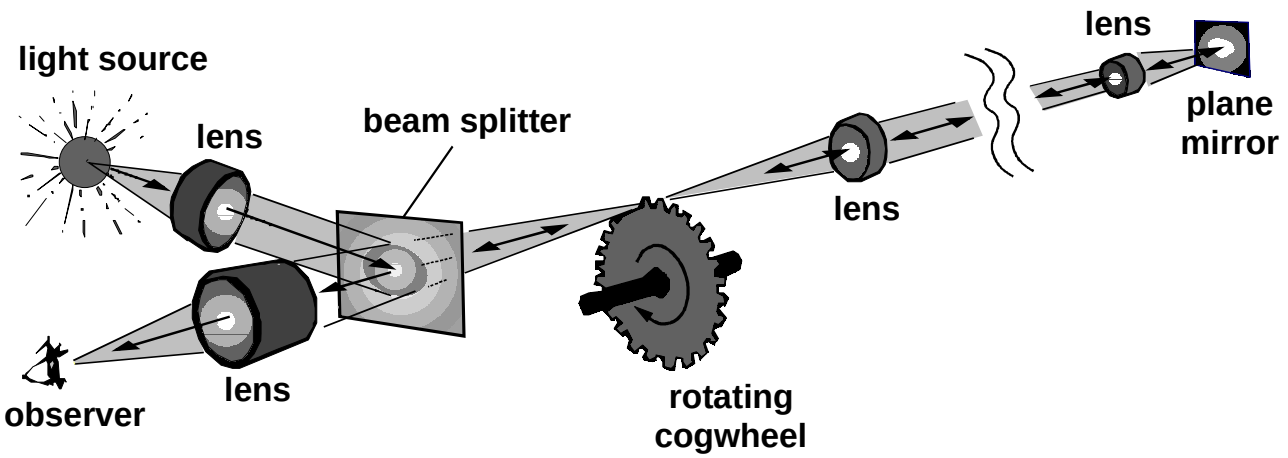

Figure 1.2 *Fizeau's experimental setup used to determine the speed of light in 1849.*

Today, the speed of light ($c=\lambda\cdot\nu$) can be determined much more precisely, for example by the simultaneous measurement of frequency ν and wavelength λ of a stabilized helium-neon-laser or by the frequency measurement of an electromagnetic wave in a cavity resonator [BRK]. Since 1983 the speed of light has been fixed by definition to $c=2.99792458\cdot10^8$ m/s. With this precise knowledge of the velocity of light, it is thus possible to modify Galilei's or Fizeau's experiments and to measure distances. This can be done "simply" by measuring the elapsed time during which light travels from a transmitter to the target to be measured and back to the receiver, as illustrated in **Figure 1.3**. In practice, the active light source and the receiver are located very close to each other. This facilitates a compact setup and avoids shadowing effects.

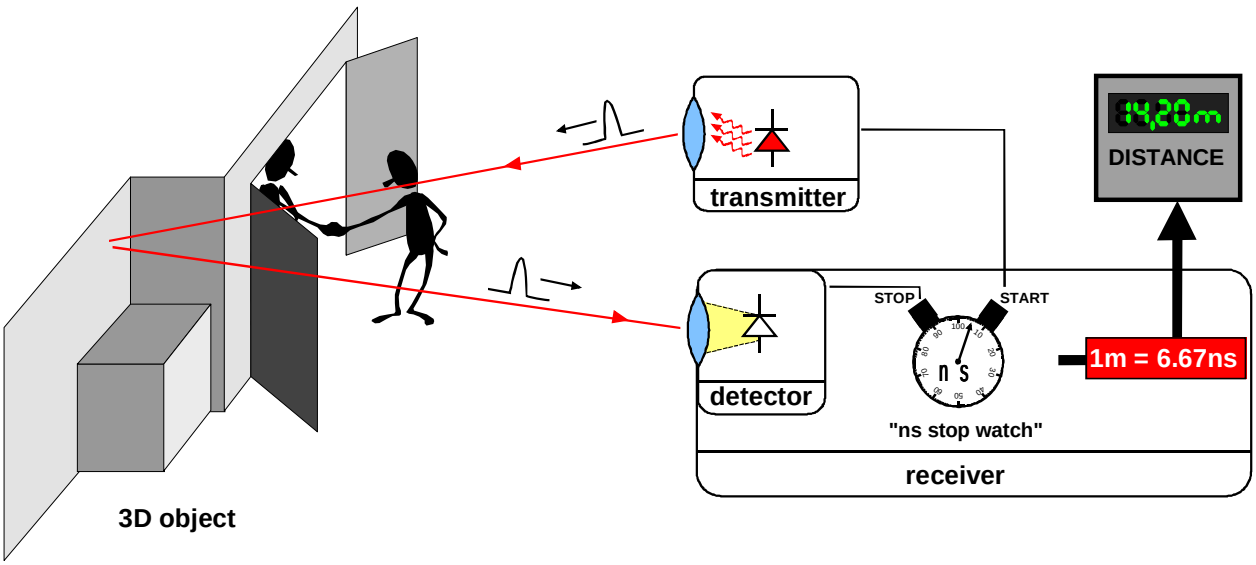

Figure 1.3 *Basic principle of an (optical) TOF ranging system.*

The basic principle can be summarized as follows: A source emits a light pulse and starts a highly accurate stopwatch. The light pulse travels to the target and back. Reception of the light pulse by the detector mechanism stops the stopwatch, which now shows the time of flight of the light pulse. Considering the fact that the light pulse travels the distance twice (forth and back), a measured time of 6.67 ns corresponds to a distance of one meter. An essential property of this setup is the fact that emitter and detector are synchronous. At this point one can recognize a significant advantage of time-of-flight over a triangulation based ranging system: The TOF ranging technique does not produce incomplete range data (no shadow effects) because illumination and observation directions are collinear. It is obvious that the basic problem of establishing a TOF-ranging system is the realization of a high accuracy time-measurement mechanism. For a resolution of 1cm, an accuracy of better than 70 picoseconds is required. The stringent requirements for the receiver are one reason that, although already in 1903 Hulsmeyer carried out some experiments with electromagnetic radar, only in 1968 was Koechner one of the first to introduce an optical TOF ranging system [KOE]. Another problem was the lack of high power (laser-) light sources. All these TOF ranging systems actually only measure the distance to a point (1D). In order to gain 3D information, the laser beam has to be scanned over the scene in two directions. This requires high accuracy laser scanners, which are mostly bulky and sensitive to vibrations.

Propagation time, however, is not the only property of light that is important for this dissertation. In the early 1900's another property of light was discovered, the so-called photoelectric effect. This is the ability of light to interact with matter, either liberating electrons from a metal plate, for example (external photoelectric effect or photoemission) or generating electron-hole pairs in semiconductor materials (internal photoelectric effect or photoconduction). Both effects can be explained by quantum physics. Albert Einstein as the first to understand the external photoelectric effect earned the Nobel Price for his explanation.

The discovery of this photoelectric effect opened the doors to electronic image sensing. Already in 1939 the first electronic imaging devices, so called Orthicons (later Vidikons), were introduced. They are based on electron tubes and have been gradually replaced by solid-state cameras with the introduction of the CCD (Charge Coupled Device) in 1971 [BOY, AME]. This all-solid-state imaging device has dominated the optoelectronic market for more than two decades now. Only in the last few years has CMOS (Complementary Metal Oxide Semiconductor) technology definitely entered the imaging market [FOS]. This technology, mainly driven by the computer industry, is not only widely available and cheaper than CCD technology, the classical technology for solid-state imaging devices, but CMOS also makes it possible to implement additional functionality on-chip. Today's CMOS sensors can offer, for example, A/D- conversion and arbitrary access to individual pixels, enabling the definition of ROI's (Regions Of Interest) [BLC]. In contrast to CCDs, CMOS sensors can be operated with low voltages (<5 V) and they consume little power. Both high resolution and high speed CMOS APS sensors are available and the image quality is gradually approaching CCD performance [LAX, VOG]. Additionally, a logarithmic response can be realized relatively easily, resulting in an enormous dynamic range (>130 dB) [VIZ, BLC]. CMOS APS technology is also used to realize so-called smart pixels, image sensors with special functionality, such as temporal or local convolution, stereo vision, color vision, motion detection or velocity measurement, often inspired by visual systems found in nature [MOI].

Until the middle of the 70's, light barriers were almost exclusively used in machine vision. Only at the end of the 70's first video cameras entered the machine vision market; they were used for object recognition and surveillance. Semiconductor imagers emerged only in the middle of the 80's [KAP].

With this dissertation, both highly interesting and powerful fields of optoelectronics are combined for the first time: TOF-range measurement and customized image sensors with special functionality. We demonstrate an array of monolithically integrated pixels, where each pixel contains the complete demodulating receiver of the TOF system. This development represents an enormous improvement for the field of 3D TOF ranging. Instead of scanning a modulated beam over the scene and serially taking point distance measurements to combine them into a 3D image, the range measurements for all observed points in the scene are now performed in parallel by the individual pixels. The actual correlation process between the received light and the synchronous reference signal, which is the essential process to measure the time delay, is performed in each pixel, immediately after the light is detected. All other electronic components within the following signal processing chain in the range camera system are more or less uncritical, since the high-speed demodulation process is already performed within the detection device. This is another advantage over conventional TOF systems, in which phase drifts of the system due to temperature variations and aging of critical electrical components are a serious problem, requiring calibrating reference measurements.

This work is subdivided into seven chapters:

Chapter 2 roughly compares time-of-flight measurement with the other state-of-the-art measurement principles: optical interferometry and triangulation. The basic working principles will be discussed, as well as typical advantages and disadvantages. Application examples will be given. Of the huge variety of operation principles for TOF ranging, a theoretical description of homodyne TOF-measurement is derived, with emphasis on the relevant questions for the four-phase measurement technique used in this work. In this homodyne operation mode, the phase delay (rather than the time delay) of a modulated light wave is measured. It is shown that by demodulating the incoming modulated light, the modulation signal's amplitude and phase can be extracted. In particular, the influence of system non-linearities, the integrative nature of natural sampling, the choice of modulation signal, the total integration time and aliasing effects are discussed in detail. It is shown that the four phase measurement technique is insensitive to 1^{st} and 2^{nd} order non-linearities and to even harmonics, assuming properly chosen integration times for the sampling points.

Chapter 3 gives a short overview and comparison of CCD and CMOS image sensors. It is pointed out that we have to distinguish between CCD principle and CCD technology, since the latter is only a dedicated, optimized process for large area CCD imagers. The CCD principle can also be realized in (slightly modified) CMOS processes. We have used a 2.0µm CMOS/CCD process for all monolithical implementations presented in this work. This process makes it possible to realize CCDs with a charge transfer efficiency (CTE) between 96 % and 99.6 % at 20 MHz transport frequency, depending on the number of electrons to be transported (96 %: 10,000 e^-, 99.6 %: 1'000'000 e^-). Dedicated CCD processes reach typical CTE values of 99.9998 % and better. In spite of the inferior CTE performance compared with a CCD process, the availability of the CCD principle offers enormous capabilities, such as virtually noise-free single electron level signal addition or fast signal sampling. For these useful properties, which have not been demonstrated with any transistor-based CMOS circuitry so far, a fair CCD performance is sufficient. This is of essential importance for an economic product development, since (1) CMOS processes are available as Multi-Project-Wafers (MPWs) for affordable prototyping and (2) additional functionality such as A/D conversion or any kind of signal processing can easily be implemented on chip. The advantages of both CCD and CMOS will be pointed out. The chapter is completed by an overview of those characteristics of silicon images sensors in general, that are of special interest for the underlying TOF-application: spectral and temporal response, optical fill factor and noise sources.

Since optical TOF ranging uses active illumination, an optical power budget is very important. In **Chapter 4** we show the relations between the optical power of the light source, the number of electrons generated in a pixel of the imager and the resulting output voltage swing. This budget is influenced by the power and wavelength of the light source, the color, reflectivity and distance of the illuminated and imaged surface, the choice of optics of the camera as well as the quantum efficiency, integration time and internal electrical amplification of the image sensor. Also an estimation of the resolution limit is carried out. For this calculation, the quantum noise is mainly considered as a final theoretical limitation. Together with the power budget, the range accuracy can then be calculated depending on the nature of the target and the technical properties of the TOF-camera.

The key element of the new 3D-range camera, the demodulation-pixel imager, is introduced in **Chapter 5**. We show that a phase delay can be measured simply by electrooptically sampling the received modulated light. After the definition and an overview of the required properties of demodulation pixels, several implemented solutions will be introduced and their working principle will be described. The pixel layout with the best performance will be treated in more detail. Characterizing measurements will show its excellent performance even at 20 MHz modulation frequency and the influence of control signal amplitude, modulation frequency and wavelength and optical power of the modulated light source on both measured contrast and time accuracy. For an optical power of only 600 fW per pixel, where only one electron is generated, statistically speaking, every 16^{th} modulation period (equivalent photocurrent: 200 fA), the measured time resolution is better than 300 picoseconds (modulation frequency: 20 MHz, integration time 4·12.5 ms=50 ms; 20 Hz frame rate). This small amount of received radiation power is therefore sufficient for a distance resolution of better than 5 cm, i.e. 0.67 % of the unambiguous distance range of 7.5 meters. A comparison of the measured results with the theoretical limitations deduced in Chapter 4 shows an excellent fit.

Based on this pixel structure, two sensor arrays, a 108-pixel line and a 64x25-pixel imager, have been implemented and build into two separate range camera systems. In **Chapter 6** we describe both, the sensor implementations and the complete camera systems in detail. Finally, the first real distance measurements carried out with these camera systems are presented. Again, the accuracy achieved agrees reasonably well with the theory. As the demodulation sensor not only delivers the phase information in every pixel but at the same time modulation amplitude and background information, the 3D-camera offers both 3D images and conventional 2D gray level images.

A brief summary and an assessment of future developments and possible improvements close this work.

2. Optical TOF range measurement

The basic principles of optical range measurement techniques (1) triangulation, (2) interferometry and (3) time-of-flight are introduced in this chapter. All these techniques mostly work with light, i.e. electromagnetic radiation fields in the wavelength range of 400-1000 nanometers (visible and NIR spectrum). We present a rough description of the basic working principles. The advantages and disadvantages of each principle are discussed and some examples are also given. More detailed and broader overviews over optical ranging principles can be found in the references [KAP], [BES], [ENG], [EN2], [SC1]. **Figure 2.1** shows the family tree of contactless 3D shape measurement techniques.

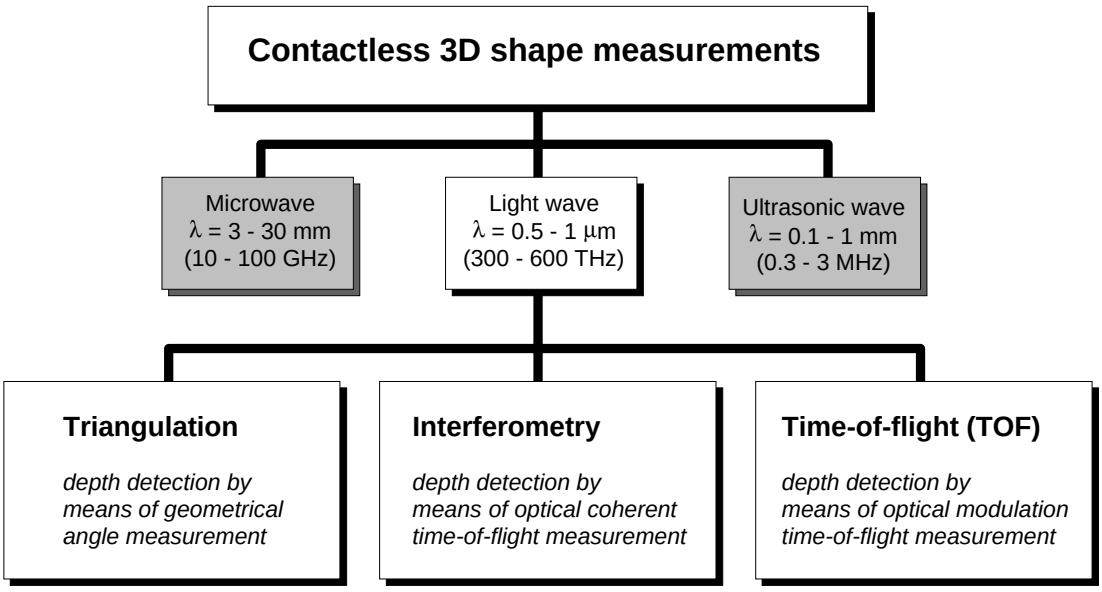

Figure 2.1 *Family tree of contactless 3D shape measurement [SC1].*

Since TOF measurement is the underlying principle of this work, it is discussed in more detail. The first part of this chapter is closed by a discussion and a comparison of the different ranging techniques. It should be mentioned that also microwave (λ=3–30 mm) and ultrasound (λ=0.1-1 mm) techniques have their application-specific advantages. However, they are not included in this comparison. Due to diffraction limitations, both techniques are not suited for range measurements with high angular resolution, at an acceptable size of the

measurement system. They find their applications in differential GPS or synthetic aperture radar (SAR) [SC1].

Out of a large variety of modulation techniques for TOF, homodyne phase-shift modulation is chosen for the operation of the ranging sensors introduced in this work. Therefore, in the second part of this chapter, the equations will be derived for the four-phase realization of homodyne modulation. We show that sampling is always also a correlation process and analyze theoretically the influences of sampling interval, modulation signal and integration time on the result of demodulation and the system performance. Aliasing effects are discussed and it is shown that 1st and 2nd order non-linearities and even harmonics have no influence on the four-phase algorithm.

2.1 Overview of range measurement techniques

2.1.1 Triangulation

This ranging technique has been known and used by nature for millions of years. It is, in the form of stereo-vision together with the depth-of-focus system (which so to speak also belongs to triangulation systems), the basis for human depth perception. Triangulation is a geometrical approach, where the target is one point of a triangle whose two remaining points are known parts of the measurement system. The distance of the target can then be determined by measuring the triangle's angles or the triangulation base. Literature distinguishes passive and active triangulation techniques. Both principles are illustrated in **Figure 2.2**.

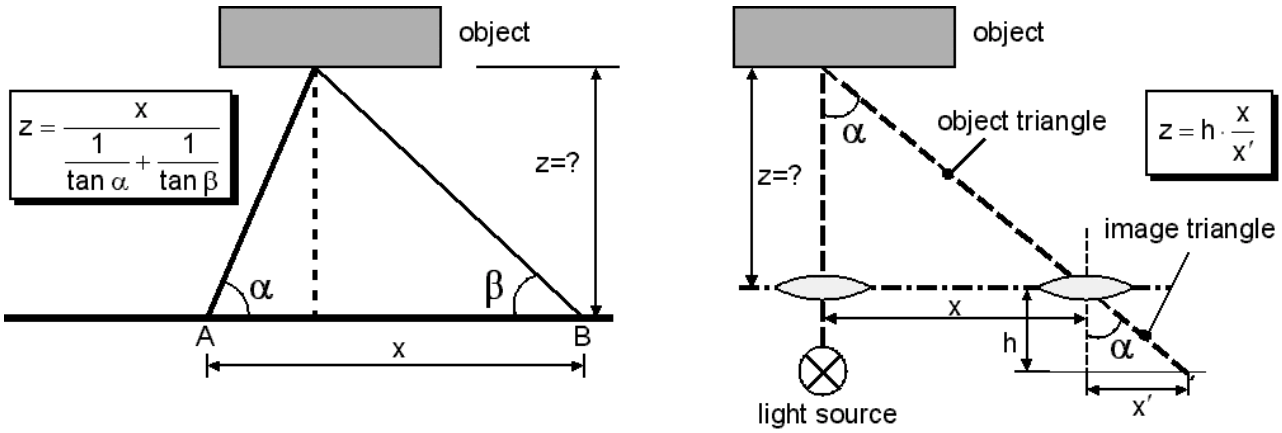

Figure 2.2 *Principles of passive (left) and active (right) triangulation rangefinding.*

Passive techniques rely on observing the same point from two different sites A and B of known distance x and measuring the viewing angles α and β with respect to the base AB. The observed point's distance z can then be calculated using the following equation:

$$z = \frac{x}{\frac{1}{\tan\alpha} + \frac{1}{\tan\beta}} \qquad \textbf{Equation 2.1}$$

Since each point to measure must be identified from both viewing positions unambiguously, passive triangulation techniques require a scene with high contrast. Stereovision is one famous 3D realization of passive triangulation [MAZ]. This technique uses at least two cameras to observe the scene from different angles.

Using 2D-correlation, typical object features are found and compared in both images. From the position of each feature's centroid in both separate images, the angles α and β can be deduced and the distance can be calculated with **Equation 2.1**, assuming that the distance of the cameras with respect to each other, as well as their orientation are known. The computational effort must not be underestimated. Shadowing effects are also typical problems with which all triangulation systems have to cope. Stereovision works pretty well for certain defined scenes, preferably chosen with rich contrast and relatively flat objects. For typical industrial scenes, however, it is often not suitable. Though the shadowing problem can be minimized by enlarging the number of cameras and realizing "multiple viewpoint triangulation systems", this improvement has to be paid for by an enormous increase in computation. Nevertheless, shadowing and the need for significant contrast in the targeted scene remain a problem. Additionally, cost and overall system size, one major drawback of triangulation systems anyhow, increase with the number of cameras. Another famous member of passive triangulation systems is the theodolite.

Active triangulation, as illustrated in **Figure 2.2**, uses a light source to project a point (in the simplest case) to the scene, which is observed by a position sensitive detector. Rather than measuring angles directly, active triangulation is based on the similarity of triangles, the object triangle and the image triangle, which is fully defined by the optical axis of the imaging device, the focal length h of the system and the position of the point projection x' on the detector. With knowledge of the displacement x of the light source from the imaging device, the distance z of the target can be determined:

$$z = h \cdot \frac{x}{x'} \qquad \textbf{Equation 2.2}$$

For a good distance resolution δz, small absolute distances z, a large triangulation base x and a good local detector resolution $\delta x'$ are required. δz estimates to:

$$\delta z = \frac{1}{h} \cdot \frac{z^2}{x} \cdot \delta x' \qquad \textbf{Equation 2.3}$$

With laser point projection, 3D information can only be gained by scanning the laser point over the scene and thus sequentially acquiring a cloud of range points [RIX, BER]. A faster approach is to project a line (or light sheet) onto the 3D scene. By replacing the position sensitive line sensor by an imaging array, a 2D distance

profile can then be measured with one shot, and for 3D data the scan only needs to be performed in one direction (light sheet triangulation). In industrial inspection applications, such a 1D scan is often available free of cost, since the objects to measure are moving anyway, for example on an assembly-line. [KRA] presents such a scanning 3D camera working with active light sheet triangulation and delivering 50 depth images per second in CCIR video format.

Further advanced techniques even use 2D structured light illumination and 2D imaging to perform 3D triangulation measurements without scanning. The most important members of this structured light group are phase shifting projected fringe, Gray code approach [BRE], phase shifting moiré [DOR], coded binary patterns, random texture [BES] or color-coded light. They typically use LCD (Liquid Crystal Display) projectors for the projection of the structured patterns.

Triangulation systems are available for applications from mm-range (depth of focus) to 100km range (photogrammetry). Their main drawback is that for a good resolution they have to be large in size, since they need a large triangulation base. On the other hand, the larger this triangulation base, the more they are restricted by shadowing effects. Also, 3D triangulation systems are relatively expensive since they require fast LCD projectors (only active systems) as well as large computational power.

2.1.2 Interferometry

Interferometry is described by the superposition of two monochromatic waves of frequency ν, amplitude U_1 and U_2 and phase φ_1 and φ_2, respectively, resulting in another monochromatic wave of the same frequency ν, but with different phase and different amplitude [SAL]. In the easiest interferometer setup, the Michelson interferometer, illustrated in **Figure 2.3**, a laser beam (monochromatic and coherent) is split into two rays by a beam splitter. One ray is projected to a mirror of constant displacement x_1 (reference path) whereas the other beam is targeted on the object of variable distance x_2 (measurement path). Both beams are reflected back to the beam splitter, which projects them onto an integrating detector.

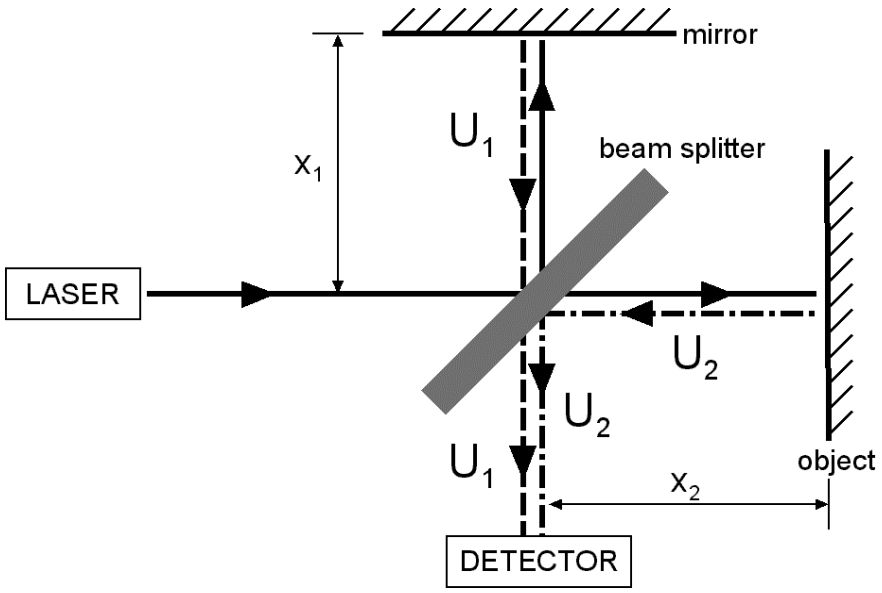

Figure 2.3 *Working principle of Michelson interferometer*

With the reference wave U_1 and the object wave U_2 defined as

$$U_1 = \sqrt{I_1} \cdot e^{j\frac{2\pi \cdot (2 \cdot x_1)}{\lambda}}$$
$$U_2 = \sqrt{I_2} \cdot e^{j\frac{2\pi \cdot (2 \cdot x_2)}{\lambda}}$$

Equation 2.4

(I_1 and I_2 are the optical intensities) we obtain the interference equation

$$I = I_1 + I_2 + 2\sqrt{I_1 \cdot I_2} \cdot \cos\left\{\frac{2\pi \cdot (2 \cdot x_2 - 2 \cdot x_1)}{\lambda}\right\}$$

Equation 2.5

Note that we have to consider the double path lengths $2 \cdot x_1$ and $2 \cdot x_2$ respectively because the light waves travel the paths twice, forth and back. For equal reference and measurement path x_1 and x_2, as well as for path differences of exact multiples of the light's half wavelength $\lambda/2$, the intensity on the detector reaches a maximum. This case is denoted as *constructive interference*. For a path difference $\lambda/4$ or $n \cdot \lambda/2 + \lambda/4$, the intensity tends to a minimum: *destructive interference*.

A movement of the object away from the system (or towards the system) results in an intensity peak of the interferogram (constructive interference) each time the object has moved by a multiple of the laser's half wavelength. By recording and counting the number of minimum-maximum transitions in the interference pattern over time, when the object moves, the distance of movement can be incrementally determined at an accuracy of the light's wavelength or even better [CRE]. Interferometry therefore uses the light's built-in scale, its wavelength, for performing

highly accurate relative distance measurements. This technique can be equivalently interpreted as a time-of-flight principle, since the runtime difference between the reference and measurement path is evaluated.

Several other interferometer setups can be found, for example in [SAL] or [HEC]. The principal drawback of classical interferometers is that absolute distance measurements are not possible and the unambiguous distance range is as low as half the wavelength. Enhanced approaches overcome this restriction. One nice example is *Multiple-wavelength interferometry,* where two very closely spaced wavelengths are used at the same time. That way beat frequencies down to GHz or even MHz range are synthetically generated, enabling absolute measurements over several tens of centimeters at $\lambda/100$ resolution [ZIM, SC1]. Especially important for high sensitivity 3D deformation measurements is the *electronic speckle pattern interferometry* (ESPI), where a reference wave front interferes with the speckle pattern reflected by the investigated object. With a conventional CCD camera the speckle interferogram, carrying information of the object deformation, can then be acquired. Like conventional interferometers, ESPI can also be improved in sensitivity and measurement range by the multiple-wavelength technique. [ENG]

Another way to enlarge the measurement range is to use light sources of low coherence length. Such interferometers (*white-light interferometry* or *low-coherence interferometry* [BOU]) make use of the fact that only coherent light shows interference effects. If the optical path difference between the measurement and reference paths is higher than the coherence length of the light, no interference effects appear. For a path difference of the order of magnitude of the coherence length, however, interference takes place. The strength of interference, depends on the path difference between the reference and object beams, and thus absolute distances can be measured.

Interferometry finds its applications predominantly for highly accurate measurements ($\lambda/100$ to $\lambda/1000$) over small distances ranging from micrometers to several centimeters.

2.1.3 Time-of-flight

Similarly to interferometry, we can measure an absolute distance if we manage to measure the absolute time that a light pulse needs to travel from a target to a reference point, the detector. This indirect distance measurement is possible since we know the speed of light very precisely: $c = 3 \cdot 10^8$ m/s = 2·150 m/µs = 2·0.15 m/ns = 2·0.15 mm/ps [BRK, BRR]. In practice, the active light source and the receiver are located very closely to each other. This facilitates a compact setup and avoids shadowing effects. The basic principle of a TOF-ranging system is illustrated in **Figure 1.3**. A source emits a light pulse and starts a high accuracy stopwatch in the detector. The light pulse travels to the target and back. Reception of the light pulse by the detector mechanism stops the time measurement and the stopwatch now shows the time of flight of the light pulse. Considering the fact that the light pulse travels the path twice (forth and back) a measured time of 6.67 ns corresponds to a distance of 1 m and a time accuracy of better than seven picoseconds is required for a distance resolution of 1 mm. An essential property of this setup is the fact that emitter and detector are operated synchronously. At this point one can already recognize a significant advantage of time-of-flight over a triangulation system: The TOF ranging technique does not produce incomplete range data (no shadow effects) because illumination and observation directions can be collinear.

Also, the basic problem of establishing a TOF-ranging system is obvious here: the realization of a high accuracy time measurement. In the following subchapters different operation modes and the associated components (light source, modulator, demodulator, detector) for TOF applications are introduced.

I. MODULATION SIGNALS

Generally, TOF ranging systems use pulsed modulation [MOR] or continuous (CW) modulation [BEH] of the light source; combinations of both are also possible (e.g. pseudo-noise modulation). Both modulation principles have their specific advantages and disadvantages, which are treated in the following. **Figure 2.4** gives an overview over the different types of modulation signals available for TOF systems.

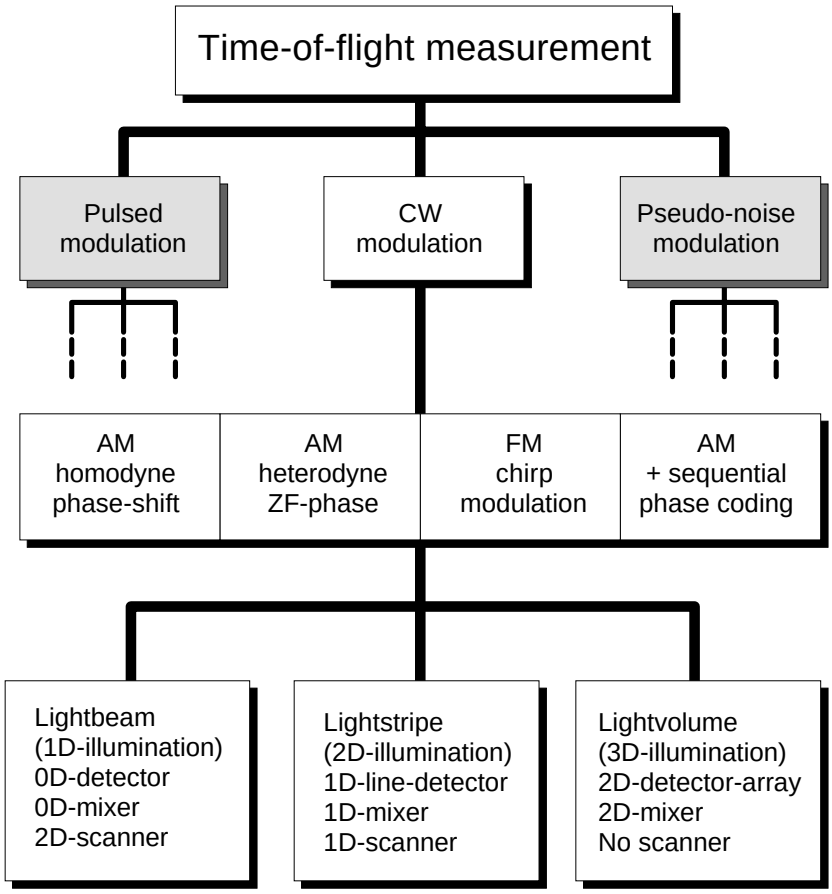

Figure 2.4 *Family tree of TOF modulation principles and 3D-TOF realization [SC1].*

Pulsed modulation

Pulsed light operation, as illustrated in **Figure 1.3**, is the most obvious method of operating a TOF system, because the time of flight is measured directly. The actual time measurement is performed by correlation of a start and stop signal with a parallel running counter. The advantage of using pulsed light is the possibility of transmitting a high amount of energy in a very short time. Thus the influence of background illumination can be reduced and a high short-term optical signal-to-noise (and signal-to-background) ratio is attained while maintaining a low mean value of optical power. This is an important factor for eye safety, which is the limiting criterion for many measurement applications. Furthermore, it reduces the demand on a very high sensitivity and signal-to-noise ratio of the detector, thus enabling long distance measurements. However, at the same time the receiver must offer high dynamics and a large bandwidth. The basic problem for the receiving path is to detect exactly the arrival time of the back-scattered light pulse.

This is because (1) the optical threshold is not a fixed value but changes with background and distance of the object, and (2) atmospheric attenuation leads to dispersion of the light pulse and flattens the slope of the received pulse. Also, it is tricky to produce very short light pulses with fast rise and fall times, which are necessary to assure an accurate detection of the incoming light pulse. Current lasers or laser diodes, the only optical elements offering the required short pulse widths at sufficiently high optical power, still suffer from relatively low repetition rates for the pulses, which typically are in the range of some 10 kHz. Such low repetition rates drastically restrict the frame rate for TOF scanners.

Nevertheless, due to the advantages gained concerning signal-to-background ratio, most of today's TOF rangefinders are operated with pulsed modulation. [LEI, RIG]

Continuous wave (CW) modulation

CW-modulation offers the possibility of using alternative modulation-, demodulation- and detection-mechanisms. Compared to pulsed modulation a larger variety of light sources is available for this mode of operation because extremely fast rise and fall times are not required. Different shapes of signals are possible; sinusoidal waves or square waves are only some examples. For CW-modulation generally the phase difference between sent and received signals is measured, rather than directly measuring a light pulse's turn-around time. As the modulation frequency is known, this measured phase directly corresponds to the time of flight, the quantity of interest.

The use of several modulation frequencies is known as *heterodyne operation* or *frequency shifting* [SC3]. Heterodyne mixing especially offers the powerful possibility of synthetically generating beat frequencies. Thus the unambiguous distance range is increased while maintaining absolute accuracy. However, this requires relatively high bandwidth and linearity for both transmitting and receiving path.

In this work we mainly whish to demonstrate the possibility of realizing 3D-TOF with custom photoASICs. Rather than examining all possible modulation modes, we focus on *homodyne operation (phase shifting technique)*, as discussed in more detail in **Chapter 2.2**. The homodyne operation works with one single frequency and does not necessarily require a large bandwidth.

Additionally, a large variety of intelligent CW modulation techniques is available. It is worth mentioning *pseudo-random modulation* and *chirping (continuous frequency modulation)* [XU]. Pseudo-random modulation, where pseudo noise words (PN modulation) are continuously repeated, offers the advantage of a very high peak in the autocorrelation function. This technique, originally developed for communication technology, is therefore very noise-robust [SC2].

A combination of both CW modulation and pulsed modulation would be ideal, combining their specific advantages of (1) better optical signal-to-background ratio than available from pure CW-modulation, (2) increased eye safety due to a low mean value of optical power and (3) larger freedom in choosing modulation signals and components. Combination in this content means, for example, a “pulsed sine” operation, i.e. a sequence of 1 ms high power sine modulation followed by 9 ms of optical dead time. This dead time can be used for example for post processing tasks.

II. COMPONENTS

In the following, the necessary components for TOF systems will be described and associated with the corresponding modulation technique.

Modulated light sources and electrooptical modulators

The emitted light can be modulated in several ways. The use of LEDs or lasers allows direct modulation of the light source by controlling the electrical current. Since the light sent does not have to be coherent or monochromatic, other light sources are possible, in combination with additional large aperture optical modulators such as Kerr cells [HEC], Pockels cells [HEC, SC3], mechanical shutters or liquid crystal shutters. Pulsed operation with fast rise and fall times is only possible with directly controlled laser sources that allow pulses of less than ten femtoseconds [SUT]. The different light sources and modulators can be characterized in terms of light intensity, cut-off frequency, linearity, wavelength, modulation depth (the ratio of signal amplitude to signal offset), eye safety properties, size and price.

LEDs are relatively inexpensive. They can be modulated up to some 100 MHz with a 100% modulation depth and a very high linearity. They are available for a wide

range of wavelengths from blue (400 nm) to the near infrared (1200 nm) with an optical power of up to several milliwatts. Lasers, even laser diodes, are much more expensive than LEDs and are often larger. However, they offer more optical power and are suited for operation up to some GHz, also at a wide range of wavelengths [SAL]. Practically, lasers and laser diodes are the only light sources suitable for pulsed TOF operation. All other light sources introduced here are actually used for CW modulated light, due to the reduced bandwidth requirements.

Kerr cells are based on the quadratic electro-optic effect, where the polarization of a polarized beam is rotated depending on the applied voltage. Together with a polarizer and a modulated control voltage of the cell, a polarized incoming beam can be modulated in intensity. Kerr cells can be used as modulators up to 10 GHz but voltages as high as 30 kV must be switched at this speed [HEC]. Pockels cells, making use of the linear electro-optic effect (pockels effect), work very similarly and also require polarized light for operation. Their cut-off frequency of more than 25 GHz is even higher than that of Kerr cells. The driving voltage requirements are a factor of 10 lower than for an equivalent Kerr cell. However, the Pockels cell still requires some kilovolts to switch from transparent to opaque mode. Therefore, the practical cut-off frequency, which is limited by the cell's capacitance, reaches only several hundred MHz [HEC, SAL, XU].

Liquid crystal shutters are limited to some kHz of modulation frequency and are therefore not suited for high-resolution measurement applications in the 10 meter range [SAL]. An interesting alternative, however, might be the realization of a mechanical shutter. Miniaturized air turbines with a rotation speed of 427'000 rpm have been reported [SLO]. If one manages to rotate a light grating disc with such an air turbine, shutter frequencies as high as 1 MHz might become possible. For example, a disc of 10cm diameter and a slot width of 1 mm at the edge of the disc would contain about 150 slots. Such a disc would offer a 1x1 mm^2 shutter aperture while allowing 1 MHz shutter frequency (=150*427000(1/min)/60(s/min)).

Detectors and Demodulation

The easiest and most straightforward way of realizing a TOF-receiver is to use any fast and sensitive electrooptical sensor as a detector. The time of flight can then be determined as follows: a linear analog ramp (or a fast digital counter) is started synchronously with the transmission of a laser pulse. Once the laser pulse reaches the detector the rise of the ramp is stopped. The resulting amplitude is then

proportional to the time of flight. The difficulty of this detection mechanism is the definition of a trigger level for the detector, because the amplitude of the received light strongly depends on the distance, background and the surface to measure.

For 1D-TOF ranging systems, high dynamic, high sensitivity PIN photo diodes or APDs (avalanche photo diodes) are used. PIN photo diodes have a very fast response. Typical cut-off frequencies are 10 GHz and beyond. After the fast detection, the modulated light, now converted to an electrical signal, is electrically demodulated (using sophisticated special purpose ICs) leading to the desired phase difference between transmitter and receiver. This electrical demodulation often suffers from temperature drifts of the electric components involved. Therefore, regular reference measurements and calibration are necessary to ensure reproducible measurements. APDs and photomultiplier tubes [PAR] can be modulated in their sensitivity, enabling a direct demodulation or mixing of the incoming light. Today, TOF rangefinders and TOF laser scanners are available with mm accuracy for cooperative and several cm resolution for non-cooperative targets over a distance of some 10 up to 100 meters and more [LEI, KAI].

All these components only allow a 1D measurement, i.e. the distance measurement of one point in the 3D scene. The operation of many such receivers in parallel appears to be impractical due to large size and enormous demand on additional electronics. Therefore, 2D depth profiles or 3D depth images can only be obtained from such 0D detectors by scanning the light beam over the observed surface. This, however, requires time, because every point has to be measured serially. It also requires mechanical scanners of very high precision. Those scanners are bulky, expensive, and sensitive to vibrations.

III. 3D TOF RANGING

Instead of scanning a laser beam and serially acquiring the range data point-wise, we can illuminate the entire scene with a modulated light surface in order to perform a 3D measurement, as illustrated in **Figure 2.5**. This, however, necessitates the use of a 2D-electrooptical demodulator and detector to measure the distances of some hundreds or thousands of points of the observed scene in parallel.

The 2D detection itself can be performed with CCDs or (active) photodiode arrays, so called active pixel sensors (APS). However, in contrast to discrete photodiodes,

these 2D detectors integrate the incoming light in every pixel and so the temporally coded information is lost. One would need to realize an electrical (de)modulator in every pixel, which demodulates the photocurrent of the pixel's photodiode. In contrast to the 1D-case, where APD point-detectors with modulation capability can be used, for an imaging 3D application such electrical 2D-demodulation devices are not available and would be hard to realize. The demodulation circuitry would have to be extremely sensitive and noise-free. Additionally, it would occupy space and thus lowers the device's optical fill factor.

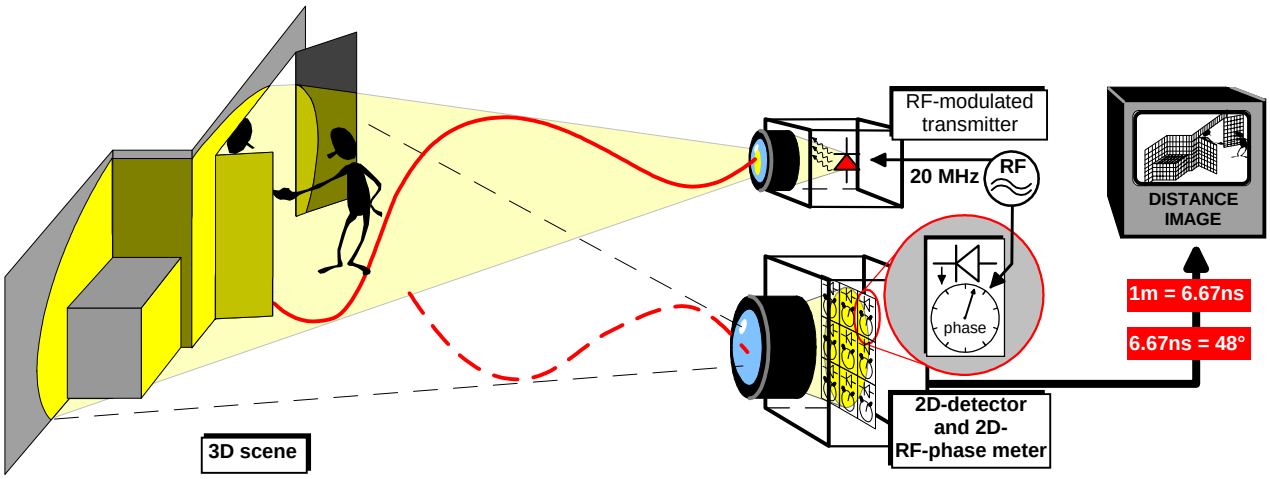

Figure 2.5 *Principle of a non-scanning 3D TOF-camera*

IV. SPECIAL COMPONENTS FOR IMAGING 3D TOF

What can, however, be done is to demodulate the light in the optical domain before it is detected. This can be achieved using large aperture optical modulators, such as Kerr cells or Pockels cells [SC3]. They enable the use of commercially available detector arrays (e.g. CCD or CMOS APS) for the optical to electrical conversion. There is no need for the detectors themselves to be very fast because they only integrate DC images containing the phase information (distance information, respectively), amplitude information and offset information (background image). An interesting alternative is to use a two dimensional photomultiplier tube as optical demodulator: the so-called microchannel plate (MCP) [KA2, PHS, SAL]. An MCP can be switched on and off in less than 500 ps (1 GHz modulation frequency). However, all these devices suffer from relatively high price and a need for elaborate electronics, since voltage amplitudes in the range of some kilovolts are necessary.

A very interesting approach is the gated operation of a conventional 2D camera in combination with pulsed light. This setup has been suggested in [KAP] and [KA1],

where an optical modulator works as an electrooptical shutter with varying sensitivity over time. A similar realization, making use of the built-in electronic shutter of a conventional CCD camera, rather than an additional optical modulator, is described in [DAS]. This system works as follows: A light pulse of some tens of nanoseconds is transmitted by a laser and it synchronously starts the integration of a standard CCD camera. With the electrical shutter mechanism of the CCD camera, only a very short period of time (also some tens of nanoseconds) is integrated. Thus, depending on the distance of the targets, only a fraction of the light pulse arrives before the integration stops. Performing two calibration measurements, one without laser illumination and one with non-pulsed, continuous laser illumination, enables distance calculation. However, compared to the total power consumption of nearly 200 Watts, the distance resolution of ± 20 cm for non cooperative targets in a 10 m range at 7 Hz frame rate is relatively poor. The reason for this low performance is that no repetitive integration is possible; the CCD has to be read out after every short time integration. This leads to a poor signal-to-noise ratio of this realization that can only be compensated by very high optical power of the laser. The power of laser sources, on the other hand, is limited by eye safety regulations.

The restriction of conventional CCDs only allowing one short-time integration, as described above, requires innovative, smarter 2D demodulation arrays realized as customized PhotoASICs. The first such device, realized in CCD technology, was, however, not intended to be used in an optical ranging system but for a 2D-polarimeter [POW]. For simplified 3D TOF measurement without mechanical scanners, the lock-in CCD sensor was invented [SP1-SP4]. Based on these lock-in structures, we present arrays of improved demodulation pixels in **Chapter 5**. In these pixels, CCD gates are arranged such that light generated charge carriers under the photo gate can be moved to different storage sites. This allows fast sampling of incoming light, enabling the measurement of phase and amplitude of the modulated light, as described later in **Section 2.2**. A related architecture, which is operated with modified sinusoidal control signals, is the photonic mixer device (PMD) [SC2, XU]. This device has a modified differential amplifier in every pixel, which integrates the sum and the difference of two demodulation currents, demodulated with 180° phase difference.

With such demodulation pixels, 3D cameras can be realized without any mechanically moving parts and with no need for expensive and elaborate large aperture electrooptical modulators. These 3D cameras of the future, presented in **Chapter 6**, are both inexpensive, small, relatively low-power (compared to existing TOF-systems) and vibration robust.

2.1.4 Discussion

In the previous sections we have introduced the three basic optical measurement principles: triangulation, interferometry and time-of-flight. To measure always means to correlate. Even the trivial process of measuring a distance with a folding rule is a correlation process, where the object to be measured is correlated with the scale of the folding rule. In this context we might describe triangulation for example as a local correlation of imaged projected stripe patterns with the pixel pattern on the image sensor. Interferometry is a temporal correlation or optical interference between the object wave and the reference wave and time-of-flight is the temporal correlation of the received modulation signal (carried by light) with the electrical reference signal. **Figure 2.6** shows a comparison of available implementations in terms of distance range and resolution.

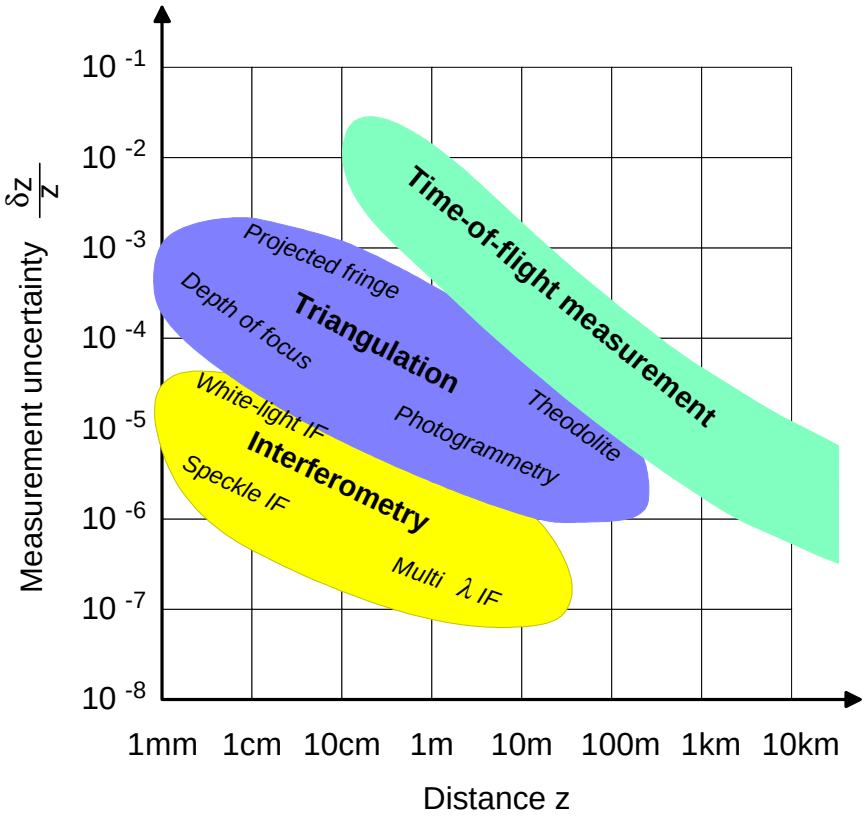

Figure 2.6 *Performance map of conventional optical 3D systems [SC1].*

Absolutely independent of the progress and steady improvements in rangefinders, we experience a continuously improving and rapidly growing field of industry: microelectronics. For sure, each of the optical ranging methods introduced before has profited in its own way from the ongoing miniaturization in microelectronics. However, while triangulation and interferometry saw more cost-effective implementations, their measurement accuracy was not substantially affected. In the case of triangulation, the measurement range and precision is critically determined by the triangulation baseline. Obviously, miniaturization of the complete system leads to a reduced triangulation baseline and therefore to reduced accuracy. The precision in interferometry is basically given by the wavelength of the employed coherent light source, a parameter that cannot be influenced greatly. The situation is completely different for time-of-flight (TOF) range imaging techniques. They have not only become cheaper, smaller and simpler to realize but their measurement accuracy is also increasing steadily. This is because, generally speaking, with decreasing minimum feature size, devices become faster and hence, a better time resolution is possible. Therefore, we believe that the time-of-flight measurement principle will be used in more and more future applications.

2.2 Measuring a signal's amplitude and phase

While in 2.1.3 we have introduced different modulation signals and demodulation concepts, this chapter restricts itself to the description and discussion of homodyne four-phase detection, or lock-in sensing with four sampling points. This technique is used to operate our demodulation pixels introduced in **Chapter 5**. In the following we show how by demodulation and sampling respectively we can measure the amplitude, offset, and above all the phase of a periodic signal (the optical input signal in our TOF application). Also, we treat the influence of signal distortions from the ideal sinusoidal case (square waves, triangle waves, ramp waves, …) – aliasing is of importance in this context – and the influence of system non-linearities

2.2.1 Demodulation and sampling

We know that for our TOF application the phase delay of a modulated light signal must be measured in the receiver. The received light is modulated in intensity and phase, where the phase modulation is caused by the scene's 3D-information. We can retrieve the signal's amplitude and phase by synchronously demodulating the incoming modulated light within the detector. Demodulation of a received modulated signal can be performed by correlation with the original modulation signal. This process is known as cross correlation. The measurement of the cross correlation function at selectively chosen temporal positions (phases) allows the phase of the investigated periodical signal to be determined. The correlation function $\varphi_{sg}(\tau)$ is defined as follows:

$$\varphi_{sg}(\tau) = s(t) \otimes g(t) = \lim_{T\to\infty} \frac{1}{T} \int_{-\frac{T}{2}}^{+\frac{T}{2}} s(t) \cdot g(t+\tau)\, dt \qquad \textbf{Equation 2.6}$$

With the received optical input signal s(t), of modulation amplitude a and phase φ and the demodulation or correlation signal g(t) defined as

$$s(t) = 1 + a \cdot \cos(\varpi t - \varphi) \quad \text{and} \quad g(t) = \cos(\varpi t), \qquad \textbf{Equation 2.7}$$

the correlation function $c(\tau)$ can be calculated:

$$c(\tau) = \varphi_{sg}(\tau) = \left[1 + a \cdot \cos(\varpi\tau - \varphi)\right] \otimes \left[\cos(\varpi\tau)\right]$$
$$= \lim_{T' \to \infty} \frac{1}{T'} \int_{-\frac{T'}{2}}^{+\frac{T'}{2}} \left[1 + a \cdot \cos(\varpi t - \varphi)\right] \cdot \left[\cos(\varpi t + \varpi\tau)\right] dt$$
$$= \frac{a}{2} \cdot \cos(\varphi + \varpi\tau)$$

Equation 2.8

We evaluate this function for different phases $\varpi\tau$. Choosing $\varpi\tau_0$=0°, $\varpi\tau_1$=90°, $\varpi\tau_2$=180° and $\varpi\tau_3$=270° allows us to recalculate the phase φ and amplitude a of the received optical signal s(t). Considering that the received signal is mostly superimposed on a background image, we must add an offset K to the correlation function to obtain the real measured values $C(\tau)=c(\tau)+K$:

$$C(\tau_0) = c(\tau_0) + K = \frac{a}{2} \cdot \cos(\varphi) + K$$
$$C(\tau_1) = c(\tau_1) + K = -\frac{a}{2} \cdot \sin(\varphi) + K$$
$$C(\tau_2) = c(\tau_2) + K = -\frac{a}{2} \cdot \cos(\varphi) + K$$
$$C(\tau_3) = c(\tau_3) + K = \frac{a}{2} \cdot \sin(\varphi) + K$$

Equation 2.9

With this evaluation of the correlation function at four selected points we can determine the phase φ and amplitude a of s(t):

$$\varphi = \operatorname{atan}\left(\frac{C(\tau_3) - C(\tau_1)}{C(\tau_0) - C(\tau_2)}\right)$$

Equation 2.10

$$a = \frac{\sqrt{\left[C(\tau_3) - C(\tau_1)\right]^2 + \left[C(\tau_0) - C(\tau_2)\right]^2}}{2}$$

Equation 2.11

Sampling a sinusoidal signal

Another, slightly different approach is to sample the modulated signal synchronously. Sampling always means to convolve the input signal with a sampling function. In that sense, if one chooses the same sampling function as the function to sample we get the same conditions as described above. Before sampling, the input signal must be bandwidth limited in order to avoid aliasing effects. Assuming that we sample a periodic signal we can use the equations of the DFT (Discrete Fourier Transform) in order to calculate both amplitude and phase of the base frequency and harmonics contained in the signal. Using N sampling points

I_k (k=0..N-1) allows us to calculate $\frac{N}{2}-1$ harmonics of the base frequency, i.e. the sampling frequency divided by the number of sampling points.

Discrete Fourier Transform:

$$DFT(I_n) = \frac{1}{N} \cdot \left[\sum_{k=0}^{N-1} I_k \cdot \cos\left(2\pi k \frac{n}{N} \right) + i \cdot \sum_{k=0}^{N-1} I_k \cdot \sin\left(-2\pi k \frac{n}{N} \right) \right] \qquad \textbf{Equation 2.12}$$

Magnitude of the n^{th} coefficient:

$$A_n = \frac{1}{N} \cdot \sqrt{\left[\sum_{k=0}^{N-1} I_k \cdot \cos\left(2\pi k \frac{n}{N} \right) \right]^2 + \left[\sum_{k=0}^{N-1} I_k \cdot \sin\left(-2\pi k \frac{n}{N} \right) \right]^2} \qquad \textbf{Equation 2.13}$$

Amplitude of the n^{th} harmonic:

$$\hat{a}_n = 2 \cdot A_n = \frac{2}{N} \cdot \sqrt{\left[\sum_{k=0}^{N-1} I_k \cdot \cos\left(2\pi k \frac{n}{N} \right) \right]^2 + \left[\sum_{k=0}^{N-1} I_k \cdot \sin\left(-2\pi k \frac{n}{N} \right) \right]^2} \qquad \textbf{Equation 2.14}$$

Offset:

$$A_0 = A_n\big|_{n=0} = \frac{1}{N} \cdot \sum_{k=0}^{N-1} I_k \qquad \textbf{Equation 2.15}$$

Argument/Phase of the n-th coefficient:

$$\varphi_n = \operatorname{atan}\left(- \frac{\sum_{k=0}^{N-1} I_k \cdot \sin\left(2\pi k \frac{n}{N} \right)}{\sum_{k=0}^{N-1} I_k \cdot \cos\left(2\pi k \frac{n}{N} \right)} \right) \qquad \textbf{Equation 2.16}$$

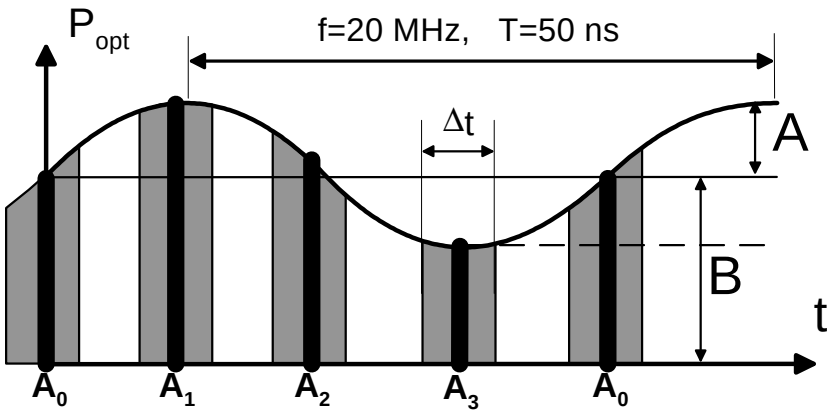

Figure 2.7 *Optical sinusoidally modulated input signal, sampled with 4 sampling points per modulation period. The signal frequency of 20MHz defines the unambiguous distance range of 7.5 m.*

These general equations are simplified for our application, where we use a sinusoidal wave (only base frequency, no harmonics) as the modulation signal and synchronously sample this wave with four equally spaced sampling points of duration Δt. The optical input signal is illustrated in **Figure 2.7**. We can thus rewrite the above equations to:

Phase φ, amplitude A and offset B of a sinusoidal signal obtained by the four sampling points $A_0..A_3$:

$$\varphi = \operatorname{atan}\frac{A_3 - A_1}{A_0 - A_2}$$ **Equation 2.17**

$$A = \frac{\delta}{\Delta t \cdot \sin\delta} \cdot \frac{\sqrt{(A_3 - A_1)^2 + (A_0 - A_2)^2}}{2}$$ **Equation 2.18**

$$B = \frac{A_0 + A_1 + A_2 + A_3}{4 \cdot \Delta t}$$ **Equation 2.19**

Using DFT, the finite number N of sampling points only allows the determination of a finite number of N/2-1 discrete frequency components. For this case (N=4), the system is only sensitive to one discrete frequency. Since this frequency selectivity is a well-known property of lock-in amplifiers, we also call the demodulation pixels lock-in pixels.

We see that we obtain nearly the same evaluation functions as with the correlation-approach. This comes as no surprise because the Fourier Transform is defined as the correlation with harmonic base functions, as selected in **Equation 2.7**. (This phenomenon is also described in the well-known Wiener-Khintchine theorem.)

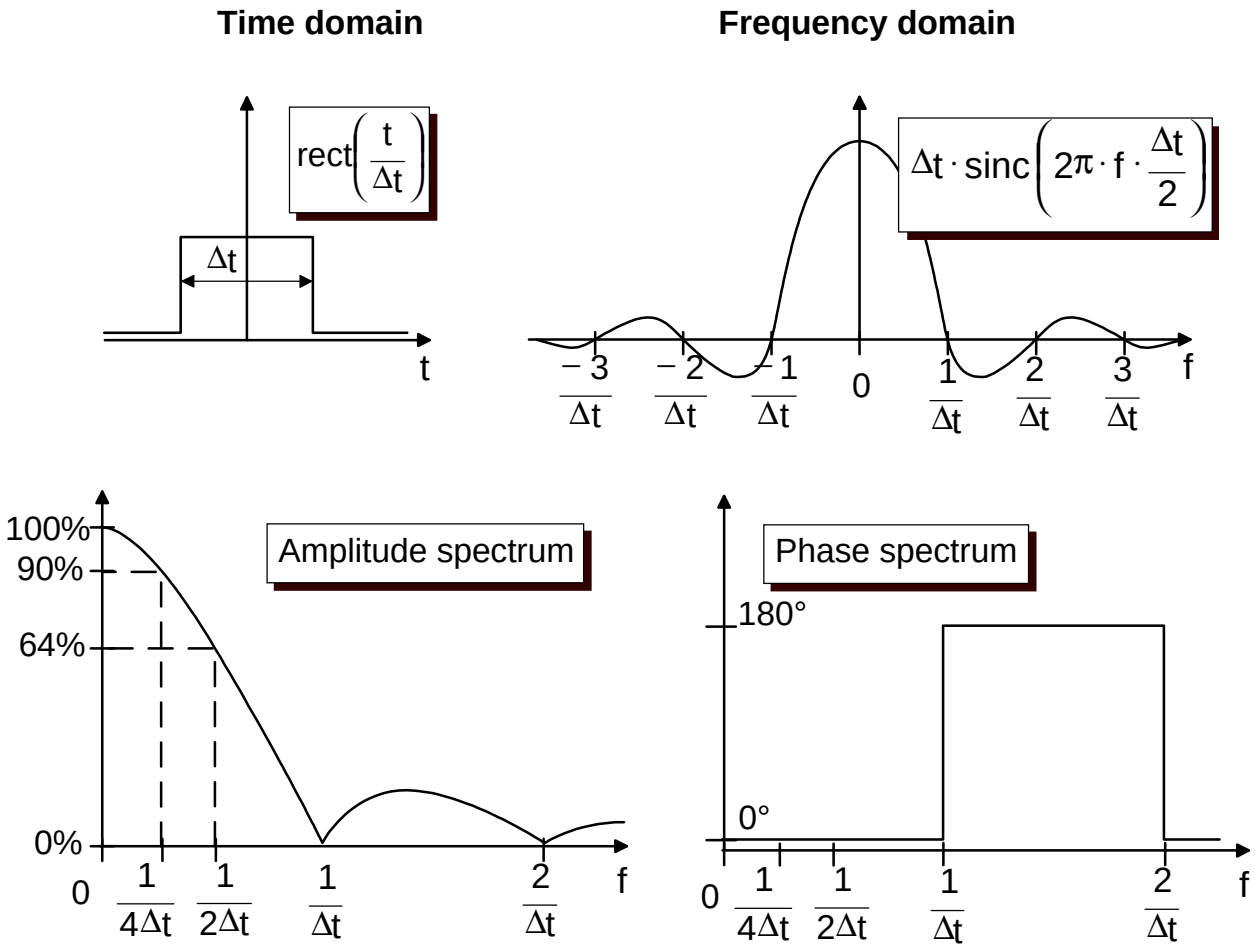

Figure 2.8 *Influence of integrative sampling nature on measured amplitude and phase. Natural sampling has no influence on the phase for reasonable integration times ∆t. Since the sinc-spectrum is axially symmetrical, only the positive part of both amplitude and phase spectrum are shown.*

Due to the fact that no ideal sampling can be performed, $A_0..A_3$ represent the integrated sampling values. For ideal sampling the system would need an infinite bandwidth. The integrative nature of this practical sampling process can be interpreted as a convolution of the ideally sampled input signal with the sampling function, a *rect*(t/∆t) function, where ∆t is the integration time. **Figure 2.8** shows the transfer function in the time and frequency domains. From the phase spectrum we can deduce that the natural sampling process has no influence on the measured

phase as long as the integration time of each sampling point is shorter than the modulation period of the sampled signal, which is a reasonable claim. Only the measured amplitude is attenuated by a factor of $\delta / (\Delta t \cdot \sin \delta)$ depending on the integration interval Δt, with $\delta = \pi \cdot \Delta t / T$, T: modulation period. This factor, already considered in **Equation 2.18**, leads to a decrease in measured amplitude to 90% of the real amplitude, if the integration time is chosen as a fourth of the modulation period $\Delta t = T/4 = 1/(4f)$. For $\Delta t = T/2$ the measured amplitude is 64% of the real amplitude.

In order to increase the SNR (signal to noise ratio) it is possible to perform a continuous, synchronous sampling of the periodic signal and to accumulate short-time integrated sampling points a_i belonging to the same phase to the long-time integrated values A_i (see **Figure 2.9**). This technique can be described as a convolution or correlation of the input function with a square wave, the sampling function.

A repetitively accumulated short-time integrated sampling point is given by:

$$A_i = \lim_{T_{int} \to \infty} \int_{-\frac{T_{int}}{2}}^{+\frac{T_{int}}{2}} \left\{ s\left(t - t_\varphi - (i \cdot t_{samp})\right) \cdot \sum_j \mathrm{rect}\left(\frac{t - j \cdot N \cdot t_{samp}}{\Delta t} \right) \right\} dt$$

$$= s\left(t - t_\varphi\right) \otimes \mathrm{squ}\left(\frac{t}{\Delta t}, N \cdot t_{samp} \right)$$

Equation 2.20

With: squ(t/a,b): square wave with pulse width a and period b.

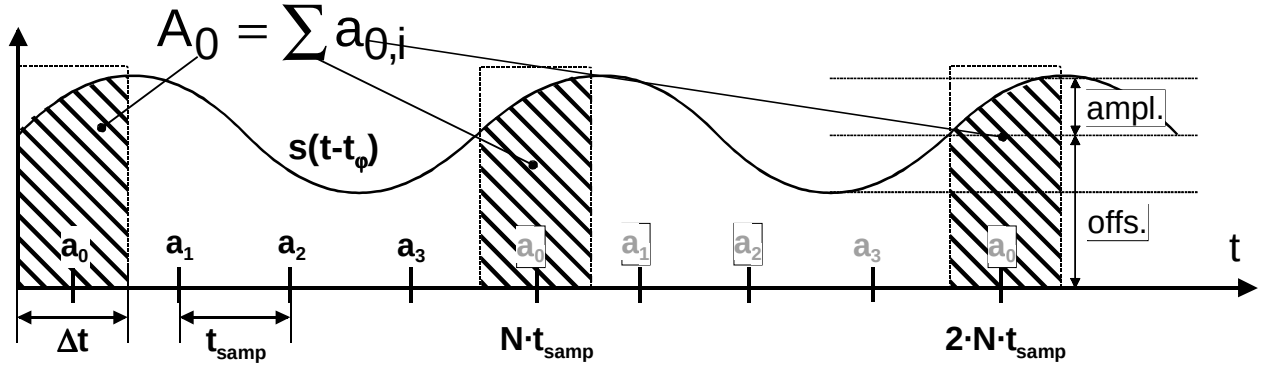

Figure 2.9 *Repetitive accumulating sampling.*

For very high frequencies a real system can no longer perform integration with sharp integration boundaries. The necessary electrooptical shutter mechanism has characteristic rise/fall times and a frequency dependent efficiency as described in

Chapter 5. Due to this low-pass characteristic of the demodulation pixel itself, the square-wave sampling function more and more approximates a sinusoidal sampling function at high frequencies. If the input signal is presumed to be a sine wave as well, the natural sampling process degenerates to an autocorrelation of a sine for a certain frequency range.

Figure 2.10 summarizes the description of natural sampling in the time and frequency domains. Being discrete in the frequency domain (=multiplication of the continuous spectrum with the infinite repetition of the Dirac function) means being infinite in the time domain (=convolution with Dirac function). The DFT continuously repeats the measured samples in the time domain.

For our TOF application we want to achieve the highest possible modulation frequency in order to achieve a good absolute distance resolution. Therefore, not only the demodulation pixel itself must offer a sufficiently large bandwidth (see **Chapter 5**), but the associated control and driving electronics (see **Chapter 6**) must also be able to provide those time-critical signals. For a high accuracy and stability we generate the control signals digitally using a microcontroller for the overall timing and a fast CPLD (Programmable Logic Device) for the fast signals. Generating four different phase relations digitally out of an 80 MHz master clock, limits the highest possible modulation frequency to 20 MHz (modulation period: T=50 ns). The phase control signals are generated as follows:

phase 0°:	"..1100..",	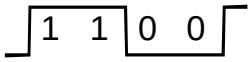
phase 90°:	"..0110..",	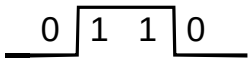
phase 180°:	"..0011..",	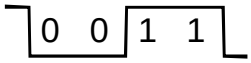
phase 270°:	"..1001..".	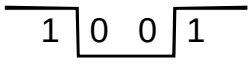

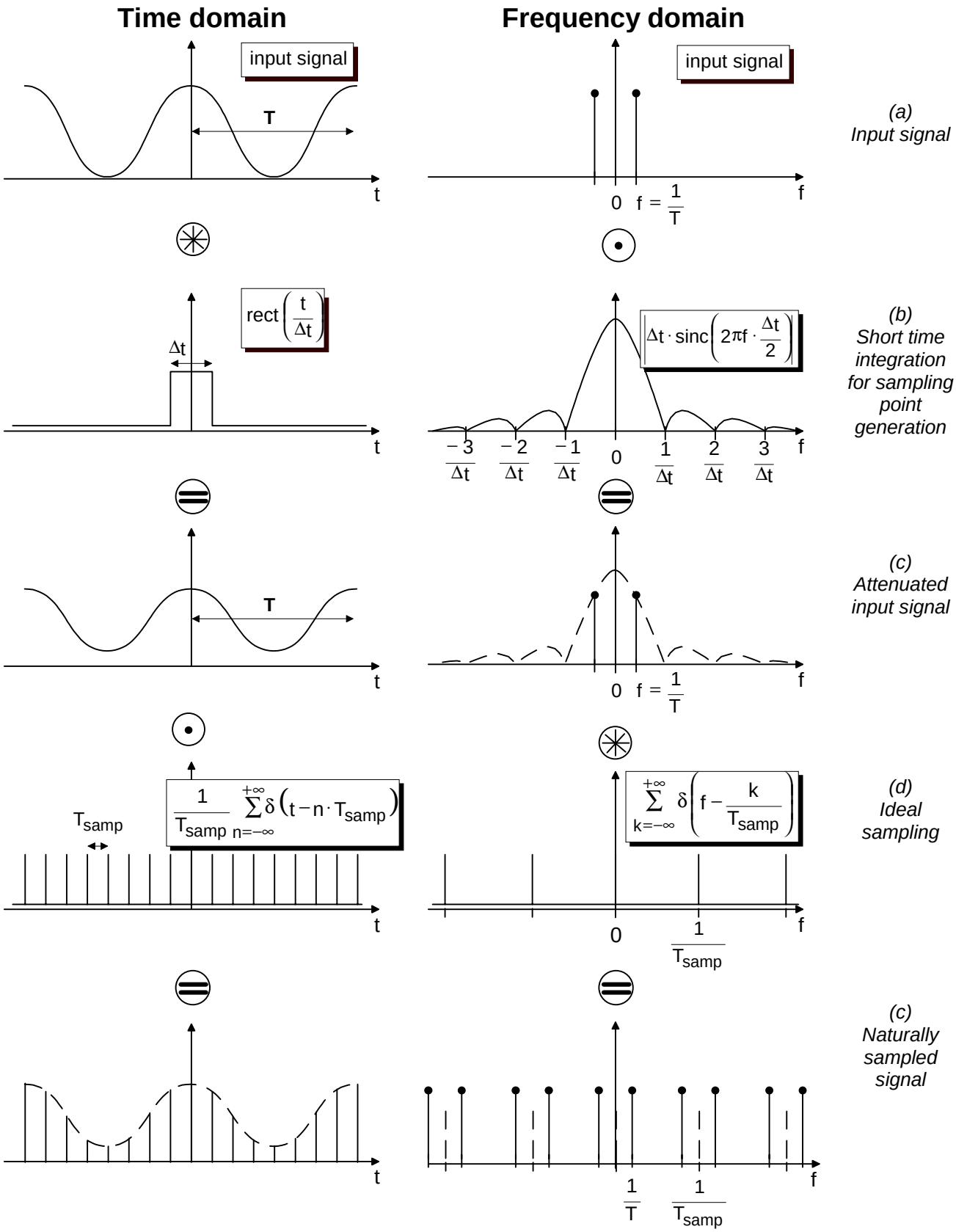

Figure 2.10 *Description of natural sampling in time and frequency domains.*

Due to the bandwidth conditions and the pixel architecture (**Chapter 5** for more details) we use overlapping integration periods for the acquisition of the single

sampling points, i.e. the short time integration time is chosen to be half the modulation period, $\Delta t=T/2=25$ ns for 20 MHz modulation frequency. This is possible, since the sampling points are acquired serially rather than in parallel. Although the amplitude decreases to $\mathrm{sinc}(0.5\pi)=64\%$ this operation mode results in the best overall performance, since it offers the most efficient use of the available optical power and additionally for shorter integration intervals a higher system bandwidth would be required.

Spectral selectivity characteristic: influence of finite observation window

To describe the situation completely we have to consider the fact that the observation window is finite. The size of the observation window is of essential importance for the spectral selectivity characteristic of the measurement. Assuming that other (asynchronously) modulated signals also reach the detector, it is obvious that, for a relatively short integration time, superimposed frequency components located near to the signal frequency will disturb the measurement. (In this context we mean the overall integration time, not the short-time integration to acquire the sampling points). This is a problem as long as the integration time is on the order of the period of the beat frequency generated by the superposition of both received signals. We will call these signals measurement signal and spurious signal from now on, and for simplification we assume the same amplitude for both.

Again, as for the short-time integration of sampling point acquisition, the integration or observation within a finite observation window (multiplication with a $\mathrm{rect}(t/T_w)$ in the time domain) leads to a convolution with a sinc-function in the frequency domain. The longer the overall integration time, the smaller is the width of the sinc function. Thus the spectral selectivity between measurement and spurious signal improves. These contents are illustrated in **Figure 2.11**.

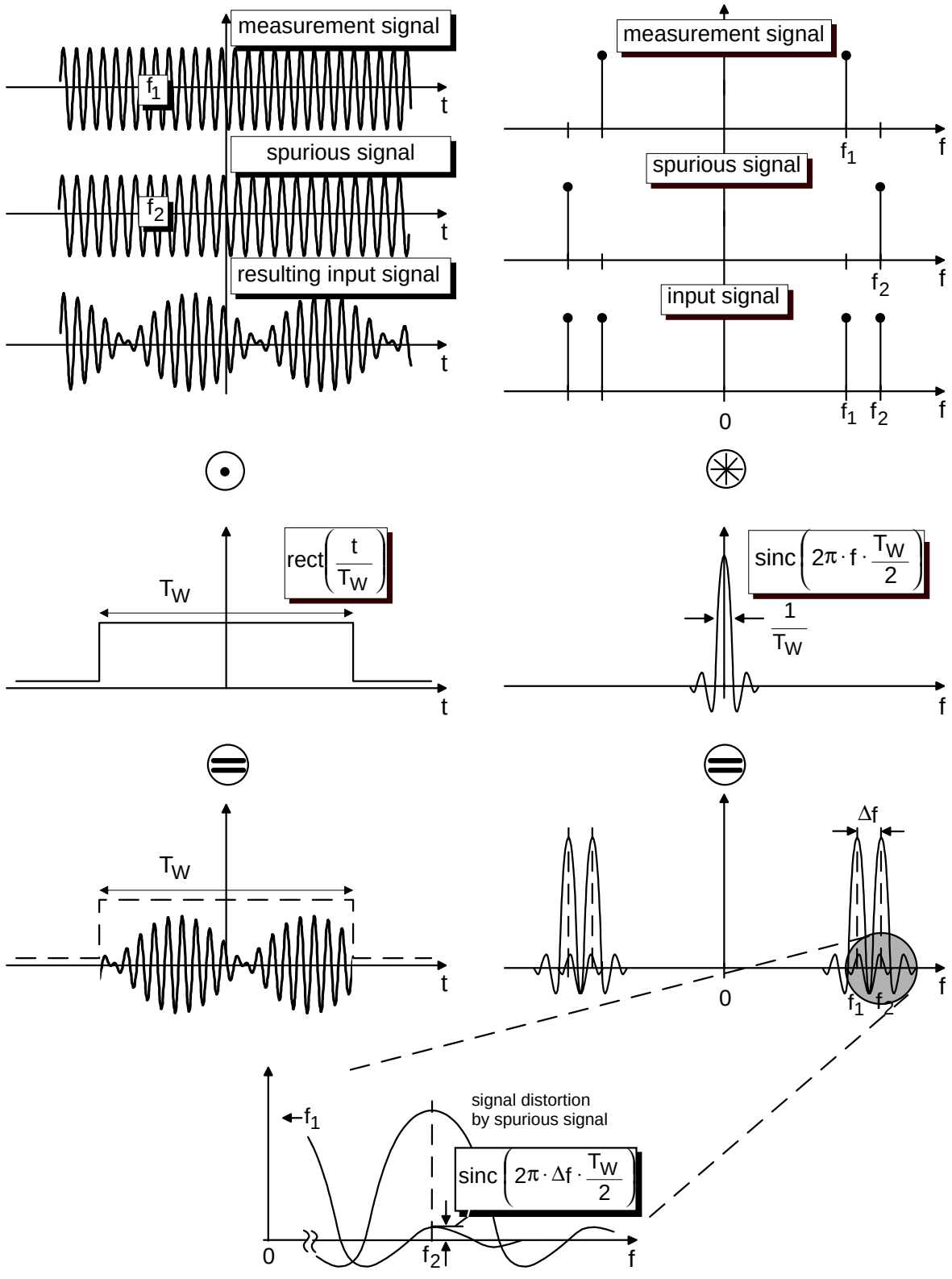

Figure 2.11 *Spectral selectivity of digital lock-in.*

We only have to consider the superimposed signal power of the spurious signal's sinc-spectrum into the spectrum of the measurement signal at its center frequency. This is because the DFT detection is only sensitive to discrete frequencies, as

mentioned before. The demodulation result for the measurement signal is then falsified due to frequency dispersion by:

$$\mathrm{sinc}\left(2\pi \cdot \Delta f \cdot \frac{T_W}{2}\right) \qquad \textbf{Equation 2.21}$$

With T_W=observation window/ integration time and Δf=difference frequency of measurement and spurious signal.

If we postulate a signal suppression of better than 40 dB (factor 100) for neighboring frequencies, we need to choose integration times as listed below:

f1	f2	Δf	T_W
20 MHz	*21.0000 MHz*	*1 MHz*	*100 µsec*
20 MHz	*20.1000 MHz*	*100 kHz*	*1 msec*
20 MHz	*20.0100 MHz*	*10 kHz*	*10 msec*
20 MHz	*20.0010 MHz*	*1 kHz*	*100 msec*
20 MHz	*20.0001 MHz*	*100 Hz*	*1 sec*

These considerations are of special importance if two or more TOF cameras observe the same area so that their radiation fields are superimposed. If for any reason these modulation signals can't be separated by using light of different wavelengths, one might want to separate the signals by using slightly different modulation frequencies. In that case the observation window defines the spectral selectivity concerning modulation frequency. Note that the above estimation presumes equal amplitudes of spurious signal and measurement signal.

2.2.2 Aliasing

Obviously the shape of the modulation signal has an influence on the measurement result. As already mentioned, we only use four sampling points to sample the offset containing signal. Therefore, Shannon's law is only obeyed for a pure sinusoidal wave. If we consider using a square-wave modulated signal (infinite spectrum), taking only four sampling points will lead to aliasing effects. In most of the literature aliasing is only treated together with the amplitude spectrum. We, however, are especially interested in the influence of aliasing on the phase spectrum. For that purpose we first take a simple signal consisting of a cosine wave and one harmonic frequency of the same amplitude and triple frequency. This is to simplify the spectra

and algorithms in order to understand clearly and easily what happens to the phase spectrum. In a next step we will transfer these results to a square wave. And lastly we will simulate aliasing effects on several other waveforms, presuming DFT detection with four sampling points.

An important boundary condition is the chosen integration interval for the sampling point acquisition. As already discussed this is chosen to be half the modulation period $\Delta t=T/2$ in the following calculations. From **Figure 2.8** we can conclude that, for $\Delta t=T/2$, all even harmonics of the basic frequency, namely 2f, 4f, 6f, … will be suppressed and do not contribute to the demodulation result. This is because these harmonics are eliminated by a zero crossing of the sinc-function. This simple example shows the importance of the choice of Δt for aliasing effects.

Aliasing phase error for 3f-harmonic using 4-tap DFT-detection.

In order to simplify explanations we use the expression “tap” for “sampling point” from now on. We consider the input signal s(t) having a harmonic of triple base frequency and amplitude “1”.

$$s(t) = \cos(\omega_0 t - \varphi_0) + \cos(3\omega_0 t - 3\varphi_0) \qquad \textbf{Equation 2.22}$$

The phase delay φ_0 is caused by the distance dependent time delay in our TOF application. This time delay causes a phase delay of $3\varphi_0$ in the 3f-harmonic component.

Transformed into the Fourier domain we obtain the spectrum S(f):

$$S(f) = \frac{1}{2}\Big\{\delta(\omega-\omega_0)\cdot e^{-j\varphi_0} + \delta(\omega+\omega_0)\cdot e^{j\varphi_0} + \delta(\omega-3\omega_0)\cdot e^{-j3\varphi_0} + \delta(\omega+3\omega_0)\cdot e^{j3\varphi_0}\Big\} \qquad \textbf{Equation 2.23}$$

Now we consider the integration of the taps, i.e. convolution of s(t) with rect(t/Δt) and multiplication of S(f) with sinc($2\pi\cdot f\cdot\Delta t/2$)=sinc($\pi\cdot f\cdot T/2$) resulting in:

$$S_{int}(f) = \frac{1}{2}\Big\{ a\cdot\left(\delta(\omega-\omega_0)\cdot e^{-j\varphi_0} + \delta(\omega+\omega_0)\cdot e^{j\varphi_0}\right) + b\cdot\left(\delta(\omega-3\omega_0)\cdot e^{-j3\varphi_0} + \delta(\omega+3\omega_0)\cdot e^{j3\varphi_0}\right)\Big\} \qquad \textbf{Equation 2.24}$$

$$\text{with } a = \frac{2}{\pi} \quad \text{and} \quad b = -\frac{2}{3\pi} = -\frac{a}{3}$$

The coefficients a and b are obtained by evaluation of sinc($\pi\cdot f\cdot T/2$) at f=1/T and f=3/T, respectively. By substituting b with a and considering $-1 = e^{j\pi} = e^{-j\pi}$ we only

obtain positive coefficients and can easily deduce the amplitude and phase spectrum. We obtain:

$$S_{int}(f) = \frac{a}{2}\left\{\left(\delta(\omega-\omega_0)\cdot e^{-j\varphi_0} + \delta(\omega+\omega_0)\cdot e^{j\varphi_0}\right) + \frac{1}{3}\cdot\left(\delta(\omega-3\omega_0)\cdot e^{j(\pi-3\varphi_0)} + \delta(\omega+3\omega_0)\cdot e^{j(3\varphi_0-\pi)}\right)\right\} \quad \textbf{Equation 2.25}$$

$$\text{with } a = \frac{2}{\pi}$$

Sampling with $f_{samp}=4f_0$ ($\omega_0=2\pi f$) leads to aliasing. For this simple function (**Equation 2.22** and **Equation 2.23**) the spectrum $S_{int,samp}$ at $f=f_0$, which is the place we are interested in, is only superimposed by the $-3f_0$ component of the actual signal spectrum displaced to $4f_0$ by convolution with the sampling spectrum:

$$S_{int,samp}(f = f_0) = \frac{1}{\pi}\cdot\left(e^{-j\varphi_0} + \frac{1}{3}\cdot e^{j(3\varphi_0-\pi)}\right) \quad \textbf{Equation 2.26}$$

We can split this into amplitude A_{f0} and phase φ_{f0}:

$$A_{f0} = \frac{1}{\pi}\cdot\sqrt{\left(\cos(-\varphi_0)+\frac{1}{3}\cos(3\varphi_0-\pi)\right)^2 + \left(\sin(-\varphi_0)+\frac{1}{3}\sin(3\varphi_0-\pi)\right)^2}$$

Equation 2.27

$$\varphi_{f0} = \operatorname{atan}\left(\frac{\sin(-\varphi_0)+\frac{1}{3}\sin(3\varphi_0-\pi)}{\cos(-\varphi_0)+\frac{1}{3}\cos(3\varphi_0-\pi)}\right) \quad \textbf{Equation 2.28}$$

With the knowledge of this relationship, the real signal phase φ_0 can be deduced from the aliasing disturbed measured phase φ_{f0}. In practical applications one could efficiently solve this by means of a look up table (LUT). **Figure 2.12** illustrates the influence of natural sampling and aliasing on the amplitude and phase spectrum for the example given above. **Figure 2.14 d** shows the relation of the real phase to the measured phase and the corresponding error. Using the signal of **Equation 2.22** rather than a pure sine would result in a maximum phase error of ±19.5° if no LUT correction were performed.

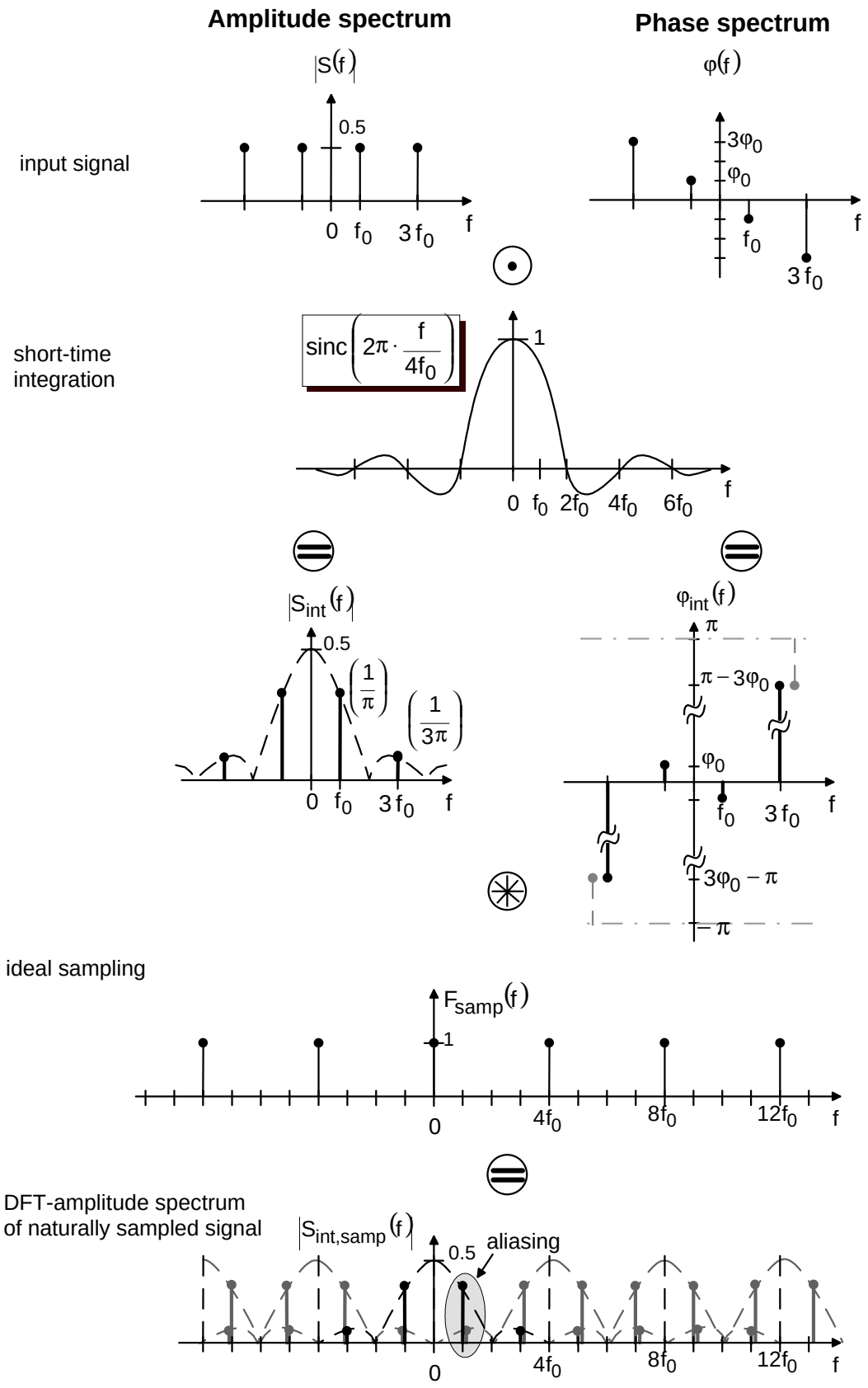

Figure 2.12 *Aliasing for* $s(t) = \cos(\omega_0 t - \varphi_0) + \cos(3\omega_0 t - 3\varphi_0)$ *sampled with only four sampling points. Influence on amplitude and phase spectrum.*

Aliasing phase error for a square wave using 4-tap DFT-detection.

The deduction of the aliasing-caused phase error, which occurs if we use a square wave as modulation signal, detected with the 4-tap approach, works in the same way as the previous deduction. The only difference is that the square wave has an infinite frequency spectrum, which makes the notation more complex. Therefore, we will simplify wherever possible. A square wave $s_{sq}(t)$ can be spilt into a sum of odd harmonics of the base frequency with decreasing amplitude for increasing frequency:

$$s_{sq}(t) = \cos(\omega_0 t - \varphi_0) - \frac{1}{3}\cdot\cos(3\omega_0 t - 3\varphi_0) + \frac{1}{5}\cdot\cos(5\omega_0 t - 5\varphi_0) - \frac{1}{7}\cdot\cos(7\omega_0 t - 7\varphi_0) + \frac{1}{9}\cdot\cos(9\omega_0 t - 9\varphi_0) - \ldots$$

Equation 2.29

In the Fourier domain this corresponds to the spectrum $S_{sq}(f)$:

$$S_{sq}(f) = \frac{1}{2}\left\{\ldots - \frac{\delta(\omega+7\omega_0)\cdot e^{j7\varphi_0}}{7} + \frac{\delta(\omega+5\omega_0)\cdot e^{j5\varphi_0}}{5} - \frac{\delta(\omega+3\omega_0)\cdot e^{j3\varphi_0}}{3} + \frac{\delta(\omega+\omega_0)\cdot e^{j\varphi_0}}{1} + \frac{\delta(\omega-\omega_0)\cdot e^{-j\varphi_0}}{1} - \frac{\delta(\omega-3\omega_0)\cdot e^{-j3\varphi_0}}{3} + \frac{\delta(\omega-5\omega_0)\cdot e^{-j5\varphi_0}}{5} - \frac{\delta(\omega-7\omega_0)\cdot e^{-j7\varphi_0}}{7} + \ldots\right\}$$

Equation 2.30

Again, considering the integration of the sampling points, we multiply $S_{sq}(f)$ with $\mathrm{sinc}(\pi\cdot f\cdot T/2)$. This time multiplication with the sinc function eliminates all negative signs:

$$S_{sq,int}(f) = \frac{1}{2}\left\{ \ldots + \frac{\delta(\omega+7\omega_0)\cdot e^{j7\varphi_0}}{7\cdot\frac{7\pi}{2}} + \frac{\delta(\omega+5\omega_0)\cdot e^{j5\varphi_0}}{5\cdot\frac{5\pi}{2}} + \frac{\delta(\omega+3\omega_0)\cdot e^{j3\varphi_0}}{3\cdot\frac{3\pi}{2}} + \frac{\delta(\omega+\omega_0)\cdot e^{j\varphi_0}}{1\cdot\frac{\pi}{2}} + \frac{\delta(\omega-\omega_0)\cdot e^{-j\varphi_0}}{1\cdot\frac{\pi}{2}} + \frac{\delta(\omega-3\omega_0)\cdot e^{-j3\varphi_0}}{3\cdot\frac{3\pi}{2}} + \frac{\delta(\omega-5\omega_0)\cdot e^{-j5\varphi_0}}{5\cdot\frac{5\pi}{2}} + \frac{\delta(\omega-7\omega_0)\cdot e^{-j7\varphi_0}}{7\cdot\frac{7\pi}{2}} + \ldots \right\}$$

Equation 2.31

Now we sample with $f_{samp}=4f_0$ ($\omega_0=2\pi f$) and observe aliasing, as in the previously examined case. The spectrum at $f=f_0$ $S_{sq,int,samp}(f = f_0)$, looks like this:

$$S_{sq,int,samp}(f = f_0) = \frac{1}{\pi}\left\{ \ldots + \frac{e^{j11\varphi_0}}{121} + \frac{e^{j7\varphi_0}}{49} + \frac{e^{j3\varphi_0}}{9} + \frac{e^{-j\varphi_0}}{1} + \frac{e^{-j5\varphi_0}}{25} + \frac{e^{-j9\varphi_0}}{81} + \frac{e^{-j13\varphi_0}}{169} + \ldots \right\}$$

Equation 2.32

We can split this into amplitude $A_{sq,f0}$ and phase $\varphi_{sq,f0}$:

$$A_{sq,f0} = \frac{1}{\pi}\cdot\sqrt{\left(\ldots + \frac{\cos(3\varphi_0)}{9} + \frac{\cos(-\varphi_0)}{1} + \frac{\cos(-5\varphi_0)}{25} + \ldots\right)^2 + \left(\ldots + \frac{\sin(3\varphi_0)}{9} + \frac{\sin(-\varphi_0)}{1} + \frac{\sin(-5\varphi_0)}{25} + \ldots\right)^2}$$

Equation 2.33

$$\varphi_{sq,f0} = \operatorname{atan}\left(\frac{\ldots + \frac{\sin(3\varphi_0)}{9} + \frac{\sin(-\varphi_0)}{1} + \frac{\sin(-5\varphi_0)}{25} + \ldots}{\ldots + \frac{\cos(3\varphi_0)}{9} + \frac{\cos(-\varphi_0)}{1} + \frac{\cos(-5\varphi_0)}{25} + \ldots}\right)$$

Equation 2.34

In **Figure 2.13** we show an illustration of the sampling influences and aliasing situation when detecting a square wave with the 4-tap mechanism.

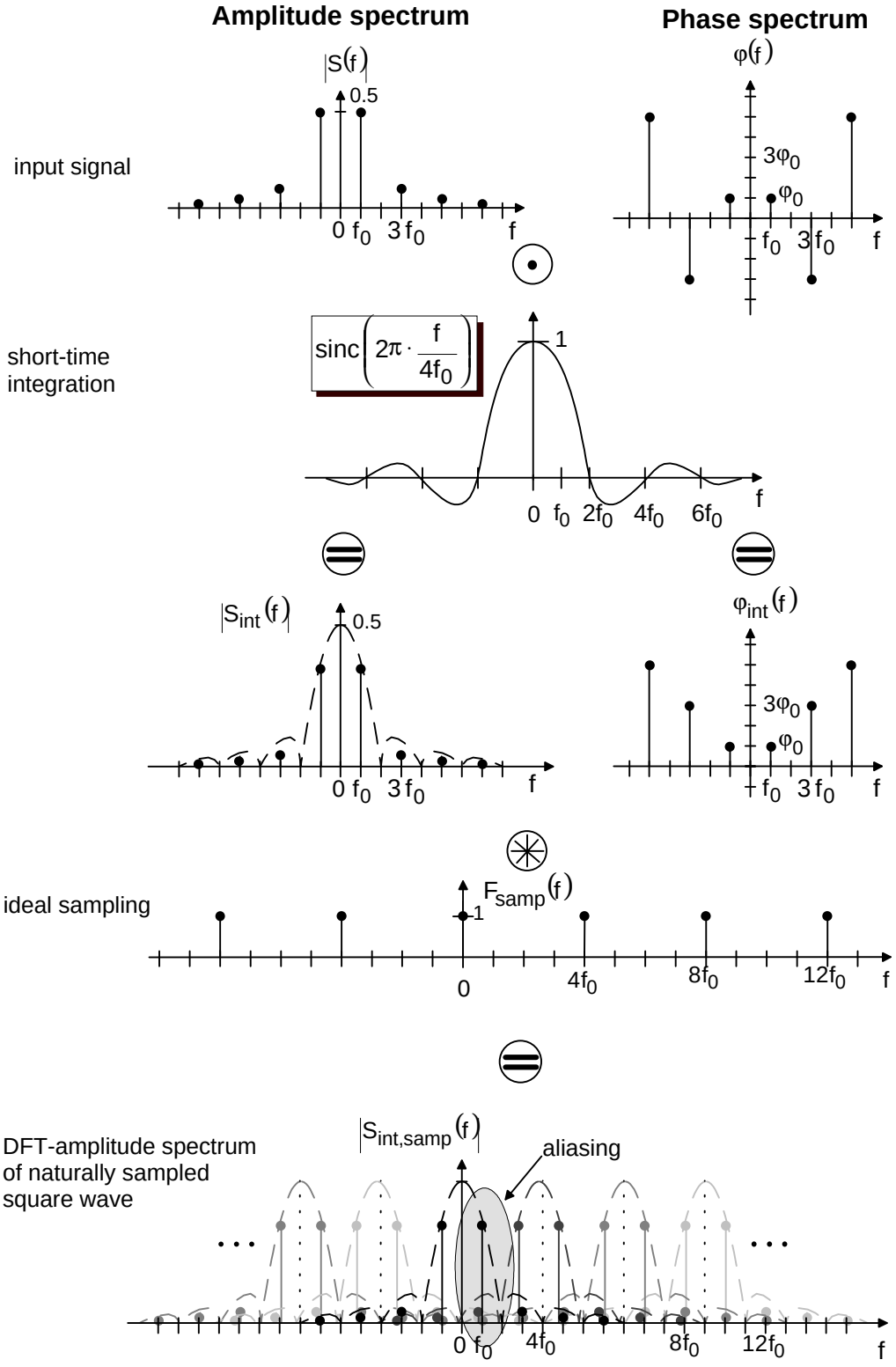

Figure 2.13 *Aliasing for a square wave sampled with only four sampling points. Influence on amplitude and phase spectrum.*

From **Equation 2.34** we can deduce that there is a predictable connection between the measured phase and the real phase. (See also **Figure 2.14 k**.)

Aliasing phase error for different input signals using 4-tap DFT-detection.

In addition to these analytical considerations, it is helpful to use numerical simulation in order to obtain the relation between measured and real phase for periodic input signals differing from the pure sinusoidal wave. We have performed those simulations for the input signals discussed above and also for several other input signals. The results are shown in **Figure 2.14**, which shows the input signal, the measured and real phase as well as the predictable phase error. **Figure 2.14** (a), (c), (e) and (g) show that, for $\Delta t=T/2$, even harmonics do not cause any phase error (see above). **Figure 2.14** (i), (j) and (l) confirm that the short-time integration Δt plays an important role.

The following table lists the harmonics and their coefficients used for the simulation. It also summarizes the resulting maximum phase error if no LUT correction is performed.

Modulation signal	even harmonics	odd harmonics	Error in degrees
cos	-	-	0
$\cos^2$	-	-	0
cos(x) + cos(2x)	2	-	0
cos(x) + cos(4x)	4	-	0
cos(x) + cos(6x)	6	-	0
cos(x) + cos(3x)	-	3	± 19.5
cos(x) + cos(5x)	-	5	± 11.5
cos(x) + cos(7x)	-	7	± 8.2
cos(x) + cos(3x), $\Delta t=T/3$	-	3	± 0.3
cos(x) + cos(5x), $\Delta t=T/5$	-	5	0
square wave	-	$^1/_3 \cdot 3$, $^1/_5 \cdot 5$, $^1/_7 * 7$, …	± 4.2
square wave, $\Delta t=T/3$	-	$^1/_3 \cdot 3$, $^1/_5 \cdot 5$, $^1/_7 \cdot 7$, …	± 3.4
triangle	-	$^1/_9 \cdot 3$, $^1/_{25} \cdot 5$, $^1/_{49} \cdot 7$, $^1/_{81} \cdot 9$, …	± 2.6
ramp	$^1/_2 \cdot 2$, $^1/_4 \cdot 4$, $^1/_6 \cdot 6$, …	$^1/_3 \cdot 3$, $^1/_5 \cdot 5$, $^1/_7 \cdot 7$, …	± 4.2
square wave with linear falling edge		*combinations of above*	± 5.4
square wave with exponential falling edge		*combinations of above*	± 3.5

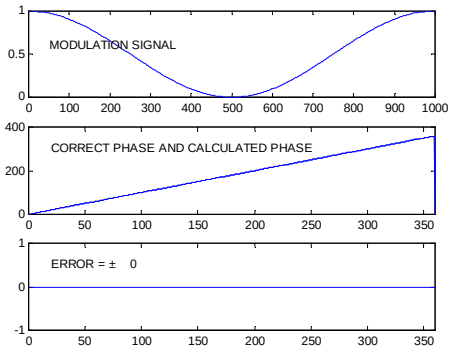

(a), (b)

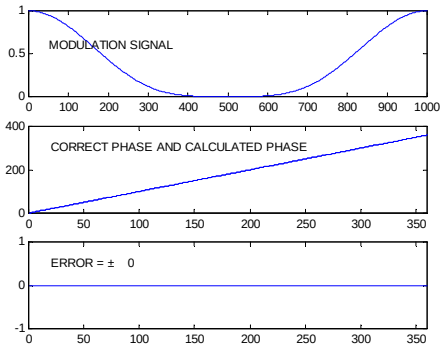

cos

$\cos^2$

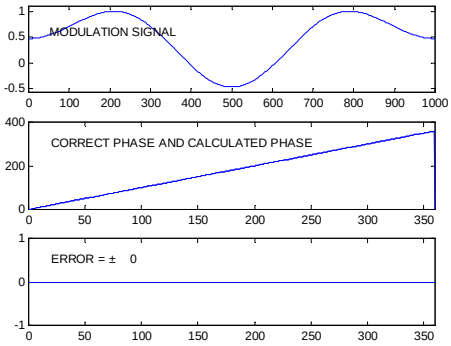

(c), (d)

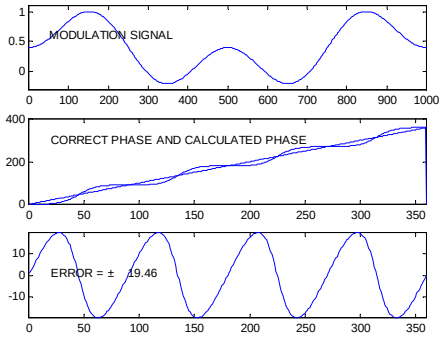

cos(x) + cos(2x)

cos(x) + cos(3x)

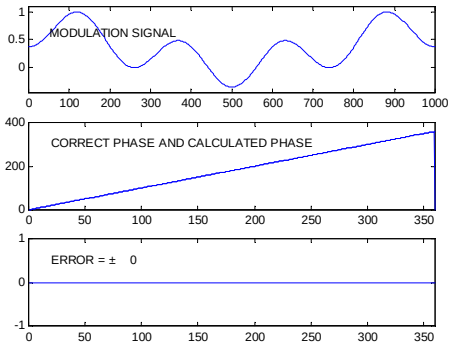

(e), (f)

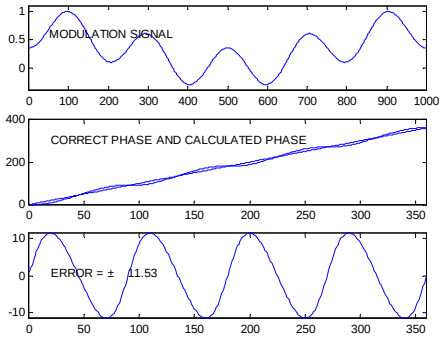

cos(x) + cos(4x)

cos(x) + cos(5x)

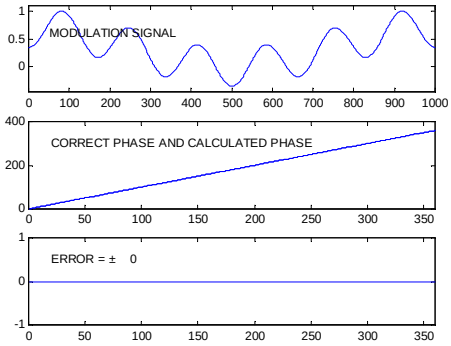

(g), (h)

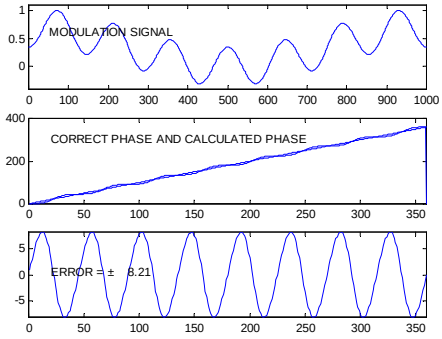

cos(x) + cos(6x)

cos(x) + cos(7x)

Figure 2.14 (a-h) *Influence of modulation signal on phase accuracy I.*

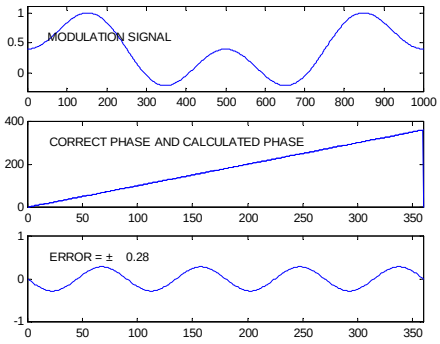

cos(x) + cos(3x), Δt=T/3

(i), (j)

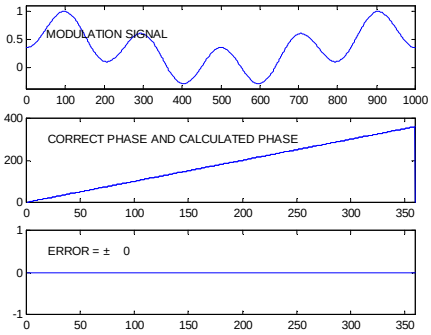

cos(x) + cos(5x), Δt=T/5

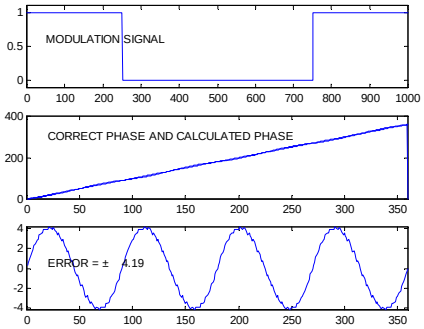

square wave

(k), (l)

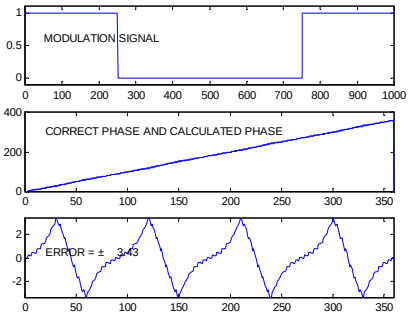

square wave, Δt=T/3

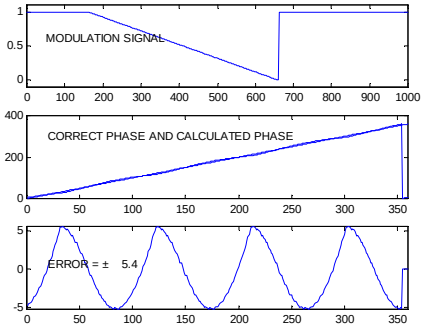

square wave with linear falling edge

(m), (n)

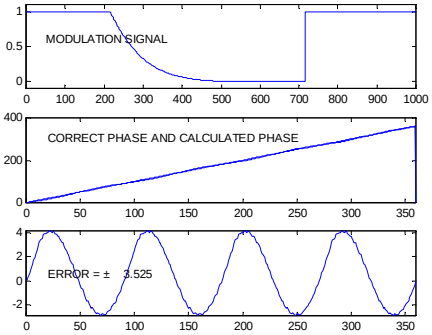

square wave with exponentially falling edge

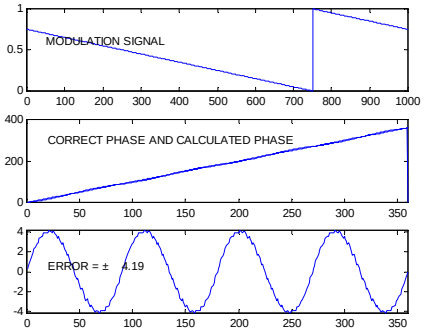

ramp

(o), (p)

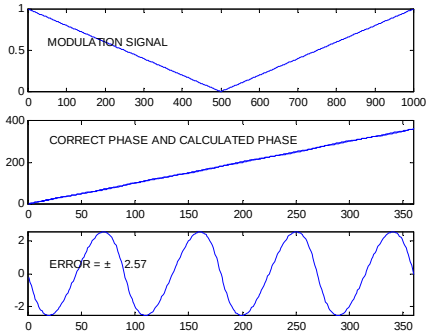

triangle

Figure 2.14 (i-p) *Influence of modulation signal on phase accuracy II.*

2.2.3 Influence of system non-linearities

Generally, the transfer characteristic of all components involved in the analogous output, ranging from the on chip output amplifier to the digitization, is not exactly linear. In this section we describe the influence of quadratic non-linearities on the measured phase using the 4-tap algorithm.

From the four acquired sampling points $A_0..A_3$ the phase φ is calculated using the following equation:

$$\varphi = \arctan\left(\frac{A_0 - A_2}{A_1 - A_3}\right)$$

Equation 2.35

Considering linear and quadratic distortions in the transfer function leads to the measurement of $a \cdot A_i + b \cdot A_i^2$ rather than A_i. For the measured phase φ_{meas} this means:

$$\varphi_{meas} = \arctan\left(\frac{a \cdot (A_0 - A_2) + b \cdot \left(A_0^2 - A_2^2\right)}{a \cdot (A_1 - A_3) + b \cdot \left(A_1^2 - A_3^2\right)}\right)$$

Equation 2.36

This can be rewritten as:

$$\varphi_{meas} = \arctan\left(\frac{(A_0 - A_2) + \frac{b}{a} \cdot (A_0 - A_2) \cdot (A_0 + A_2)}{(A_1 - A_3) + \frac{b}{a} \cdot (A_1 - A_3) \cdot (A_1 + A_3)}\right)$$

Equation 2.37

As can be seen from **Figure 2.7**, the sum "A_0+A_2" and "A_1+A_3" equal two times the offset B. This is because cos(x) = -cos(x+180°). So we obtain:

$$\varphi_{meas} = \arctan\left(\frac{(A_0 - A_2) + \frac{2 \cdot B \cdot b}{a} \cdot (A_0 - A_2)}{(A_1 - A_3) + \frac{2 \cdot B \cdot b}{a} \cdot (A_1 - A_3)}\right) = \arctan\left(\frac{\left(1 + \frac{2 \cdot B \cdot b}{a}\right) \cdot (A_0 - A_2)}{\left(1 + \frac{2 \cdot B \cdot b}{a}\right) \cdot (A_1 - A_3)}\right)$$

$$= \arctan\left(\frac{A_0 - A_2}{A_1 - A_3}\right) = \varphi$$

Equation 2.38

This means that the 4-tap algorithm is not sensitive to linear or quadratic distortions in the analogous transfer characteristic.

2.2.4 Summary

To summarize, demodulation pixels can be realized by giving them the ability to sample the incoming light in the time domain synchronously with its modulation frequency. With the DFT it is only possible to measure discrete frequencies. In order to enlarge the SNR, the sampling process must be repeated a large number of times, integrating the small signal amounts of each sampling point to a larger signal value. This successive integration of the sampling points (1) sharpens the system's sensitivity to discrete frequencies only: spectral selectivity, (2) lowers the (unwanted) sensitivity to neighboring frequency components and (3) improves the SNR by increasing the signal strength. Due to this frequency selective integrating nature we also call our pixels "lock-in pixels". Like a lock-in amplifier, they are only sensitive to the modulation frequency itself.

With analytical calculations as well as some numerical simulations we have shown that the 4-tap algorithm is not sensitive to quadratic system non-linearties and is also insensitive to even harmonics of the modulation signal. Odd harmonics, as present in a square wave for example disturb the measured phase. This is caused by aliasing. In practice this is not a serious problem, since there is (usually) an unambiguous relationship between the real phase and the measured phase, so that the error can be corrected using a look up table (LUT). In the TOF application such a LUT correction was not necessary due to the low pass characteristics of both the demodulation pixels and the LED illumination. Although the LEDs are controlled by a digital signal (ideally a square wave), their output at 20 MHz is more sinusoidal (c.f. **Chapter 5**).

3. Solid-state image sensing

Solid-state imaging has experienced a rapid growth, especially in the last ten years. This development has benefited from the steady improvements and miniaturization in the semiconductor industry and is also part of today's multimedia revolution. The first semiconductor solid-state imagers were photodiode arrays, where each diode was directly connected to the output by a metal wire. The large capacitance of these metal wires, resulting in a relatively slow signal readout speed and poor noise performance was, however, the killing factor that prevented a wide propagation of photodiode arrays, at least at that time.

In 1970 Boyle introduced a new, amazingly simple device for semiconductor image sensing [BOY, AME], the so-called charge coupled device: CCD. These elements collect optically generated charge carriers under locally separated photogates. Bundled to charge packets in the single pixels, the optically generated charge carriers can then, after a certain integration time, be moved through the semiconductor into certain storage areas by making use of the charge-coupling principle. This method is explained in more detail below. From these storage areas they are then sequentially shifted to *one* output stage, where the charge is converted into a voltage (**Figure 3.1 c.**) The use of only *one* low-capacitance output stage is still one of the essential advantages of CCDs since it means both low noise and very high homogeneity between the single pixels. Additionally, with the charge-coupling principle, it is possible to perform certain sorts of signal processing [SP4]. The essentially noise-free charge addition of single charge carriers is only one example of CCD's amazing *charge domain* signal processing capabilities. However, to operate CCDs, voltages between 10 and 20V are necessary, very often requiring large currents of up to some amperes, since capacitances of some nanofarads have to be charged and discharged within nanoseconds. This results in relatively large power dissipation, a major drawback of CCDs compared to some of today's CMOS APS sensors. Other weak points of CCDs are the facts that (1) the complete sensor always has to be read out in order to reset the pixel values and to start a new image acquisition and (2) the image is after-exposed during readout, known as

the *smearing* effect, resulting in lines in the image having an origin in very bright points [TEU].

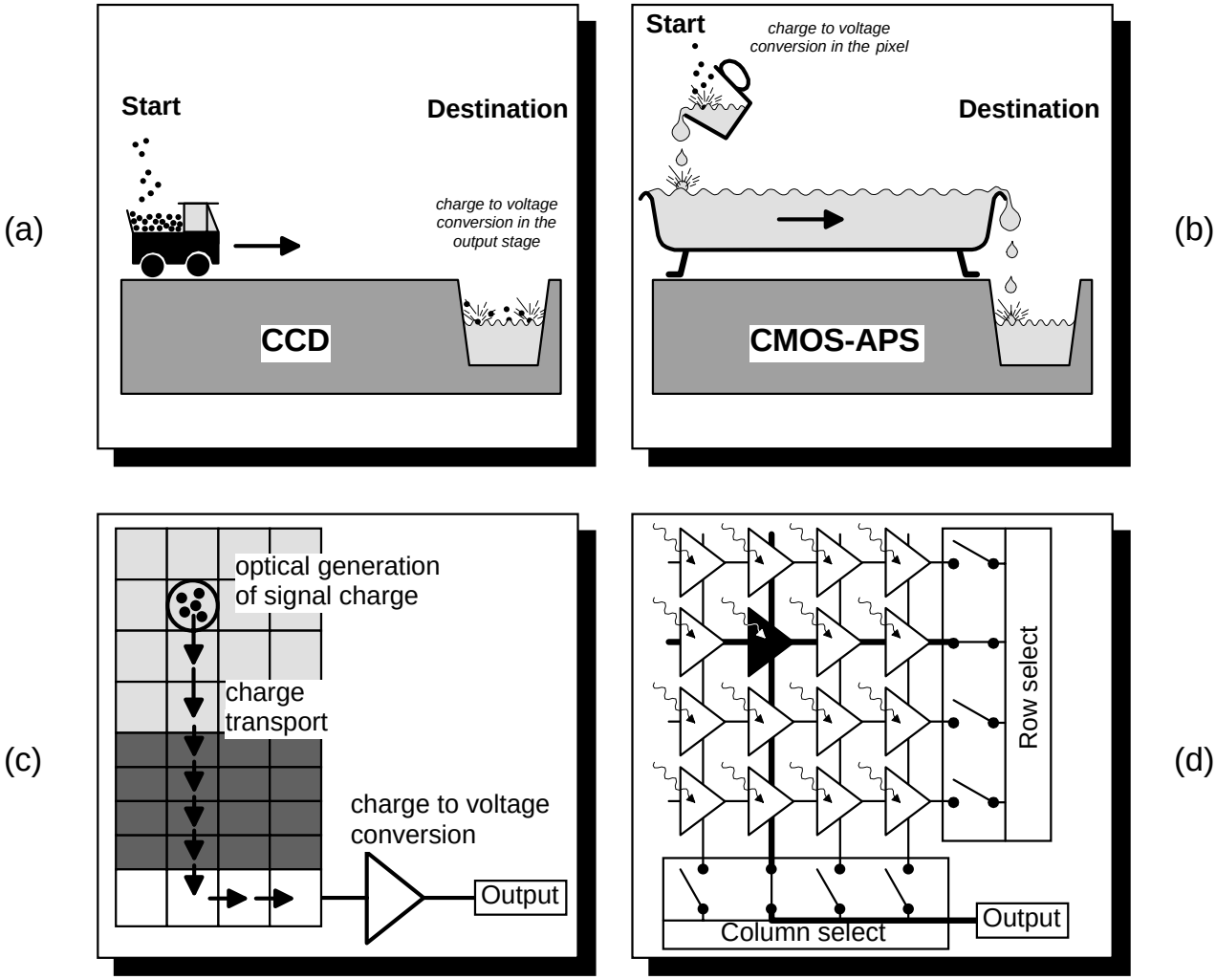

Figure 3.1 *CCD and CMOS-APS principle: Hydrostatic equivalent and principle architecture.*

Due to the steady miniaturization in microelectronics, photodiode arrays, in the form of CMOS APS sensors (Active Pixel Sensor), have experienced a sort of renaissance in recent years. They are gradually beginning to replace CCDs in certain market areas, such as low-cost applications or applications where certain features/functionality are required (high speed, low power, logarithmic response, no blooming or smearing, temporal convolution, …). CMOS APS sensors, in contrast to the classical photodiode arrays, give each pixel its own buffer amplifier, which converts the charge signal into a voltage (or current) within the pixel. With this principle it is avoided that the small photocurrent of each pixel has to drive the relatively large capacity of metal wires. The optical signal information is then read

out by sequentially connecting the low impedance pixel-amplifier to the output, rather than the high-impedance nodes of the photodiodes. The APS principle, sketched in **Figure 3.1 d**, offers low conversion capacitance and hence good sensitivity and low noise performance, gradually approaching CCD performance. Another advantage is the possibility to read out and reset single pixels by selecting them with the proper address at the row- and column- address decoder. This makes it possible to define so-called regions of interest (ROI) and to increase the image frame rate locally. Also, in general each pixel can be operated with an individual integration time. However, compared to CCDs, CMOS APS imagers often have a poorer image quality. This is because they suffer from an effect known as *fixed pattern noise* (FPN): due to variations in oxide thickness, size of gate area and doping concentrations over the sensor, each pixel has a different offset (up to some 10mV differences) and a slightly different gain, (which can usually be neglected). Therefore, external FPN correction is required; an effort, which is not necessary if using CCDs. FPN correction subtracts a locally stored dark image from the actually acquired image, thus eliminating the fixed pattern noise. Recently, approaches such as sensor-integrated correlated double sampling (CDS) or the active column principle have been demonstrated, offering ways to overcome the FPN problem [HOP, DEC, VOG].

The basic difference between CCD (charge domain signal processing) and CMOS APS (in general voltage domain signal processing) is illustrated by the hydrostatic equivalents in **Figure 3.1 a+b**. CCD imagers locally collect charge carriers to transport them physically to the output stage, where they are converted into a voltage. In contrast, CMOS APS sensors generate the signal voltage already in the pixel. The information can then be directly connected to the output.

Both CCD and CMOS APS are realized in MOS-technologies (Metal Oxide Semiconductor), mostly in silicon. The special processes, however, are optimized towards different goals. So it is usually not possible to realize good CCDs with a CMOS process or to realize efficient CMOS circuitry in a CCD technology. An overview of the most important and relevant electrical and optical properties of silicon for image sensing is given in **Section 3.1**. The following sections then focus on specific principles and properties of CCD (**Section 3.2**) and CMOS APS sensors (**Section 3.3**). More detailed information can be found in the references [TEU, BEY, SEQ, SZ1, SZ2, PS1, PS2, FOS].

3.1 Silicon properties for solid-state photo-sensing

Assuming that the energy of a photon penetrating the semiconductor is higher than the bandgap of the semiconductor material, it will be absorbed ("band to band" transition) and generate electron-hole pairs, a procedure known as *photoconversion*. Once generated, these free charge carriers generally move within the semiconductor by thermal diffusion and self-induced drift before they recombine again after a certain *lifetime* τ [SZ1]. See also **Figure 3.12**. When they have recombined, they can no longer be detected and the optical information carried by the charge carriers is lost. In order to detect the carriers, the electron-hole pairs have to be separated by an electrical field, either in the space charge region of a (reverse biased) pn-junction, as is the case for photo diodes, or in the depletion zone of a photogate, as is the case in CCD imagers.

3.1.1 Photodiodes in CMOS

For conventional CMOS processes, (we assume p-substrate processes in the framework of this dissertation,) the designer has the freedom to realize different types of photodiodes with the available process mask sets, e.g. using the n+ active layer for an n+ in p-substrate diode (n+ diode) or the n-well layer for an n^- in p-substrate diode (n-well diode). **Figure 3.2** schematically shows these diodes in a cross sectional view. They are biased in reverse direction. Assuming that the doping concentration of one side of the pn junction is much larger than the concentration on the other side, nearly the complete space charge region of size w_{sc} of the pn-junction extends to the lower doped region. The following is an approximation for an abrupt pn junction and complete depletion:

$$w_{sc} = \sqrt{\frac{2 \cdot \varepsilon_0 \cdot \varepsilon_{Si}}{q \cdot N_{lower}} \cdot (V_{bi} + V_r)} \qquad \textbf{Equation 3.1}$$

(V_{bi}: built in potential $\approx 0.7..0.8$ V; V_r: reverse bias voltage; N_{lower}: doping concentration of the lower doped region). The table in **Figure 3.2** gives typical process characteristics of a 0.5µm standard CMOS process and calculates the corresponding width of the space charge region for a reverse bias of 5 V. The active region (active depth), in which optically generated charge carriers are

immediately separated and captured, extends up to $d_0 + w_{sc}$, where d_0 is the position of the pn-junction.

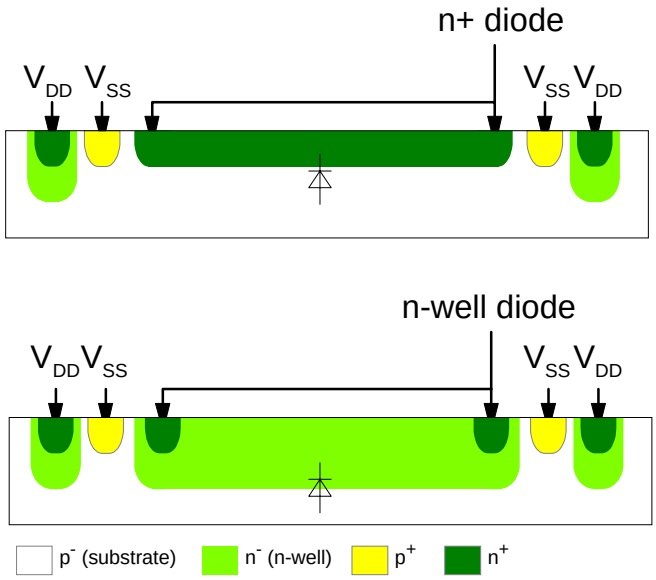

Diffusion	Depth of junction	Doping concentration
n+ diffusion	200 nm	$2 \cdot 10^{20}$ cm^{-3}
n-well	3700 nm	$5 \cdot 10^{16}$ cm^{-3}
p-substrate		$5 \cdot 10^{15}$ cm^{-3}

Photodiode	w_{sc} for V_r=5 V	Active depth (w_{sc} + junct. depth)
n+ diode	1.2 µm	1.4 µm
n-well diode	1.2 µm	4.9 µm

Figure 3.2 *Realizations of photodiodes in a CMOS process. The tables give typical values of doping concentration and depth of the diffusion regions for 0.5µm CMOS process. Also the width of the space charge region is calculated.*

Penetration depth of light

The absorption of photons entering the semiconductor material is a statistical process. The sites of photon-absorption are statistically distributed with an exponential dependence of distance from the semiconductor surface and wavelength of the incoming light. The distance where an amount of $\frac{1}{e} = 37\%$ of the total photon flux $\Phi(x)$ is already absorbed is called the *penetration depth*. That is the inverse of the *absorption constant* α [Sze].

$$\Phi(x) = \Phi_0 \cdot e^{(-\alpha \cdot x)} = \Phi_0 \cdot e^{\left(\frac{-x}{\text{penetration depth}}\right)} \qquad \textbf{Equation 3.2}$$

Figure 3.3 illustrates the exponential attenuation of the photon flux in silicon.

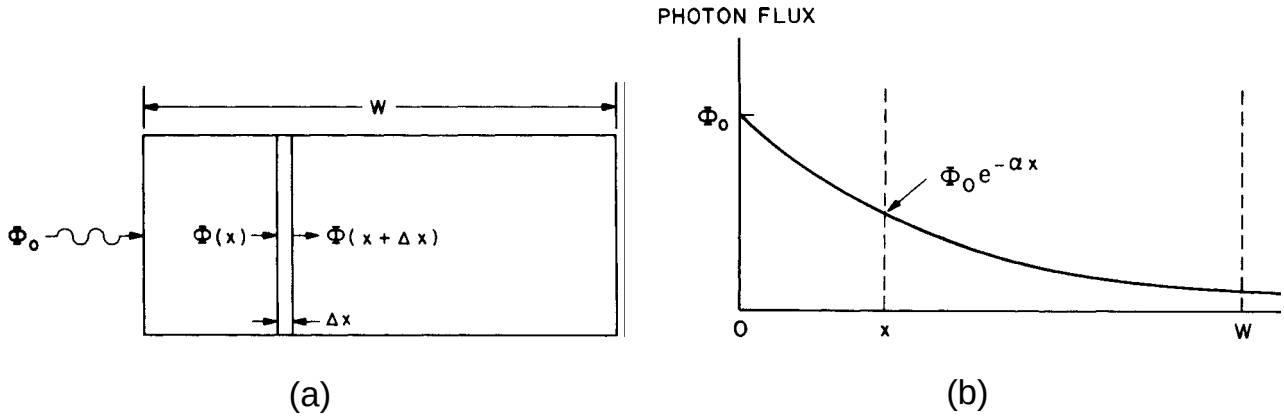

Figure 3.3 *Optical absorption. (a) Semiconductor under illumination. (b) Exponential decay of photon flux. [Sze].*

The absorption coefficient and hence the penetration depth depends on the light's wavelength. The longer the wavelength the deeper in the semiconductor photoconversion takes place. This behavior is shown in **Figure 3.4**.

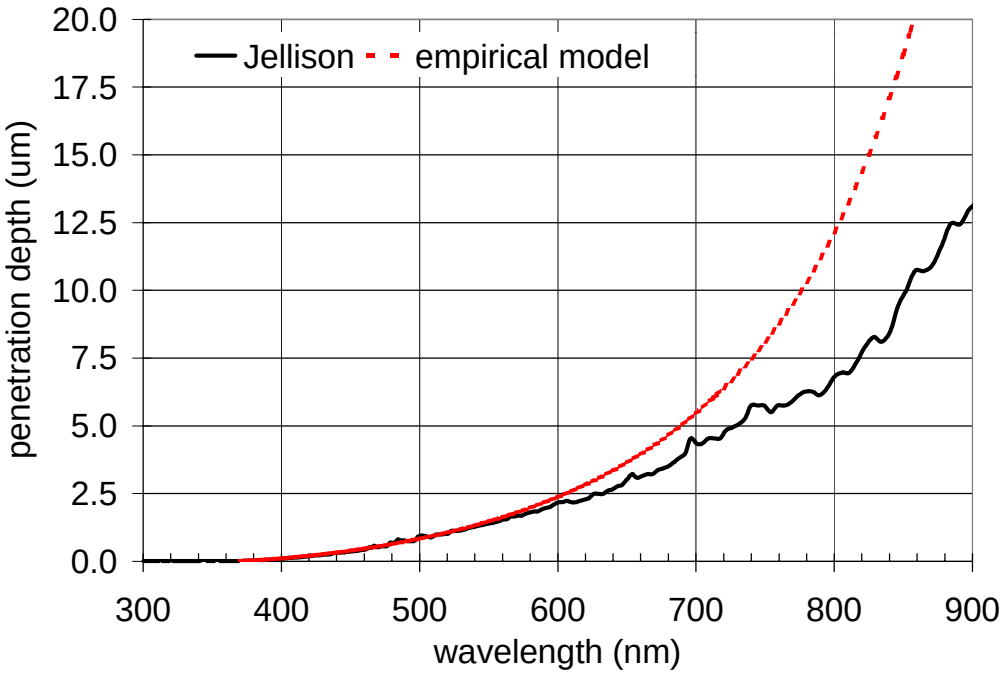

Figure 3.4 *Optical penetration depth of light into silicon. Theory and practical measurements differ for long wavelengths. The available models predict a deeper penetration depth than can be observed by measurements. (Dashed: theoretical model, solid: measured data.) [JE1], [JE2].*

For light of long wavelength a large number of electron-hole pairs is generated far from the depletion region in the semiconductor bulk. After their generation, these charge carriers move by diffusion in random directions. The further away from the surface they have been generated, the higher is the probability that they either (1) are not detected at all, an effect lowering the spectral responsivity towards long wavelengths, or (2) they are detected in neighboring pixels. This effect leads to an increased crosstalk for long wavelengths.

On the other hand, for very short wavelengths, photons are already absorbed in the covering thin-film layers (passivation layers for scratch protection and inter-layer dielectrics, mostly of SiO_2 or Si_3N_4 type) leading to a responsivity decrease towards blue and UV.

Quantum efficiency

In the framework of this dissertation we have also realized some test diodes in a 0.5µm CMOS technology. The measured quantum efficiency curves for the classical n+ and n-well diodes (sketched in **Figure 3.2**) are summarized in **Figure 3.5**. Quantum efficiency is the ratio of the number of collected electron-hole pairs to the number of incoming photons, hence the efficiency with which optical radiation of a certain wavelength is converted into an electrical signal. In addition to the decrease in efficiency towards short wavelengths (UV) and long wavelengths (IR), one can observe interference peaks in the curves, which are caused by reflections in the thin-film structure on top of the semiconductor [PS2, SP4].

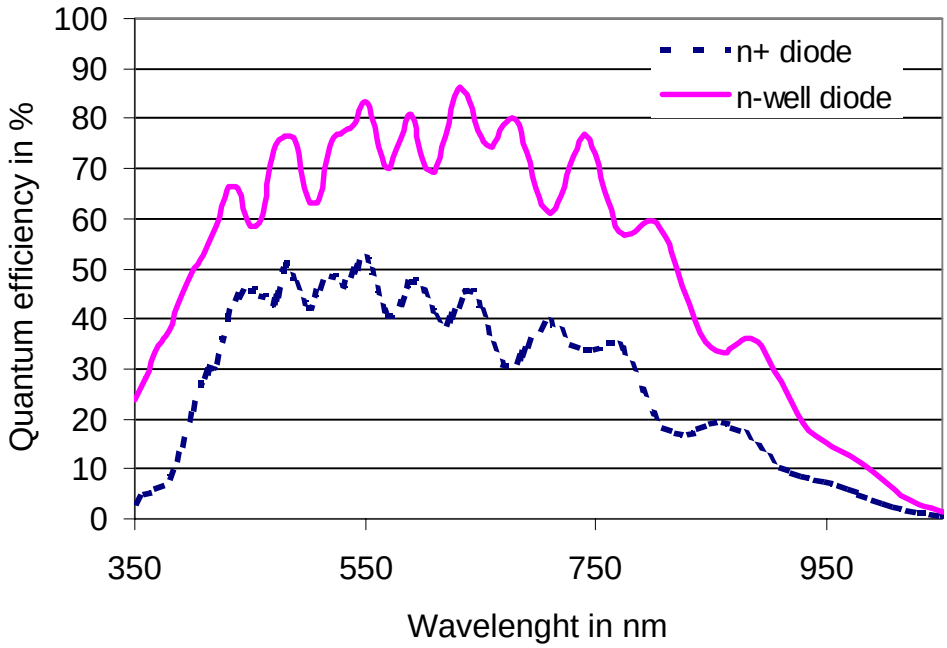

Figure 3.5 *Measured quantum efficiency curves of n+ and n-well photo diodes realized in a 0.5µm CMOS process.*

A way to increase the quantum efficiency, especially towards UV, is shown in **Figure 3.6**. This improved performance is achieved by realizing small stripes of photodiodes (finger structures) rather than one large area diode. In this way a space charge region and hence an electrical field is also present up to the semiconductor surface, where most of the blue light is absorbed.

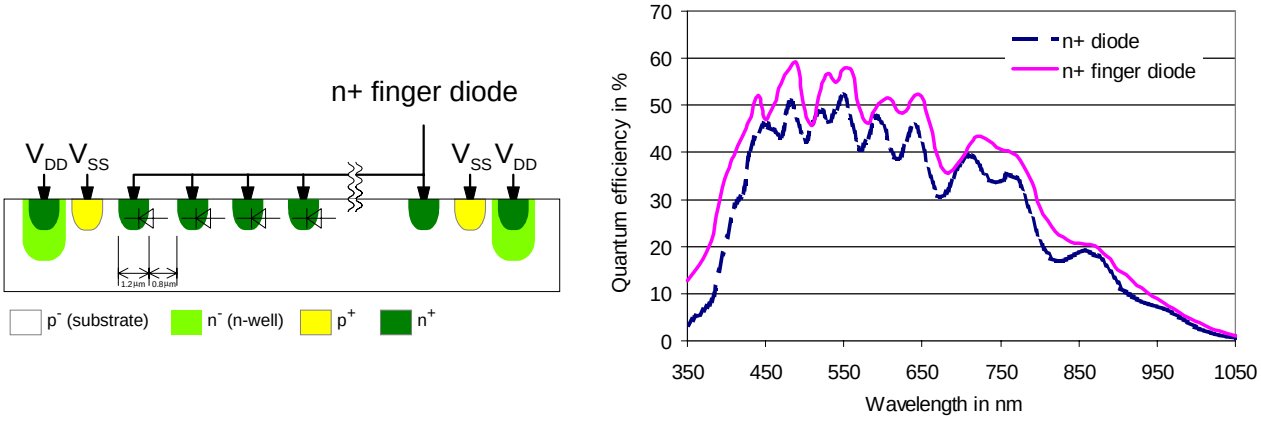

Figure 3.6 *Quantum efficiency of n+ photo diode and n+ finger photo diode. Note the improved blue and UV response for the finger structure (15 % rather than 5 % quantum efficiency at 350 nm).*

3.1.2 MOS photogate

The physical basis for a CCD device is the MOS photogate, also known as MOS capacitor or MOS-diode [SZ2]. This gate is biased in deep depletion mode, which means that a volume of depth x_d in the semiconductor underneath the photogate is totally depleted. In this depletion zone no free charge carriers are available. (Here electrons correspond to minority carriers and holes to majority carriers, since a p-substrate process is used for this work.) If free minority carriers were available, the MOS gate would be in strong inversion, causing an inversion layer of electrons below the gate. For a MOS transistor this assumption is usually valid because free charge carriers come from the source and the drain. This is, however, not the case if we look at a photogate or CCD gate. In the latter case free charge carriers are only available if either generated optically (optical signal) or thermally (dark current). We therefore call this operation mode *deep depletion* (a sort of non-equilibrium mode of strong inversion).

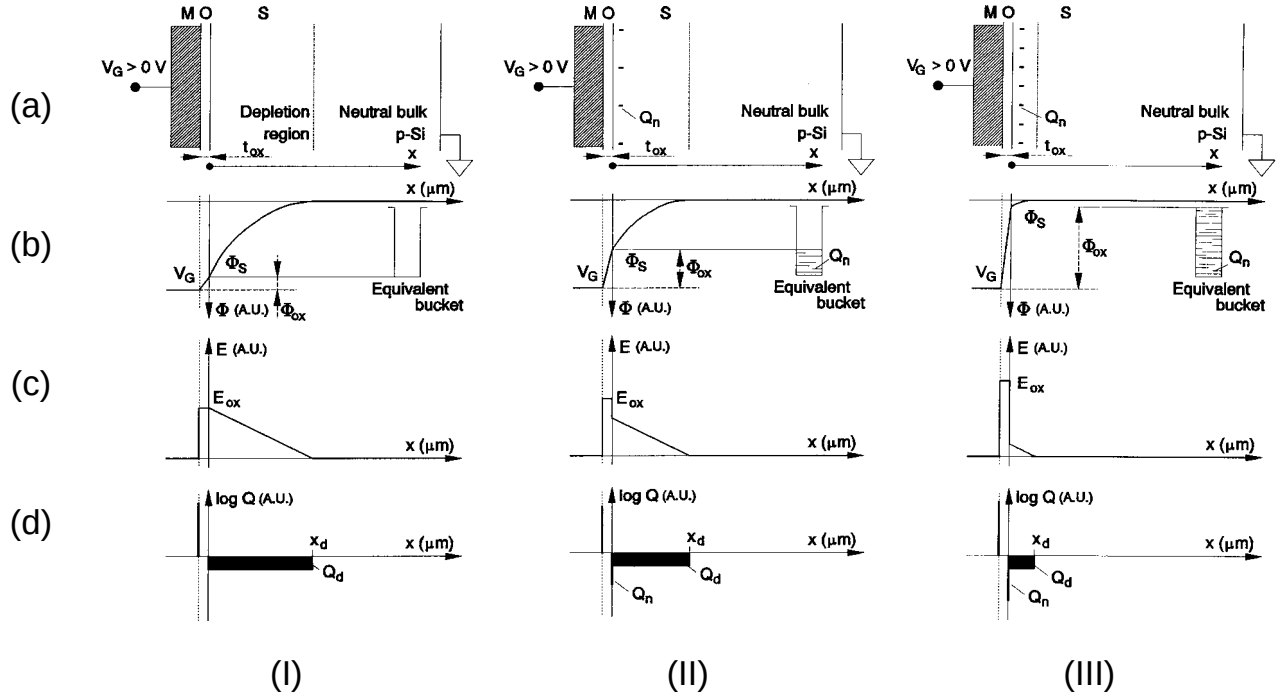

Figure 3.7 *MOS gate on p-type silicon (I) in deep depletion, (II) in weak inversion after integration of optically generated photoelectrons, (III) in strong inversion: saturation of photogate. (a) principle figure, (b) electrostatic potential and equivalent potential bucket, (c) electric field and (d) charge distribution diagram. [TEU].*

The different operation modes of the MOS gate are illustrated in **Figure 3.7**. **Figure 3.7 (I)** shows the conditions when no free charge carriers are available. This causes the depletion region to extend deep into the semiconductor resulting in a deep space charge region (*deep depletion*). This mode can be interpreted as an empty potential bucket, since it offers the capability to store electrons in the same way that an empty water bucket offers the possibility to be filled with water.

With the (preferentially) optical generation of electron hole pairs free charge carriers become available. The electron-hole pairs are separated in such a way that the electrons (minority carriers) are collected at the semiconductor surface while the holes (majority carriers) are rejected into the semiconductor bulk, where they recombine after a certain lifetime. The electrons begin to form an inversion layer and at the same time decrease the depth of the space charge region. This mode is known as *weak inversion*. Continuing the comparison with the water bucket, this integration process of optically generated electrons corresponds to filling the bucket with water (**Figure 3.7 (II)**). We call the sum of integrated electrons, which are acquired in the potential bucket, *charge packets*.

After a certain number of electrons are generated, the potential bucket will be filled and no more free charge carriers can be held by the MOS diode (**Figure 3.7 (III)**). This mode is known as *strong inversion*. It is the equilibrium condition of the MOS diode for the gate voltage applied. It is also the mode a MOS transistor would be in for the applied voltage, since, in contrast to the MOS capacitor the MOS transistor offers the required number of free electrons directly from its source and drain. In the CCD application *strong inversion* is the point which limits the charge handling capability of the CCD gate. If more electrons were generated, they would move to a neighboring pixel, a process called blooming.

Width of depletion region

The width of the depletion region x_d, and thus the size of the “capture volume”, as a function of the doping concentration N_A (p-type substrate) and the gate voltage V_G is given by:

$$x_d = \sqrt{\frac{2 \cdot \varepsilon_0 \cdot \varepsilon_{Si} \cdot \Phi_S}{q \cdot N_A}} \qquad \textbf{Equation 3.3}$$

with the channel potential Φ_S:

$$\Phi_S = V_G - V_{FB} + \frac{Q_n}{C_{ox}} + \left\{ \frac{\varepsilon_0 \cdot \varepsilon_{Si} \cdot q \cdot N_A}{C_{ox}^2} \cdot \left(1 - \sqrt{1 + \frac{2 \cdot C_{ox}^2 \cdot \left(V_G - V_{FB} + \frac{Q_n}{C_{ox}} \right)}{\varepsilon_0 \cdot \varepsilon_{Si} \cdot q \cdot N_A}} \right) \right\}$$

Equation 3.4

In this equation Q_n is the charge of integrated electrons per unit area. (This charge is of negative polarity, because electrons are collected. q, the elementary charge, is of positive polarity → $Q_n = -n_e \cdot q$). V_G is the gate voltage, V_{FB} is the flatband voltage and (V_G - V_{FB}) is the effective gate voltage. (See [TEU] for more details). The oxide capacitance per unit area C_{ox} is given by:

$$C_{ox} = \frac{\varepsilon_0 \cdot \varepsilon_{ox}}{t_{ox}}$$

Equation 3.5

In **Figure 3.8** the depletion width is shown as a function of typical doping concentrations and gate voltages. The higher the gate voltage and the lower the substrate doping, the deeper the depletion region is. For CCD applications the depletion region should usually be as deep as possible in order to directly capture as many optically generated charge carriers as possible.

(a)

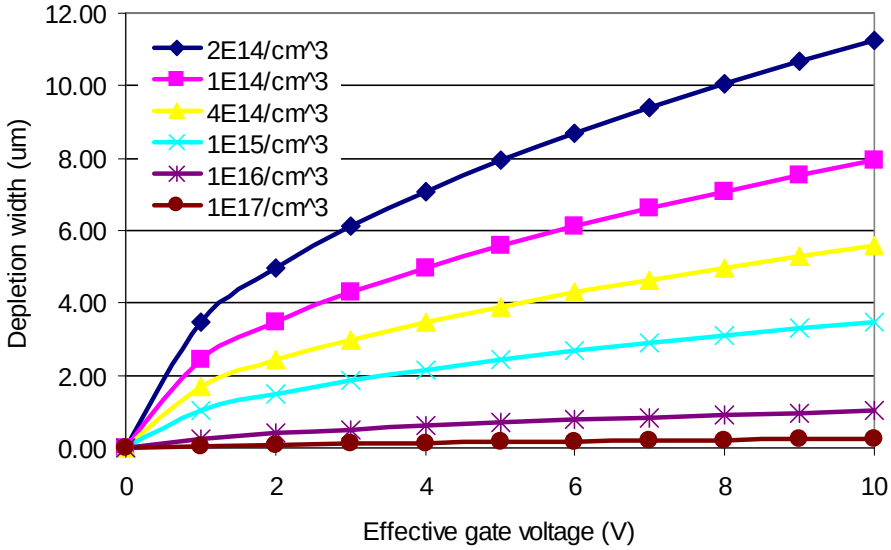

(b)

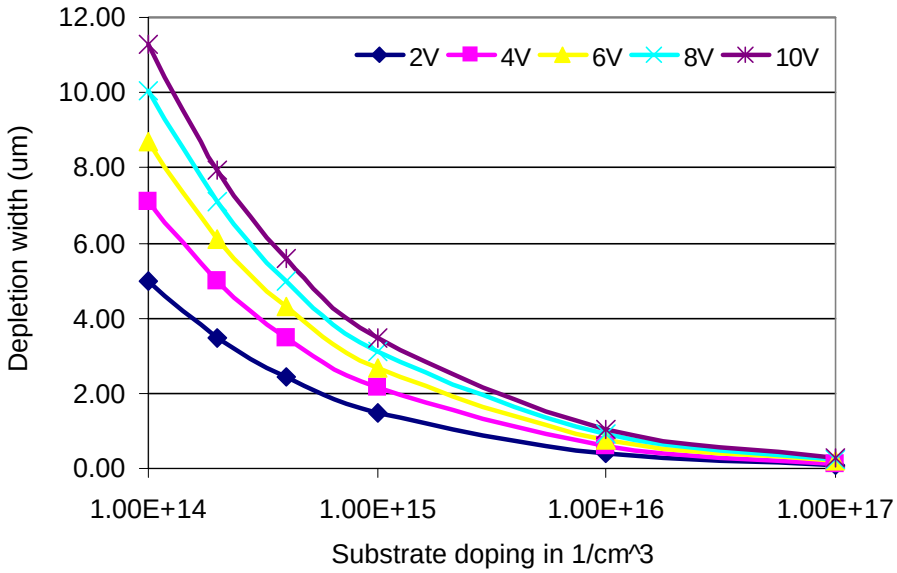

Figure 3.8 *MOS photogate: (a) Depletion width versus gate voltage for fixed substrate doping. (b) Depletion width versus substrate doping for fixed effective gate voltage (V_G-V_{FB}). (Q_n=0).*

The decrease in depletion depth as a function of optically generated electrons is illustrated in **Figure 3.9** for typical CCD dimensions.

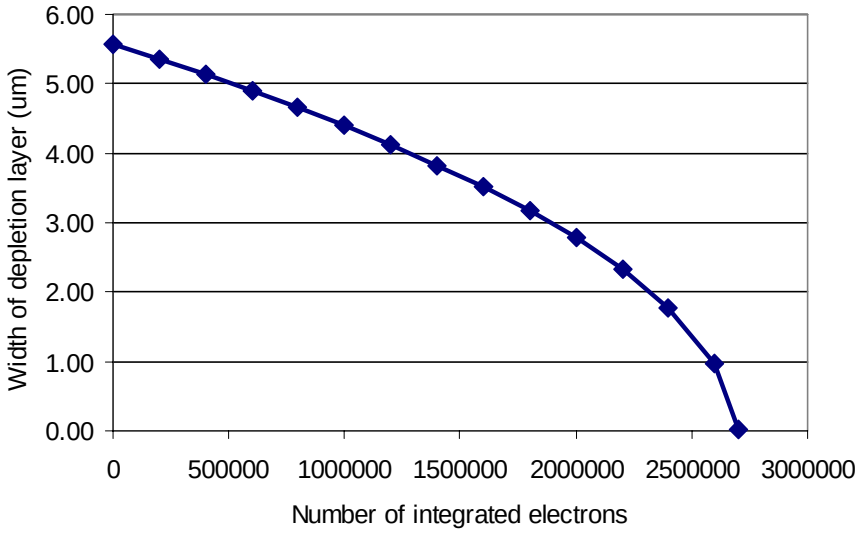

Figure 3.9 *MOS photogate: Depletion width versus number of integrated free electrons. (Effective gate voltage:10 V, substrate doping $4 \cdot 10^{14}$ cm^{-3}, gate size: 10 µm x 5 µm, oxide thickness: 40 nm).*

Free charge carriers (electron hole pairs) are generally generated both optically and thermally. It is, however, not possible to distinguish between optically generated and thermally generated electrons. Both are integrated in the same potential bucket. The thermal generation is therefore an unwanted effect (*dark current*) which is sometimes reduced by cooling the CCD devices.

At this point we also understand the relatively large voltage requirements for CCDs. The larger the voltages applied to the CCD gates, the higher the CCD's charge handling capability is. High voltages, on the other hand, increase the risk of oxide break-through. This again is the reason why CCD processes use relatively thick oxides, making them less suited for the realization of good MOS transistors.

Most CCDs have transparent photogates of polysilicon and are illuminated from the front side (as the CCDs in this work). The polysilicon gates cause some additional losses in quantum efficiency, especially in the blue (short wavelengths) and also additional thin film interference peaks. **Figure 3.10** shows the quantum efficiency measurements of (CCD-) photogates (poly1 and poly2 photogates) realized in 2.0µm Orbit CMOS/CCD process, the process we used in the framework of this dissertation for the realization of the demodulation pixels.

Very special processes avoid the reduced blue response by thinning the substrate to only several tens of microns, which is a quite complicated and expensive process. Such CCDs are illuminated from the back side and usually have a very good quantum efficiency.

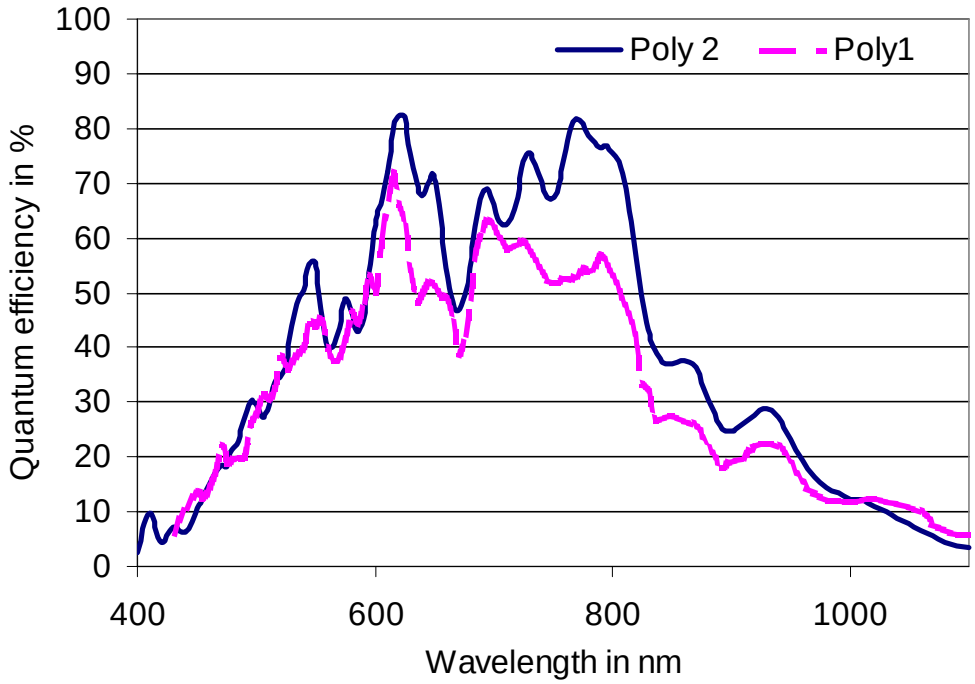

Figure 3.10 *Measurement of quantum efficiency for poly1 and poly2 photogates realized in Orbit 2.0µm CMOS/CCD process. [HEK].*

3.1.3 Transport mechanisms for charge carriers

Basically there are three independent transport mechanisms for free charge carriers in the semiconductor (**Figure 3.11**):

1. Self-induced drift
2. Thermal diffusion
3. Drift due to an electric field.

Self-induced drift

Self-induced drift is based on the coulomb forces between free charge carriers of the same polarity. It makes the charge carriers tend to move away from each other. In practice self-induced drift only contributes significantly to the overall charge

transport if many free charge carriers are located close to each other. We will see later that for typical optical conditions in our TOF application, we deal with the transportation of single electrons. Therefore, self-induced drift is neglected.

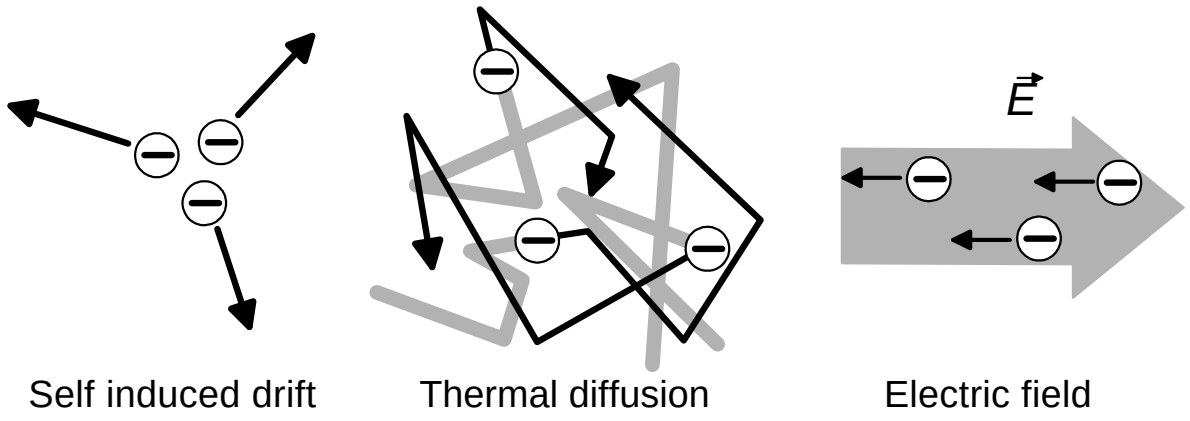

Figure 3.11 *Transport mechanisms for free electrons in a semiconductor.*

Thermal diffusion

For temperatures larger than T=0°K, free charge carriers have thermal energy, which results in a permanent movement in random directions. The thermal velocity v_{th}, i.e. the amount of the microscopic movement velocity, is given by:

$$v_{th} = \sqrt{\frac{3kT}{m_{eff}}} \qquad \textbf{Equation 3.6}$$

At room temperature (300K) we get $v_{th} \approx 10^7$ cm/s for Si and GaAs. The charge carriers move fairly quickly but steadily change their directions due to collisions with the fixed lattice or impurity atoms or other free charge carriers. The sum of these microscopic movements results in a macroscopic movement, again in random directions. This movement process, known as thermal diffusion, only ends when the free carriers recombine after a certain *lifetime* τ_n and τ_p respectively. Statistically speaking, after this time they have traveled a certain distance, the so-called diffusion length L_n:

$$L_n = \sqrt{D_n \cdot \tau_n} \qquad \textbf{Equation 3.7}$$

This diffusion length depends on the doping concentration of the semiconductor. This is expressed in the diffusivity D_n, which contains the doping dependent carrier mobility (electron mobility μ_n):

$$D_n = \frac{1}{3} \cdot v_{th} \cdot l_{diff} = \mu_n \cdot \frac{kT}{q}$$ **Equation 3.8**

Equivalently the electron needs a mean time t_{diff} to travel the distance l_{diff} by thermal diffusion:

$$t_{diff} = \frac{l_{diff}^2}{D_n}$$ **Equation 3.9**

In **Equation 3.8** l_{diff} is the mean free path between collisions of the charge carrier with the lattice or other carriers. Carrier diffusivity, mobility and lifetime depend on the state of the charge carrier, whether they are the majority carriers or the minority carriers. Generally, in photo elements, the minority carriers contribute to the photocurrent and are therefore of interest. In the case of the p-type process we used, electrons are the minority carriers. Therefore, we only gave the equations for electron diffusivity and diffusion length above.

Figure 3.12 shows the dependency of mobility, lifetime and diffusion length as a function of the doping concentration for both electrons and holes in silicon at 300° K.

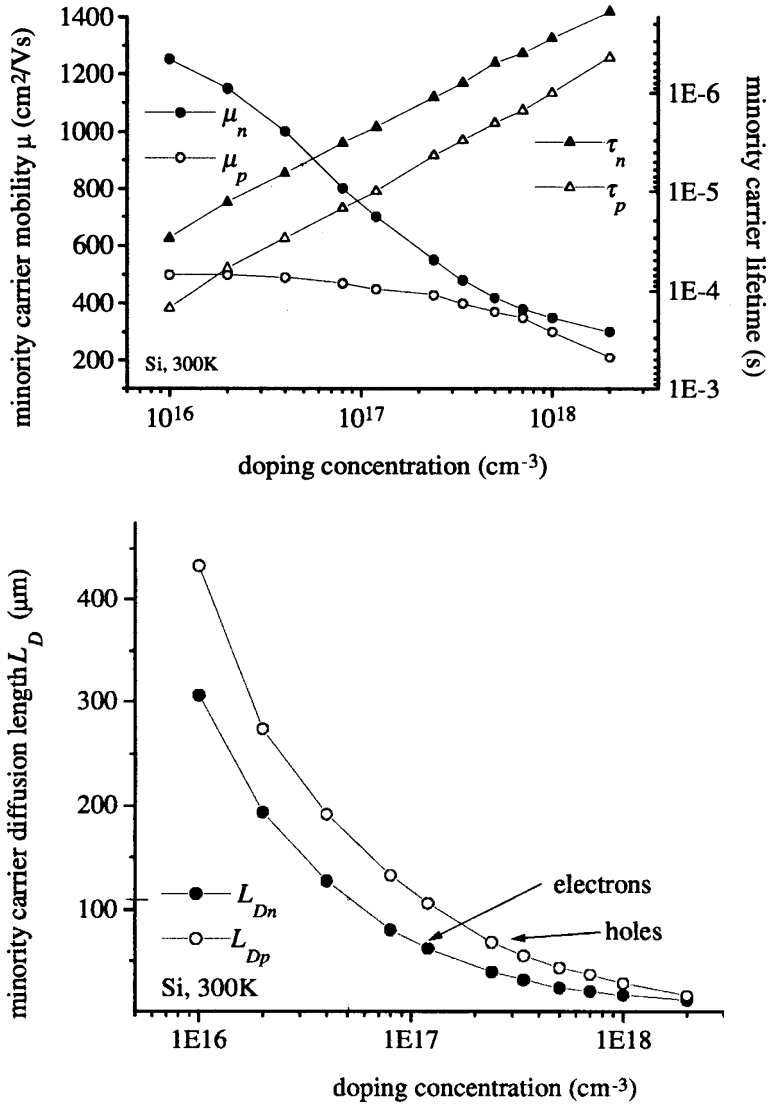

Figure 3.12 *Mobility, lifetime and diffusion length of minority carriers versus impurity concentration in silicon. [SZ1, WON].*

Drift in an electric field

When an electric field E is applied to a semiconductor sample, each electron will experience a force -q·E from the field and will be accelerated along the field (in the opposite direction) until it comes to a collision with the lattice atoms or impurity atoms. An additional velocity called the drift velocity will therefore be superimposed upon the random thermal motion of electrons. For low electrical fields E this mean drift velocity v_n of free electrons is given by:

$$v_n = -\mu_n \cdot E \qquad \textbf{Equation 3.10}$$

The proportionality factor between the electrical field and the drift velocity is the carrier mobility μ_n (here electron mobility), given by:

$$\mu_n \equiv \frac{q \cdot \tau_c}{m_{eff}} \qquad \textbf{Equation 3.11}$$

τ_c is the mean free time, or the average time between collisions of the carriers with the lattice or impurity atoms. It strongly depends on the semiconductor material, the temperature and the doping concentration in the semiconductor (see also **Figure 3.12**).

For very high electric fields this drift velocity approaches the thermal velocity, which cannot be exceeded in silicon and thus defines the maximum drift velocity v_{max} (or saturation velocity) in an electric field (10^7cm/s for Si) (see **Figure 3.13**):

$$v_{max} = v_{th} = \sqrt{\frac{3kT}{m_{eff}}} \qquad \textbf{Equation 3.12}$$

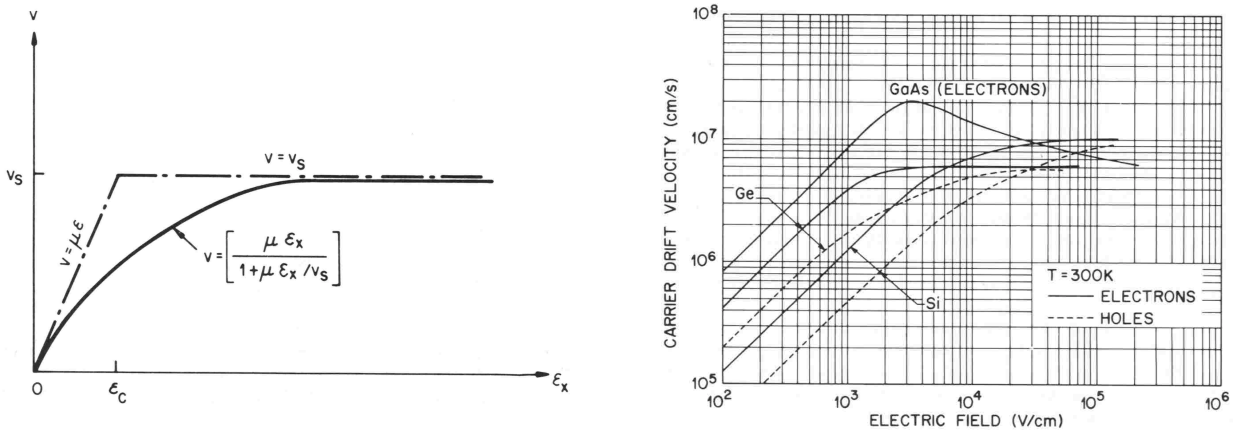

Figure 3.13 *Drift of free charge carriers in an electric field: saturation velocity. [SZ2].*

The correct expression for the drift velocity, considering the saturation velocity is:

$$v_n = \frac{\mu_n \cdot E}{1 + \frac{\mu_n \cdot E}{v_{max}}} \qquad \textbf{Equation 3.13}$$

At this point it is worth mentioning two points:

(1) Generally, the carrier drift velocity in metal is much lower than in semiconductors because of the lower mobility.

(2) GaAs devices achieve higher cut-off frequencies than silicon devices, since electrons have a six times higher mobility in low doped GaAs than in low doped silicon ($N=10^{14}$).

Temporal response - numerical examples

The following numerical example shows for the different influences of both thermal diffusion and drift in an electric field on the overall carrier movement. Generally, thermal diffusion is a non-directed random movement process. In the configuration illustrated in **Figure 3.14 (a)**, however, the free electron can only move in a plane parallel to the semiconductor surface. This is because it is prevented from moving towards the semiconductor bulk by the electrical field created by the biased MOS gate. Also it cannot move to the left, since it sees a potential barrier there to the left neighboring gate, which is biased at 0V. Hence, the only direction the electron is allowed to move is towards the right neighboring gate. The abrupt potential steps between the gates and the flat shape of the potential under the single gates are idealized conditions, chosen to illustrate the diffusion mechanism only. For the p-substrate doping of $4 \cdot 10^{14}$ cm^{-3} of the process we used, we have an electron mobility of about 1300 cm^2/Vs. With the Boltzmann constant $k=1.3807 \cdot 10^{-23}$ J/K and elementary charge $q=1.6 \cdot 10^{-19}$ C, this leads to a diffusivity D_n of 33.6 cm^2/s at T=300° K. Assuming a gate length of 10 µm (=0.001 cm) we obtain a mean diffusion time of 30 nanoseconds. For a gate length of 30µm, however, the mean diffusion time would already be 270 nanoseconds, since the diffusion time increases with the square of the distance to travel.

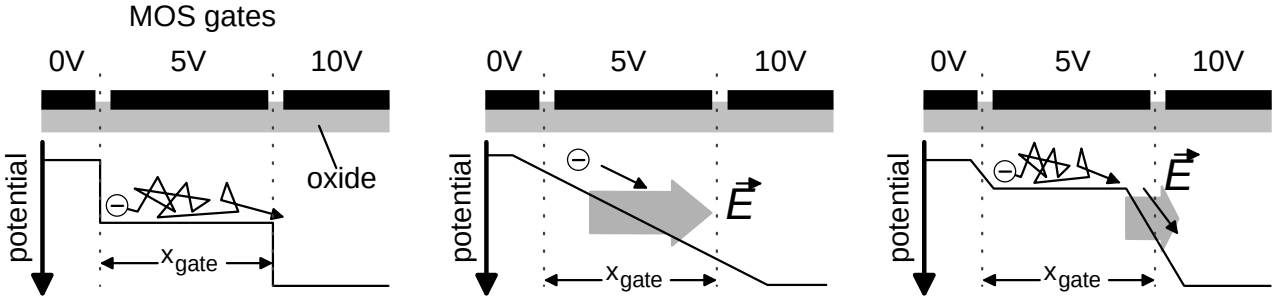

(a) Thermal diffusion (b) Drift in an electric field (c) Combination

Figure 3.14 *Transport mechanisms (II).*

For a linearly falling potential between two gates, as illustrated in **Figure 3.14 (b)**, we obtain a constant electric field between the gates. Applying a potential

difference of only 1 V between the gates of 10 μm length, this field is 10^5 V/m, a value at which the saturation velocity is not yet reached. The drift in such an electric field would take the electron only about 0.8 nanoseconds. For 30 μm gate length the traveling time would be 7 nanoseconds for the same potential difference. Also, for a fixed potential difference, the E-field drift time increases with the square of the drift length.

In reality the process of carrier movement is a superposition of both cases discussed above. However, the real potential distribution is also a superposition of both extreme cases sketched in **Figure 3.14 (a+b)**, we do not have an abrupt potential step between two gates at different potential nor do we have a linearly falling potential distribution over the entire gate length. Generally, for typical doping concentrations, the horizontal electrical field in the semiconductor, caused by a potential gradient between two neighboring gates, the so-called fringing field, only extends to a relatively small area between the gates [BEY]. Therefore, for relatively long gates, the charge transport will be dominated by pure thermal diffusion and only for very short gates do the fringing fields have an influence. **Figure 3.14 (c)** shows a more realistic potential distribution.

The estimation of the fringing field extension is relatively complex and also difficult to simulate, since it strongly depends on the semiconductor's doping concentrations. Unfortunately semiconductor foundries keep these exact doping profiles secret. At least we know that there are additional impurities and implants, especially directly beneath the semiconductor surface (e.g. anti-punch through implants). Due to this lack of process-parameter knowledge and the complexity of available simulation tools, it appears to be more practical, in the framework of this dissertation, to measure rather than to simulate the actual speed performance.

3.1.4 Noise sources

The performance of solid-state imagers is limited by several different noise sources. These can generally be divided into three classes: (1) photon shot noise, (2) photocharge conversion noise and (3) quantization noise.

Shot noise (or quantum noise) describes the statistical Poisson-distributed nature of the arrival process of photons and the generation process of electron-hole pairs.

The standard deviation of the photon shot noise ΔN_{shot} is equal to the square root of the number of photons or photogenerated charge carriers N:

$$\Delta N_{shot} = \sqrt{N}$$ **Equation 3.14**

Photocharge conversion noise includes all noise sources that disturb the “optical“ information in the process chain of converting the optically generated electron hole pairs into an analogous output signal. **Figure 3.15** illustrates a source follower stage as a typical example of a detection stage in semiconductor imagers. Photocharge conversion noise is composed of several contributions, viz. reset noise, 1/f noise (flicker noise), amplifier Johnson noise (thermal noise) and shot noise of dark current. All these contributions increase with temperature.

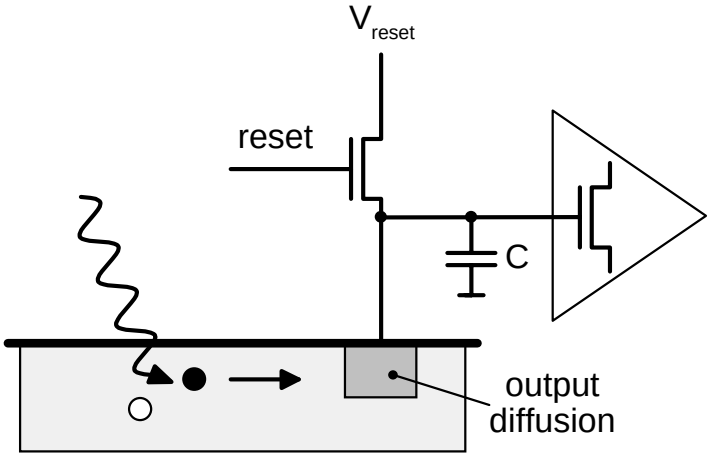

Figure 3.15 *Source follower photo detection stage. The output diffusion is directly connected to the gate of a source follower transistor. The light-proportional amount of charge collected on the capacitance C of the output diffusion node controls the current in the first amplifier stage. By activating the reset switch, the charge on the output node can be dumped to the reset source. [PS2].*

Reset noise, also known as kTC noise, describes the Johnson noise (resistor noise) influence of the transistor channel of the reset transistor on the charge at the output diffusion. Every time the reset transistor is activated, the output diffusion is charged to the reset voltage V_{reset}. This corresponds to a certain amount of reset charge Q_{reset} on the conversion capacitance C (capacitance of the output diffusion node) varying by the reset charge noise ΔQ_{reset}.

$$\Delta Q_{reset} = \sqrt{k \cdot T \cdot C}$$ **Equation 3.15**

Flicker noise is caused by so-called semiconductor traps, which randomly capture and release charge carriers, leading to statistical variations of the mobility and concentration of free charge carriers in the transistor channel of the source follower transistor [PS2]. Referred back to an input equivalent amount of charge, one obtains the flicker noise contribution $\Delta Q_{flicker}$:

$$\Delta Q_{flicker} = C \cdot \sqrt{\frac{4 \cdot k \cdot T \cdot f_l}{g_m \cdot f_s} \cdot B} \qquad \textbf{Equation 3.16}$$

where f_l is the corner frequency, a process and layout dependent parameter, fs is the sampling/ readout frequency, g_m the transistor transconductance and B is the bandwidth.

The noise equivalent input charge of the resistor noise in the channel of the source follower transistor (Amplifier Johnson noise) is:

$$\Delta Q_{amp} = C \cdot \sqrt{\frac{4 \cdot k \cdot T \cdot \alpha}{g_m} \cdot B} \qquad \textbf{Equation 3.17}$$

(α: 0.7..1, CMOS transistor parameter.)

Neglecting the amplification of the source follower output stage (usually about 0.8-0.9) we can transform the above mentioned input noise out of the charge domain into the equivalent output noise in the voltage domain:

$$\Delta V_{reset} = \sqrt{\frac{k \cdot T}{C}}$$
$$\Delta V_{flicker} = \sqrt{\frac{4 \cdot k \cdot T \cdot f_l}{g_m \cdot f_s} \cdot B} \qquad \textbf{Equation 3.18}$$
$$\Delta V_{amp} = \sqrt{\frac{4 \cdot k \cdot T \cdot \alpha}{g_m} \cdot B}$$

Dark current corresponds to the thermal generation of free electron hole pairs, which competes with the optical generation and adds an offset charge to the optically generated signal. Since thermally generated charge carriers are also quantized, dark current adds an additional Poisson-distributed shot noise contribution to the overall noise.

The sum of photocharge conversion noise can be drastically suppressed if the sensor is operated at low temperatures (cooled imagers). With decreasing minimum feature size of current and future semiconductor processes, lower

conversion capacitances C can be realized and that is one reason for steady improvement of imager performances. These and many other additional clever techniques (such as correlated double sampling) can be used to reduce photocharge conversion noise.

Photon shot noise is a very important noise source, since it cannot be suppressed and, therefore, is the ultimate theoretical limitation of all photo detectors. Also, since photon shot noise increases with the amount of incoming photons, it finally dominates all other noise sources and hence limits the effective signal-to-noise-ratio for higher illumination levels. **Figure 3.16** summarizes the above discussion.

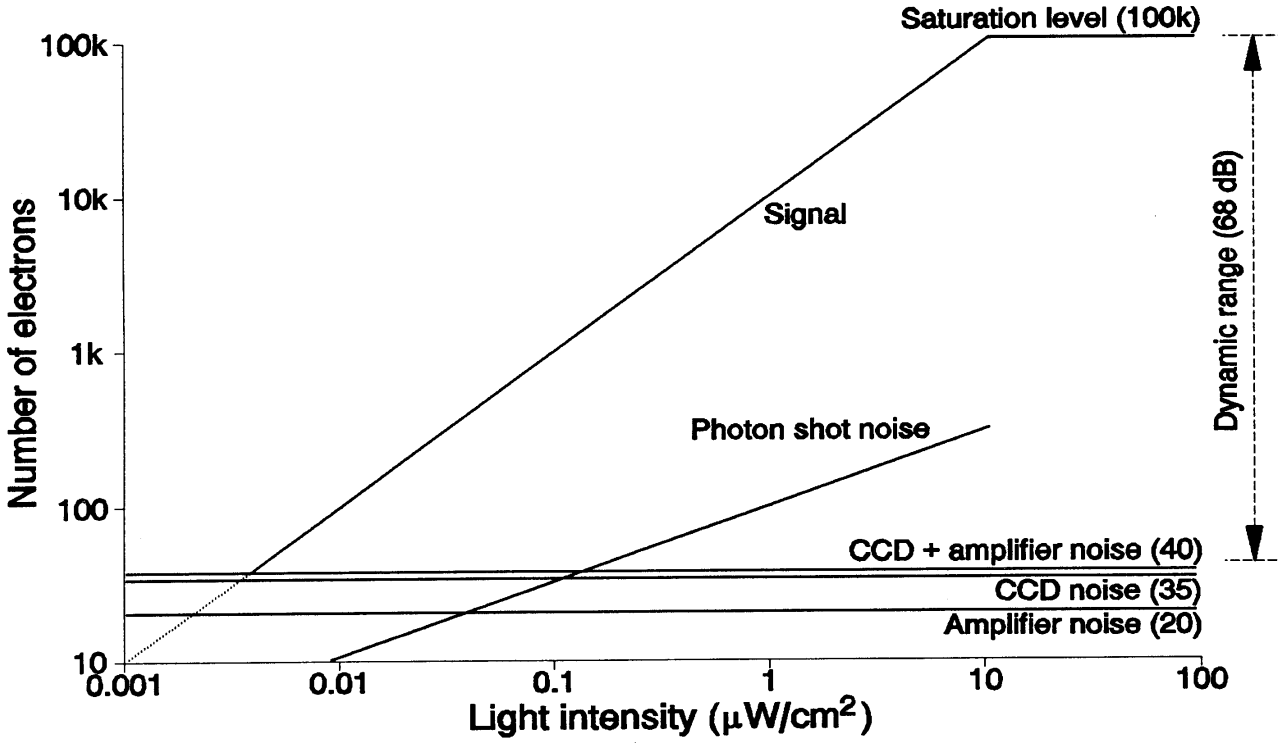

Figure 3.16 *Influence of single noise sources on the SNR. [TEU].*

3.1.5 Sensitivity and Responsivity

The sensitivity s characterizes the conversion process of the optically generated charge into an analogous output voltage. In essence it is determined by the size of the conversion capacitance C and the amplification A_{sf} of the output stage, in this work, a two-stage source follower (C=40 fF and A_{sf}=0.9). It is usually specified in terms of volts per electron.

$$s = \frac{A_{sf}}{C} \cdot q \quad \left[\frac{V}{electron}\right] \qquad \textbf{Equation 3.19}$$

A small conversion capacitance C therefore leads to both low noise and high sensitivity.

The responsivity r additionally takes into account the quantum efficiency of the optical detection mechanism. It is expressed in terms of volts per photon and depends on the wavelength of the light:

$$r = QE(\lambda) \cdot s = QE(\lambda) \cdot \frac{A_{sf}}{C} \cdot q \quad \left[\frac{V}{photon}\right] \qquad \textbf{Equation 3.20}$$

3.1.6 Optical fill factor

The last important measure we would like to mention for solid-state photo-sensing is the optical fill factor. This is the ratio of light sensitive pixel area to the total pixel area. In APS sensors a certain amount of pixel area is occupied by the in-pixel amplifier. Photons impinging on these areas do not in general contribute to the optically generated signal. They are either reflected or absorbed by opaque metal regions or they generate electron hole pairs, which are directly drained to a diffusion. CMOS APS sensors have typical optical fill factors between 30% and 50%. In CCDs the optically generated charge is sometimes - depending on the CCD architecture - stored in an opaque region of the pixel, also decreasing the optical fill factor. CCDs usually have optical fill-factors between 50% and 100%.

For our TOF application a large optical fill factor is of essential importance since we use active illumination. The optical power of the modulated illumination source is both expensive and limited by eye-safety regulations. This requires the best possible optical fill factor for an efficient use of the optical power and hence a high measurement resolution.

3.2 Charge coupled devices: CCD - basic principles

The underlying physical structure for charge-coupled devices is the MOS diode in deep depletion (see **Section 3.1.2** for details). The operation sequence of CCD devices is to integrate optically generated charge carriers (photoelectrons) locally and to bundle them into charge packets in each pixel. The charge carriers are then physically transported to one output stage by a clever sequence of charging and discharging neighboring photogates. Each pixel-charge packet is subsequently transferred to the output stage, where it is converted into an analog voltage at the output.

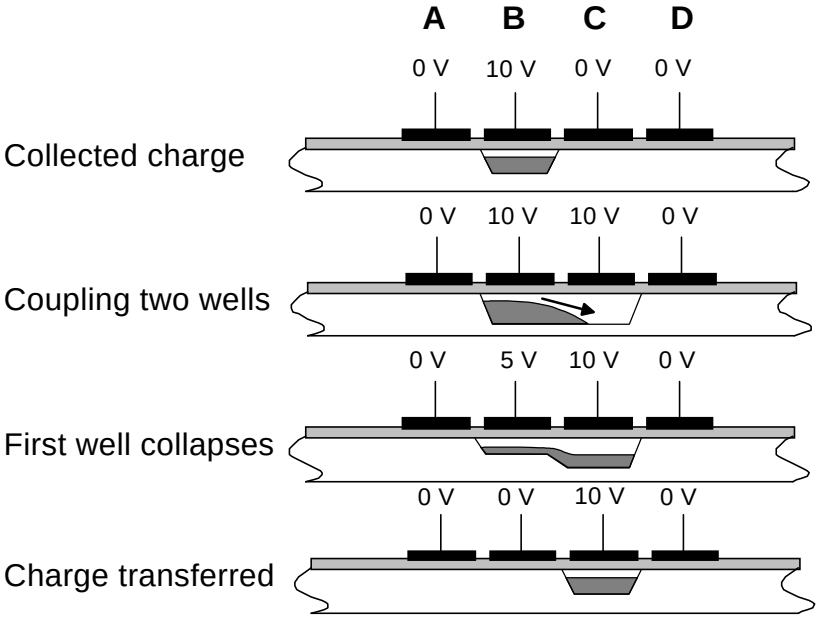

Figure 3.17 *Charge transport in charge-coupled devices. [HEK].*

The CCD-transport mechanism, first demonstrated by Boyle, Smith, Amelio and Tompsett [BOY, AME], is illustrated in **Figure 3.17**. After an integration period in which the charge is collected under the only biased CCD-gate B, in a first step the neighboring gate C is biased to the same potential as gate B. Thus the two potential wells merge to one and the charge will equally distribute under both gates due to self induced coulomb drift and thermal diffusion. This process is called charge-coupling. In the next step the bias voltage of gate B is decreased and the potential well under this gate collapses. This results in the transport of the complete charge packet towards gate C. By repeating these steps the charge can be moved through the semiconductor. This transport mechanism works with a very high efficiency, the so-called charge transfer efficiency CTE. The CTE is defined as the

amount of the charge packet that remains after the transport losses δ resulting from the transport from one pixel to the next. One pixel mostly consists of three or four CCD gates (three- / four-phase CCDs), however, also two-phase or even one-phase CCDs have been reported (TEU).

$$CTE = (1 - \delta) \qquad \textbf{Equation 3.21}$$

After transportation of the charge packet by N pixel positions, the following share of the original charge remains:

$$CTE^N = (1 - \delta)^N \qquad \textbf{Equation 3.22}$$

Typical CCD processes offer CTE values between 0.9999 and 0.99999. The following table shows the influence of both CTE and number of charge transfers (number of pixels) on the remaining charge packet.

	CTE=0.99	CTE=0.999	CTE=0.9999	CTE=0.99999
N=10	90%	99%	99.9%	99.99%
N=100	37%	90%	99%	99.9%
N=1000	0%	37%	90%	99%

Remaining charge after N transfers for different CTE values.

The CCDs as we have described them so far are called surface channel CCDs (SCCD). As can be seen in **Figure 3.7 (b)** the potential minimum in the vertical direction for the classical MOS diode in deep depletion or strong inversion mode is located directly at the junction between semiconductor and gate oxide. Since the photoelectrons tend to stay at the potential minimum, the charge transport, which is due to a superimposed potential difference in the horizontal direction, takes place at the junction between semiconductor and oxide surfaces. Unfortunately, this junction region is characterized by charge traps (caused by lattice mismatch, surface states and impurities), which typically capture free electrons and randomly release them at later times. This is one main technical limitation for a good CTE in SCCDs.

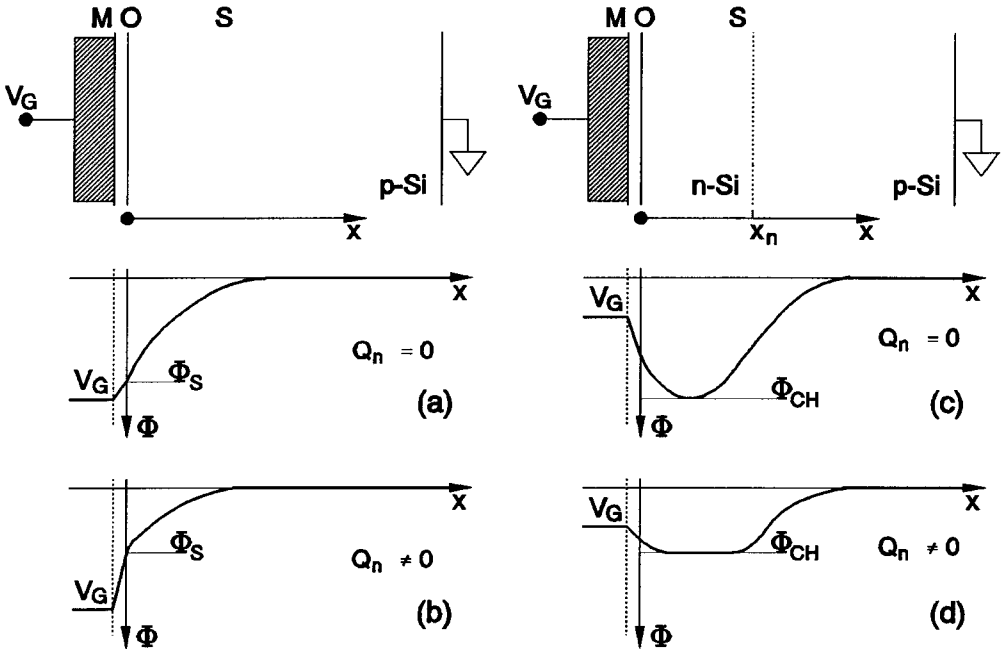

(I) SCCD (II) BCCD

Figure 3.18 *Structure and potential distribution in SCCD (I) and BCCD (II) structures for empty (a and c) and filled (b and d) potential buckets. [TEU].*

In order to avoid these transportation losses, low doped n-channels are implanted into the semiconductor between the oxide and the bulk (illustrated in **Figure 3.18 II**). These so-called buried channels (the corresponding CCD is called buried channel CCD: BCCD) are positively biased with a voltage high enough to completely deplete the n-implant (usually done over the reset diffusion). This leads to a vertical potential minimum near the pn-junction between buried implant and p-substrate rather than at the semiconductor surface. The charge transport mechanism remains the same. The absolute potential level of the buried potential minimum can be influenced by the gate voltages, again enabling a switchable horizontal potential gradient, the basis for the CCD charge transport. Since the charge is transported in the buried channel some 100 nanometers away from the oxide/semiconductor junction, charge trapping losses are avoided. Therefore, BCCDs reach CTE values between 10 to 100 times better than SCCDs. The total width of the depletion region for BCCDs can be estimated by adding the depth of the pn-junction to the extension of the space charge region into the lower doped

substrate (**Equation 3.1**). The capture volume is comparable to that of SCCDs for similar voltages.

Figure 3.19 shows another advantage of BCCD devices over SCCDs. The transport deeper in the semiconductor additionally profits from increased fringing fields. The further away from the surface, the more blurred is the potential influence from neighboring CCD gates. Near the oxide there are regions under the photogate without a potential gradient. In these regions charge transport can only take place by thermal diffusion and self-induced drift, slow transport processes compared to the drift in an electric field (compare **Section 3.1.3**).

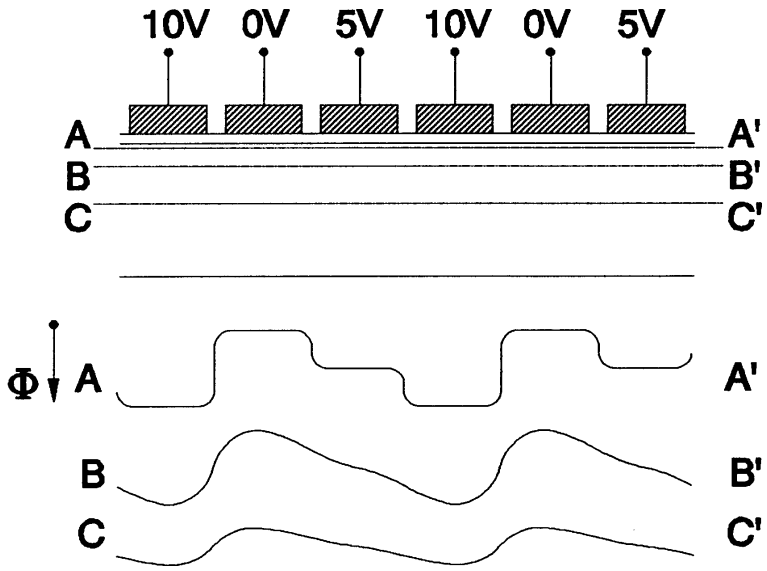

Figure 3.19 *Horizontal potential distribution at different distances from the surface. [TEU].*

To summarize, in BCCDs the depletion of the semiconductor is not achieved by the voltages on the CCD gates but by properly biasing the pn-junction between the low-doped buried implant and the semiconductor substrate. The voltages on the CCD gates are only used to generate potential differences in the horizontal direction, which makes the charge transportation possible.

(a)

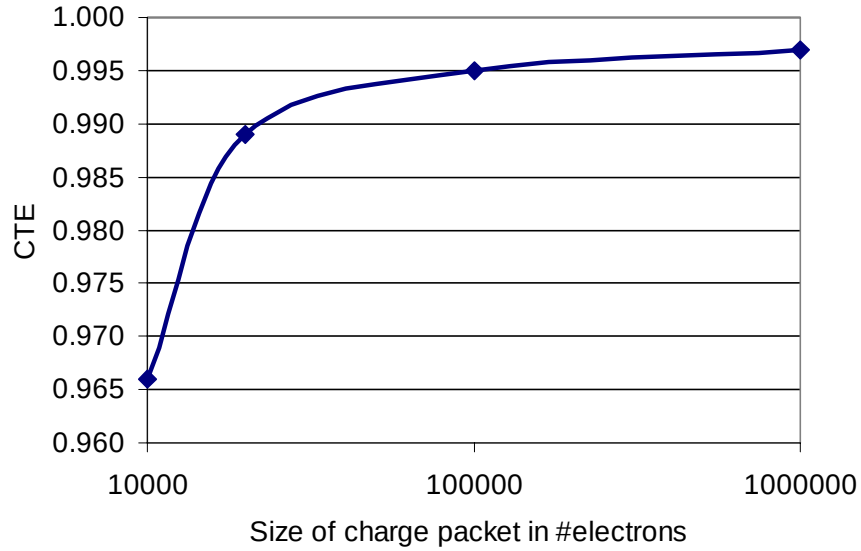

(b)

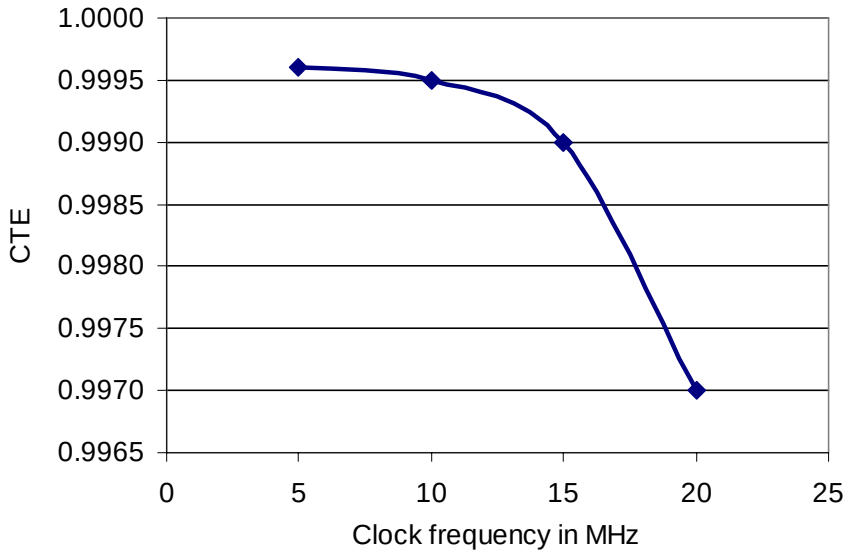

Figure 3.20 *Charge transfer efficiency of a SCCD realized in Orbit 2.0µm CMOS/CCD technology. (a) CTE vs. number of transported electrons @ 20 MHz clock frequency. (b) CTE vs. clock frequency @ 1,000,000 electrons charge packet. Gate amplitude for both measurements: 10 V. [BLU].*

The CTE decreases for high modulation frequencies and small charge packets, as the measurements of a surface channel CCD line shows (**Figure 3.20**). We realized this CCD line to characterize the CCD performance of the ORBIT 2.0µm CMOS/CCD technology, the same technology that we used for the demodulation pixels. At high frequencies an increasing number of charge carriers does not have enough time for the transfer from one pixel to the next. For a small number of

charge carriers the CTE decreases due to the missing or at least reduced contribution of self-induced drift on the charge transport; also trapping is a more serious problem for a small number of electrons to transport. [CAR] gives a very detailed description of how different parameters influence the CTE of a CCD.

Today's CCDs are realized with two or three different polysilicon layers. With these layers it is possible to overlap the single CCD gates in a small area. This leads to very thin gaps between the single gates, small enough that no potential barriers arise between the gates, which would possibly prohibit a complete charge transfer.

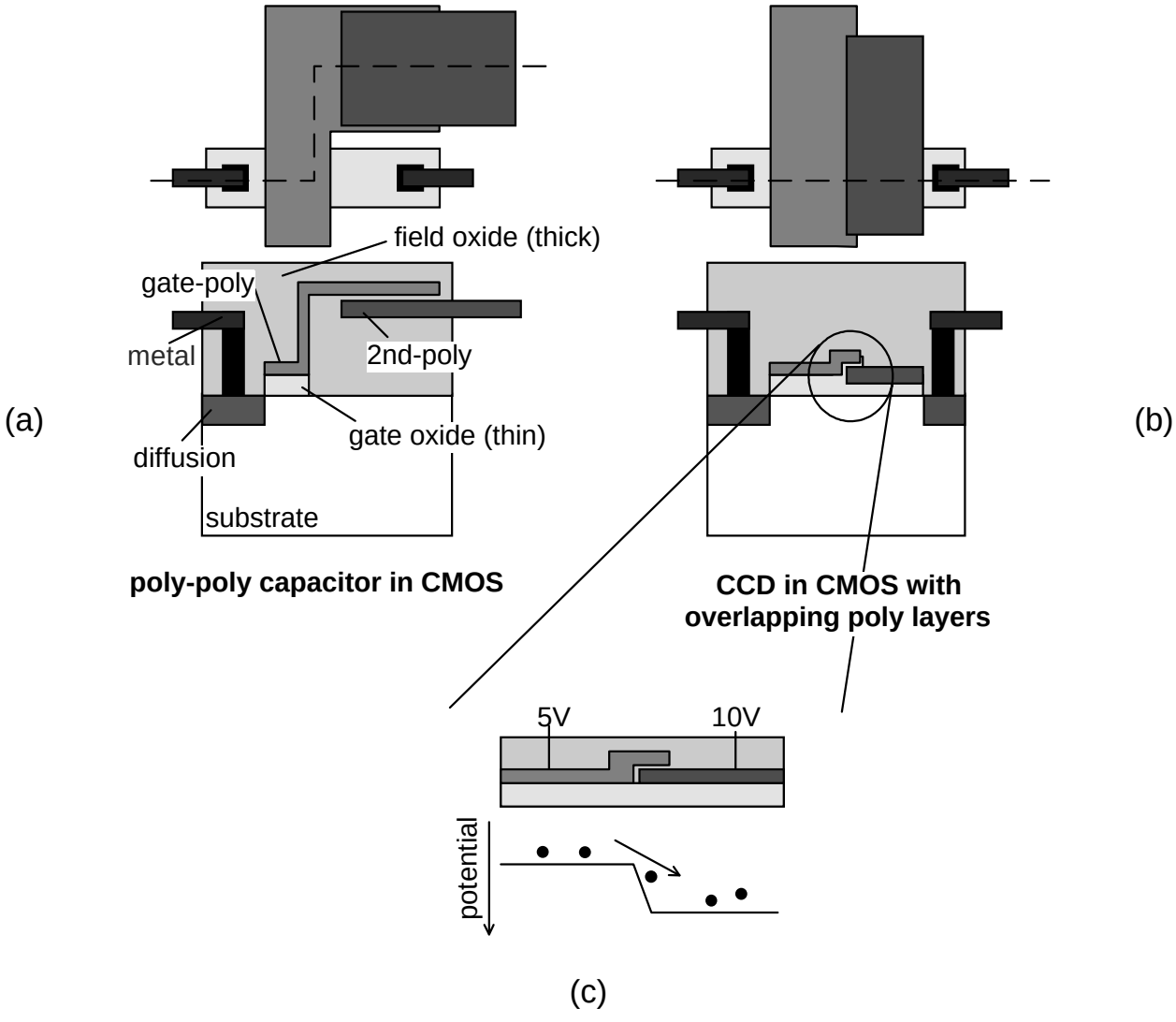

Figure 3.21 *SCCD realization with a 2 poly MOS process: SCCD with overlapping poly layers (poly: polysilicon).*

Many available CMOS processes offer two polysilicon layers. However the design rules prohibit the realization of transistor gates with the second poly layer. This

could possibly cause gate breakthroughs. The second poly layer is offered only to realize poly-poly capacitors only on top of the thick field oxide instead of the thinner gate oxide. With a typical field oxide thickness of 0.6 µm (in contrast to 0.04 µm gate oxide) the voltage on the polysilicon plate over the field oxide has nearly no influence on the semiconductor potential. For this reason most CMOS processes are not suitable for realizing CCDs with overlapping poly (see **Figure 3.21 a**). The Orbit CMOS/CCD process allows the overlap of both poly layers over thin gate oxide and thus enables the realization of surface channel CCDs with overlapping polys (see **Figure 3.21 b** and **c**).

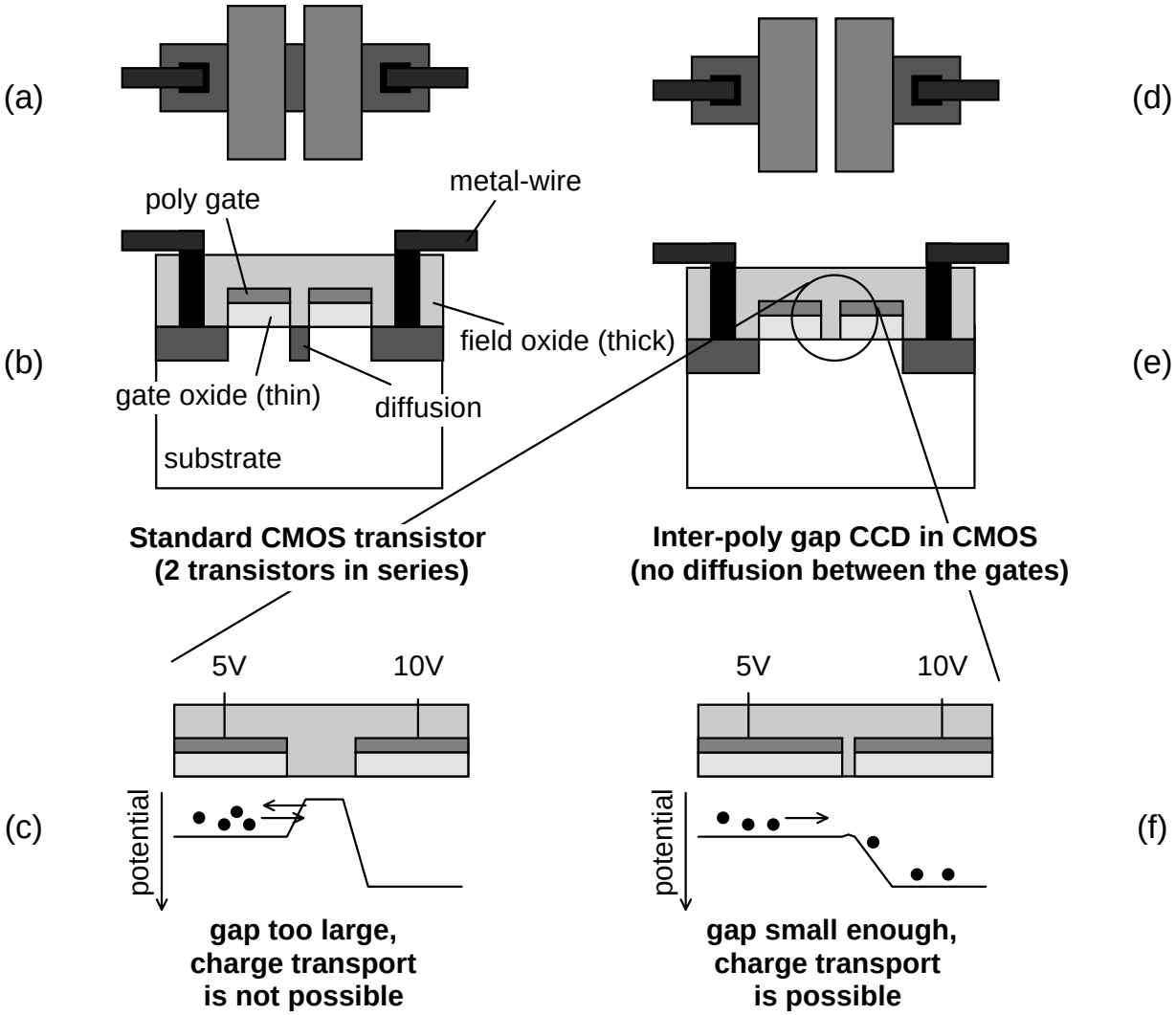

Figure 3.22 *SCCD realization with a one-poly MOS process: Inter-poly-gap SCCD.*

Generally, CCDs can also be realized in a technology with only one poly layer. However, that the gap between two neighboring gates must be made small enough

without causing short circuits. Actually, the first CCDs [BOY, AME] were produced as one poly CCDs. Other successful implementations of CCDs with inter-poly gaps are reported in [HOP], [FUR] and [KRA]. In most CMOS processes, however, it is not possible to realize two neighboring gates without highly doped implant between the gates (see **Figure 3.22 a** and **b**). Only a few processes offer special masks ("non active implant" masks) to prohibit such a diffusion between the MOS gates (**Figure 3.22 d** and **e**). Only if, additionally, the gap between the gates is small enough (only a hundred to a few hundred nanometers) will the potential barrier (**Figure 3.22 c**) disappear and a charge transfer become possible (**Figure 3.22 f**). Today such CCDs with inter-poly gaps still require special processes but, with the predictable future decrease in minimum feature size, sufficiently small inter-poly gaps will become available and allows the implementation of CCDs with pure CMOS processes. However, most of today's CMOS processes only offer silicide poly-layers for improved conductivity. Silicide gates are opaque and therefore not suited for the realization of photogates.

The Orbit 2.0µm CMOS/CCD process additionally allows the realization of overlapping polys over thin oxide, and hence makes possible the realization of SCCDs. Also, as an option, a buried channel implant is available, which allows BCCD realization. However, according to our measurements, the Orbit BCCDs are only slightly better than the SCCDs. The Orbit 2.0µm CMOS/CCD process is primarily a CMOS process, i.e. optimized for transistor structures rather than for CCDs.

CCDs require relatively high control voltages to completely deplete the semiconductor (in the case of SCCDs). Also the voltage amplitude defines the charge-handling capability and hence the maximum signal amplitude (dynamic) that the device can handle. Since many CCD gates are connected, the total gate capacitance is often in the range of some nanofarads. Therefore, not only high voltages but also high power is necessary to control CCD imagers, a serious drawback for battery-powered systems. Charging and discharging the CCD gates can require up to several amperes for some 10 MHz clocking speed.

3.3 Active pixel sensors: CMOS APS

A possible realization of a CMOS APS sensor is shown in **Figure 3.23**. It is based on a photodiode that is reversely biased by connecting it to a reset source over the active channel of an MOS switch, the reset transistor. After this reset operation, the reset switch is opened and the photodiode floats. Optically generated free charge carriers now lead to a decrease in diode potential. Since the diode is also connected to the gate of a source follower transistor, the change in the diode potential leads to a change in conductivity of this transistor.

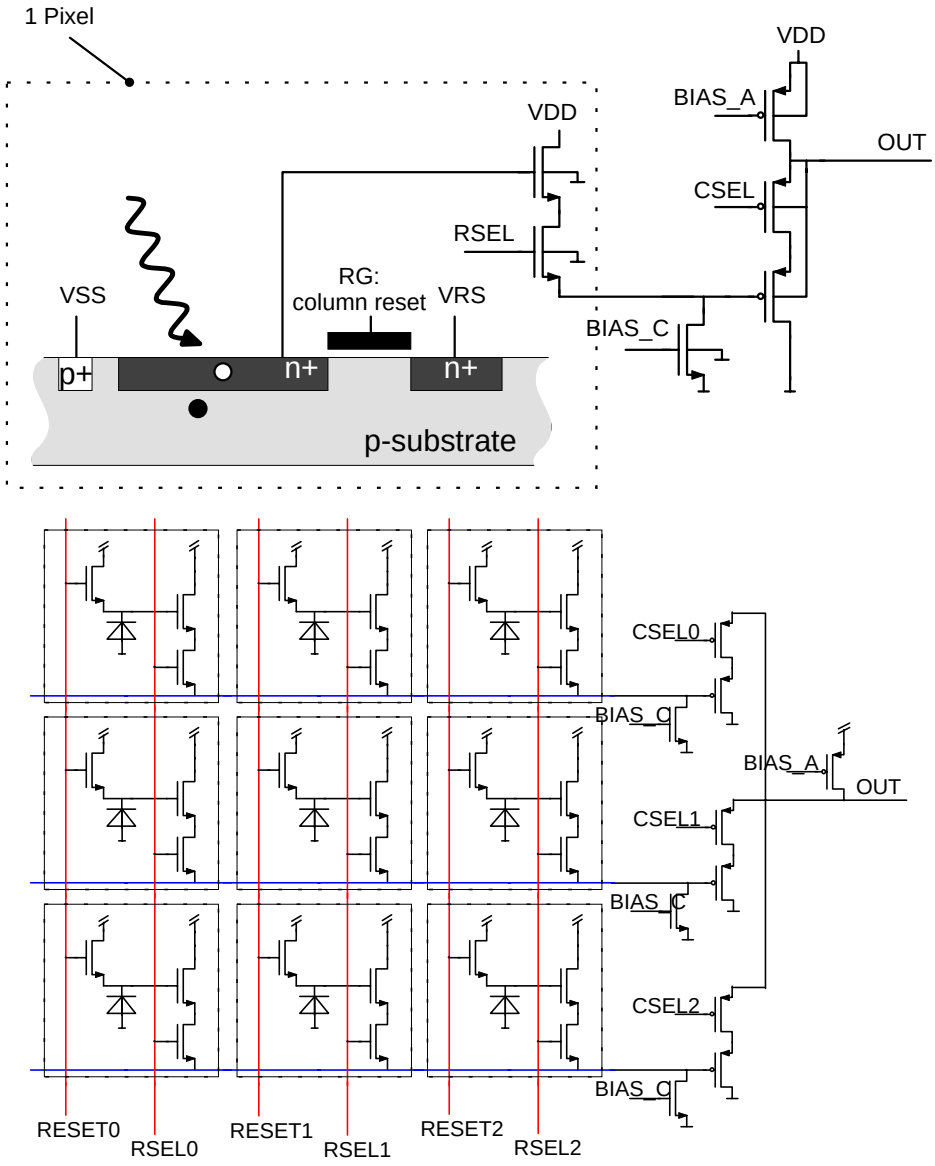

Figure 3.23 *Concept of a CMOS APS imager.*

Over an address decoder matrix each pixel can be accessed individually by activating the corresponding row select and column select transistor switches. In this way each in-pixel source follower transistor can selectively be switched into a complete 2 stage source follower stage and change the output signal by it's light dependent conductivity.

CMOS APS, however, is not necessarily restricted to photodiodes; the light sensitive areas could also be realized as photogates [FOS] or even some CCD structures (see **Chapter 5**). APS only describes the principle of realizing active pixels, that means pixels with an active stage (buffer transistor).

What has made CMOS APS a serious competitor on the imager market is above all the (more or less) unmodified use of relatively cheap, widely available CMOS processes. Not only are they available for prototyping services, enabling widely spread research activity in this area, but they also benefit from the steady process development driven by other industries (mainly computers).

For the customer, essential arguments for using CMOS sensors instead of CCD is their low price, high functionality (digital cameras on a chip), low voltage (1.2V-5V) and extremely low power consumption (20mW) [EMM]. Also they do not require elaborate driving electronics but can be directly controlled by microcontroller, DSP or FPGA logic.

3.4 Discussion

Both CCD and CMOS technologies are special MOS technologies. They differ in optimizations of process parameters with different emphases. In a CCD line the defect of a single CCD gate (oxide breakthrough) may make a complete column unusable, whereas for CMOS APS only a single pixel would be unusable for a comparable defect. CCDs therefore have thicker gate oxides and are characterized by a certain process softness. In addition to the possibility of realizing overlapping CCD gates for a barrier-free potential coupling in the semiconductor, today's CCD processes offer buried channel implants for enhanced CTE performance. Also the substrate doping concentrations are usually lower than for CMOS processes, leading to deeper depletion regions for the same gate voltages. Usually with CCD processes only one type of transistor (p- or n-type) can be realized. Therefore only limited electronics can be realized on-chip.

CMOS processes are optimized for fast reliable transistors with both n and p channel. They are available in prototyping services - so called MPWs (Multi project wafer). This allows the relatively cheap and uncomplicated realization of test structures. Unfortunately such MPW services are not available for CCD processes.

Concerning this work, we would like to benefit from both the functionality of the CCD principle (note: not necessarily CCD process) and the flexibility of CMOS processes. As we will see in **Chapter 5**, we do not need CCD structures with a very good CTE performance. This is because the demodulation principle only requires a few charge transfers. The advantage of the CCD principle (also if realized in CMOS) over CMOS circuitry is that it offers noise-free signal addition and defined local and temporal charge separation, assuming proper CCD structures and timing. In this way first signal processing steps (temporal sampling or demodulation in our application) can already be realized in the pixel.

Orbit's 2.0μm CMOS/CCD process offers this possibility to realize both CCD and CMOS structures. For our application it is not important to have the best CCD performance as with pure CCD processes. A 2.0μm process is, however, coarse compared to today's CMOS processes (0.18μm), a clear indication that such a process will probably not be supported for much longer. With future sub-micron CMOS processes it will be possible to realize 1-poly surface channel CCDs with sufficient transfer efficiency. This will open the door to the realization of further signal processing tasks already in the pixel, using both the CCD principle and CMOS circuitry, while maintaining reasonable fill factors.

4. Power budget and resolution limits

Since the time-of-flight principle uses active illumination, it is important to know the requirements for the optical power of the light source. For this purpose, two things have to be known: (1) how much optical power of modulated scene illumination is necessary to generate a given number of photoelectrons in one pixel and (2), how many photoelectrons per sampling point and pixel are necessary to achieve a certain range resolution? Both questions will be investigated and answered in this chapter.

4.1 Optical power budget

The number of generated electrons is related to the number of photons over the quantum efficiency of the imager. With the energy $h \cdot c/\lambda$ of one photon, the integration time T_{int}, the size of the light sensitive pixel area A_{pix}, and the size of the image in the sensor plane A_{image}, one can calculate the total amount of optical power P_{image} that must arrive at the sensor. Consideration of optical losses k_{lens} of the lens and filters leads to the power P_{lens} in front of the lens over the aperture area. If the observed object is a Lambert reflector, one can calculate the optical power on the observed scene, which has to be a factor of $(D/2R)^2$ higher than the power in front of the lens (D: aperture of the lens, R: distance to target). One obtains the above factor by taking the ratio of the cosine-weighted (Lambert reflection characteristics) integral over the spherical cap of diameter D, (i.e. the share of optical power entering the lens), to the cosine-weighted integral over the complete hemisphere (c.f. **Equation 4.1**, **Figure 4.1**).

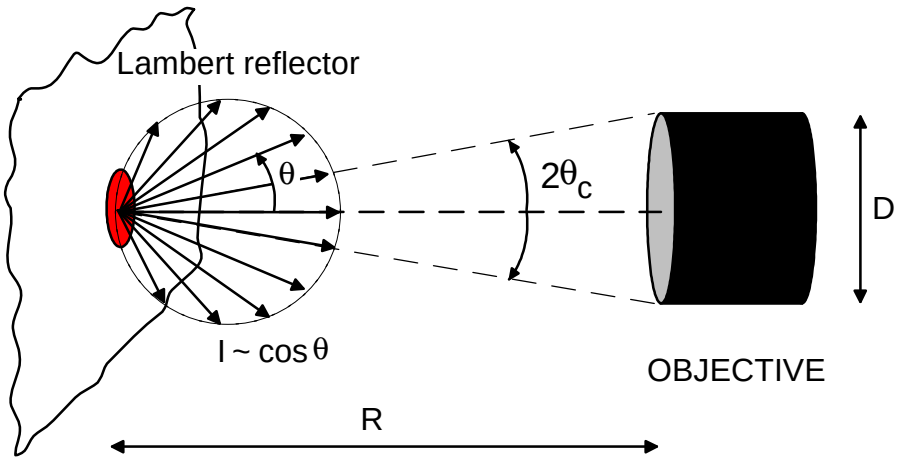

Figure 4.1 *Lambert reflector.*

$$P_{lens} = P_{obj} \cdot \frac{\int_0^{2\pi}\int_0^{\theta_c} \cos\theta \cdot \sin\theta \; d\theta \, d\varphi}{\int_0^{2\pi}\int_0^{\frac{\pi}{2}} \cos\theta \cdot \sin\theta \; d\theta \, d\varphi} = P_{obj} \cdot (\sin\theta_c)^2 = P_{obj} \cdot \left(\frac{D}{2 \cdot R}\right)^2$$

$$= P_{obj} \cdot \left(\frac{f}{R}\right)^2 \cdot \left(\frac{1}{2 \cdot F/\#}\right)^2$$

Equation 4.1

With the reflection coefficient ρ of the object we can then calculate the power of the light source needed. These relationships are illustrated in **Figure 4.2** and summarized in the following equations:

Optical power per pixel P_{pix} (A_{pix} is the light sensitive pixel area):

$$P_{pixel} = \left(\frac{P_{light\ source} \cdot \rho \cdot \left(\frac{D}{2 \cdot R}\right)^2 \cdot k_{lens}}{\frac{A_{image}}{A_{pix}}} \right)$$

Equation 4.2

Expressed in terms of power density P_i' (watts per square-meter) one obtains the simple relation:

$$P'_{pixel} = P'_{obj} \cdot \left(\frac{1}{2 \cdot F/\#} \right)^2 \cdot k_{lens}$$ **Equation 4.3**

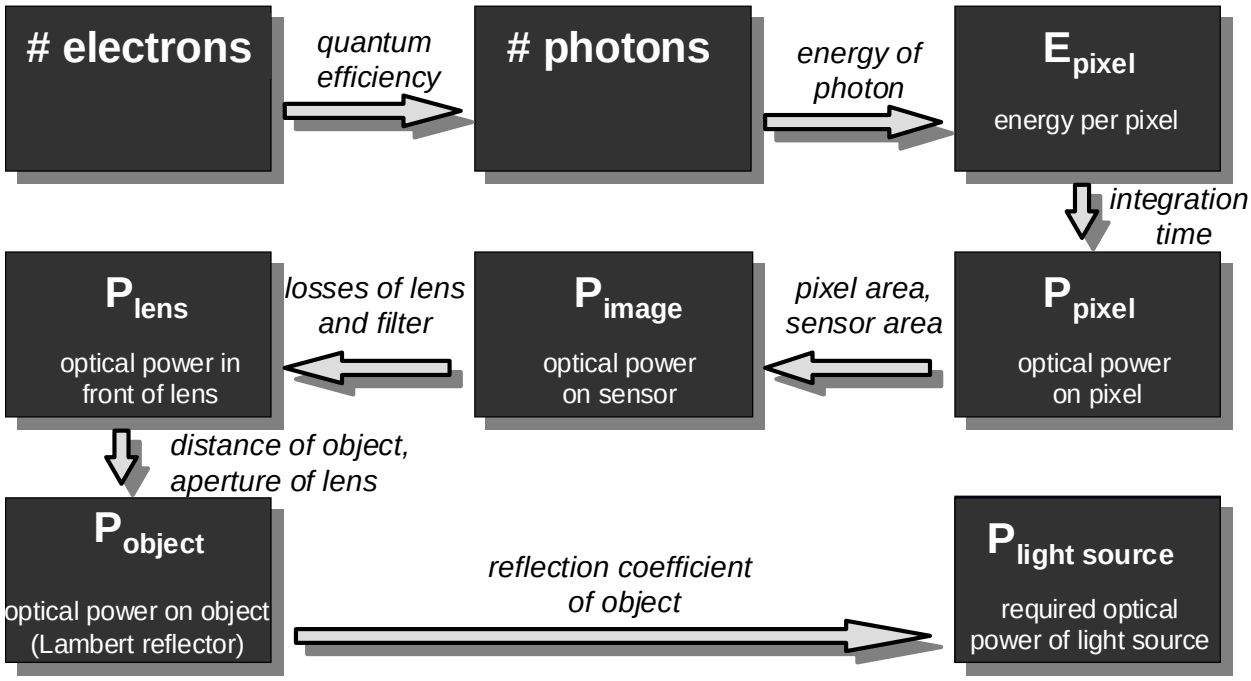

Figure 4.2 *Optical power budget: Strategy to estimate the optical power of the illumination required to generate a given number of electrons in a pixel as a function of scene and camera parameters.*

Optical energy per pixel E_{pix}:

$$E_{pixel} = P_{pixel} \cdot T_{int}$$ **Equation 4.4**

Number of photons N_p per pixel:

$$N_p = \frac{E_{pixel}}{E_{photon}} = P_{pixel} \cdot T_{int} \cdot \frac{1}{\frac{h \cdot c}{\lambda}}$$ **Equation 4.5**

Number of electrons N_e generated per pixel (see also **Figure 4.3**):

$$N_e = N_p \cdot QE(\lambda) = P_{pixel} \cdot T_{int} \cdot \frac{1}{\frac{h \cdot c}{\lambda}} \cdot QE(\lambda)$$ **Equation 4.6**

Required optical power of emitter $P_{light\ source}$:

$$P_{light\ source} = \frac{N_e \cdot \frac{A_{image}}{A_{pix}} \cdot h \cdot c}{\rho \cdot \left(\frac{D}{2 \cdot R}\right)^2 \cdot k_{lens} \cdot QE(\lambda) \cdot \lambda \cdot T_{int}}$$

Equation 4.7

N_e	number of electrons per pixel	D	aperture of lens
A_{image}	image size in sensor plane	R	distance of object
A_{pix}	light sensitive area of pixel	k_{lens}	losses of objective and filters
h	Planck's constant	$QE(\lambda)$	quantum efficiency
c	speed of light	λ	wavelength of light
ρ	reflectivity of object	T_{int}	integration time

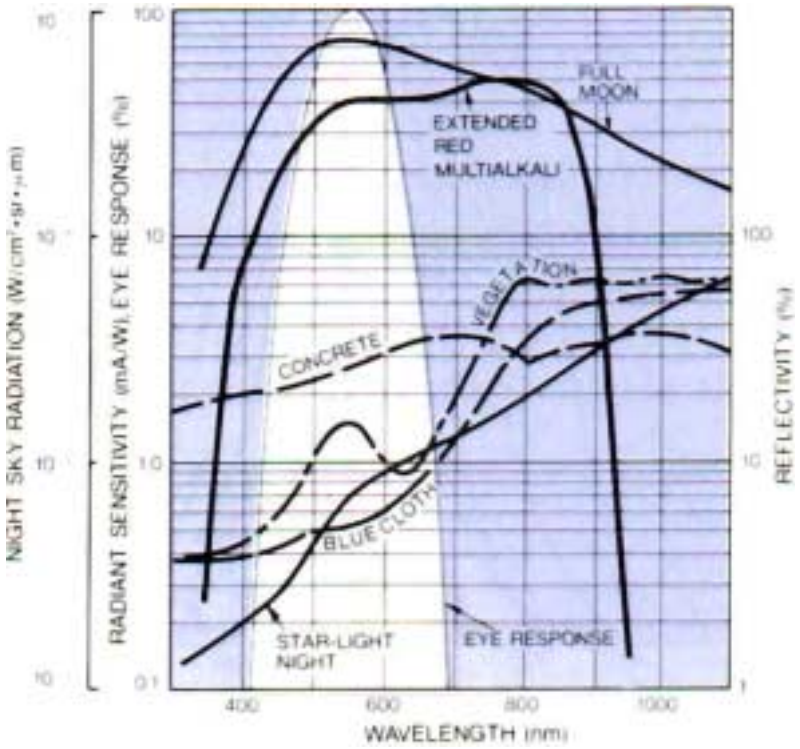

Figure 4.3 *Reflectivity of concrete, blue cloth and vegetation and response of human eye [HAM].*

This estimation assumes that the target is a Lambert reflector, i.e. the intensity distribution of back-scattered light does not depend on the illumination angle. The reflected intensity decreases with the cosine of the observation angle with respect

to the surface normal. The reflection coefficient has values between zero and one for Lambert reflectors (ρ=1 for a white sheet of paper). Retro-reflectors, for example in traffic signs, and mirrors lead to a directed reflection, which depends on the illumination angle with respect to the surface normal. In the reflection direction the equivalent reflectivity can then be larger than 1 (retro-reflector: ρ=100-1000, mirror: ρ=1000). **Figure 4.3** shows the wavelength dependent reflection coefficients of concrete, vegetation and blue cloth. **Table 4.1** gives an overview over reflectivity values of typical diffusely reflecting materials at a wavelength of 900 nm.

White paper	up to 100%	Carbonate sand (dry)	57%
Snow	94%	Carbonate sand (wet)	41%
White masonry	85%	Rough clean wood pallet	25%
Limestone, clay	up to 75%	Smooth concrete	24%
Newspaper	69%	Dry asphalt with pebbles	17%
Deciduous trees	typ. 60%	Black rubber tire	2%
Coniferous trees	typ. 30%		

Table 4.1 *Typical reflectivity values for various materials [RIG].*

It is interesting to note that a given optical power density on the object always leads to the same number of electrons in the pixel, independent of its distance. If the same light power is used to illuminate an area of one square meter, one 5 m away from the sensor and another 50 m away from the sensor, the number of electrons generated in one pixel stays the same. This is because the angle of view for the observation of a fixed area also decreases with the distance of the object. Hence, the illumination beam has to have a smaller divergence to illuminate the object at a greater distance with the same power density. Put another way, with increasing distance of the target, assuming that the power density on the target remains the same, only the number of pixels illuminated by the target changes, not, however, the power in each of the illuminated pixels (c.f. **Equation 4.3**).

4.2 Noise limitation of range accuracy

In **Chapter 3** we discussed the fact that the performance of solid state imagers is limited by noise and that there are several different noise sources in both CCD sensors and photodiode arrays. The essential ones are electronic and optical shot noise, thermal noise, reset noise, 1/f noise and quantization noise. All of these noise sources can be reduced or eliminated by different signal processing techniques or cooling, except photon shot noise. Therefore, we first only investigate the influence of shot noise on the ranging accuracy.

Quantum noise as final limitation

Shot noise describes the statistical Poisson-distributed nature of the arrival process of photons and the generation process of electron-hole pairs. The standard deviation of shot noise is equal to the square root of the number of photons (optical shot noise) or photogenerated charge carriers (electronic shot noise). In the following the required number of photoelectrons per sampling point and pixel to achieve a given range resolution is derived.

As introduced in **Chapter 2**, the phase can be calculated from the sampling points with the following equation (four-tap approach):

$$\varphi = \operatorname{atan}\left(\frac{A_1 - A_3}{A_0 - A_2}\right). \qquad \textbf{Equation 4.8}$$

Following the rules of error propagation

$$\Delta\varphi = \sqrt{\left(\frac{\partial\varphi}{\partial A_0}\right)^2 \cdot \Delta^2(A_0) + \left(\frac{\partial\varphi}{\partial A_1}\right)^2 \cdot \Delta^2(A_1) + \left(\frac{\partial\varphi}{\partial A_2}\right)^2 \cdot \Delta^2(A_2) + \left(\frac{\partial\varphi}{\partial A_3}\right)^2 \cdot \Delta^2(A_3)}$$

Equation 4.9

and considering that each of the integrated sampling points $A_0..A_3$ shows a standard deviation of $\Delta A_i = \sqrt{A_i}$, one obtains the quantum noise limited phase error $\Delta\varphi$:

$$\Delta\varphi = \sqrt{\left(\frac{\partial\varphi}{\partial A_0}\right)^2 \cdot A_0 + \left(\frac{\partial\varphi}{\partial A_1}\right)^2 \cdot A_1 + \left(\frac{\partial\varphi}{\partial A_2}\right)^2 \cdot A_2 + \left(\frac{\partial\varphi}{\partial A_3}\right)^2 \cdot A_3}$$

. **Equation 4.10**

Solving for special phase values (0°, 45°, 90°, 135°, 180°, …), and considering that all sampling points are composed of an Offset B (background plus DC-component of active illumination) and a phase-dependent component proportional to $A \cdot \cos(\varphi_0)$, where A and B are given in *number of electrons*, we obtain the range resolution ΔL:

$$\Delta L = \frac{L}{360°} \cdot \Delta\varphi = \frac{L}{\sqrt{8}} \cdot \frac{\sqrt{B}}{2 \cdot A} \qquad \textbf{Equation 4.11}$$

L: Non-ambiguity distance range ($L = \frac{\lambda_{mod}}{2} = \frac{c}{2 \cdot f_{mod}}$).

A: (De)modulation amplitude, i.e. the number of photoelectrons per pixel and sampling point generated by the modulated light source. A depends on the modulation depth of the modulated signal and the demodulation contrast of the pixel (c.f. **Section 5.2.2**) but also on the optical power of the modulated light source and the target's distance and reflectivity.

B: Offset or acquired optical mean value, i.e. the number of photoelectrons per pixel and sampling point generated by incoming light of the scene's background and the mean value of the received modulated light (c.f. **Figure 2.7**).

This range accuracy (**Equation 4.11**), which can only be improved by averaging, is the absolute limit of a lock-in range sensor working with four sampling points. One can see from the equation that a large background brightness (B-A B for A<<B) not only restricts the number of available quantization levels but also drastically increases the quantum noise of the system. Background illumination can be reduced by measuring in the dark or by using spectral filters that only transmit the spectrum of the modulated light. Since, generally, the "active" optical power density on the illuminated scene increases with decreasing distance to the object, the ranging accuracy also increases for smaller distances. This is an important fact for navigation applications, where a high accuracy is often only needed close to the target.

Influence of thermal noise sources

Based on the above discussion, the additional noise sources (1/f- , reset- and thermal noise) can easily be included in **Equation 4.11** by adding an additional

number of pseudo-background-electrons N_{pseudo} to B. (They are not correlated to the modulation signal and thus contribute to B rather than A.)

$$\Delta L = \frac{L}{\sqrt{8}} \cdot \frac{\sqrt{B + N_{pseudo}}}{2 \cdot A} \qquad \textbf{Equation 4.12}$$

One obtains this number of pseudo-electrons N_{pseudo} simply by squaring the noise-equivalent number of noise electrons.

$$N_{pseudo} = (\#\ \text{dark noise electrons})^2 = \left(\frac{V_{dark\ noise} \cdot C_{conv}}{q \cdot A_{sf}} \right)^2 \qquad \textbf{Equation 4.13}$$

Example: We assume a measured dark noise of $V_{dark\ noise}$=0.63 mV rms, containing all noise sources except the photoelectron shot noise, namely the dark current shot noise and the thermal noise floor. With a typical output amplification of A_{sf}=0.9 and a conversion capacitance of C_{conv}=40 fF this corresponds to an equivalent number of 175 dark noise electrons, leading to 30,000 pseudo-background-electrons.

$V_{dark\ noise} \approx 0.63$ mV rms

$A_{sf} \approx 0.9$

$C_{conv} \approx 40$ fF

$$Q_{equivalent} = \frac{V_{dark\ noise}}{A_{sf}} \cdot C_{conv} \approx 2.8 \cdot 10^{-17}\ \text{C}$$

$$\#\ \text{dark noise electrons} = \frac{Q_{equivalent}}{q} \approx 175$$

$N_{pseudo}=(175)^2 \approx$ **30,000**.

Demodulation amplitude and effective offset

A closer look at **Equation 4.11** and **Figure 2.7** shows that the modulated light source contributes to both offset and demodulation amplitude. Integrated over a certain integration time T_{int}, the mean optical power $P_{opt,pixel}$ directly adds a number of photoelectrons PE_{opt} to the *effective offset* B_{eff} :

$$B_{eff} = \text{background} + N_{pseudo} + PE_{opt} \qquad \textbf{Equation 4.14}$$

Also the *number of demodulation-photoelectrons A* can be expressed as a function of the optical mean power or the total number of photoelectrons per pixel generated by the modulated light source PE_{opt}. Only the modulation contrast C_{mod}, a parameter of the modulated light source, (usually 100%), and the demodulation

contrast C_{demod}, which depends on the pixel performance, (usually less than 100%), have to be considered:

$$A = C_{mod} \cdot C_{demod} \cdot PE_{opt} \qquad \textbf{Equation 4.15}$$

For 100% modulated optical signal we obtain:

$$A = C_{demod} \cdot PE_{opt} \qquad \textbf{Equation 4.16}$$

Thus we can rewrite **Equation 4.11**:

$$\Delta L = \frac{L}{\sqrt{8}} \cdot \frac{\sqrt{background + N_{pseudo} + PE_{opt}}}{2 \cdot C_{mod} \cdot C_{demod} \cdot PE_{opt}} \qquad \textbf{Equation 4.17}$$

For the following example we assume a 100% modulated light source (C_{mod}=1) with a total optical power of P_{opt}=700 mW. The light source emits at 630 nm, where the sensor has a quantum efficiency of 65%. We use a CS-mount lens with a focal length of f=2.6 mm and a F/# of 1.0. The pixel size is 12.5 µm x 14.4 µm. With a beam divergence of 50° (LED) we get an image size at the sensor plane of 4.6mm^2 ({2.6 mm * tan25°}^{2}·π). With optical losses of lens (0.7) and interference filter (0.5) we obtain k_{lens}=0.35. Choosing an integration time of T_{int}=25 ms we can easily calculate the *number of electrons N_e generated in one pixel* by rearranging **Equation 4.7**:

$$N_e = \left(\frac{P_{light\ source} \cdot \rho \cdot D^2 \cdot k_{lens} \cdot QE(\lambda) \cdot \lambda \cdot T_{int}}{4 \cdot \frac{A_{image}}{A_{pix}} \cdot h \cdot c} \right) \cdot \frac{1}{R^2} \qquad \textbf{Equation 4.18}$$

Choosing a target with 20% reflectivity we get the number of electrons per pixel, which now only depends on the distance R in meters (R/[m]): *$N_e \approx 170{,}000$ photoelectrons / (R/[m])^2*. Hence, for a distance of 5 meters, we will integrate a number of 34,000 electrons in one pixel. The following overview summarizes the chosen parameters.

C_{mod}	= 1	QE(λ)	= 0.65	k_{lens}	= 0.35
P_{opt}	= 700 mW	lens	1:1.0, 2.6 mm	T_{int}	= 25 ms
λ	= 630 nm	D	= 2.6 mm	ρ	= 0.2
beam divergence	= 50°	A_{pixel}	= 180 μm^2	A_{image}	= 4.6 mm^2

Figure 4.4 to **Figure 4.8** clarify the influence of the single parameters and give numerical values for the range resolution that can be expected under certain conditions.

Figure 4.4 shows both the received power and the number of generated electrons per pixel depending on target distance and reflectivity. **Figure 4.5** illustrates the corresponding range resolution. In **Figure 4.6** the demodulation contrast varies; this was previously chosen as 40%. The influence of an additional background illumination on the range resolution is shown in **Figure 4.7**.

Figure 4.8 plots the range resolution versus the optical power per pixel rather than the distance in meters. Additionally the integration time varies. This figure is of special importance. In **Chapter 5** we present real range measurement values and compare them to the prediction of **Figure 4.8**. We will demonstrate an excellent fit between measurement and theory, which also confirms the predicted range accuracies of **Figure 4.5, Figure 4.6** and **Figure 4.7.**

Assuming an integration time of T_{int} = 25 ms, the modulation period of T_{mod}=50 ns, which we choose for our TOF application (f_{mod}=20 MHz, L=7.5 m), is a factor of 500,000 times shorter than T_{int}. Therefore, if a number of 50,000 photoelectrons (c.f. **Figure 4.4**, light power: 700 mW) is generated in one pixel within the integration time, only one photoelectron is collected every 10^{th} modulation period statistically speaking. Therefore, the demodulation pixels introduced in **Chapter 5** will have to work with single photoelectrons, and at this point we understand, why self-induced drift does not contribute to the charge transport in our application (compare **Chapter 3.1.3**). According to **Figure 4.8**, the number of only 50,000 photoelectrons (1000 fW @ T_{int}=25 ms) leads to a range accuracy of about 2 centimeters.

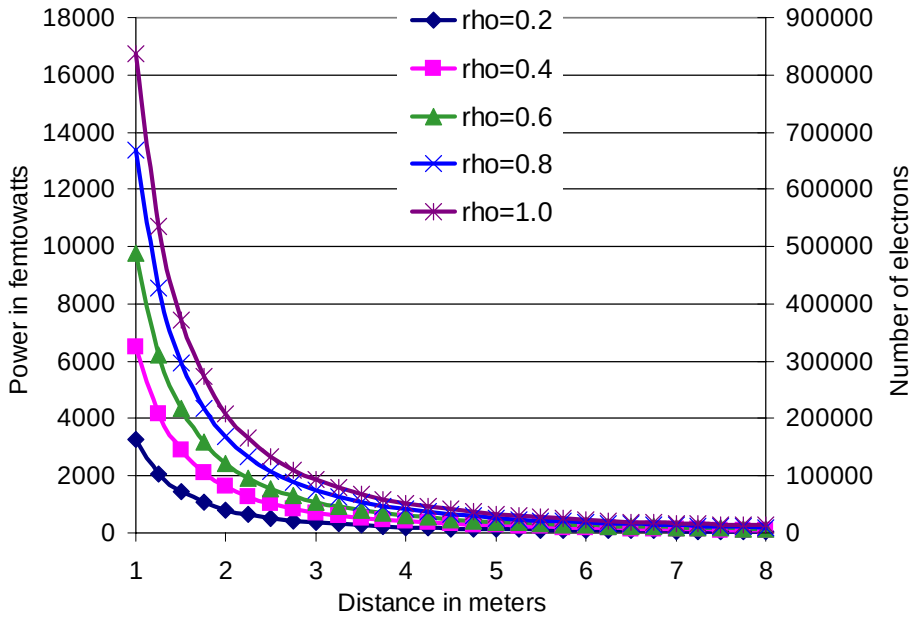

Figure 4.4 *Received optical power per pixel and corresponding number of generated electrons per pixel versus target distance R and reflectivity ρ.*

Light source: 700 mW, 50° beam divergence, pixel size: 12.5 x 14.5 µm², wavelength: 630 nm, quantum efficiency 65%, integration time T_{int}=25 ms, k_{lens}: 0.35, lens aperture: 2.6 mm.

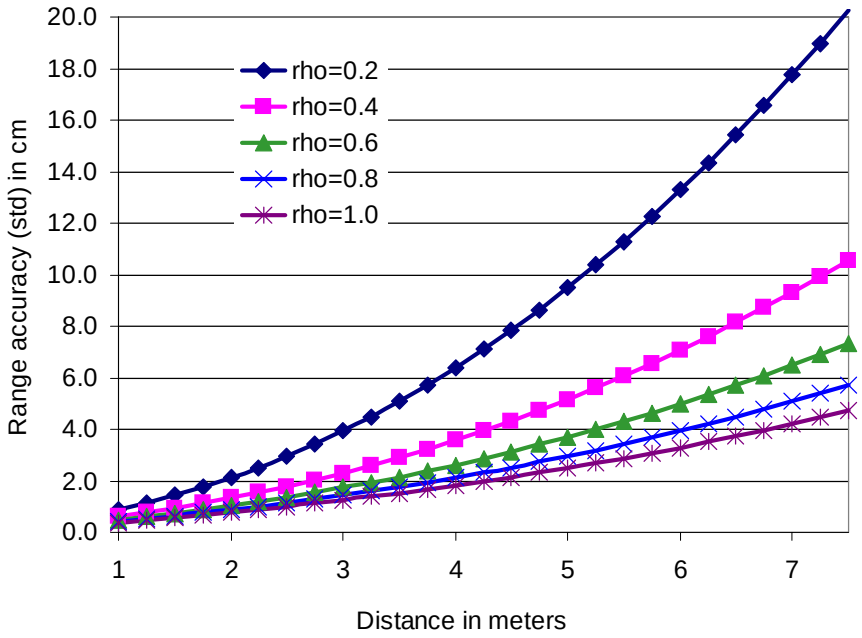

Figure 4.5 *Range accuracy ΔL versus target reflectivity ρ and distance R according to* ***Equation 4.17****.*

Demodulation contrast C_{demod}=40%; noise-equivalent number of noise electrons N_{pseudo} = 30,000; additional background = 0; non-ambiguous distance range L = 7.5 m (f_{mod}=20 MHz); all other conditions as for Figure 4.4.

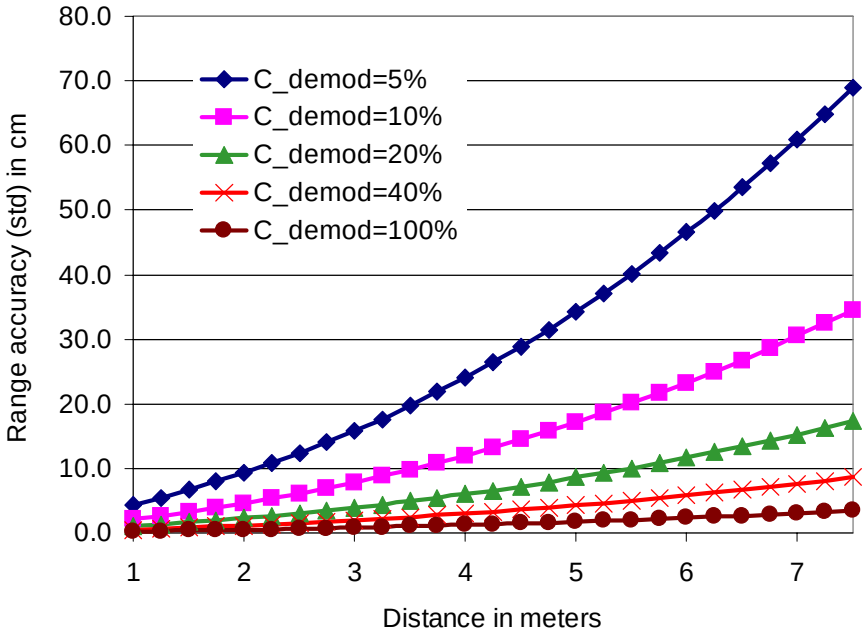

Figure 4.6 *Range accuracy ΔL versus demodulation contrast C_{demod} and target distance R according to* ***Equation 4.17****.*

Target reflectivity ρ = 0.5; all other conditions as for Figure 4.4 and Figure 4.5.

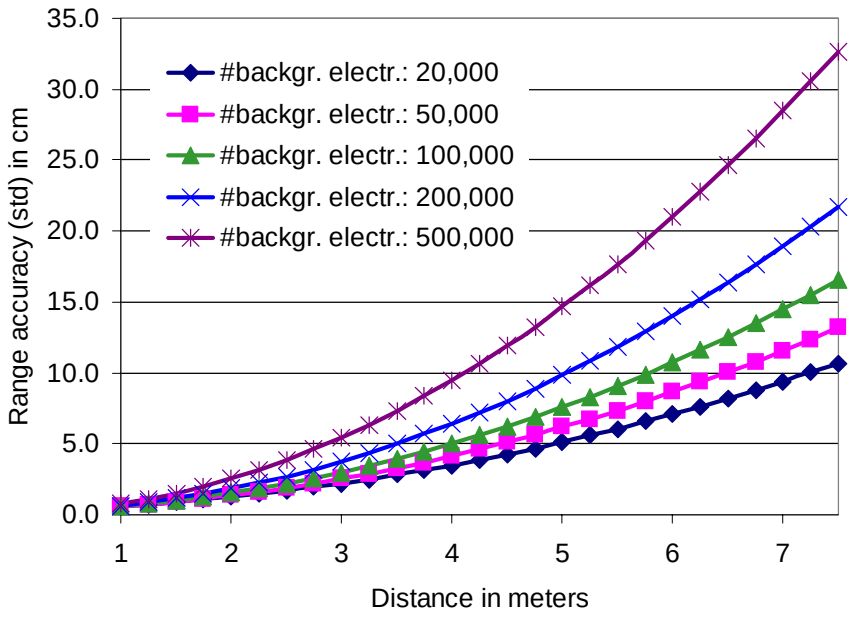

Figure 4.7 *Range accuracy ΔL versus background brightness and target distance R according to* ***Equation 4.17****.*

Target reflectivity ρ = 0.5; C_{demod} = 40%; all other conditions as for Figure 4.4 and Figure 4.5.

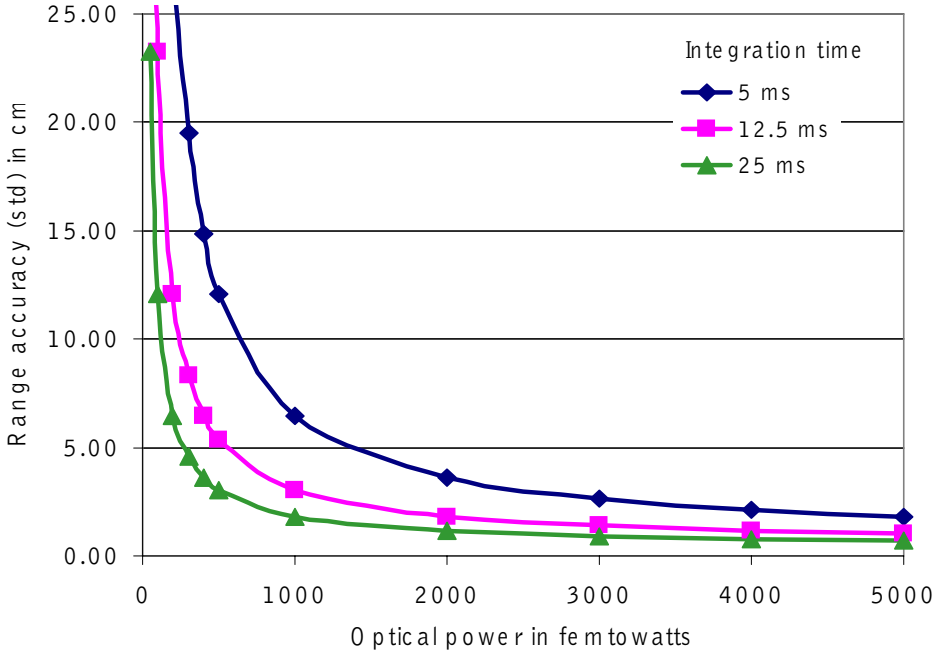

Figure 4.8 *Range accuracy ΔL versus optical input power per pixel and integration time according to* ***Equation 4.17****.*

C_{demod} = 40%; all other conditions as for Figure 4.4 and Figure 4.5.

5. Demodulation pixels in CMOS/CCD

In **Section 2.1.3** and **2.2** we have explained that we can measure distances by measuring the phase of an RF-modulated optical radiation field. We have suggested measuring these phases in an array of so-called demodulation pixels, which are additionally capable of measuring the modulation signal's amplitude as well as the background brightness. Such an array of demodulation pixels would make possible the realization of a 3D range camera without moving parts. This is because, rather than scanning the laser beam over a scene, the scene can be illuminated simultaneously with a light cone and each pixel in the imager array individually measures the distance of the corresponding point in the scene. We also suggested realizing the demodulation task by temporal sampling of the modulated optical wave.

To realize such a fast sampling demodulation pixel, an efficient electrooptical shutter mechanism is needed. A quick estimate gives an idea of the required speed performance: Using a sinusoidal wave as modulation function for the TOF-application restricts the non-ambiguous measurement range to half a modulation period π, not 2π because the modulated wave has to travel the distance from the 3D camera to the target twice: forth and back. If we postulate a distance resolution of 7.5 cm and expect $\lambda/200$ phase resolution of the system, a reasonable value compared to existing systems, we need a 15 m rf-wave. With $f=c/\lambda$ we obtain the modulation frequency of 20 MHz. For these values we have to take the single sampling points A_i at a repetition rate of 20 MHz, corresponding to an effective sampling rate of 80 MHz for 4 sampling points.

For a better SNR, the pixels should offer the possibility of successively adding short-time integrated sampling points without additional noise. This technique also makes the system insensitive to frequencies other than the modulation frequency, and that's why we also call our pixels *lock-in pixels* (c.f. **Section 2.2** and **Figure 2.10**). All sampling points (four, to keep the previous definitions) have to be stored within the pixel because the complete high-resolution detector array cannot

be read out at a frame rate of some tens of MHz. As the system uses active illumination and the information of interest is carried by the modulated light, the fill factor has to be as high as possible for good sensitivity (c.f. **Chapter 3**). Also the dynamic range of the pixels is of high importance. The intensity of back-scattered light decreases with the square of the target's distance to the range camera (c.f. **Chapter 4**). Another boundary condition for the pixel realization is that, due to a limited research budget for this project, we only have access to semiconductor technologies offered as MPWs (multi project wafers) that are more or less standard processes. We can summarize the physical demands on our detector into four principal tasks:

***1. Energy conversion*.**

→ Conversion of photons into electron-hole pairs.

2. Fast separation of optically generated charge carriers (photoelectrons).

→ Avoidance of temporal blurring of the received time critical information.

3. Repeated, noise-free addition of separated photoelectrons.

→ Improvement of SNR and insensitivity to spurious frequencies.

4. In-pixel storage of the acquired sampling points.

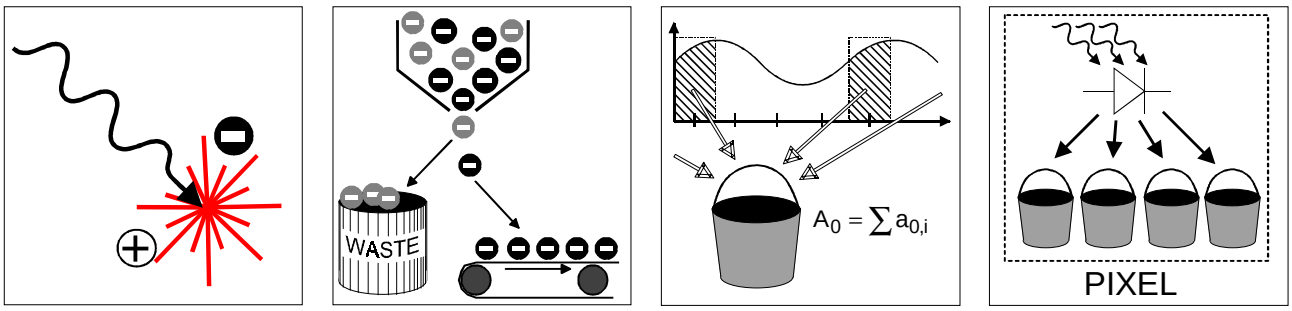

Figure 5.1 *Physical demands on a demodulation pixel.*

All these demands, illustrated in **Figure 5.1**, can be realized excellently with the CCD principle. Better than any other electronic principle used in integrated circuits, the CCD principle allows nearly loss-free addition and directed transport (spatial distribution / shutter mechanism) of electrical signals in the charge domain.

This chapter is divided into three main sections: In **Section 5.1** we introduce different realizations of demodulation pixels. They have all been realized in Orbit 2 µm CMOS/CCD technology, a process offered as MPW. This process has two different polysilicon layers (poly1 and poly2) that can both be used as transistor gates. Additionally the design rules allow these poly gates to overlap over the thin gate oxide. Hence it is possible to realize CCDs with this CMOS/CCD process (c.f. **Section 3.2**). The realized demodulation pixels vary in operational architecture, maximum demodulation frequency and fill factor, the latter being a very important parameter for realizing highly sensitive devices. All pixels fulfill the four physical demodulation demands described above. The characteristic features of the pixels introduced are summarized in **Table 5.1** and **Figure 5.8**.

Section 5.2 then summarizes the results of a detailed characterization of the demodulation performance for the 1-tap pixel, which is the pixel-realization with the best electrooptical properties (demodulation bandwidth and optical fill factor). This pixel has been fabricated twice; (1) with surface channel (SCCD) CCD structures and (2) with buried channel (BCCD) structures, allowing a direct comparison of both CCD types. Especially we focus on the efficiency of the shutter mechanism (sampling efficiency or demodulation contrast) and its dependency on sampling frequency and wavelength. Also, we present the measured phase accuracy as a function of the optical power received in the pixel and compare these results to the theory presented in **Section 4.2**. The 1-tap pixel is the basis for two lock-in sensor arrays we realized, a line-sensor with 108 pixels and an image sensor with 64x25 pixels. Both arrays are implemented as range cameras, which are introduced in **Chapter 6**.

Motivated by the outstanding results presented in **Section 5.2**, we present a very simple and only slightly modified pixel structure in **Section 5.3** that overcomes the restrictions of the 1-tap pixel (serial integration of the single sampling points) by offering two optically identical photosites.

5.1 Pixel concepts

5.1.1 Multitap lock-in CCD

This device, introduced in [SP2] and [SP4], consists of a light sensitive photogate that is connected to a 4-phase CCD-line, the pipeline-CCD. Every CCD-element, consisting of four CCD gates, is connected to an identical CCD-line, the readout-CCD, by so-called transfer gates (see **Figure 5.2**).

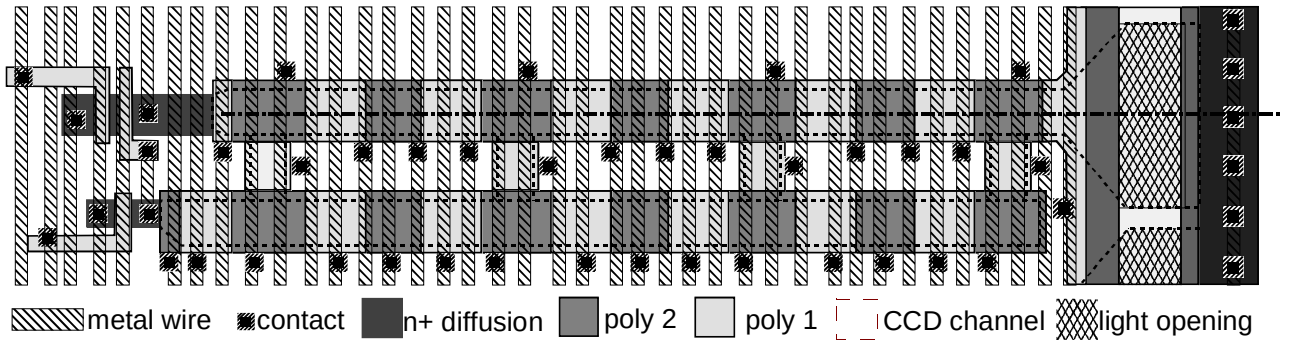

Dimensions: photogate: 45x15 µm², pixel: 45x270 µm², aspect ratio: 1:6, fill factor: 5.6%.

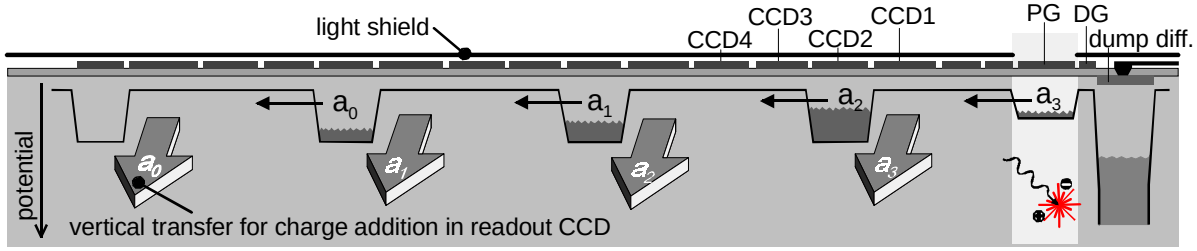

Figure 5.2 *Multitap lock-in pixel: layout and cross-sectional view.*

During the demodulation operation the upper CCD-line is clocked at maximum loss-less speed so that photoelectrons from the photogate are transported into this CCD line. With an appropriate choice of the modulation frequency (modulation period equals the time of four CCD shifts) each CCD element within the pipeline CCD carries one sampling point of the received modulated light after four CCD shifts. By clocking the pipeline CCD, the temporal modulation is converted into spatial charge distribution. This is the actual process of demodulation in the multitap-pixel. After these four sampling points have been taken, they can be stored into the readout-CCD by activating the transfer gates. During this transfer the additional photoelectrons generated under the photogate can be dumped to a diffusion so that

no parasitic charge will be integrated. This complete procedure can be repeated until the amount of charge collected in the readout-CCD is large enough for a sufficient SNR. Now the acquired sampling points can be transported to the detection stage by clocking the readout-CCD. Each pixel has its own detection stage (APS-concept, active pixel sensor) that can be selected for readout with an address decoder.

A general problem in using CCD technology is the CCD's speed performance. The larger the length of a CCD gate, the longer the charge carriers need to travel from this gate into the neighboring CCD gate. In **Chapter 3** we have discussed that (1) thermal diffusion, (2) self-induced drift (Coulomb forces) and (3) movement in an electrical field (fringing field) are the only transport mechanisms for free charge carriers in a semiconductor. Of these three the only directed and thus predictable mechanism is the movement in a fringing field, the others being statistical processes. Fringing fields, however, strongly depend on the semiconductor's impurity concentration, which is orders of magnitudes higher in the CMOS process that we used than in a real CCD-process, used for commercial CCD sensors. Therefore, in our CMOS-CCDs the fringing fields only extend to a very small region between two adjacent gates. The transfer efficiency, only caused by thermal diffusion, decreases with the square root of the gate length. This is why, for good separation efficiency, the CCD gates have to be as short as possible, especially in our CMOS/CCD process. For the same reason the size of the photogate may not be chosen too large, otherwise the photoelectrons do not arrive in the pipeline-CCD in time and the demodulation efficiency decreases. This limits the fill factor that can be realized [CAR, SZ2].

In order to transfer charge-packets from the pipeline CCD into the readout CCD, transfer gates had to be inserted between both CCD lines. Since only two poly-layers are available and we have to follow special design rules, the insertion of transfer gates forces the layout of relatively long gates in the pipeline CCD. This stands in contradiction to our requirement for a high transport speed and a high fill factor. The advantage of this pixel compared to other implementations is the possibility of realizing any number of storage sites. For this reason we call it the "multitap-approach". It has been introduced as an 8-tap pixel in [SP2] but has also been realized with 16 taps for a special application. A larger number of storage sites offers the possibility of operating a TOF-ranger with more complex modulation

signals as pseudo random noise. However, realizing a large number of in-pixel storage sites is always a trade-off with the large fill factor desired.

The fill factor of the multitap-CCD pixel illustrated in **Figure 5.2** is 5.6%, which is an improvement of a factor 14 compared to the pixel originally introduced in [SP2]. This improvement was achieved (1) by reducing the number of storage sites from 8 to 4, (2) by using APS-readout and (3) by guiding the connecting metal wires perpendicular to the CCD, which allows the realization of an enlarged photo-gate. The multitap-CCD's rectangular rather than square shape (aspect ratio of 1:6, if realized with 4 taps) makes it poorly suited to be arranged in an array. Building a line instead of a two-dimensional array improves the fill factor to 100%. However, the long gates in the pipeline CCD only allow 4 MHz clocking frequency. That corresponds to a maximum demodulation frequency of only 1 MHz using 4 sampling points per modulation period.

Summarizing, the multitap-pixel offers a flexible number of in-pixel storage sites. With only 5.6% it has a poor fill factor. The large gate dimensions restrict the demodulation frequency to 1 MHz, which is not fast enough for high-resolution distance measurements in the range of 0-10 m.

5.1.2 4-tap lock-in pixel

Instead of connecting the photogate on only one side to a complete CCD line, as described before, the 4-tap lock-in pixel follows a modified approach. The square photogate is symmetrically connected to a transfer gate on each of its four sides. These transfer gates can transport photoelectrons from the light sensitive photogate into storage gates (see **Figure 5.3**). The demodulation process happens immediately near the photo site. Only one CCD gate, the transfer gate, has to be passed by the photoelectrons to reach the storage gate, where they can repetitively be added over a large number of integration cycles. During demodulation operation of the device the transfer gates are successively opened and closed synchronously to the modulated input signal. With this mode of operation the input signal can be rapidly sampled and the sampling points are stored in the storage gates. After this accumulative demodulation process the sampling points can be read out.

(a)

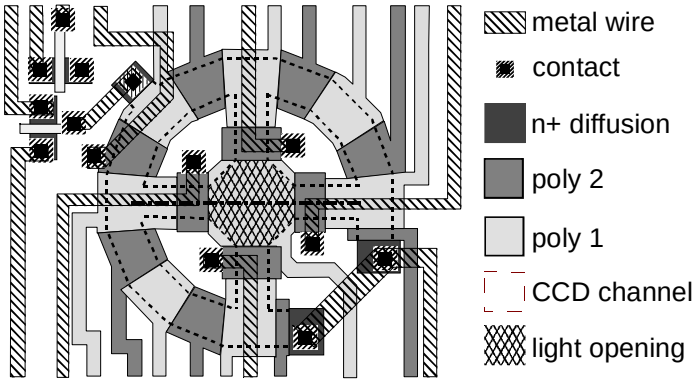

Dimensions: photogate: 15x15 µm², pixel: 95x110 µm², aspect ratio: 1:1, fill factor: 2.2%.

(b)

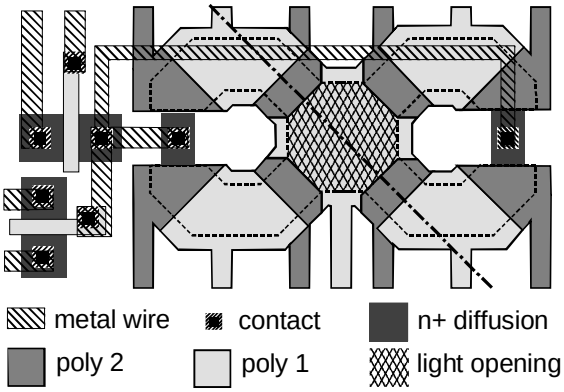

Dimensions: photogate: 15x15 µm², pixel: 40x85 µm², aspect ratio: 1:2, fill factor: 6.6%.

(c)

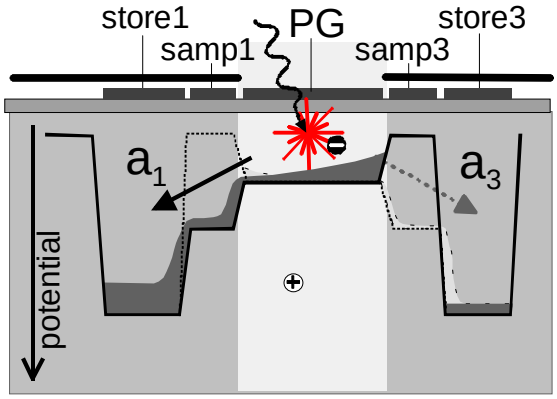

Figure 5.3 *Four-tap lock-in pixel realized with (a) one- and (b) two output diffusions: layout and cross-sectional view (c).*

The 4-tap device has been realized in two different versions, one with a wheel-shaped readout CCD, ending in only one sense diffusion node and one with two separate sense diffusion nodes, doubling the conversion capacitance and thus leading to only half the output voltage amplitude. The wheel-shaped CCD occupies

a lot of space and diminishes the pixel's fill factor to only 2.2%. In spite of the lower conversion gain the 2-side readout version is the preferable realization of both 4-tap pixels, because it offers a three times higher fill factor (6.6%) and has a reduced demand on a highly efficient CCD charge transport. This is because the photoelectrons only have to pass three CCD gates from their generation site, the photogate, to the detection diffusion. The influences of the unconventionally shaped CCD gates of both realization versions have to be investigated thoroughly.

The array-friendlier aspect ratio of 1:2 (1:1 respectively for the wheel-shaped version) and the short transport paths of the photoelectrons in the demodulation process are the major advantages of this 4-tap device compared to the multitap-CCD. However, it is not possible to realize more than four storage sites with this pixel architecture without drastically enlarging the photogate. The photogate, on the other hand, should be as small as possible for a fast and efficient charge separation. This appeared to be a problem in the first implementation of this technique [SP1], where, due to an over-dimensioned size of the photogate compared to the relatively narrow transfer gates, an inhomogeneous sensitivity of the single sampling points could be measured. By the modified, highly symmetrical pixel layouts shown in **Figure 5.3** this problem of inhomogeneities between the sampling points was partly overcome, at least for low sampling frequencies.

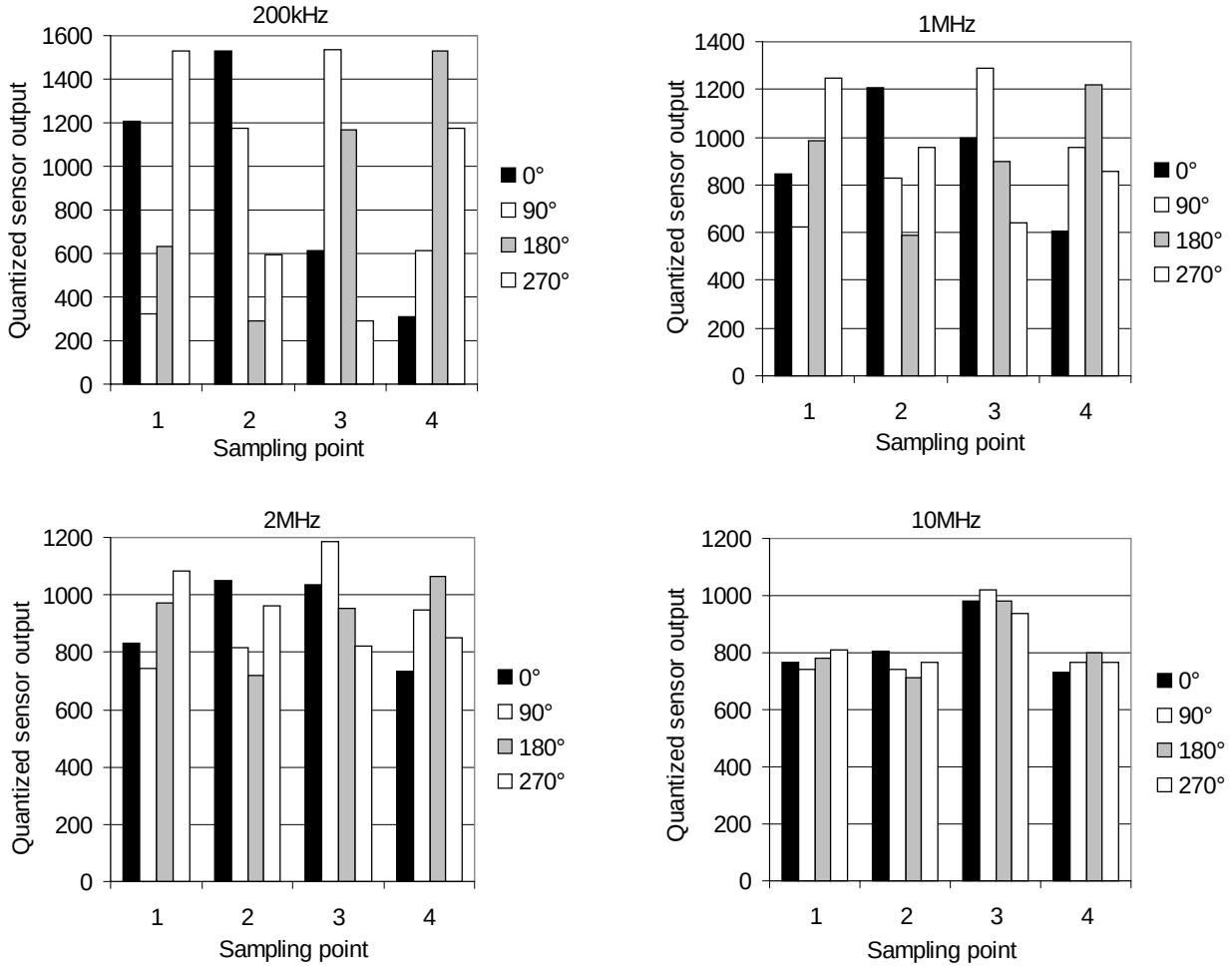

Figure 5.4 *4-tap lock-in pixel (with one output diffusion): Demodulation measurements at 0°, 90°, 180° and 270° phase for different modulation frequencies (200 kHz-10 MHz, → sampling frequencies: 800 kHz-40 MHz). Integration time: 0.5 ms, LED: 630 nm, square wave modulated, 50% duty cycle.*

Demodulation measurements with the 4-tap lock-in pixel are shown in **Figure 5.4** for different modulation frequencies. We see from this figure that the demodulation works excellently for frequencies up to 1 MHz. For higher frequencies the contrast decreases and the 3rd sampling point integrates an additional signal offset, probably due to different transfer efficiencies of the single transfer gates.

(a)

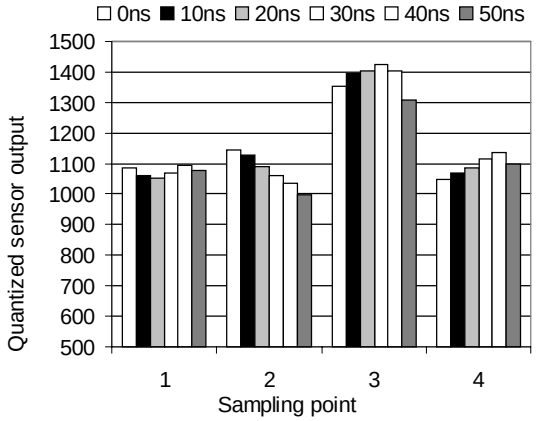

(b)

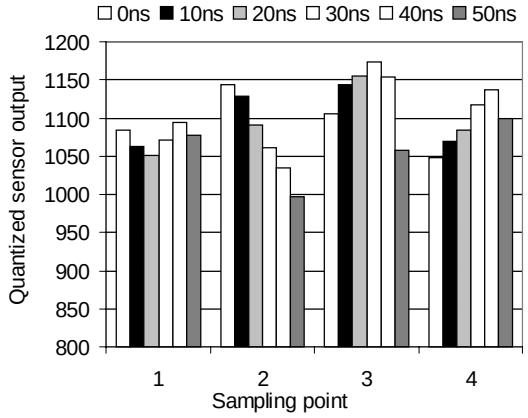

(c)

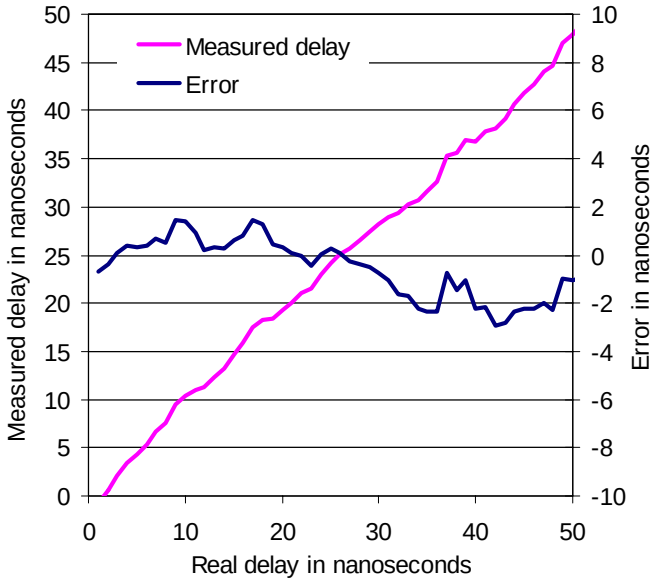

Figure 5.5 *4-tap lock-in pixel (with one output diffusion): Phase measurements at 10 MHz, (a) without and (b) with correction of 3rd sampling point. (c) Measured delay vs. real delay after correction of 3rd sampling point. Standard deviation of measurement error: 1.2 ns. (1.2% of modulation period).*

Phase measurements performed with the 4-tap pixel at 10 MHz modulation frequency (40 MHz sampling frequency) are shown in **Figure 5.5**. For these measurements an offset value of 250 quantization levels (estimated empirically) had to be subtracted from the 3rd sampling point. **Figure 5.5 (a)** illustrates the originally measured sampling point data for different signal delays, **(b)** shows the same data after the offset subtraction from the 3rd sampling point. The achieved time resolution is pretty poor: 1.2 nanoseconds. Also, in a real application, the measurement of the different sampling point sensitivities for each pixel in the array

and the necessary correction of the measured data appear to be impractical. Summarizing, the 4-tap pixel approach is only partly suited to range measurements, since, for modulation frequencies higher than 1 MHz, it suffers from transfer inhomogeneities between the single transfer gates.

5.1.3 1-tap lock-in pixel

Both pixel concepts introduced so far suffer from a low optical fill factor. In-pixel storage always occupies space, in proportion to the number of sampling points to be stored. The multitap approach only works up to 1MHz modulation frequency (realized with 4 storage sites) because the demodulation process happens in the extended area of a CCD line with design-rule-limited long CCD gates. The four-tap lock-in pixel accesses the photogate with four different transfer gates, resulting in an inhomogeneous response of the four sampling points. All of these limitations can be traced back to the requirement of realizing four independent in-pixel storage sites. The one-tap lock-in pixel ignores this requirement and offers only one storage site but attempts to maximize the fill factor. Therefore, the sampling points have to be stored externally.

Figure 5.6 shows the layout and a cross-sectional view (including the potential distribution in the semiconductor) of the 1-tap pixel. The left and the right light sensitive photogates (PGL and PGR) have a length of 6 μm, the middle photogate a length of 2.5 μm; the pixel width is 21 μm. Each pixel also includes a reset transistor, a source follower transistor (buffer amplifier) and the select transistor (cascode with source follower). This leads to a pixel size of 65 μm by 21 μm and an optical fill factor of more than 20%. The pixel's working principle is illustrated in **Figure 5.7**: By applying proper gate voltages to the photogates, the potential gradient in the semiconductor can be influenced (c.f. **Chapter 3**). If the control voltages of the photogates are changed synchronously with the modulated incoming light, optically generated charge carriers can either be integrated (if they belong to the sampling interval) or they are dumped to the dump diffusion (if they do not belong to the sampling interval). This process can be repeated until the integration gate (IG) has accumulated a sufficiently large signal. The addition or accumulation of single electrons under the integration gate is essentially noise free. This sampling mechanism is shown in **Figure 5.7 (a)**, whereas **(b)** describes the

same process in terms of a correlation of the optically generated input signal s(t) with the sampling signal f(t+τ). The fast channeling of the optical input signal and distribution either to the dump diffusion or to the integration gate can be interpreted as a multiplication of the electrooptical signal s(t) with the sampling function f(t+τ). With the integration under the IG this corresponds to a correlation process. See also **Section 2.2.1**.

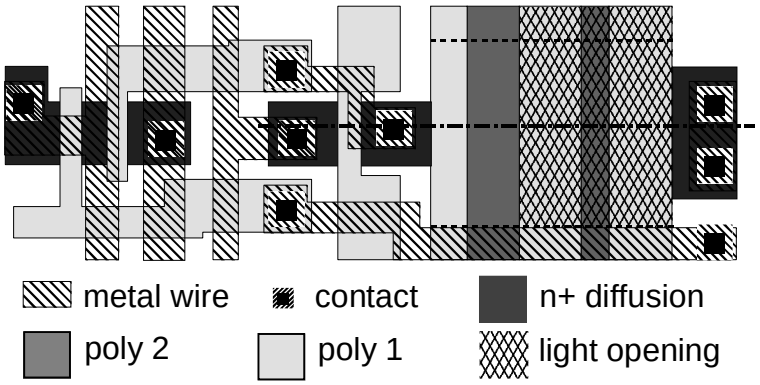

Dimensions: photogate: 21x14.5 µm², pixel: 21x65 µm², aspect ratio: 1:3, fill factor: 22%.

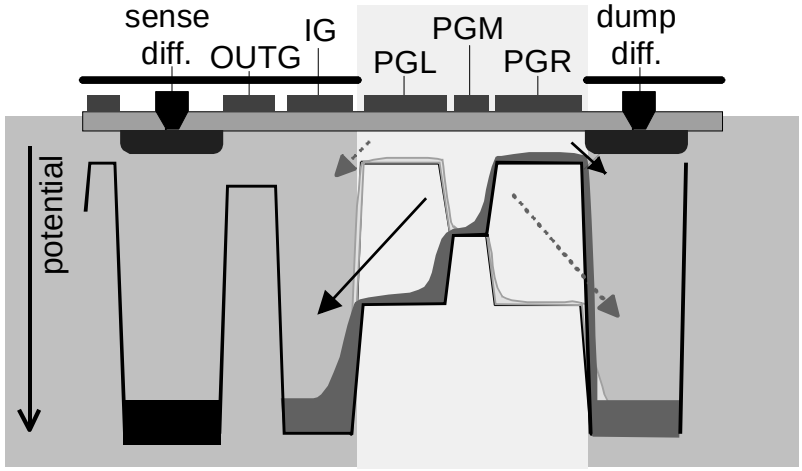

Figure 5.6 *One-tap lock-in pixel: Pixel layout and cross sectional view of the CCD part. (IG: integration gate; PGL/ PGM/ PGR: left/ middle/ right photogate).*

The tradeoff of this mode of operation is that the overall integration time is longer than for the previously introduced pixels and a certain amount of light is wasted because the incoming light is either integrated or rejected. In both previous approaches, the dead-time of one sampling point was always the active-time of some other sampling point, thus all incoming modulated light was used for evaluation during the demodulation period. This drawback can be partly compensated by choosing half the modulation period as integration time for each

sampling point, so that 50% of the received modulated light is evaluated and only 50% is lost. This is an acceptable compromise when compared with the enormous improvement in fill factor (20% rather than 5%). This integration time of half the modulation period has no influence on the measured phase; it only attenuates the measured amplitude to 64% of the real amplitude, which is a consistent and predictable error (c.f. **Section 2.2**).

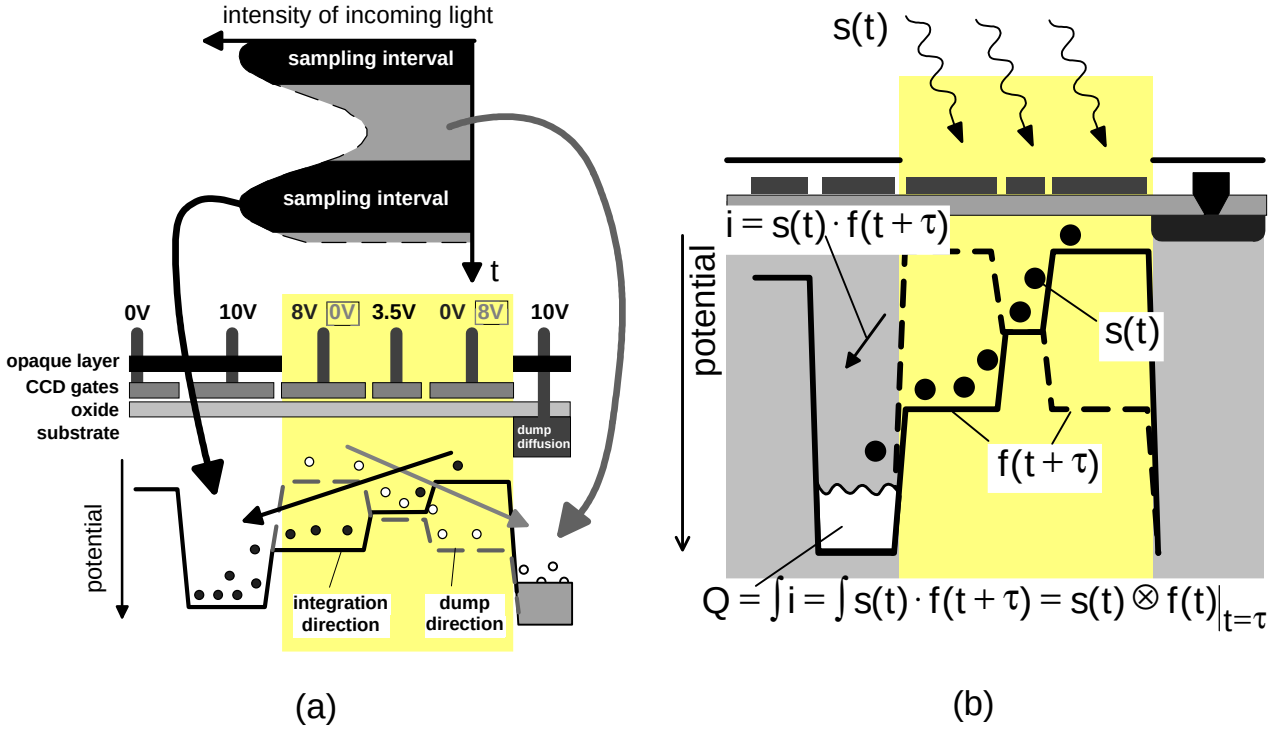

Figure 5.7 *One-tap lock-in pixel: illustration of (a) sampling and (b) correlation process.*

The more serious drawback is the fact that the sampling points have to be acquired serially. This "*serial tap-integration*" reduces the application area of the pixel in 3D-measurement to scenes with relatively slow movements. The integrated sampling points A_i in **Equation 2.17** contain both a fraction of integrated modulated light and a fraction of background light. If the sampling points are all taken at the same time (in parallel) they carry the same offset, even if the scene changes (moves) during integration. With the subtraction of two sampling points the offset disappears. The same is the case if the reflectance of an observed point changes during integration. However, if we acquire the sampling points serially and the reflectance or background intensity (offset) changes from one sampling point to the other, the algorithm is no longer able to eliminate offset and reflectance. Therefore, the 1-tap

device reacts very sensitively to such modulation of the scene that may be superimposed on the temporal modulation. The good fill factor and the outstanding demodulation performance and speed compensate this drawback by making short integration times (only a few milliseconds) possible. For this reason the 1-tap device is the most promising pixel-architecture for this 2.0 μm CMOS/CCD process.

Since all sampling points of one pixel are acquired with the same structure and stored at the same storage site, this pixel has a highly uniform response for all sampling points. The one side readout allows the photo site to be subdivided into three short CCD gates. With these three gates a potential gradient of temporally adjustable direction can be applied in the light sensitive region itself. Compared to the 4-tap pixel, the transfer gates are implemented in the photogate itself, which is now responsible for (1) optical generation, (2) fast separation and (3) repetitive addition of photoelectrons. Therefore, by neglecting the task of in-pixel sampling point storage, all demodulation requirements could be fulfilled in a small, completely light sensitive spatial area giving the pixel an improved speed response and fill-factor. Detailed measurements are presented in **Section 5.2**, an improved pixel realization that overcomes the restriction of serial tap-integration is introduced in **Section 5.3**.

This 1-tap device has been realized as a line sensor with 108 pixels and as an array with 64 by 25 pixels. Both sensors are integrated in an all solid-state real-time TOF range camera showing excellent performance (see **Chapter 6**).

5.1.4 Summary: Geometry and speed performance

We have introduced different realizations of demodulation pixels. All have their individual advantages and disadvantages. These can be put down to the local sites and the spatial extension of the four demodulation mechanisms (c.f. **Figure 5.1**). These facts are summarized in **Figure 5.8**; the characteristic pixel features are listed in **Table 5.1**.

Pixel structure	Storage sites	Photo sensitive area	Fill factor	Aspect ratio	Maximum demodulation frequ.
Multitap-CCD	*4 *)*	*45 x 15 μm^2*	*5.6%*	*1 : 6*	*500 kHz*
4-tap CCD	*4*	*15 x 15 μm^2*	*6.6%*	*1 : 2*	*10-20 MHz*
1-tap CCD	*1*	*21 x 13 μm^2*	*22.3%*	*1 : 3*	*> 20 MHz*
*) Pixel concept allows easy extension to a larger number of storage sites.					

Table 5.1 *Comparison of pixel features*

Figure 5.8 shows once more that realizing in-pixel storage of the sampling points lowers the optical fill factor. Also we see that only in the 1-tap pixel are the local sites of physical demodulation requirements located very close to each other in the light sensitive area. By contrast, the multitap-CCD uses dedicated CCD structures for each of the demodulation tasks: photogate → optical to electrical energy conversion, pipeline CCD → separation of charge carriers, transfer CCD → addition of charge carriers, readout CCD → storage of charge packets. Long paths unfortunately always mean low speed performance and system bandwidth. This can also be seen from **Table 5.2**, which shows the mean charge transfer time either exclusively caused by thermal diffusion or by drift in an electric field as a function of the gate length (c.f. **Section 3.1.3**).

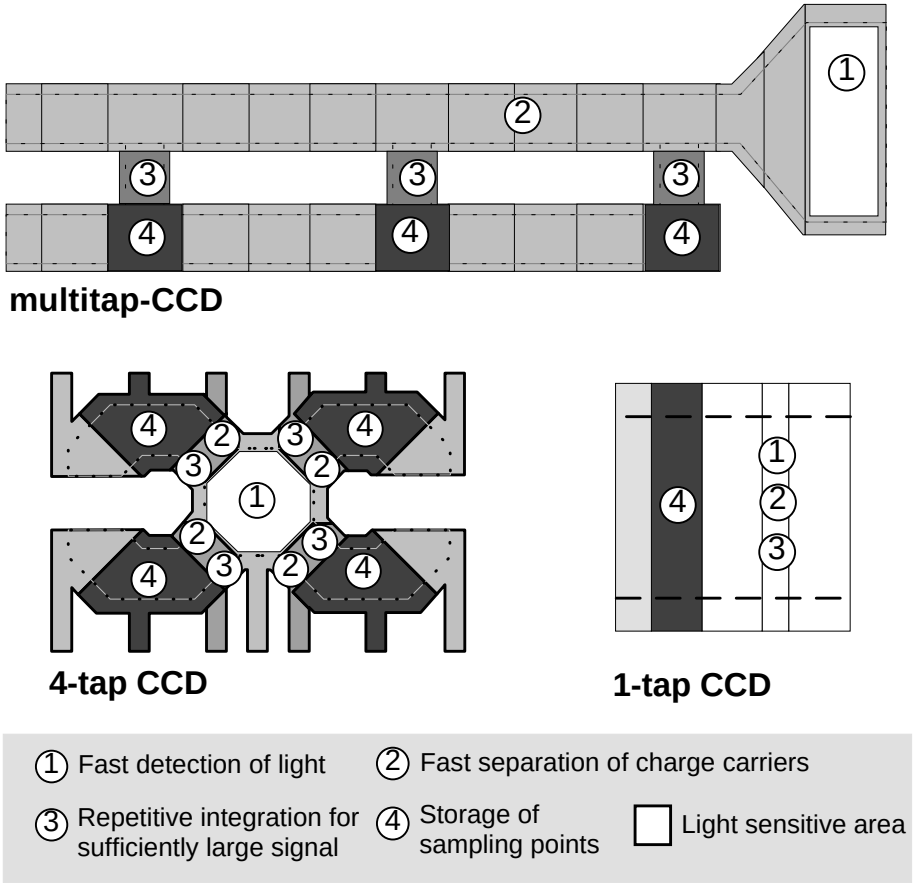

Figure 5.8 *Local sites of physical demodulation requirements: Energy conversion, fast separation, addition and storage of charge carriers.*

For the multitap structure the charge carriers have to travel 4 gates each of about 15 μm length to reach the next storage site. Since the fringing field influence on the charge transfer decreases more and more with increasing gate length for very long CCD gates, the complete transfer will be dominated by the diffusion process. Therefore, we expect a mean transfer time of about 68 ns per gate for the multitap-CCD pixel. Since this is only a statistical value we postulate a 10 times higher transfer time for a complete charge transfer of all charge carriers (important, because the remaining charge carriers would contribute to a wrong sampling point). Hence, the transfer time from one sampling point to the next should be about 3 μs (4·10·68 ns), resulting in a sampling frequency of about 350 kHz. Real measurements show a slightly better performance than this rough estimate, which completely neglected fringing field influences. The multitap structure can be used up to 2 MHz sampling frequency, which, however, only enables a modulation frequency of 500 kHz.

Thermal diffusion drift		***E-field drift (1 V)***	
Transport distance	Transport time	Transport distance	Transport time
30 µm	*270 ns*	*30 µm (1 V)*	*7 ns*
15 µm	***68 ns***	*15 µm (1 V)*	*1.8 ns*
10 µm	*30 ns*	*10 µm (1 V)*	*0.8 ns*
5 µm	*7.5 ns*	*5 µm (1 V)*	*0.2 ns*
3·10 µm	*90 ns*	*3·10 µm (1 V=3·0.33 V)*	*7 ns*
3·5 µm	***23 ns***	***3·5 µm (1 V=3·0.33 V)***	***1.8 ns***

Table 5.2 *Transfer time estimation with pure diffusion and pure E-field model. (p-substrate, $N_A=4\cdot10^{14}$ cm^{-3}, $\mu_n=1300$ cm^2/Vs, $D_n=33.6$ cm^2/s).*

The 1-tap structure benefits from stronger fringing fields, since the pixel architecture allows the realization of shorter CCD gates. Also the transfer does not necessarily require high charge transfer efficiency, as in the multitap approach. According to **Table 5.2** we can expect transfer times between 2 and 10 ns (depending on the actual fringing field influence) corresponding to demodulation frequencies up to 100 MHz or even 500 MHz. The subdivision of the photogate into three separate gates results in a speed improvement of at least a factor of three (considering only diffusion), more probably a factor of 10 to 20, since with (1) smaller gate lengths and (2) more gate junctions (three instead of one) the fringing field influence increases. We demonstrate the 1-tap pixel with demodulation frequencies up to 20 MHz (actual operation frequency of the 3D cameras introduced in **Chapter 6**). For higher frequencies it would be even more difficult to realize the highly accurate control and driving electronics. But another fact also reduces the demodulation performance at high modulation frequencies, the penetration depth of the modulated light. So far we have only considered the transfer times of electrons that are already captured by the electric field of the CCD gates. Generally, however, depending on the wavelength (c.f. **Figure 3.4**), the electron hole pairs are generated (far) away from the semiconductor surface. They will first have to diffuse to the top, before being captured by the CCD-field. This random diffusion process takes time and additionally limits the pixel-bandwidth, especially for modulation light of long wavelength.

5.2 Characterization of 1-tap pixel performance

In this section, we present the characterization measurements for the 1-tap pixel. In the first part we characterize the on-chip output stage (source follower) in terms of sensitivity, linearity and saturation. Then we outline the motivation for the measurements, describe the measurement setup and discuss the results to be expected. With this knowledge, we present the measurements of demodulation contrast and phase accuracy as a function of the control voltage amplitudes, the modulation speed, the wavelength and the power of the modulated light. We also present the results of noise measurements and compare the measured phase accuracy with the prediction we presented in **Section 4.2**. We try to specify all measurement parameters completely so that the measurements may be reproduced. In order not to confuse the reader and to keep the measured data clearly presented, we summarize some measurement details in the appendix (coded as measurement conditions: **MCDxyS** for SCCD measurements and **MCDxyB** for BCCD measurements).

The 1-tap pixel has been realized (1) as a linear array containing 108 pixels and (2) as a 2D-array with 64 by 25 pixels. The line-sensor has been fabricated in two technologies: as BCCD and as SCCD. The pixel characterizations have been carried out with the line sensors. This offers the possibility to compare the buried channel and surface channel CCD performance. More details of the overall sensor architectures can be found in **Chapter 6**, where the camera implementations are described.

5.2.1 Charge to voltage conversion

Sensitivity and Responsivity

The sensitivity is defined as the ratio of output voltage to input charge (unit: Volt/electron). It is characterized by the output stage's conversion capacitance and amplification. Since, in our implementation, the input charge can only be generated optically or thermally, it cannot be measured directly. So the sensitivity cannot really be distinguished in isolation from the responsivity, which is the ratio of output voltage to input light (unit: V/photon). The responsivity additionally contains the quantum efficiency and therefore depends on the wavelength. None of the

quantities quantum efficiency, conversion capacitance and amplification can be measured directly or independently from each other in the present implementation. Since we never know the exact process parameters, we can only roughly estimate amplification and conversion capacitance with an accuracy of about ± 10%:

Conversion capacitance: $C_c = 40$ fF

Amplification of SF stage: $A_{SF} = 0.9$

Quantum efficiency at 630nm: 65%

→ Sensitivity: $S = A_{SF} \frac{q}{C_c}$ =3.6 μV/electron

→ Responsivity: $R(\lambda) = QE(\lambda) \cdot S = QE(\lambda) \cdot A_{SF} \cdot \frac{q}{C_c}$ =2.35 μV/photon @ 630 nm

With the measurement conditions listed in MCD02 in the appendix we measure an output voltage swing of 3.60 V. The theoretical calculations (all parameters in MCD02) predict a swing of 3.25 V, which agrees very well with the measurement (within the expected uncertainty range of ± 10%).

Saturation of output stage and CCD gates

The maximum signal (charge) that can be handled by a CCD structure is limited by two independent (saturation) mechanisms. Firstly the charge must not exceed the CCD gate's *charge handling capability* and secondly the output voltage swing caused by the signal charge must be within the *operation range of the output amplifier*. The charge handling capability is essentially influenced by the voltage difference between the single CCD gates ($Q_{max}=C_{gate} \cdot \Delta V_{max}$). A high voltage difference allows more charge carriers to be integrated than a low voltage difference.

It is the purpose of this section to investigate the voltage difference between the integration gate and the modulated photogate that defines a charge handling capability just leading to saturation of the output stage. In general, we expect the demodulation contrast to increase with high voltage amplitudes on the modulated photogates. It is obvious, however, that for a certain modulation amplitude, depending on the actual voltage of the integration gate IG and the amount of

charge already integrated, it will be possible for charge carriers integrated under IG to be transported back into the light sensitive pixel area and to be dumped to the dump diffusion. The maximum charge to be integrated within the pixel is defined by the output stage. The conversion capacitance of 40 fF, together with the amplification of 0.9 and a maximum output voltage swing of 4 V, leads to a maximum number of about 1,100,000 electrons that can be integrated without causing signal clipping due to saturation of the output stage.

To determine the charge that leads to saturation of the output stage, we bias the gates PGM and PGR with 10 V (so that they are definitely at a higher potential than PGL) and use PGL as a variable barrier. In this way the potential difference between PGL and IG adjusts the amount of charge that IG can hold (c.f. **Figure 5.9**). The integration gate IG is always biased at 10.7 V, a reliable amplitude that avoids device damage by oxide break through. The illumination time is chosen to be long enough that the potential well, generated by the potential difference between IG and PGL, is always totally filled. Additionally generated charge carriers can no longer be held by IG.

As the result of this measurement we find that a potential-difference of 2.2 V between IG and PGL defines the full-well charge that leads to saturation of the output stage (IG=10.7 V, PGL=8.5 V). For lower PGL voltages (e.g. 8 V) the output signal does not increase further, because the amount of charge that will be integrated then leads to saturation of the output stage. For higher PGL voltages (e.g. 9 V), the output signal decreases, because the full-well charge is smaller than the maximum charge that the output stage can handle. Therefore, the amplitude of PGL should not exceed 8.5 V for the demodulation application (assuming IG = 10.7 V). Otherwise, the maximum signal that can be handled is no longer limited by the output stage but by the actual potential difference between IG and PGL.

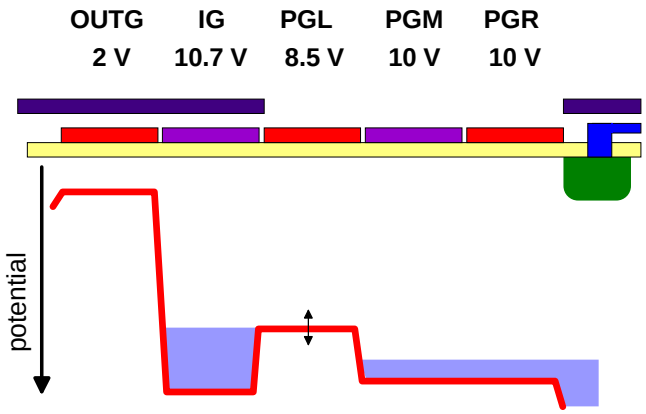

Figure 5.9 *Connection between CCD-saturation (full well capacity) and saturation of the output stage.*

Linearity of the output stage

In **Section 2.2.3** we already discussed the insensitivity of the 4-tap algorithm to linear or quadratic distortions in the transfer characteristics. However, the algorithm is sensitive to higher order non-linearities. For this purpose we measure the linearity of the complete analog and digital conversion chain, containing the output stage implemented on the demodulation pixel chip and the additional analog electronics of the camera board and A/D conversion unit. This can be done by illuminating the pixels with a highly accurate, constant light source and measuring the output voltage swing versus the integration time. We choose a maximum integration time of 50 ms and we measure 22 points with an increment of 2.3 ms in integration time.

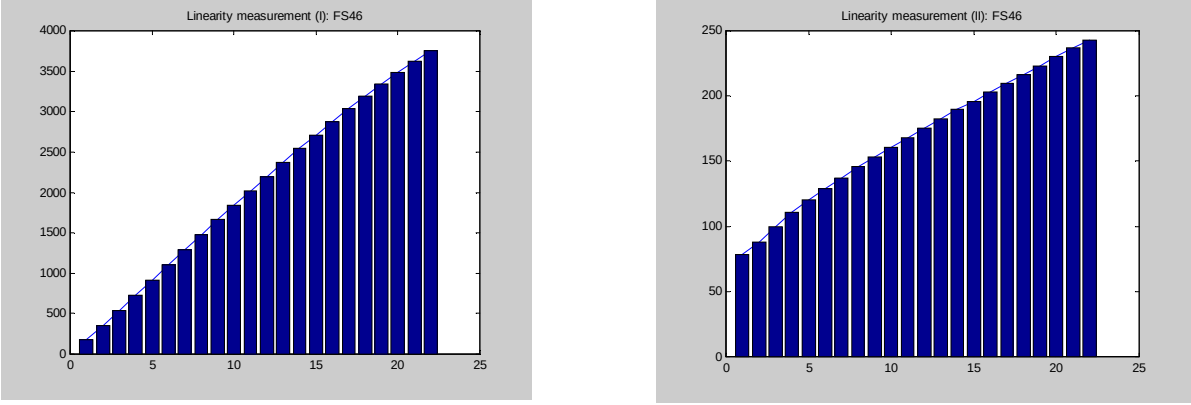

BRIGHT measurement

DARK measurement

Figure 5.10 *Linearity measurements of the output stage for different illumination intensities and integration times (0-50 ms).*

The measurement (**Figure 5.10**) is performed for two illumination intensities, one nearly leading to saturation of the output stage for the longest integration time (*BRIGHT* measurement) and the other with a factor of 100 lower intensity (*DARK* measurement). The measurement conditions chosen are summarized in **MCD01** in the appendix. For the quantization of the analog output, we use the EPPI (Enhanced Parallel Port Interface, a CSEM product), a 12 bit frame grabber that can be connected to the parallel port of a PC.

We can already judge by eye that the overall system linearity appears to be good (**Figure 5.10**). Only for very low output voltages (DARK measurement) does the linearity deteriorate. To judge the actual influence of this DARK measurement nonlinearity, we approximate the measured curve with a polynomial. This can easily be done with MATLAB (polynom: $13.2 \cdot x - 0.53 \cdot x^2 + 0.02 \cdot x^3 - 0.0003 \cdot x^4$, for 0<x<22). With the knowledge of this nonlinearity, the resulting phase error for the range measurement application can be estimated (as in **Section 2.2.2**). We find that the maximum phase error caused by the actual measured nonlinearities of our system is less than ± 0.5 degrees. Hence, the linearity of our output transistor and A/D conversion chain is sufficient for the targeted range imaging application.

5.2.2 Measurement setup, expectations and predictions

Before we present the measurements for the 1-tap pixel in Sections **5.2.3 - 5.2.8** we will first outline the motivation and describe these measurements. In this section,

we describe the measurements that we will perform later and the setup that we use for these measurements. In addition, we will make predictions about how the pixel performance will change as a function of different parameters.

What is "demodulation contrast"?

We already discussed in **Section 4.2** that, for a good phase accuracy, not only the contrast (or modulation depth) of the modulated light source but also the shutter efficiency is of essential importance. Both define the measured contrast, which directly influences the ranging accuracy (c.f. **Equation 4.10**). In optics the modulation is defined as follows:

$$\text{modulation} = \frac{I_{max} - I_{min}}{I_{max} + I_{min}} \qquad \textbf{Equation 5.1}$$

Similarly, we define the demodulation contrast C_{demod} as:

$$C_{demod} = \frac{\text{measured amplitude}}{\text{measured offset}} \qquad \textbf{Equation 5.2}$$

There are several parameters attenuating the measured amplitude. In **Chapter 2** we mentioned that the integrative acquisition process of the sampling points A_i leads to a decrease in measured amplitude (c.f. **Equation 2.18**). For the distance measurement, we operate the lock-in sensor at a modulation frequency of 20 MHz with a sampling interval of 25 ns. Thus, the integration time for the sampling point acquisition is half the modulation period. Therefore, according to **Figure 2.7**, the measured amplitude is only 64% of the real amplitude. In addition to this more system theoretical amplitude attenuation, there are also physical effects (shutter inefficiency) that lower the measured amplitude and increase the measured offset.

The demodulation contrast quantifies the CCD's (im)perfection of charge separation. It should be as high as possible in order to achieve large signal amplitude and hence a good signal-to-noise ratio for the phase detection. The shutter efficiency depends on the following parameters:

- *Demodulation frequency*: The higher the demodulation frequency (or sampling frequency) the shorter is the time available for the single charge carriers to travel

from their site of optical generation to the storage area. If they do not reach the right storage site in time, they will contribute to a wrong sampling point and lower the demodulation amplitude.

- *Fringing fields*: The higher the fringing fields between two adjacent electrodes the higher is the speed of charge transfer and thus the resulting demodulation efficiency increases, especially at high frequencies.
- *Gate length*: The smaller the gate length the more quickly the photoelectrons arrive at the storage sites and the higher becomes the influence of fringing fields. A small gate length is therefore the key parameter for a fast demodulation performance.
- *Wavelength*: The use of long wavelength light leads to a large penetration depth of the incident light. This again causes long diffusion times and blurred diffusion directions. The effective charge capturing area grows. This reduces the sharpness (crosstalk) and leads to a lower demodulation contrast. Long diffusion times lower the demodulation cut-off frequency, while the blurring effect (also opaque CCD gates directly collect photogenerated charge) also appears at low modulation frequencies or even under DC conditions.

Optical measurement setup

Figure 5.11 shows the optical test setup for the measurements described below. The lock-in sensor chip is mounted on the camera board, which is fixed to an XY-table under a microscope. This microscope is used to illuminate the chip with a variable amount of optical power. LEDs of different wavelength are used to illuminate the pixels. They can be plugged into a fast LED driver module (MV-LED1 [CS1]), which is capable of modulating them up to 20 MHz, depending on their internal capacitances.

The light of the LED passes through an iris (or pinhole) and the objective of the microscope. The distance from the objective to the lock-in chip is adjusted such that the light beam is not in focus on the chip. In this way we get a homogenous light spot on top of the chip, leading to an equal illumination of all the pixels. By varying the distance of the objective to the chip we can adjust the size of the light spot and, hence, the illumination intensity on the chip. By measuring the total power of the light spot and the diameter of the spot, the total optical power on the photogate can

than be determined with the ratio of the spot size to the size of the photogate. Additionally it is possible to attenuate the optical power by introducing neutral density filters into the light path. This is the preferred method of changing the light intensity, since it is fairly fast and highly accurate.

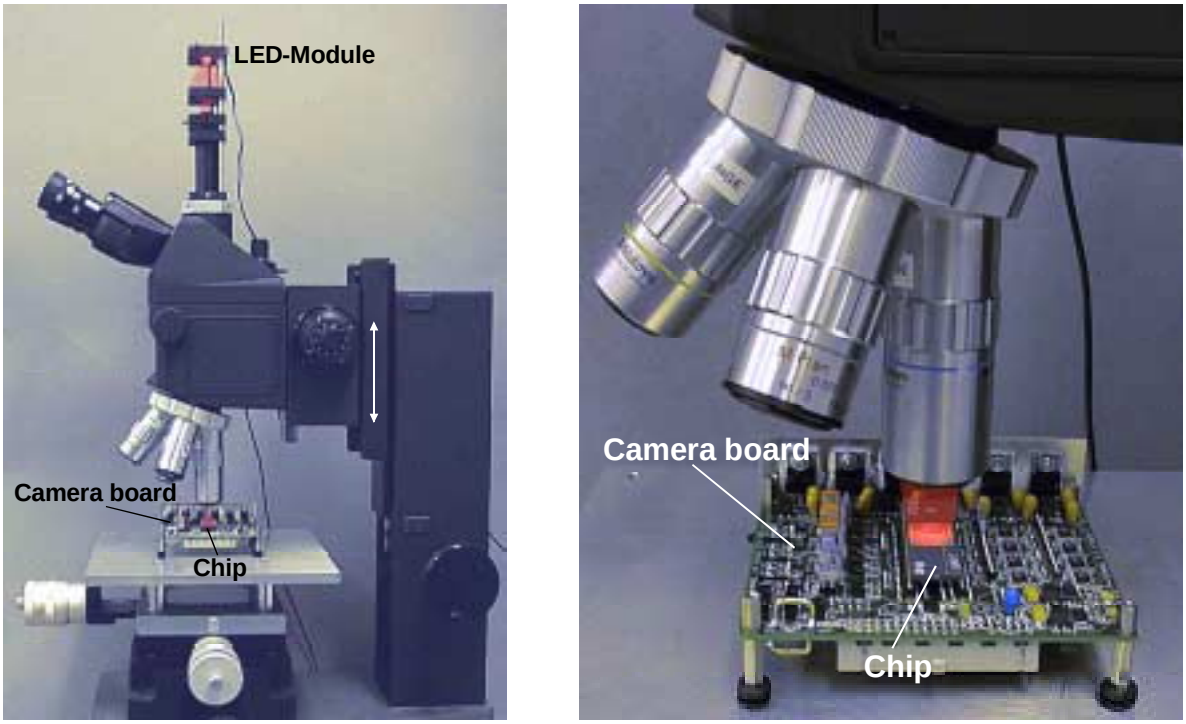

Figure 5.11 *Optical measurement setup.*

The signals to control the LED-module are TTL signals, generated by a digital pattern generator (sequencer, c.f. **Chapter 6**) that also controls the camera board, especially the demodulation gates PGL and PGR, so that modulation and demodulation are synchronous.

The optical input signal: AC-Performance of LEDs

Since the control signal for the LEDs is digital, we get a square wave modulated LED output signal, at least for low modulation frequencies. **Figure 5.12** shows the optical output signal of the 630 nm HP-LED for different modulation frequencies.

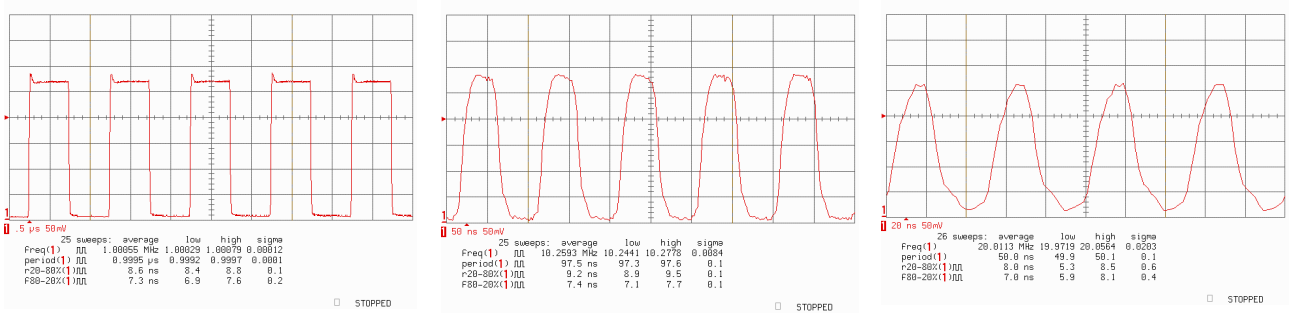

Figure 5.12 *Speed performance and modulation shape of the LED light source for different modulation frequencies.*

(LED: Hewlett Packard HPWT-DH00, Detector: Siemens SFH203P photodiode)

One can see from these measurements that the cut-off frequency of the 630 nm LEDs used is in the range of 20 MHz. The low-pass characteristic of the LEDs leads to an attenuation of the square waves' harmonics for larger frequencies. This results in an optical output that gradually looks sinusoidal for frequencies larger than 5-10 MHz.

Measuring the amplitude of a square- or sine-wave

From **Section 2.2.2** we know that sampling of a square wave with only four sampling points leads to *aliasing*. This is because a square wave is composed of an infinite number of harmonics. We also discussed in **Chapter 2** that the fact of integrating the single sampling points over half the modulation period leads to low-pass filtering of the signal (convolution of the spectrum with a *sinc*-function), which decreases the measured amplitude (of the first harmonic) to 64% of the real amplitude.

With our measurement setup, described above, we get a square wave modulation for lower modulation frequencies and a more sinusoidally shaped modulation for modulation frequencies beyond the LED's cut-off frequency. To determine the amplitude of a square wave exactly one would have to use an infinitesimally small (short) integration interval for the sampling process. For our integration interval of half the modulation period, the measured amplitude, assuming 4-tap sampling of a

square wave and evaluation with **Equation 2.13**, strongly depends on the phase of the sampled signal. This effect can easily be simulated. The simulation results for a pure square wave, a sine wave and the first harmonics of a square wave are shown in **Figure 5.13**. On the left hand side of the figure the input signals are shown. The graphs on the right hand side show the calculated amplitude of the corresponding signal with respect to the signal's phase.

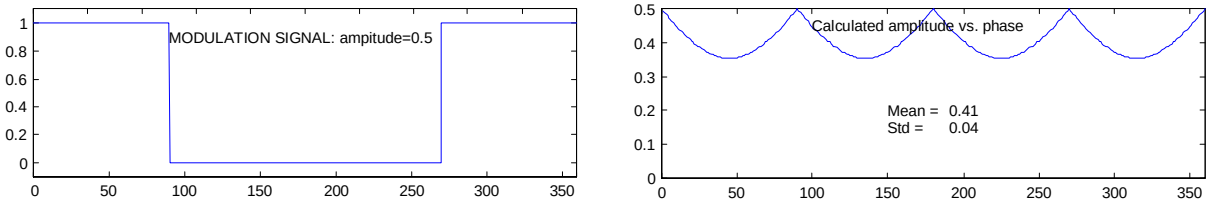

Square wave

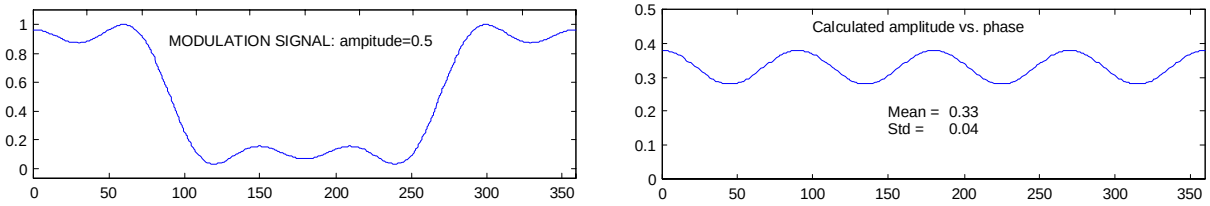

Basic frequency and first two harmonics of a square wave

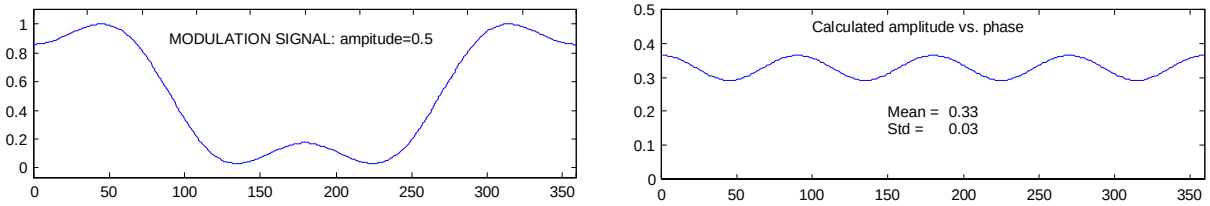

Basic frequency and first harmonic of a square wave

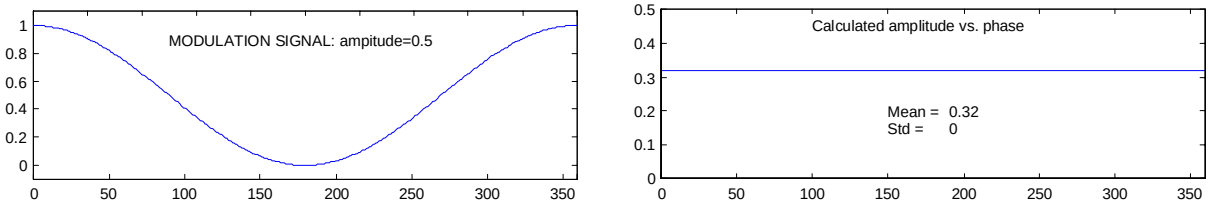

Sine wave

Figure 5.13 *Measured amplitude versus actual signal phase for different modulation signals. Left hand side: input signal, right hand side: calculated amplitude vs. the signal's phase. The simulation of the measured amplitude is based on* $A = 1/2 \cdot \sqrt{[(A_0-A_2)^2+(A_1-A_3)^2]}$ *where* $A_0..A_3$ *have been integrated over half the modulation period.*

As one would expect, for the sine wave the measured amplitude does not depend on the actual phase (no aliasing). The calculated amplitude has a constant value of 0.32, 64% of the real amplitude 0.5. For the square wave, however, the measured amplitude indeed depends on the actual phase. It varies with a standard deviation of 0.04, which is a relative amplitude error of $\pm$ 8%. Therefore, if we measure the amplitude of the square wave input signal in order to determine the demodulation contrast of the pixels, we have to take into account the actual phase between the optical input signal and the sampling signal of the demodulation pixel.

Now, what does that mean for our measurements? If we look at the optical input signals, we see that the light source has a low-pass characteristic. For frequencies higher than about 5 MHz, the optical signal gradually looks like a sine wave (concerns the 630 nm LEDs that are also used for the range camera realizations). The delay between the optical modulation signal of the LEDs and the control voltages for the photogates (signal demodulation) is about 6 ns (measured). This corresponds to the following phases at the different modulation frequencies:

1 kHz	*6 ns = 0.00216°*
10 kHz	*6 ns = 0.0216°*
100 kHz	*6 ns = 0.216°*
1 MHz	*6 ns = 2.16°*
10 MHz	*6 ns = 21.6°*
20 MHz	*6 ns = 43.2°*

We see that for frequencies less than 10 MHz the delay of 6 ns does not have a significant influence on the phase. One can see from **Figure 5.13** that, as long as the phase is 0° or any multiple of $\pi/2$, the calculated amplitude of a 4-tap sampled square wave is correct. Therefore, we can use the algorithm $A = 1/2 \cdot \sqrt{[(A_0-A_2)^2+(A_1-A_3)^2]}$ to calculate the amplitude and hence the demodulation contrast without taking into account the actual signal phase. For frequencies lower than 10 MHz the phase of the optical input signals is about 0°, so we do not make any error in calculating the amplitude of the square wave. For 10 MHz and 20 MHz, the input signal is nearly a sinusoidal wave, where the measured amplitude does not depend on the phase. We measure the amplitude with a systematic error of 64% in that case. Strictly speaking, for an isolated determination of the pixels' demodulation performance at high frequencies one would have to correct the measured amplitude by a factor of 1 / 0.64 = 1.56. This is because, due to a

sinusoidal rather than square shaped input signal, the measured amplitude is attenuated to 64%, independently of the actual demodulation performance of the pixels. We do not make this correction, for two reasons: (1) We use exactly the same LEDs (HPWT-DH00, 630 nm) modulated at 20 MHz for the range cameras introduced in **Chapter 6**. The contrast values presented in **Section 5.2.3 - 5.2.5** therefore represent the real measured contrast, including the modulation shape and modulation depth of the optical input signal. And (2), as can be seen from **Figure 5.12**, for 20 MHz modulation the optical signal is not exactly a sinusoidal wave so that an amplitude correction by 56.25%, which corresponds to the pure sinusoidal wave, would not be absolutely correct.

DC case: Stationary charge-separation/ shutter efficiency

Before presenting the first measured values, we would like to introduce a very simple model, which gives a first feeling for the *working principle of the pixel* and for numerical values we can expect for the *demodulation contrast*. **Figure 5.14** illustrates why we do not get a 100% demodulation contrast even under ideal stationary conditions.

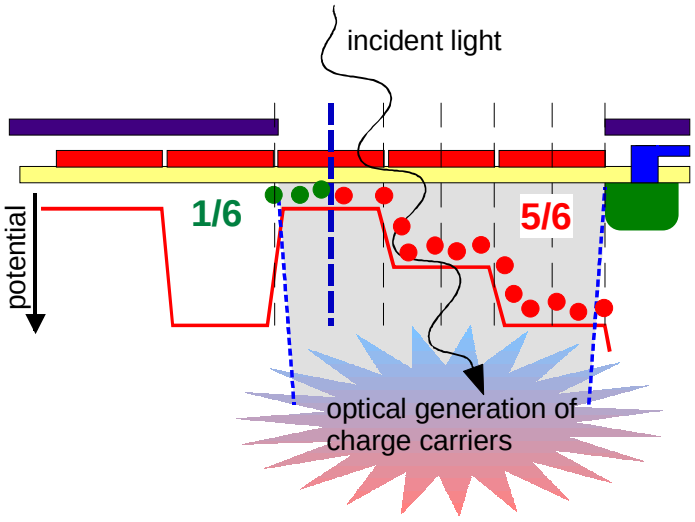

Figure 5.14 *Simple model of shutter inefficiency (I).*

(1) A fraction of charge generated under the left photogate will always travel to the left and be integrated under the integration gate, independent of the photogates' bias conditions. This is because there is no potential barrier between this photogate and the integration gate. The same is the case for the

right photogate, where a fraction of charge will always travel directly into the dump diffusion and will never be detected.

(2) Charge carriers are not only collected under the transparent photogates but also under the adjacent opaque photogates, because (a) the geometry and position of the optical shield is never 100% precise. And (b), even more important, depending on its wavelength the light penetrates deep into the semiconductor before it generates electron hole pairs (c.f. **Figure 3.4**). Then it diffuses in all directions, not only perpendicularly to the semiconductor surface. This leads to the blurring effect, which we have already mentioned above.

Here ideal perpendicular diffusion has been assumed. Nevertheless 50% of the charge generated under the left photo gate cannot be separated and will be collected under the integration gate. Such a behavior would correspond to a **demodulation contrast of** (5/6-1/6) / (5/6+1/6) = 4/6 = **67%.**

This means that, for this simple model, we cannot expect the demodulation contrast to be better than 67%, even for these idealized DC-conditions. So far, however, we have neglected two important parameters: (1) the demodulation frequency (the demodulation contrast will decrease with increasing frequencies) and (2) the influence of the light's wavelength.

Influence of the wavelength

As already mentioned, we expect the wavelength of the light source used to have an influence on the achievable demodulation contrast. This is due to the wavelength-dependent penetration depth of incoming light, introduced in **Section 3.1.1**. Since, generally, electrical fields within a CMOS-processed semiconductor exist only near the semiconductor surface, substrate-regions more than about 2 μm - 5 μm away from the surface are nearly field-free. Charge carriers that are optically generated in these regions move by thermal diffusion in any random direction. Either they recombine within the substrate or they are collected by an electrical field near the surface. However, they can travel up to 100 μm before being captured by an electrical field (**Section 3.1.3**). Since red-light photoelectrons are generated deeper in the semiconductor than blue-light photoelectrons, their tendency to travel before being detected (crosstalk) is much higher.

To clarify the point: “A red-light-electron might diffuse directly into the integration gate (IG) although the photogates (PGL/ PGR) are biased in ‘ dump-direction’. The blue-light electron, however, will be captured by the photogate’s electrical field before diffusing to the IG and will then be forced to travel to the dump site.” Therefore, we expect a better demodulation efficiency for short-wavelength-light than for long-wavelength light. This expectation will be confirmed in **Section 5.2.3**.

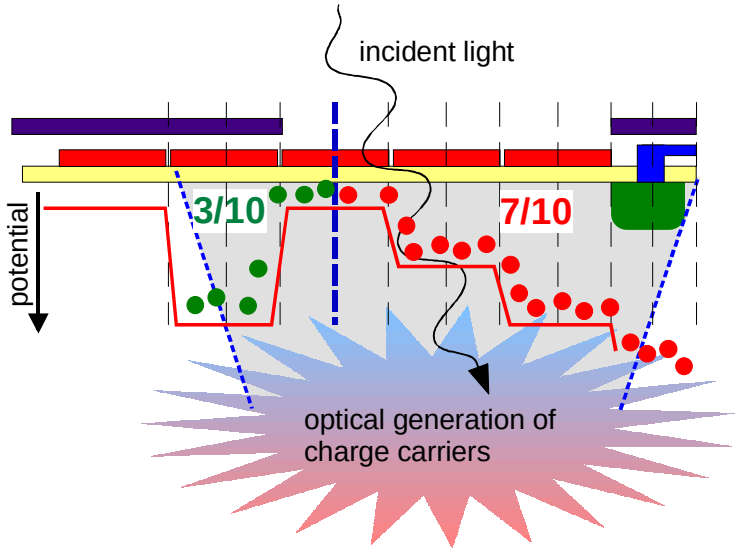

Figure 5.15 *Simple model of shutter inefficiency (II), now considering a larger penetration depth of the light.*

In **Figure 5.15** we have added these considerations to the previous shutter non-efficiency model: A certain proportion of the optically generated charge carriers also diffuses directly into the storage sites (and probably into gates even further away). For the dimensions chosen in **Figure 5.15** this corresponds to a **demodulation contrast of only** (7/10-3/10) / (7/10+3/10) = 4/10 = ***40%.***

Additionally, photoelectrons generated far from the electrically active zone need time to reach the demodulating electrical field. This temporal delay in arrival time will lead to an additional wavelength-dependent decrease in demodulation contrast for high frequencies.

5.2.3 Determination of optimal control voltages

It is obvious that the demodulation contrast depends on the amplitude of the control voltages of the photogates. With our control and driving electronics we can switch the control signals between 0 V and an adjustable voltage value. Additionally, the setup allows the rise and fall times to be varied by changing an additional capacitive load on the driver's output. Also, the pulse width can be varied by some nanoseconds. The rise and fall times as well as the duty cycle (pulse width) gain importance only for high modulation frequencies. Since, however, the exact adjustments of both rise and fall time and signal pulse width are very time-consuming, we determine the best voltages firstly for 1 MHz and, based on these results, we only perform a fine-tuning for 20 MHz modulation. For both realizations, the demodulation contrast reaches a maximum for PGL/PGR modulated with 8 V amplitude (**Figure 5.16**). The ideal voltage of the middle photogate at 20 MHz modulation frequency is 3.5 V for the BCCD version and 6.5 V for the SCCD.

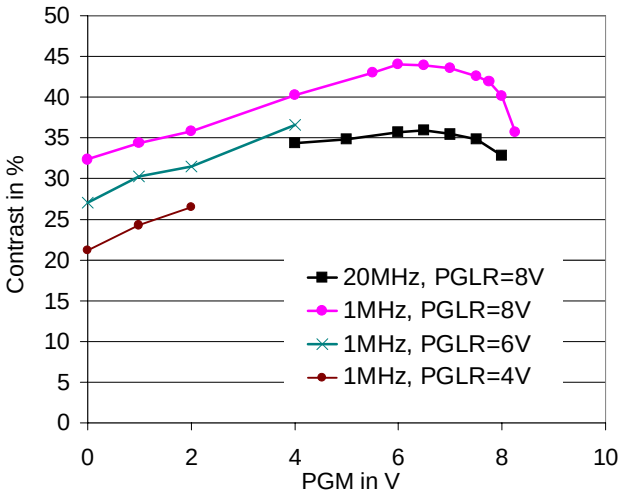

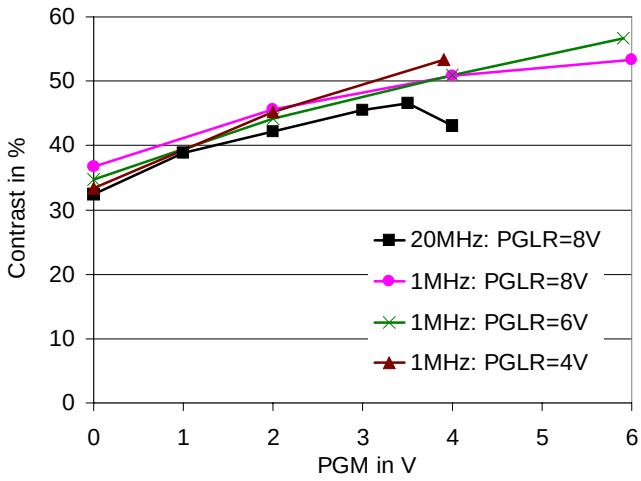

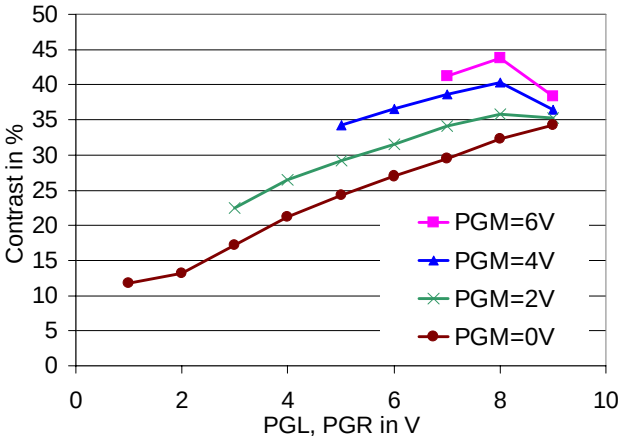

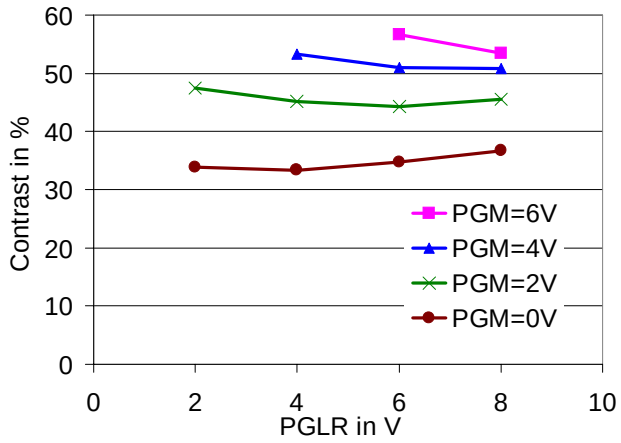

Modulation frequency: 1 MHz

SCCD

Modulation frequency: 1 MHz

BCCD

Figure 5.16 *Demodulation contrast vs. gate voltages @ 1 MHz and 20 MHz. PGLR: voltage amplitude of the left (PGL) and the right (PGR) photogate. [MCD03S; MCD03B; MCD04S; MCD04B].*

For 20 MHz operation, the shape of the modulation signal also gains importance. We find an optimal contrast for the following shape of gate voltage signals (**Figure 5.17**):

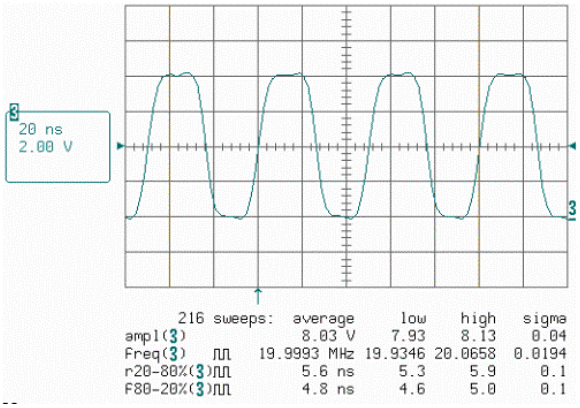

Figure 5.17 *Control signal shape for modulated photogates (8 V, 20 MHz).*

It is significant that, for the BCCD realization, the difference of the PGM-voltage and the voltage amplitude of the modulated photogates does not have a great influence on the demodulation contrast. For a good contrast, above all the voltage of the middle photogate is important. As illustrated in **Figure 5.18**, this voltage, (to be more precise, the *voltage difference* between PGM and the zero-biased modulated photogate, PGL or PGR), determines the position of the potential minimum in the horizontal direction and hence the junction, which decides whether the photoelectrons travel to the left or to the right. The larger this potential difference, the more this potential minimum moves to the borders of the light sensitive area and the larger is the resulting shutter efficiency and demodulation contrast. This effect is most significant for the buried channel structure since the potential shapes in the buried channel (away from the surface) are smoother than directly at the surface, but it can also be observed for the surface channel device.

In contrast to the BCCD, where the depletion width depends on the biasing of the buried channel, in SCCDs the voltage amplitude of the CCD gates also influences the depletion width. Since a deep depletion width results in a faster capturing process of the photoelectrons, we observe an increase in demodulation contrast for increasing modulation amplitudes. In addition, the size of the fringing fields grows for larger potential differences between two adjacent gates. In BCCDs a relatively small potential difference between the single CCD gates already leads to a sufficient fringing field.

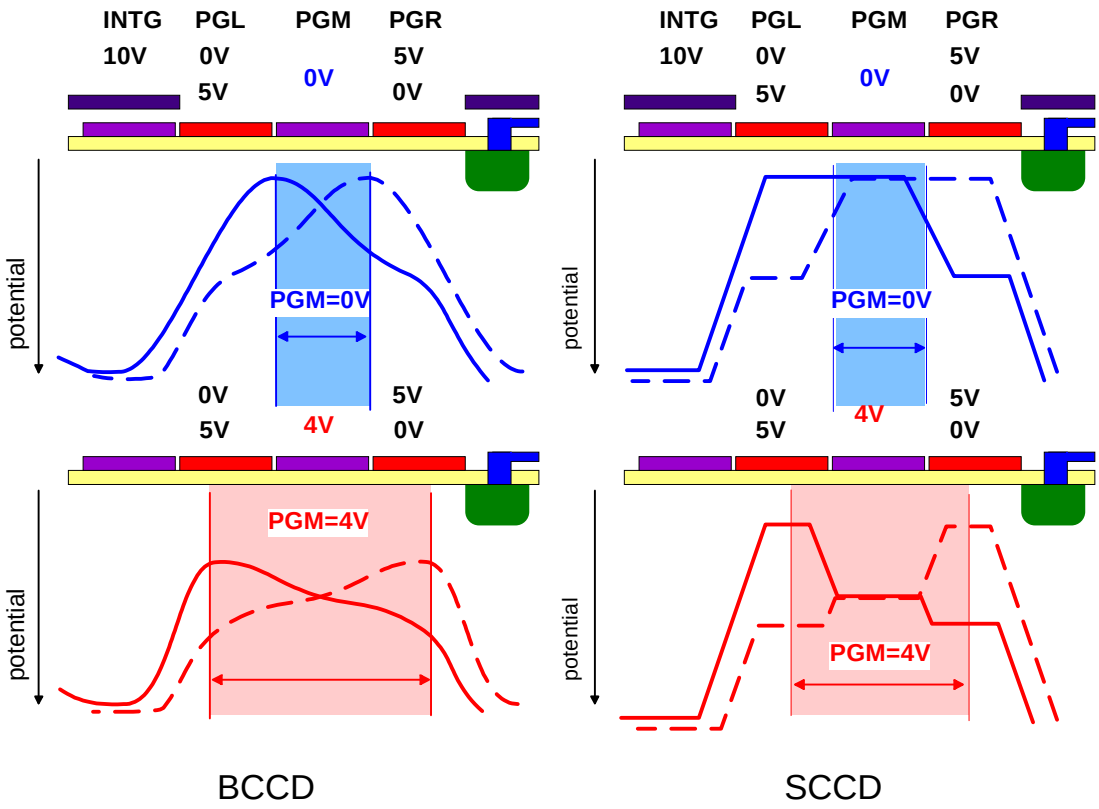

Figure 5.18 *Influence of the PGM voltage on the demodulation contrast for BCCD and SCCD realizations.*

Saturation velocity

We know that the velocity of charge carriers increases linearly with the applied electrical field only for small electrical fields. For higher fields the velocity reaches a saturation value (10^7 cm/s in silicon). Now we want to examine if the saturation velocity is already reached for a potential difference of 10 V between two adjacent gates.

Estimation:	
Gate length:	6 µm
Potential difference:	10 V
Electrical field:	$1.7 \cdot 10^4$ V/cm
Doping concentration (BCCD):	$4 \cdot 10^{16}$ cm^{-3}.
Electron mobility @ doping concentration	10^3cm^2/Vs
Saturation velocity v_s	10^7 cm/s
Drift velocity: $v = \frac{\mu \cdot E}{1 + \frac{\mu \cdot E}{v_s}}$	$0.63 \cdot 10^7$ cm/s = $0.63 \cdot v_s$

We see that even for 10 V the saturation velocity is not yet reached. The results we presented (increase in demodulation contrast for increased PGL / PGR voltage) are reasonable because an increase in electrical field still causes an increased drift velocity and hence faster response of charge carriers to the electrical field, leading to a better demodulation contrast at high modulation frequencies.

5.2.4 Influence of optical power and integration time @ 20MHz

We discussed in **Section 3.2** that the charge transfer efficiency of CCDs strongly depends on the number of charge carriers that are contained in the charge packet to transport (c.f. **Figure 3.20**). Therefore we expect the optical power, i.e. how many photoelectrons are generated (and hence have to be transported) per unit time, to have a noticeable influence on the demodulation contrast. This is investigated in the current section.

In order to measure the influence of the number of generated photoelectrons per unit time on the contrast, two parameters are changed: (1) the optical power and (2) the integration times. For a good reproducibility of the measurements we keep the output power of the LED constant and use neutral density filters (ND) to attenuate the power on the pixel. This has the advantage that the LED can be operated with the same mean current (50 mA) for all measurements. (Because of a current-dependent operating temperature, the LED changes its dynamic characteristics for different control currents). For each integration time we chose a different spot size (by adjusting the distance of the microscope's objective to the sensor chip), the exact parameters are summarized in **MCD05** in the appendix.

We carry out measurements of the demodulation contrast for 4 different optical power conditions (1) without ND filter, (2) with 27% ND filter (3) with 8% ND filter and (4) with both intensity filters (2% attenuation). Since the total optical power and the size of the light spot are measured, we can recalculate the optical power on the light sensitive area of each pixel. The dark current is measured separately and subtracted from the measured values before calculating the demodulation contrast. These measurements have only been performed for the surface-channel realization (SCCD); the results are shown in **Figure 5.19** and **Figure 5.20**.

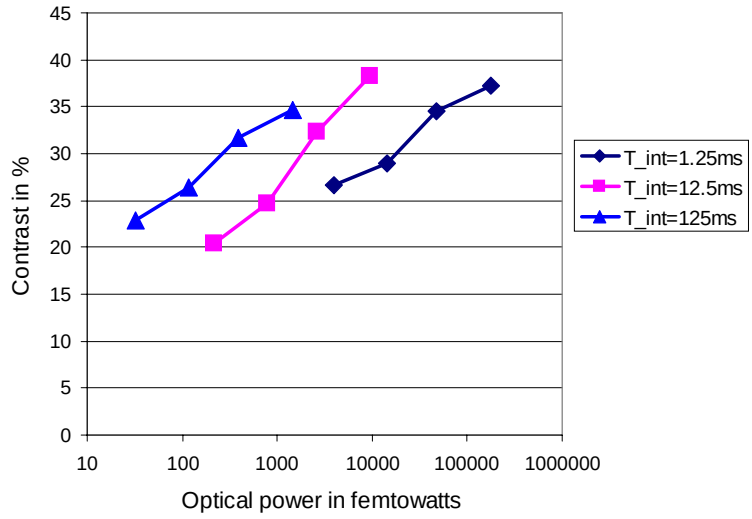

Figure 5.19 *Demodulation contrast versus optical power per pixel for different integration times (f_{mod}=20 MHz). [MCD05].*

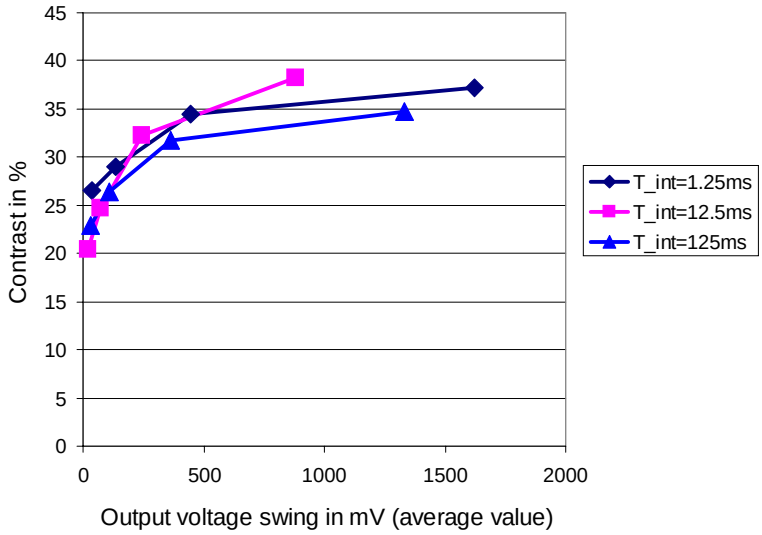

Figure 5.20 *Demodulation contrast versus total number of integrated electrons (output voltage swing) for different integration times (f_{mod}=20 MHz). (Same data as for Figure 5.19). [MCD05].*

We see that the demodulation contrast does not depend on the optical power but only on the energy in each pixel (product of power and integration time). Assuming a reasonable integration time (optically generated signal must dominate the dark current signal), a large output voltage swing, either caused by high optical input power or by a long integration time, leads to a good demodulation contrast.

This is only possible, since the CCD-performance of adding and storing signals in the charge domain is nearly noise-free. Normally, one would expect a lower optical power to lead to a worse demodulation contrast, since we know, from CTE measurements of CCDs that are realized in the same technology, that the CTE is better, the more charge is to be transported (c.f. **Figure 3.20**). This is because all three transport mechanisms (self-induced drift, diffusion and fringing fields) contribute to the charge transport. Self-induced drift strongly depends on the number of integrated electrons, because a smaller number of electrons leads to a reduced influence of self-induced drift on the overall charge transfer.

For 20 MHz modulation, the short-time integration lasts only 25 ns (50 ns modulation period). In this period, only few electrons are generated and transported to the integration gate. In fact, as one can see from **MCD05**, for 175,000 femtowatts, the highest optical power used, only 18 electrons are generated within 50ns, statistically speaking, i.e. only 9 electrons within the active sampling time. For the lowest optical power used the conditions are much worse: one electron is generated, statistically speaking, only every 300^{th} modulation period. From these numbers, we understand that, under the above conditions, self-induced drift can have no influence at all on the charge transfer. We really move single electrons. Demodulation only works here with the help of statistics. This enormous performance is a big welcome surprise.

In addition to the total optical power on one photogate, the average resulting output voltage swing is also listed in MCD05. This can be calculated with known quantum efficiency, wavelength, integration time, conversion capacitance and amplification of the output stage. Also the total number of electrons generated during the integration time is listed, as well as the number of electrons statistically generated during only one modulation period. Since these values are smaller than one, it is more meaningful to list the inverse value, which is the number of modulation cycles that have to pass until one electron is optically generated by the modulated light source, statistically speaking.

5.2.5 Demodulation contrast versus frequency and wavelength

The application areas of the TOF- range cameras are essentially restricted by two important parameters: the required range resolution and the wavelength of the light used. While almost all range measurement applications demand the best possible range resolution, which requires a good demodulation bandwidth of the pixels, some applications additionally require the use of near infrared light (invisible for the human eye).

In this section we present the measurements of demodulation contrast for different modulation frequencies and wavelengths of the light source. As light sources, we use different kinds of LEDs. They all have a characteristic response time and dynamic behavior. We operate them with the MICROCHOP module MV-LED1 [CS1], a fast LED driver module for the microbench. **Figure 5.21** shows the measured modulated output signal of all the LEDs that we use.

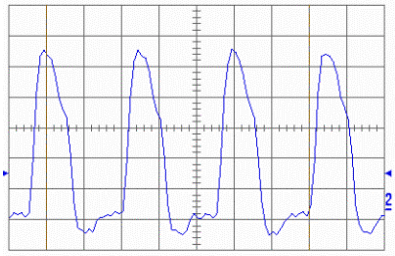

470 nm-LED signal @ 20 MHz
(20 ns/div)

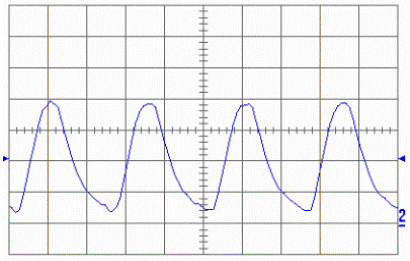

740 nm-LED signal @ 20 MHz
(20 ns/div)

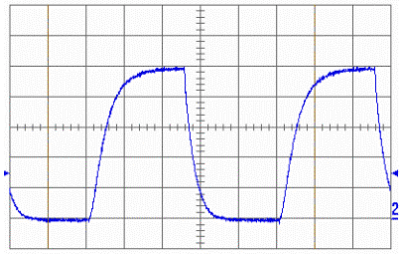

850 nm-LED signal @ 200 kHz
(1 µs/div)

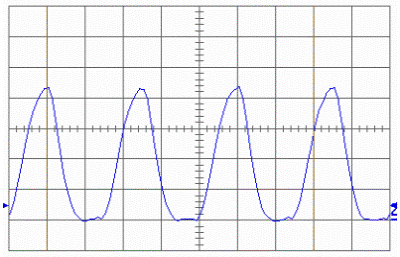

630 nm-LED signal @ 20 MHz
(20 ns/div)

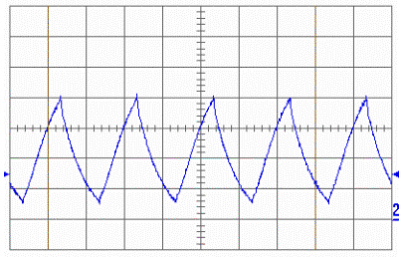

850 nm-LED signal @ 1 MHz
(0.5 µs/div)

Figure 5.21 *Signal shape of the used LEDs for different modulation frequencies. (Measured with FEMTO 500 MHz photodiode module [FEM] PR-X-500M-SI-DC).*

The 850 nm LED can obviously only be used up to 1 MHz, since its characteristic 20% / 80%-rise time of about 500 ns does not allow faster modulation. The output

signal of the 850 nm LED for 1 MHz is more saw-tooth shaped rather than a square wave. This also lowers the demodulation contrast. The real demodulation performance of the pixel for 850 nm light at frequencies higher than 200 kHz is therefore better than we can show with this slow LED.

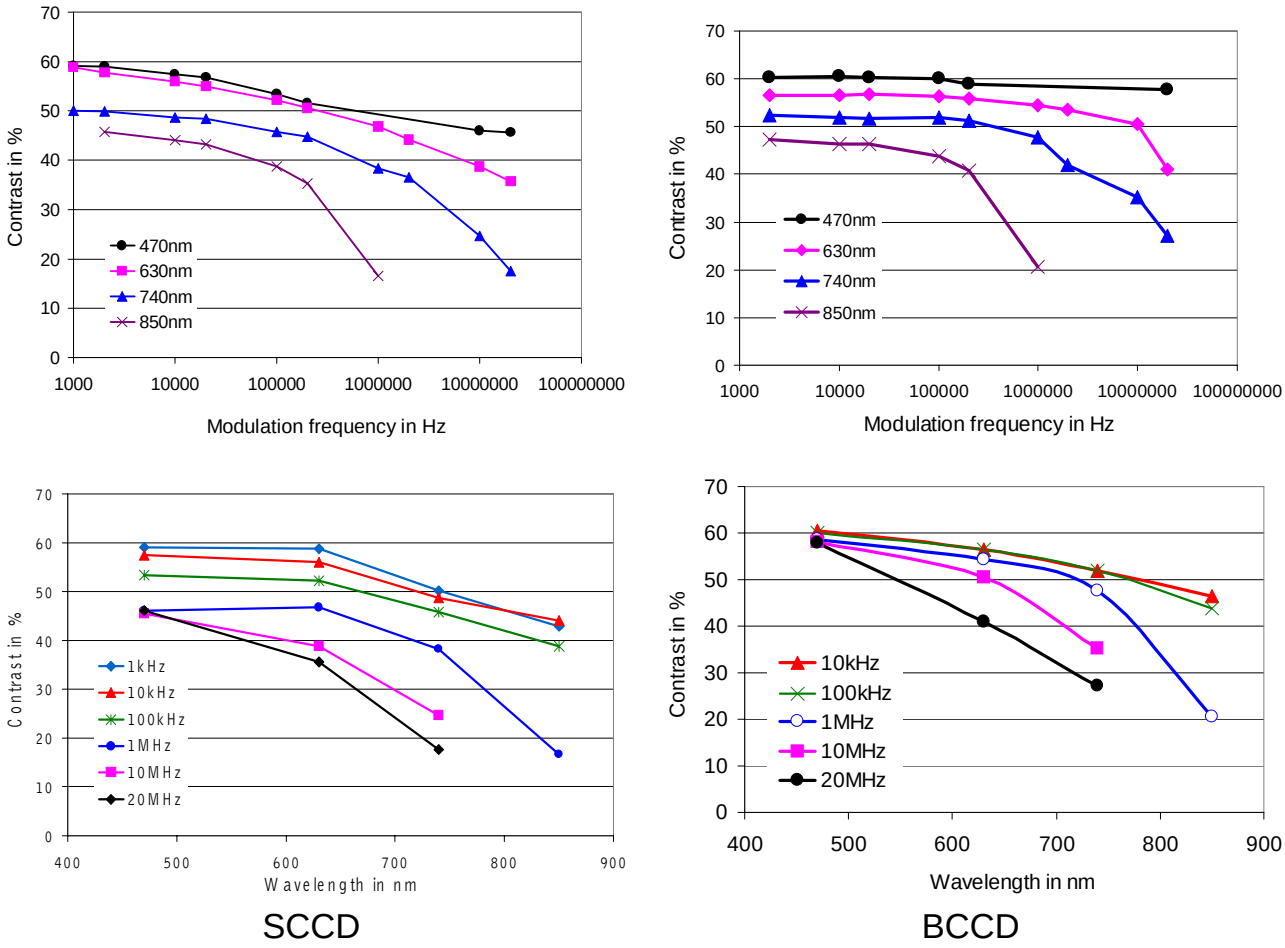

SCCD BCCD

Figure 5.22 *Demodulation contrast vs. modulation frequency and wavelength. Note that the optical output signal for 850 nm and 1 MHz is saw tooth shaped rather than a square wave. We obtain a better performance for faster NIR light sources. [MCD06S; MCD06B].*

The optical power for the 630 nm measurement at 20 MHz is 900 femtowatts per pixel. The power is measured only for the red LED. All other LEDs are operated with the same current and the optical power on each photogate is adjusted such that the output amplitude of the sensor is similar for all measurements. (This can be achieved by different sizes of the LED spot). This means that, independently from the quantum efficiency at the specific wavelength, the power is chosen such that nearly the same number of electrons is generated per unit time. The absolute

optical power, used for the other wavelengths (470 nm, 740 nm, and 850 nm), can be recalculated from the ratio of the measured mean values of the sampling and the quantum efficiency of the specific wavelength, which is known. The measurement results are summarized in **Figure 5.22**. With another infrared LED, emitting at 810 nm (manufacturer: EPIGAP), we obtain a demodulation contrast of better than 25% at 20 MHz.

The measurements show the expected contrast decrease for high frequencies and longer wavelengths (c.f. **Section 5.2.2**). Especially for high frequencies, the BCCD performance is superior to that of the SCCD. For 20 MHz modulation and 630 nm wavelength we still achieve a modulation contrast of better than 40% with the BCCD version, which is still quite good compared to the DC performance of about 60%. Furthermore, we can state that the simple model described in **Figure 5.14** and **Figure 5.15** makes an astonishingly good performance prediction for the DC case.

5.2.6 Phase accuracy measurements

In the previous sections, we presented measurements of the 1-tap pixel's demodulation contrast versus several parameters for the BCCD and the SCCD realization of the 1-tap pixel. In the following we will only consider the BCCD version. In fact, however, we are interested in the time or phase resolution offered by the demodulation pixels. For a real distance measurement, the received optical power varies with the distance of the target. It is therefore not practical to characterize the time resolution with a distance measurement setup, because at the same time the time delay (distance) changes; also the received power would change. With such a setup one cannot measure the time resolution isolated from the received power.

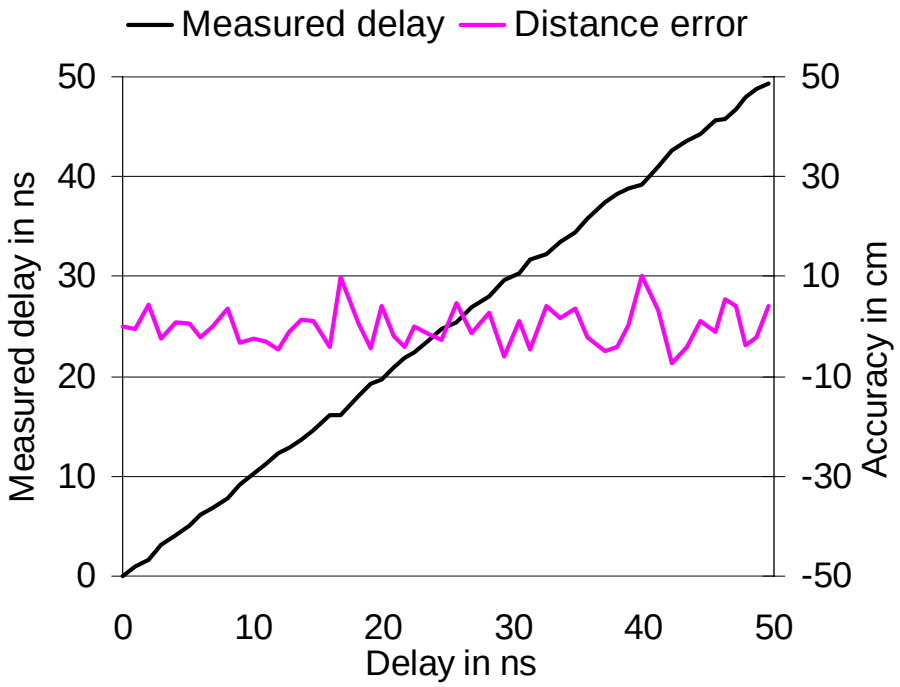

Figure 5.23 *Phase delay for 736 fW optical power on one pixel (time error: 260 ps rms → distance accuracy: 3.84 cm rms). [MCD07].*

For this reason we use the setup described in Section 5.2.2 for the phase accuracy measurements presented below. With an analog delay line (EG&G-ORTEC 425A) we can delay the optical 20 MHz modulated signal in steps of nanoseconds. This allows different delays of the same light power to be measured with the demodulation pixels. As an example, one measurement is shown in **Figure 5.23**. The time error is converted into an equivalent distance error in this figure (50 ns=7.5 m, 500 ps=7.5 cm). For the optical power of 736 fW per pixel, we get an accuracy of 260 picoseconds.

By attenuating the LED light (with ND-filters) the optical input power can be varied. For higher optical power, the distance accuracy increases and for lower power it decreases. This gives the possibility of measuring the range accuracy (or time resolution) versus the optical power received in each pixel. The results of these measurements are shown in **Table 5.3** and in **Figure 5.24**. All measurements have been performed (1) without averaging and (2) with an average over 16 runs.

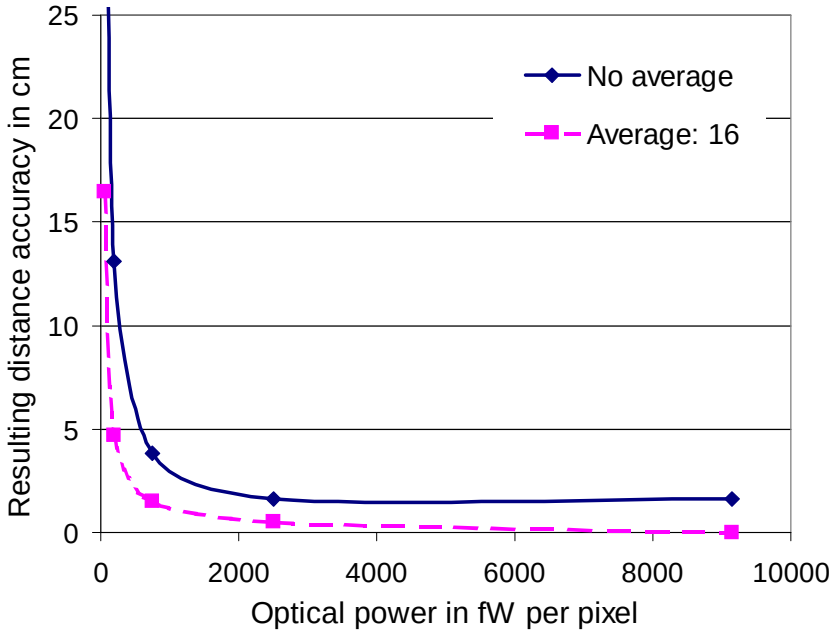

Figure 5.24 *Measured distance accuracy versus the received optical power per pixel.*

Table 5.3 transforms the optical power per pixel into the equivalent number of electrons integrated totally and integrated per modulation period. We see that we still get a distance resolution of 4 cm if only one electron is generated, statistically speaking, every 13th modulation period. Since the sampling interval is only half the modulation period, this means that one electron will be integrated to the sampling point only every 26th modulation period for this range resolution. For generation of a photoelectron every 4th modulation cycle, the range accuracy is 1.6 cm, i.e. a time resolution of 100 picoseconds or a phase resolution of 0.75 degrees. In [SP4] a phase resolution of 0.9 degrees has been reported for an 8-tap demodulation pixel operated at 8kHz modulation frequency, i.e. more than 3 orders of magnitude slower.

In **Section 5.2.8** we compare these measured results with the theory introduced in **Section 4.2**.

modulation frequency: 20 MHz				Frame rate: 20 Hz = 1/(4·12.5 ms)		
Integration time per tap: 12.5 ms						
Filter transmit.	Optical power in fW	Average output voltage swing in mV	Total #electrons in T_{int}	#electr. in T_{mod}	#mod. periods for gen. of 1 electron	STD of distance error in cm
No averaging						
100%	9150 fW	941 mV	235200	0.94	1.1	1.6 cm
27%	2500 fW	258 mV	64400	0.26	3.8	1.6 cm
8%	750 fW	77 mV	19300	0.077	13	3.8 cm
2%	200 fW	20 mV	5100	0.02	50	13 cm
0.55%	50 fW	5.2 mV	1300	0.0051	200	55 cm
Average: 16 runs						
100%	9150 fW	941 mV	235200	0.94	1.1	0.0 cm
27%	2500 fW	258 mV	64400	0.26	3.8	0.5 cm
8%	750 fW	77 mV	19300	0.077	13	1.5 cm
2%	200 fW	20 mV	5100	0.02	50	4.7 cm
0.55%	50 fW	5.2 mV	1300	0.0051	200	16.5 cm

Table 5.3 *Distance accuracy vs. received optical power, total number of integrated electrons and number of integrated electrons per modulation cycle.*

5.2.7 Noise performance and dynamic range

In this section, we present the measurements of the noise floor, dark noise, “bright noise”, fixed pattern noise and also the resulting dynamic range D/R and signal-to-noise ratio SNR. The noise floor is measured in the dark without previous signal integration (no integration time). It includes thermal noise, reset noise, 1/f-noise and the additional noise of all amplifiers in the acquisition path. Dark noise is measured in the dark with a certain integration time, it therefore includes the noise of the dark current. “Bright noise” is measured with integrated light; it includes photon shot noise and dark current noise. The *dynamic range D/R* is the ratio of maximum voltage swing to the floor noise; the *signal-to-noise ratio SNR* is the ratio of maximum voltage swing to the “bright noise”.

Signal-to-noise ratio SNR:

$$SNR = 20 \cdot \log\left(\frac{\text{voltage swing in V}}{\text{rms noise of voltage swing in V}} \right)$$ **Equation 5.3**

Dynamic range D/R:

$$D/R = 20 \cdot \log\left(\frac{\text{maximum voltage swing in V}}{\text{floor noise in V}} \right)$$ **Equation 5.4**

Table 5.4 summarizes the measured noise performance, SNR and D/R of the BCCD realization of the demodulation pixel. The additional noise of the analog electronics of the camera board and the frame grabber is only 54 µV rms and can be neglected.

Fixed pattern noise:	38 mV
Noise floor:	0.60 mV
Dark noise (12.5 ms):	0.63 mV=**175 electrons**
Bright noise (12.5 ms, 9000 fW):	3 mV
Voltage swing (9000 fW):	1100 mV
Maximum voltage swing:	3000 mV
Signal-to-noise ratio SNR:	**50 dB**
Dynamic range D/R:	**73 dB**

Table 5.4 *Noise performance of buried channel 1-tap demodulation pixel. Integration time for the bright noise measurement: 12.5 ms.*

5.2.8 Comparison of measured distance accuracy with theory

With the knowledge of the dark noise, we can now estimate the range accuracy of the demodulation pixels by means of **Equation 4.16**. The demodulation contrast at 20 MHz is C_{demod}=40%, the modulation depth of the LEDs about C_{mod}=100%. The dark noise of 0.63 mV and 175 noise-equivalent electrons results in a number of N_{pseudo}=30,000 pseudo electrons. The measurements have been performed under the microscope without additional background illumination. The results are illustrated in **Figure 5.25**.

#Pseudo background electrons (floor noise):	*30'000*
Modulation depth of the LEDs C_{mod}:	*1*
Demodulation contrast C_{demod}:	*0.4*
"L" (Non-ambiguity distance range):	*750cm*

Optical mean power in fW:	*9150*	*2500*	*750*	*200*	*50*
Resulting #photoelectrons PE_{opt}:	*235000*	*64000*	*19000*	*5100*	*1300*
Sigma in cm (theory):	***0.7***	***1.6***	***3.9***	***12.2***	***45.1***
Sigma in cm (measured):	***1.6***	***1.6***	***3.8***	***13.1***	***55.3***

These results are also plotted in the following graph and referenced in **Section 5.2.6**.

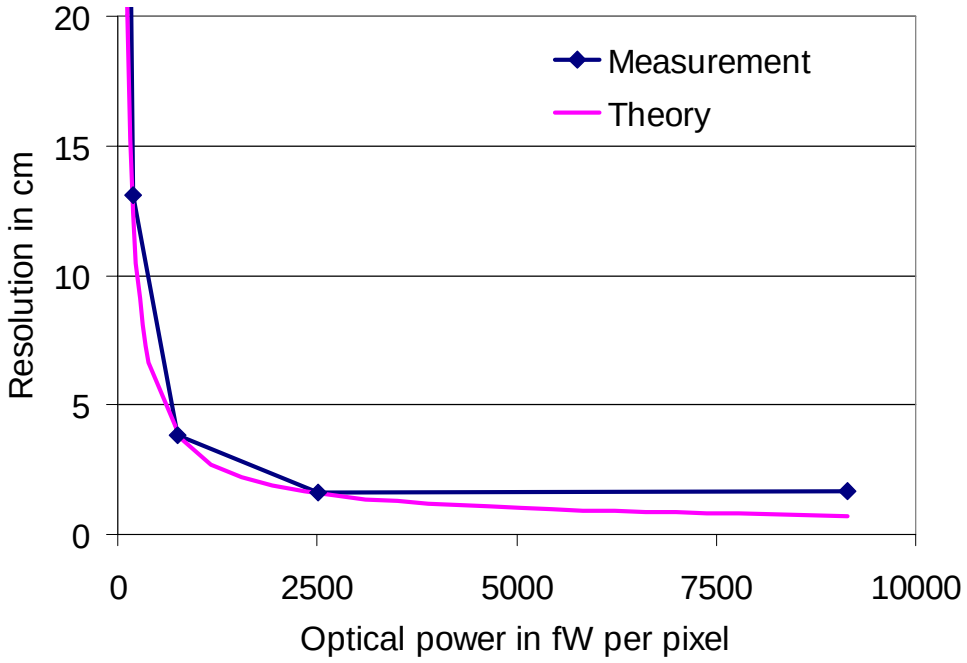

Figure 5.25 *Estimated and measured distance resolution versus received optical power per pixel. (Integration time: 12.5 ms per sampling point, total 50 ms.)*

This excellent fit between measurement and theory confirms the validity of **Equation 4.16**, which gives us the possibility to predict the range accuracy for given measurement conditions.

5.2.9 Summary

The demodulation contrast depends on several parameters: amplitude of gate voltages, demodulation frequency, received optical power density and wavelength of modulated light. Since the CCD shutter mechanism used never has 100% efficiency, even under DC conditions, the demodulation contrast is never better than about 60%.

The contrast decreases with higher modulation frequencies, since the photoelectrons do not have enough time to reach the storage site (dump site respectively). The gate voltages PGL and PGR should be chosen to be as high as possible. This is in order to generate high electrical fields in the semiconductor. Even for a voltage difference of 10 V between two adjacent photogates, the saturation velocity of electrons is not yet reached. Therefore, the experimentally measured optimum gate voltages of about 8 V are reasonable: an increase in electrical field still causes an increased drift velocity and hence faster response of charge carriers to the electrical field. For modulation voltages higher than 8 V the maximum signal that can be handled decreases, since the charge handling capability of the pixel is essentially influenced by the potential difference between the modulation gate PGL and the integration gate IG (10.7 V).

Furthermore, the demodulation contrast decreases with increasing wavelength. This is because the light penetrates deeper into the semiconductor before photoelectrons are generated. These photoelectrons then need more time to reach the depletion region, where they are separated to the dump- or integration site, depending on their arrival. Also photoelectrons generated far from the surface diffuse in random directions, so that they are equally likely to travel directly to the integration or dump site, independently of the actual biasing conditions of the modulated photogates PGL and PGR.

For the BCCD realization of the 1-tap demodulation pixel we have measured a contrast of 40% using 20 MHz (more or less) sinusoidally modulated light of 630 nm wavelength. The SCCD performance is only slightly worse, so that the availability of a buried channel process option is not necessarily needed. For lower modulation frequencies and blue light the contrast is better than 60%, quite close to the prediction of the simple model introduced in **Figure 5.14**. The contrast decrease towards higher modulation frequencies can at least partly be attributed to the more

sinusoidal rather than square shaped modulation signal. This also explains the less significant contrast decrease for the faster blue LED at high modulation frequencies (c.f. **Figure 5.21** and **Figure 5.22**).

With our measurements we could prove the validity of the theoretical range accuracy predictions presented in **Chapter 4**. The actual surprise of the measurements is that demodulation still works excellently if single electrons appear only every 10^{th} (3 cm range resolution) or even 50^{th} (13 cm range resolution) modulation cycle (50 ns), assuming an integration time of 50 ms. This astonishingly low optical generation rate of photoelectrons corresponds to a photocurrent of only 320 fA (1 electron in 10·50 ns) or even only 64 fA, respectively (1 electron in 50·50 ns).

5.3 Outlook: Two-photosite demodulation pixel

The 1-tap pixel, introduced and characterized in the previous sections, suffers from one major drawback compared to pixel realizations with more storage sites: Since only one storage site is available per pixel, the sampling points have to be acquired sequentially rather than in parallel and therefore the pixel has problems in measuring fast changing scenes that require long integration times. In such scenes, each of the sequentially acquired sampling points per pixel could possibly belong to another region of the scene, assuming that the scene has changed (moved) between the acquisition of the sampling points.

This problem can be overcome by a slightly modified pixel structure, the *two-photosite demodulation pixel*, which we suggest in this section for a future realization. The following things are changed with respect to the 1-tap device:

(1) Since we use an integration time of half the modulation period, the photoelectrons that are dumped during integration of a sampling point directly correspond to the 180° delayed sampling point. Instead of draining this charge to a dump diffusion it will now be integrated in a second storage site within the pixel.

(2) The two-photosite demodulation pixel will consist of two equal structures according to the description under (1), which are operated in quadrature. In this way the first site acquires the sampling points A_0 and A_2 (phase 0° and 180° respectively) and the second site acquires the sampling points A_1 and A_3 (phase 90° and 270°), so that all sampling points are acquired in parallel.

(3) In order to achieve this, both photosites within the pixel are illuminated with the same optical scene information. A special microlens array is suggested, which (a) makes an optical averaging of the complete optical information imaged to one pixel and (b) focuses the spatially averaged pixel information in equal proportions to both light sensitive photosites. In addition to the generation of two optically identical photosites, such a microlens structure can increase the optical fill factor up to 100%, a factor of 2 compared to the realization without microlens array, and even a factor of 5 compared to our current 1-tap pixel realization. The microlens structure is relatively simple to realize and mount, since the chip structure only varies in one dimension.

When we implemented the 1-tap pixel realization, we considered implementing at least point (1) (2-tap instead of 1-tap pixel), since it is obvious that the photocharge that we currently dump with the 1-tap pixel corresponds exactly to the 180° shifted sampling point. However, we preferred at that early time to implement the easiest demodulation pixel in order to get a reliable demonstrator, rather than running the risk of receiving non-functional devices from the foundry by trying to implement too much functionality at a time.

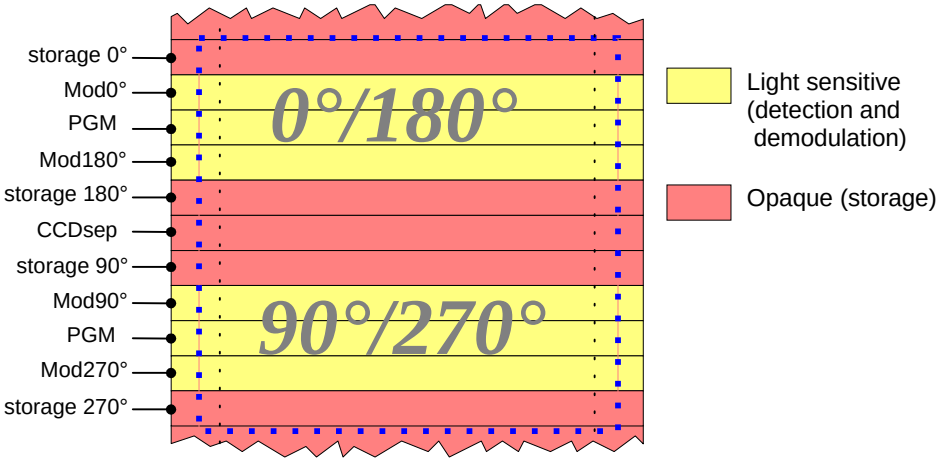

Figure 5.26 *Two-photosite demodulation pixel: basic architecture.*

The basic structure of the new pixel is illustrated in **Figure 5.26**. The pixel consists of two light sensitive areas. Each of these areas is divided into two or three light sensitive modulation gates (here a 3-gate realization is shown). During demodulation/integration operation, the middle gate (if present) is kept at a fixed potential and the outer modulation gates are modulated in a balanced manner. Optically generated charge carriers are then distributed to the neighboring storage gates, depending on the actual potential gradient under the modulation gates. The storage gates are isolated from each other by an additional transportation gate. The two modulation-gate-pairs within one pixel are operated with a relative phase difference of 90°, so that the one pair integrates the in-phase component (1st and 3rd sampling point) and the other pair integrates the quadrature-phase component (2nd and 4th sampling point respectively). Each gate within the pixel can be controlled individually.

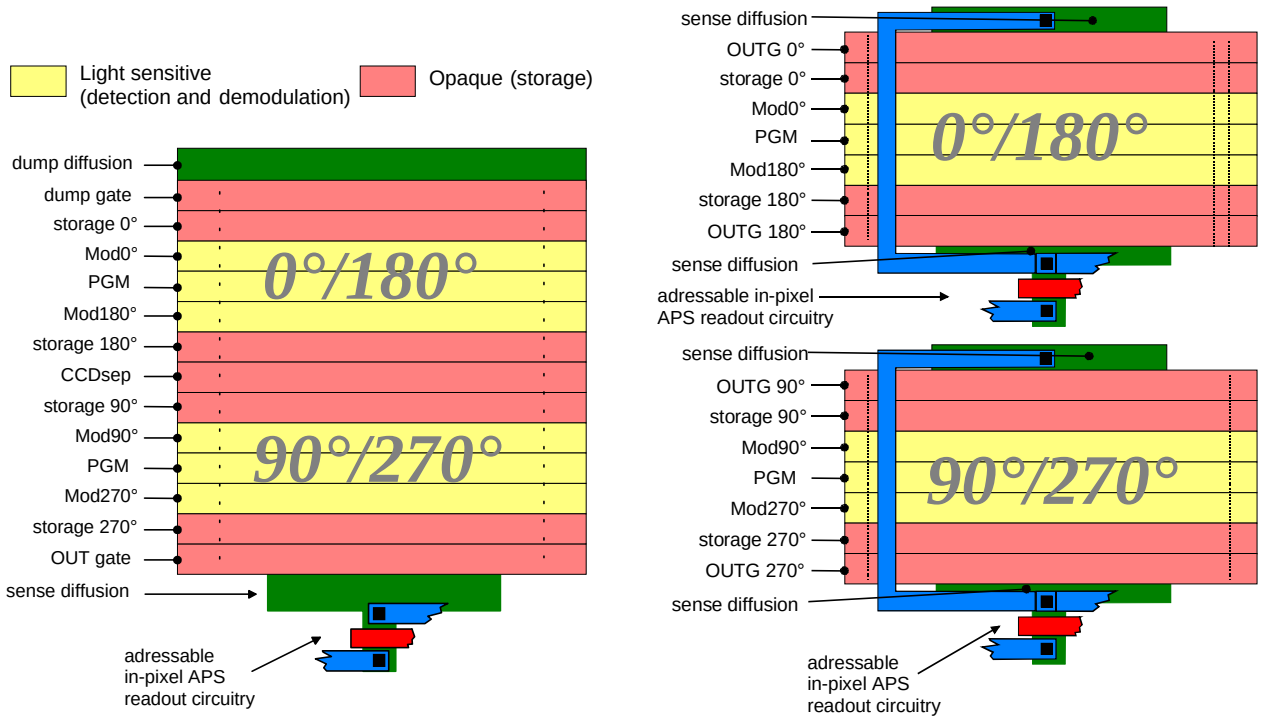

Figure 5.27 *Realization of the two-photosite pixel (a) with one and (b) with two readout stages per pixel.*

Figure 5.27 shows two possible realizations, with either one readout stage for all four sampling points or with two readout stages per pixel. For (b) two diffusions are short-circuited to one sense diffusion node, which can be accessed from two sides. This enables the readout of two sampling points per readout stage without moving the sampled values through the light sensitive CCD gates. The drawback that the sense diffusion will have a larger capacitance (less than a factor two) and hence a worse conversion factor (voltage increase per electron) can be tolerated. It is important to mention that fixed-pattern noise due to the use of two readout stages per pixel is not a problem. This is because the balanced-mode sampling points are subtracted from each other in the phase algorithm (c.f. **Equation 2.17**). Fixed pattern noise mainly adds an offset component to the pixel values. This offset disappears after the subtraction, leading to pair-wise offset-free charge integration.

Due to the highly parallel, simple architecture, optical microstructures can be easily realized, produced and assembled, fulfilling the task of averaging the received light on each pixel and equally distributing the averaged light onto the *two* light sensitive areas. This results in two optically identical photo sites per pixel and makes it

insensitive to edges or, generally speaking, to any spatial inhomogeniety imaged on one pixel. Such an optical structure is sketched in **Figure 5.28**.

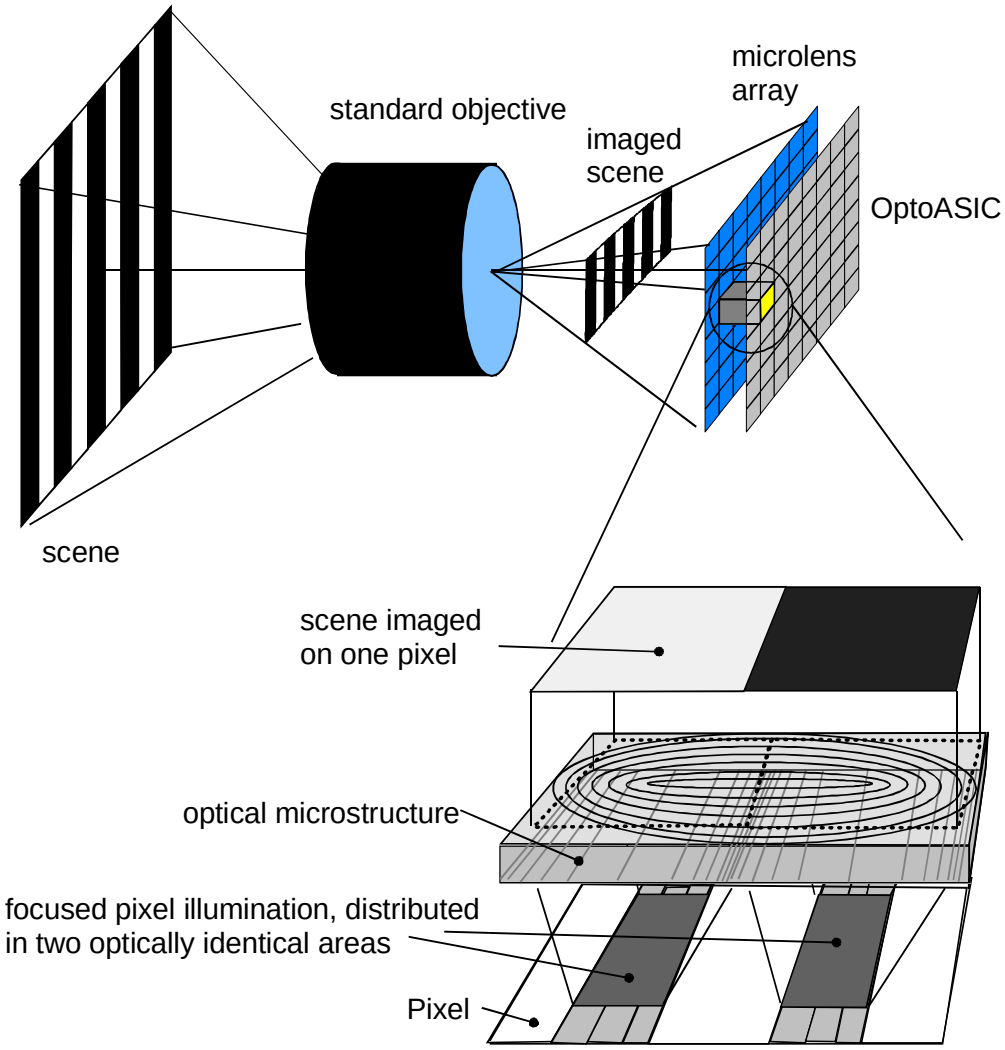

Figure 5.28 *Microlens structure.*

Like the 4-tap lock-in pixel (**Section 5.1.2**), the two-photosite demodulation pixel also contains four storage sites. But rather than accessing only one photosite from four sides, which leads to unsymmetrical sampling point sensitivity due to process inaccuracies, with this new pixel, two optically identical photosites are accessed from only two opposite sides. This two-side access is far less sensitive to process variations than the access from 4 sides. Also the photo site can be easily divided into several gates to accelerate photoelectrons and to achieve an efficient charge transfer.

6. Imaging TOF range cameras

Now we introduce the time-of-flight range cameras that we realized with our 1-Tap lock-in pixel arrays. As mentioned before, we have implemented the demodulation pixel as a line sensor, carrying 108 pixels and, in a second fabrication run, as a TOF-imager with 64 by 25 pixels. With these sensors we realized both a 2D TOF line camera and a 3D TOF imager. Both range cameras are controlled by a fast, flexible and compact digital sequencer. The sensor chip itself is plugged into a specially designed driver board, also a very flexible realization that allows the connection of nine DC levels and 24 AC signals (generated by the sequencer) of variable amplitude, variable rise and fall time and variable pulse width to any of the sensor's pins. The architectural setup of these camera PCBs is roughly described below. Also we introduce the LEDs that we use for the modulated light source as well as the corresponding driving electronics.

In the second and third section of this chapter we then present both range camera realizations, which mainly differ in the LED arrangement of the illumination unit, the demodulation detector itself and the control-firmware loaded into the sequencer. Each of these sections starts with an overview of the sensor architecture, then describes the overall camera system architecture and finally introduces typical range measurements of non-cooperative scenes that we performed with the cameras.

6.1 Camera electronics

6.1.1 Digital sequencer board

The task of the digital sequence unit is to generate bit patterns that control both the TOF-sensor chip and the modulated illumination unit. Since no delay lines are used, the four phase relations between sensor timing and illumination timing (0°, 90°, 180°, 270° and 1st to 4th sampling point respectively), have to be generated digitally. For our targeted modulation frequency of 20 MHz we therefore need flexible digital circuitry that can be operated at 80 MHz and beyond.

One possible solution is the realization of a RAM-based sequencer, where a complete bit-pattern is loaded into a memory, which is then repeatedly read out at 80 MHz frequency (T_{bit}=12.5 ns). Assuming a 5 Hz frame rate (T_{frame}=200 ms), however, a memory size of 2 megabytes per digital channel (200 ms/12.5 ns =16,000,000 bit) would be necessary, i.e. 48 megabytes for 24 channels (@ 80 MHz and 200 ms frames). Such a RAM-based sequencer solution is surely possible but appears rather overkill for the required task. Also the generation and download of 48-megabyte bit patterns into the RAM would be time consuming and complicated.

A closer look at the required timing shows that the necessary bit patterns actually contain far less information than 48 MB. The reason why such a large memory would be necessary is the quickly alternating modulation signal of 20 MHz frequency at four different phase relations. All other signals, such as those for addressing, reset, readout and frame synchronization of the external A/D converter, are slower (<1 MHz).

Our solution takes this into account. We use a PIC microcontroller clocked at 10 MHz for the overall system timing and generation of addressing, readout and synchronization signals. Only during the demodulating signal acquisition is a faster CPLD circuit (Lattice 1032E @ 80 MHz) activated by the microcontroller. When activated, the CPLD takes control of the modulation signals applied to the light source and the TOF-sensor. Both devices, the microcontroller and the CPLD, can be programmed electrically. This allows easy adaptation of the sequencer board to

control both the lock-in line sensor and the lock-in imager by programming different firmware . Photographs of the digital high-speed sequencer are in **Figure 6.1**.

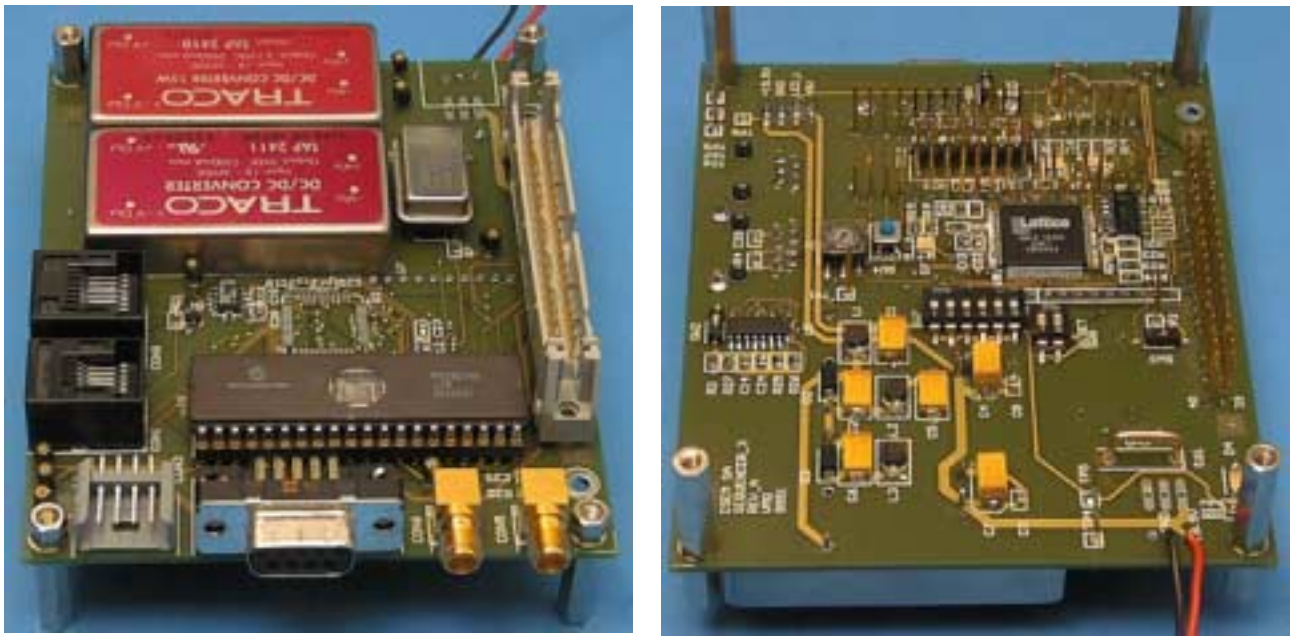

Figure 6.1 *Digital high-speed sequencer. Left: top-view with microcontroller and 40 PIN connector to driver board; right: bottom view with CPLD and freely programmable control switches. (Size: 90 mm x 110 mm).*

In addition, the sequencer board contains two DC/DC converters that generate the DC voltages 5 V and 8 to be supplied to the LED-drivers and the sensor drivers. All 24 digital channels and the DC voltages are available at a 40 Pin plug, the connection to the driving electronics board.

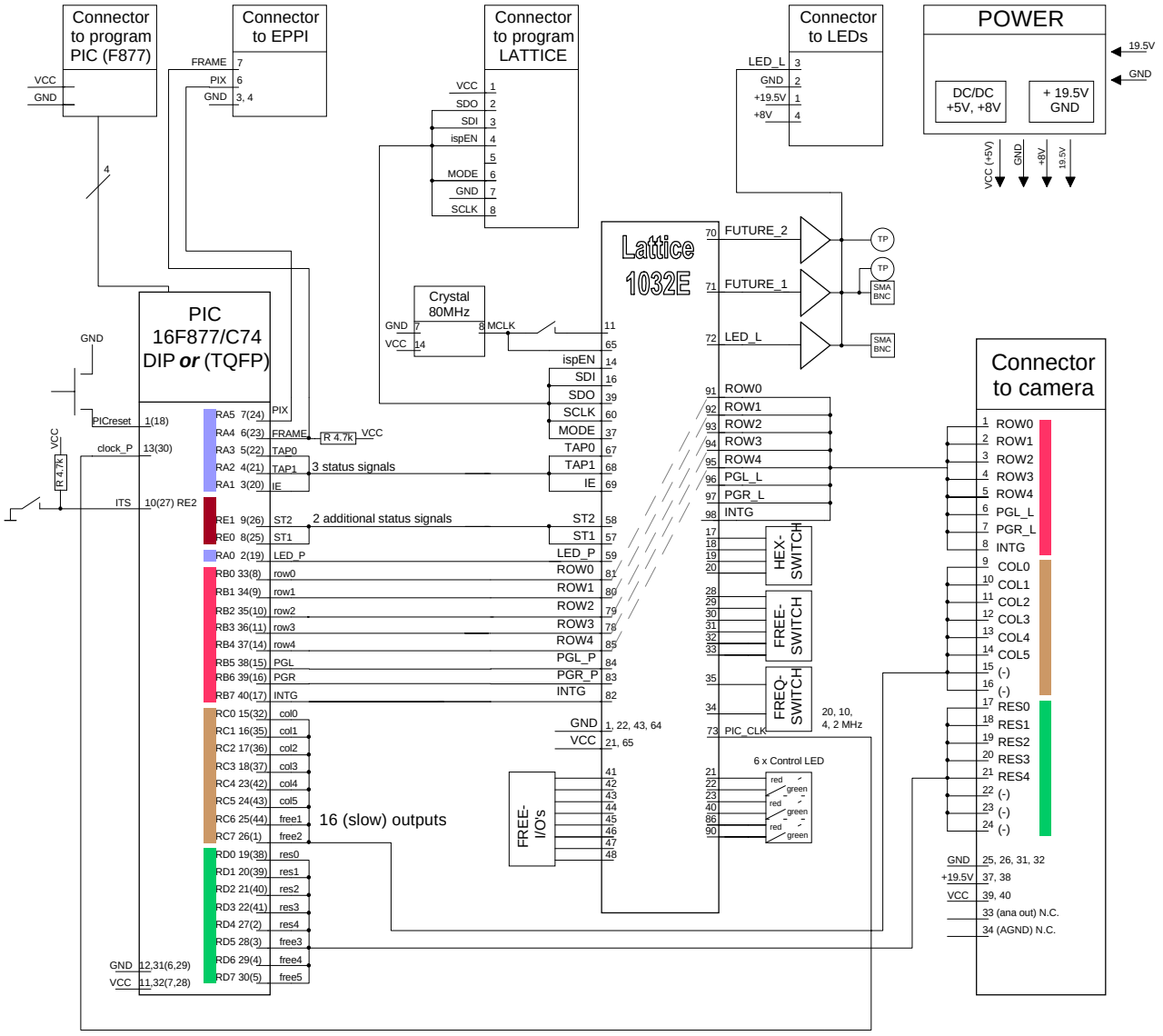

Figure 6.2 *Digital high-speed sequencer: Block diagram.*

In **Figure 6.2** we show the block diagram of the sequencer board. With several freely programmable control switches for both the CPLD and the microcontroller, the board offers flexible adaptation to different needs. For example, it can be programmed in such a way that the integration time or the readout speed for the single pixels can be changed during operation by different switches. Other variations are possible. A total number of eight (+1 for the LED control) fast control signals (80 MHz) can be generated by the CPLD (or simply fed through the CPLD if the microcontroller should take control). Additionally, the operation mode of the CPLD can be controlled by the microcontroller via five separate status lines.

6.1.2 Driving electronics board

We already discussed in **Chapter 3** and **Chapter 5** the need for relatively large voltages for the operation of CCDs. To summarize, the reasons are (1) good charge handling capability, (2) higher charge transfer efficiency and thus higher bandwidth due to increased fringing fields and, for surface channel CCDs, (3) deeper depletion region and hence larger capture volume. For the demodulation pixels, however, not only has the voltage to be high in amplitude (up to 10 V) but also the CCD gates (modulation gates, PGL and PGR to keep the definitions of Chapter 5) have to be charged and discharged sufficiently quickly.

Assuming a demodulation frequency of 20 MHz (50 ns modulation period) we want to achieve a rise-time of 5 ns to charge the modulation gates. With a typical capacitance of about 100 fF (to be more precise, modulation gates of the lock-in line sensor: 70 fF and those of the lock in imager: 90 fF) and a demanded voltage amplitude of 10 V, we estimate a charge of $Q=C \cdot V=1$ pC to be generated at each modulation gate. For our lock-in imager with 64 x 25 pixels (resulting in 160 pF load), this results in 1.6 nC to be generated within 5 ns, requiring a driver current of 320 mA. This appears not to be a problem but, for an array of 64 x 64 pixels, one already requires 820 mA driver current and for 128 x 128 pixels even 3.3 Amperes would be necessary. Since the driving electronics should be flexible and also suited to the operation of future generations of lock-in sensors, the gate drivers have to be realized with sufficient driving reserve.

An interesting and very powerful realization for such gate drivers is the use of 74AHCXX logic family ICs, operated beyond specification at 10 V. The 74AHC08, a quadruple 2-input positive AND in Advanced High Speed CMOS technology, has rise and fall times of less than 7 ns for 220 pF load and a voltage swing of 10 V. This enables operation up to 50 MHz. Additionally, there are special, powerful gate drivers commercially available. In our driving electronics board we are using 2 Ampere CMOS gate drivers, with specified 10 ns rise and fall times for 1000 pF load [ELA]. The driving electronics, however, does not only have to be powerful in terms of driving current but also offer a good flexibility to adjust the voltage amplitudes, pulse widths and rise/fall times. Also, the signals have to be freely connectable to each of the sensor's pins, since, in general, the prototyping PhotoASICs have different pinouts. In order to achieve this, the driver outputs are

connected to the sensor's pins by loose wires, which can be plugged very flexibly into dedicated sockets. A photograph of the driver board is shown in **Figure 6.3**.

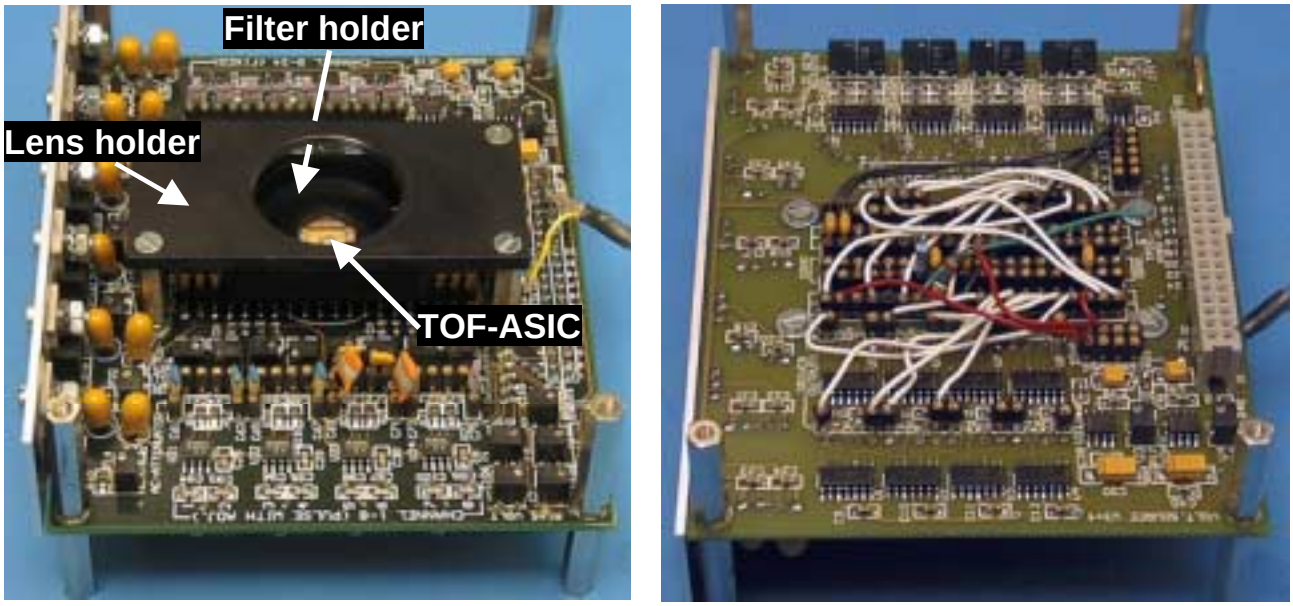

Figure 6.3 *Driver board. Left: top-view with mounted TOF-chip, filter holder on top of the sensor chip (filter not inserted), lens holder, gate drivers and shielded analog output; right: bottom view with flexible plugged wire-connections, trigger circuitry for signal recovery and 40 Pin connector to the sequencer board. (Size: 90 mm x 110 mm).*

The task of realizing adjustable signal amplitudes, rise and fall times and pulse widths is solved by the circuitry illustrated in **Figure 6.4**. First, the digital signal from the sequencer is recovered by two inverters in series (74AC14 contains a Schmitt trigger). The rise/fall time of the recovered signal is then synthetically enlarged by an RC low-pass filter and the amplitude is adjusted by the potentiometer P1. With the Schmitt-trigger in the gate driver, this circuitry allows the adjustment of the signal's pulse width within some nanoseconds. (For the operation of our 1-Tap pixel at 20 MHz we found a performance optimum for a duty cycle of 1:1.)

The gate driver is supplied by an adjustable voltage (4.5 V to 15 V) that also defines the coarse output voltage amplitude. The output amplitude adjustment with this regulation alone is not sufficient, since the gate driver requires a minimum supply voltage of 4.5 V and is not capable of generating smaller voltage amplitudes necessary for high system flexibility. The fine adjustment is achieved by an ohmic (DC) and capacitive (AC) voltage divider, also introduced in [TIE]. The slope of the signal, fed to the CCD gates, can be varied by the absolute capacitive load of the

gate drivers (CCD load plus load capacitors) on the camera board. This rise/fall time of the CCD gate signals influences the efficiency of the charge transfer (c.f. [SP4]) and the effective ON/OFF shutter ratio of the demodulation pixels.

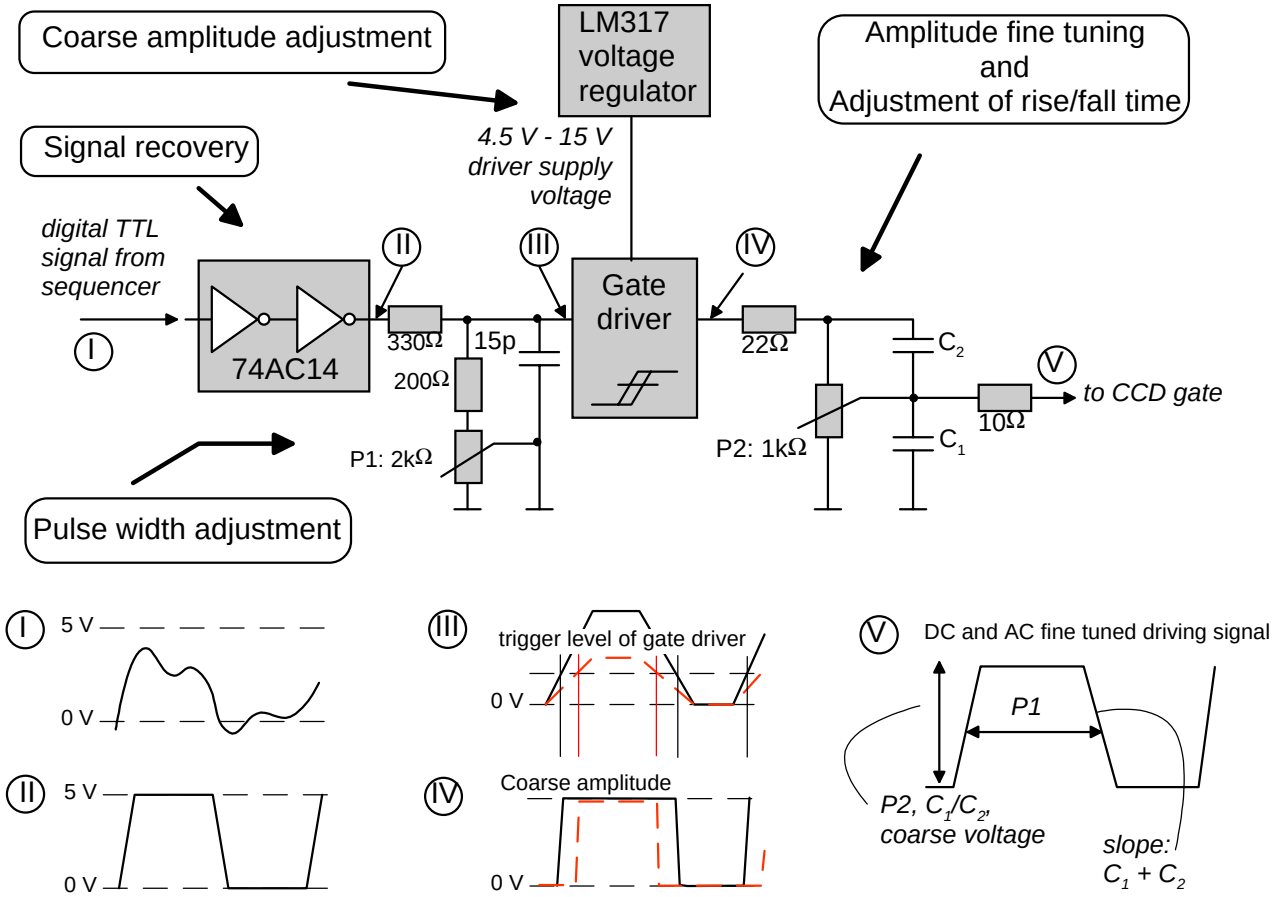

Figure 6.4 *Driver circuitry including signal recovery (I, II), pulse width adjustment (III, IV), coarse amplitude adjustment (IV) and fine amplitude tuning (V). For the fine-tuning of the signal amplitude a capacitive (AC) and ohmic (DC) voltage divider is used. The dimensions of these capacitors and resistors determine the signal slope. (RC low-pass).*

The driver board illustrated in **Figure 6.3** contains 24 separate CCD driver channels. Eight of these channels offer the above described pulse width and signal slope adjustment. The remaining 16 channels can be adjusted in amplitude by the coarse amplitude setting of the gate drivers and in signal slope by an additional capacitive load. For high flexibility, the discrete capacitors are plugged into sockets rather than being soldered (c.f. **Figure 6.3 left**). In addition, nine different DC signals can be provided to the PhotoASIC, four of which are targeted for use as

power supplies (1.25 V to 11.7 V with up to 40 mA each) and five DC channels to be used as fixed gate bias voltages (0 V to 13 V DC, 10 μA maximum).

Figure 6.3 also shows the lens holder and the holder for an interference filter (filter not mounted in the photograph). We use an EALING interference filter (42-7344) with 633 nm center-wavelength and 38 nm half-intensity-bandwidth (HBW). The mean filter transmission within the HBW is about 75 %. The interference filter is used to suppress background illumination by transmitting only the spectrum of the LED illumination used.

6.1.3 Modulated illumination

As modulated light source we use LEDs arranged in arrays (LED line for the line sensor and 2D LED-array for the TOF imager). Because of its excellent optical output power we use the Hewlett Packard (now Agilent) HPWT DH00 LEDs. They emit at a center wavelength of 630 nm with a spectral bandwidth of about 35 nm (FMHW) and a beam divergence of typically $\pm 25°$. The optical output power (specified as luminous flux) depends on the LED category. It is specified with 2.5 lumens (10 mW) for the D-category LEDs that we use for the 2D camera [HP1, HP2]. The LEDs are driven by a special current-protected and stabilized fast switching driving electronics developed at CSEM.

In the Appendix we give the equations to calculate the optical power in terms of watts from the luminous flux in terms of lumens, depending on the wavelength. The measured optical power of the LEDs we use in our illumination modules is 8.5 mW @ 50 mA for the line camera and 5 mW @ 50 mA for the 3D camera. For the 3D camera, we unfortunately only received LEDs of lower power category from our distributor.

6.2 2D range camera

We describe the line range camera in this section. This is the first non-scanning, imaging TOF range camera that is based on a customized PhotoASIC. This PhotoASIC is a line arrangement of the 1-tap pixel introduced and characterized in **Chapter 5**. Before introducing the camera setup and the first measured distance profiles, we first give a rough overview of the sensor architecture.

6.2.1 108 pixel lock-in line sensor

So far, in **Chapter 5**, we have only described the 1-tap pixel itself. Here we discuss the line array arrangement of the pixel.

Chip layout and architecture

The lock-in line sensor was fabricated in ORBIT 2.0 μm CMOS/CCD technology using the American MOSIS (http://www.mosis.com) prototyping program The chip size is 2 mm by 2 mm (TINY), which allows the realization of 108 pixels. The pixel pitch is 16 μm, limited by the minimum pitch of the address decoder (design rule limited), which is used to readout the pixel of interest. Due to its extension in the horizontal direction, the realization of the lock-in line left a lot remaining space in the vertical direction. We used this available free space to connect the light sensitive demodulation part of each pixel to a 16 stage 4-phase CCD line that is accessed by the address decoder at the bottom end. This CCD line offers additional flexibility to acquire and store several “line-images” before reading out the sensor. (For our measurements we did not make use of this feature). The architectural overview of the 108-pixel lock-in line is shown in **Figure 6.5** together with a micrograph of the sensor.

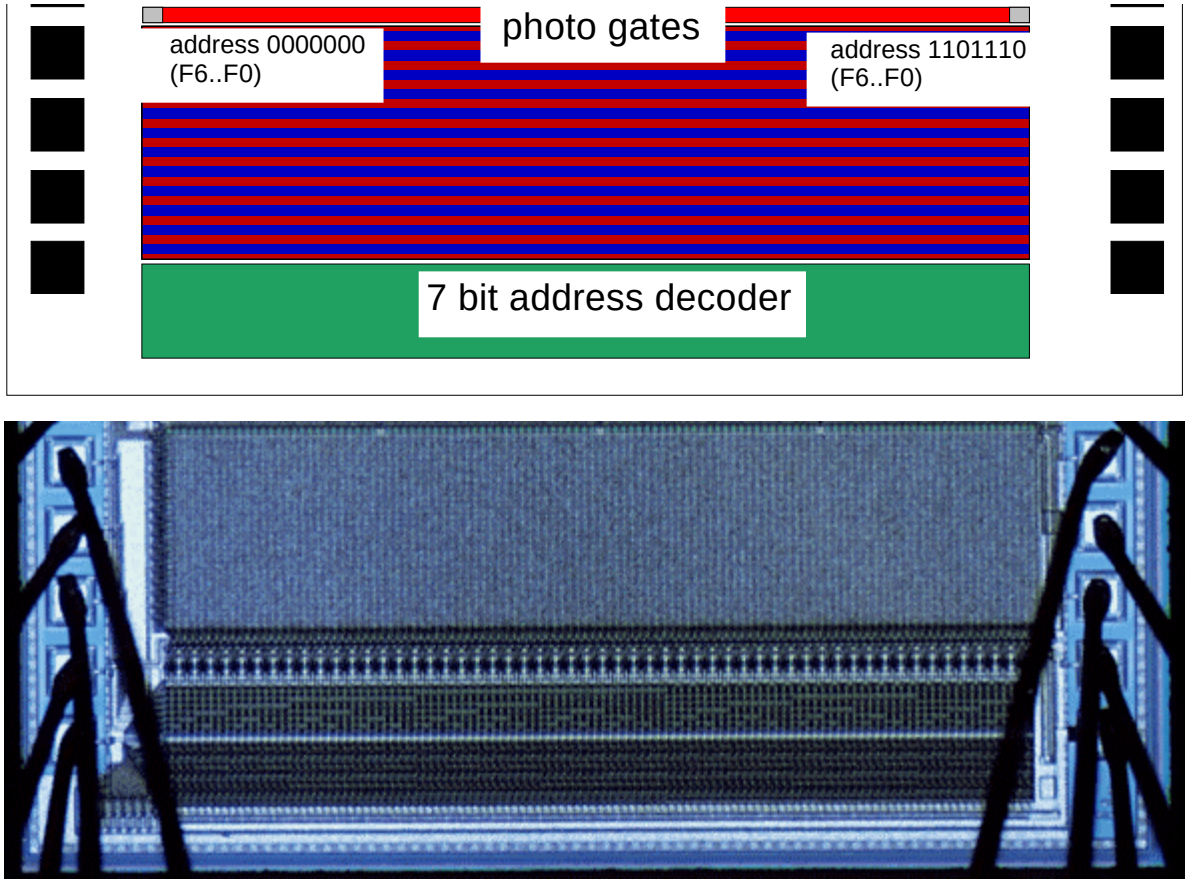

Figure 6.5 *TOF line detector: 108 one-tap pixels accessed by a 7-bit address decoder. Top: architectural overview, bottom: micrograph of the chip.*

Line arrangement of pixels: RC string

The arrangement of 1-tap pixels in a line leads to a problem that must not be neglected. Since all CCD gates driven by one signal driver are connected in series, the result is a relatively long and narrow polysilicon strip, which has to be interpreted as an RC string (c.f. **Figure 6.6**).

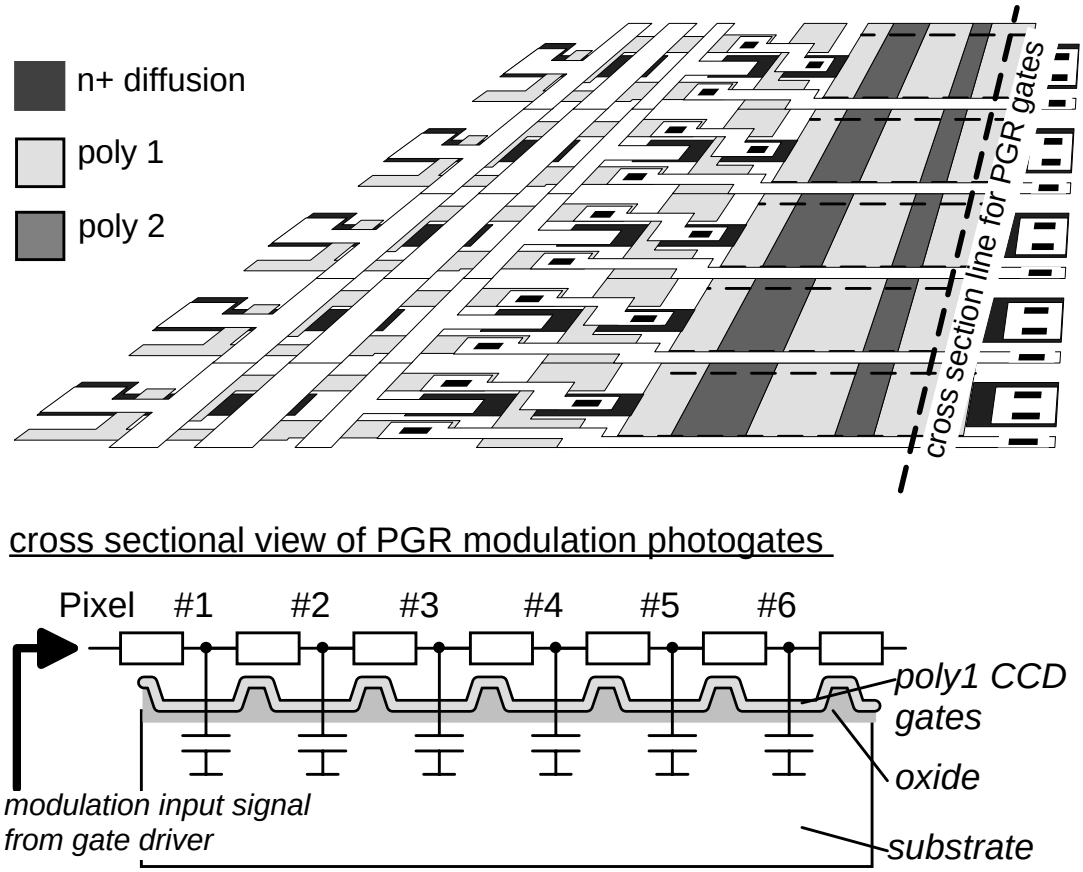

Figure 6.6 *Cross sectional view of the right modulation CCD gate PGR for a line arrangement of 1-tap demodulation pixels. The sheet resistance of the poly layer, together with the capacitance of each CCD gate, results in an RC string that reduces the electrical bandwidth of the pixel. For ease of understanding, the light-shield mask, the 16-stage CCD line between demodulation region and sense circuitry and the address decoder are not shown.*

With a size of 16 μm by 6 μm, a sheet resistance of 21 Ω/square and a gate capacitance of $85 \cdot 10^{-5}$ pF/μm^2, each of the modulation gates has a typical ohmic resistance of 56 Ω and a capacitance of 82 fF ($82 \cdot 10^{-15}$ F). With these parameters, we can simulate the time response and the amplitude spectrum of the RC string using SPICE. The simulation results are in **Figure 6.7**. For this simulation, we assume the polysilicon strip forming the modulated CCD gates to be connected only from one side. One can see from the simulation results that, for the one-side connected modulation gate, the low pass filter effect of the RC string prevents the operation of the CCD gates beyond 2-5 MHz. The 3 dB cut-off frequency is only 5 MHz for the 108th CCD gate, the last gate in the RC string.

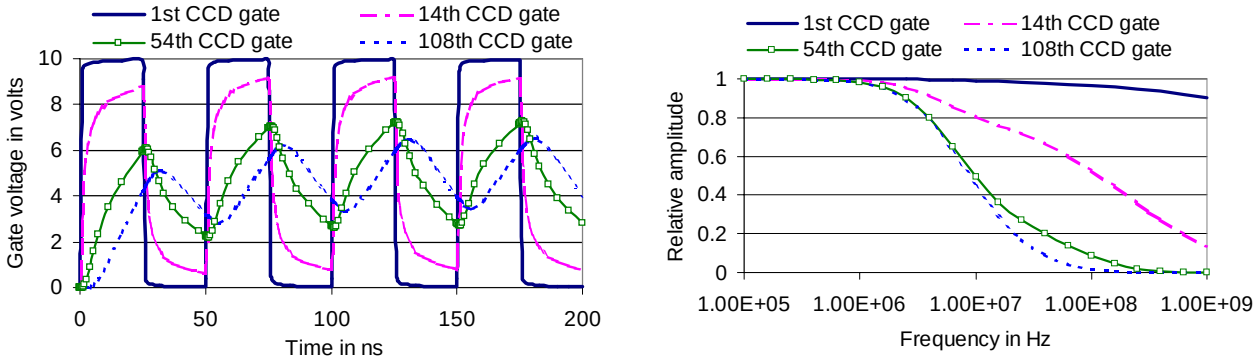

Figure 6.7 *<u>One-side connected</u> modulation gates: Time response and amplitude spectrum for the photogates, modulated with a 20 MHz square wave. The electrical bandwidth of the CCD gates is worse, the farther away they are located from the connection to the driving electronics. The cut-off frequencies are, for the 1st gate: > 1 GHz, for the 14th gate: 27 MHz, for the 54th gate: 5.3 MHz and for the 108th gate: 5 MHz.*

This poor frequency response can be avoided by connecting the photo gates from both sides. The slowest response can then be observed for the CCD gates in the middle of the string. The SPICE simulation results for the 2-side connected modulation gate string are given in **Figure 6.8**. The 3 dB cut-off frequency for the "slowest" gate (54th CCD gate) is now about 20 MHz, an improvement by a factor of 4 compared to the one-side connected gate.

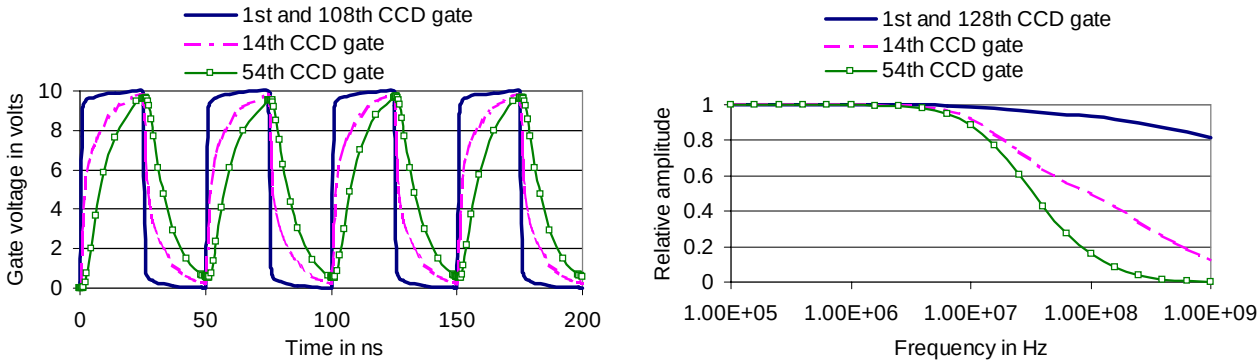

Figure 6.8 *<u>Two-side connected</u> modulation gates: Time response and amplitude spectrum. The cut-off frequencies are now, for the 1st and the last (108th) gate: > 1 GHz, for the 14th gate: 29 MHz and for the 54th gate: 19 MHz (improvement by a factor of 4).*

However, even for the two-side connected modulation gates the time-response is still too slow for 20 MHz modulation. Therefore, for the implementation of the 108

pixel 1-tap lock-in CCD line, we have interrupted the RC string after every 27th modulation gate in order to insert metallic connections to the polysilicon strips, in addition to connecting the modulation gates from two sides. This means that the load one has to drive consists of four 27-pixel RC-strings in parallel instead of a non-terminated 108 pixel RC string. According to our SPICE simulations (**Figure 6.9**) this results in a 30 times higher electrical cut-off frequency for the slowest gate.

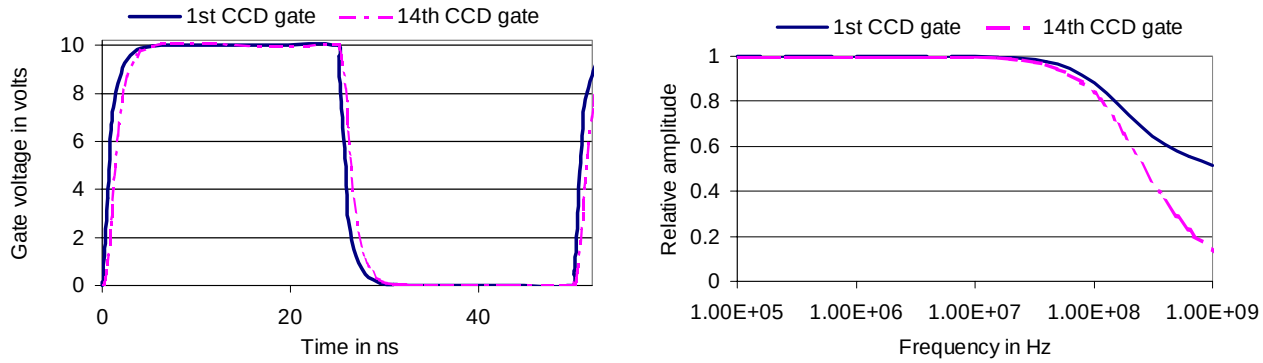

Figure 6.9 *Five-site connected modulation gates: after every 27th pixel the RC chain is broken for a metal connection of the modulation gates: Time response and amplitude spectrum. The cut-off frequencies are now, for the 1st gate: 230 MHz and for the 14th gate: 150 MHz (improvement by a factor of 30). This realization has been chosen for the 108-pixel TOF-sensor.*

6.2.2 System architecture

The 2D-camera

Photographs of the TOF line camera are in **Figure 6.10**. In the middle of the camera one can see the objective (f=4 mm, F/#=1.2) mounted to the driver board, which is connected to the sequencer board. The modulated illumination module consists of a line arrangement of 64 HPWT-DH00 LEDs.

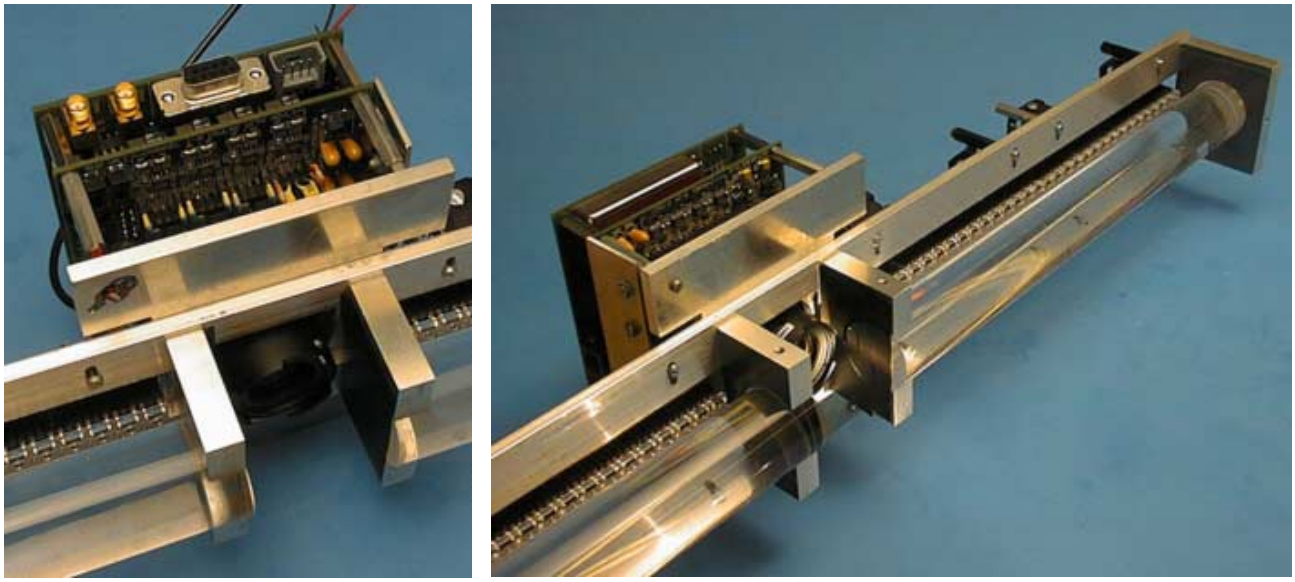

Figure 6.10 *Photograph of the 108 pixel TOF line camera. The modulated light source consists of 64 LEDs (630nm, HPWT-DH00-00000), focused by a cylindrical lens. Between both LED arms is the camera module with the objective in the middle. On the top of the left photograph one can see the sequencer board and the driver board plugged together.*

Setup and performance of the modulated illumination unit

The measured beam profile is shown in **Figure 6.11**. Each LED has a light power of approximately 8.5 mW at 630 nm (50° beam divergence). By focusing the LED light with a cylindrical lens in the vertical direction the optical power density can be locally increased by a factor of 7.5 in the (horizontal) observation plane, resulting in a power density of 10 $\mu W/cm^2$ at 7.5 m distance. With the objective used (1:1.2, 4 mm) and a spectral filter with 50 % attenuation, this results in an optical power of 885 fW per pixel for a diffusely reflecting object of reflectance 0.7 (blue pair of jeans) (c.f. **Chapter 4**). Such objects (reflectance of 0.7) at 7.5 m distance can be measured with an accuracy of better than 5 cm for 50 ms integration time (4·12.5 ms; 20 Hz frame rate). The accuracy increases for smaller distances or longer integration times and decreases for less reflecting targets (c.f. **Section 4.2**). This power budget is summarized in **Table 6.1**.

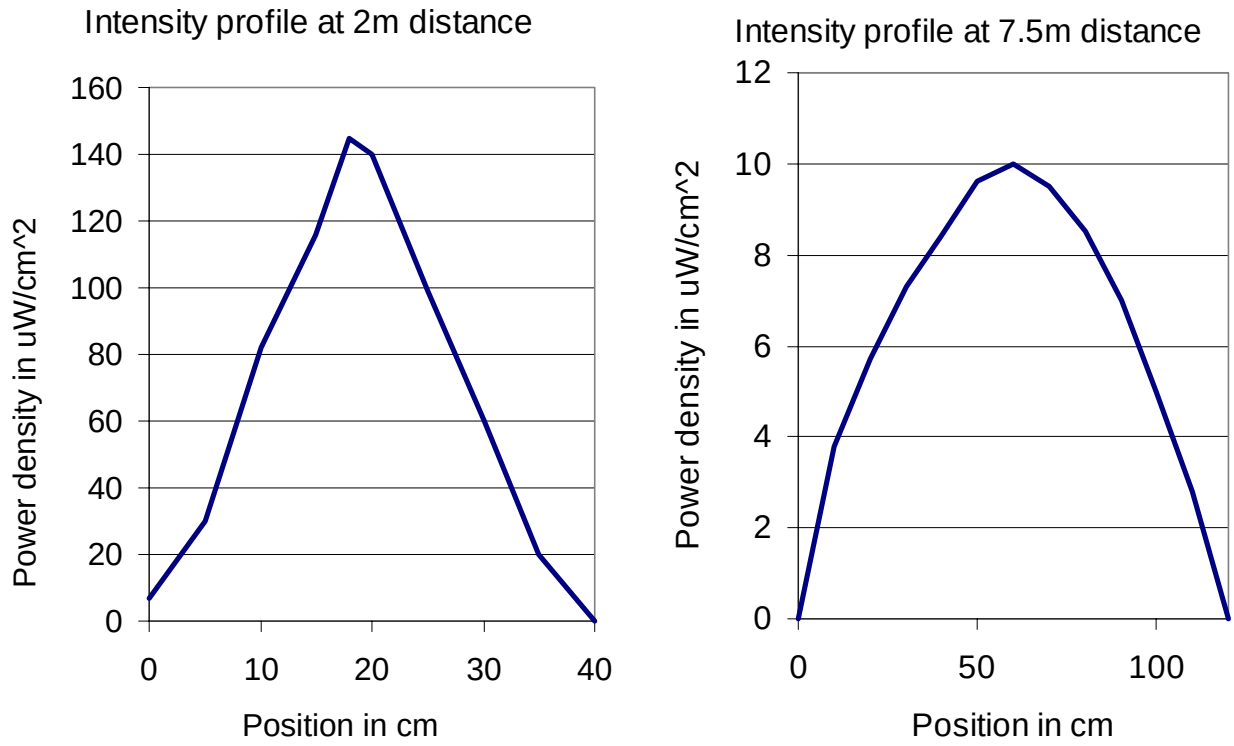

Figure 6.11 *Vertical beam profile: profile perpendicular to the optical line-sensor plane (measured with Newport 840 HandHeld™ optical power meter).*

In spite of the use of a cylindrical lens, only a small fraction of the modulated light is effectively used for the range measurement. With a total size of light sensitive pixel area of 16 μm (H) x 13 μm (V) and a focal length of 4 mm, the projected observation area of 1 pixel at 7.5 m distance is 30 mm (H) x 25 mm (V). Compared to the vertical beam profile (**Figure 6.11**) one can estimate that only about 4% of the optical power is imaged onto the light sensitive pixel area.

The optical setup for the line sensor is therefore not ideal, since a lot of “expensive” optical power is lost. In the application of this line sensor one would be better using a more narrow illumination plane (e.g. a 1D expanded laser beam) or modified imaging optics instead of the standard lens we are currently using. The reason we did not further improve this setup nor evaluate the use of laser illumination is that we regard this line camera as the first step towards the development of the 3D camera introduced in **Section 6.3**. For the 3D application the problem of illuminating only a small strip disappears.

Boundary conditions		***Calculation***	
Optical power at 7.5m distance	*10 µW/cm²*	*Projected pixel size on the target*	*30 mm x 25 mm*
(The area, projected to one pixel, is only 22.5 mm high, therefore the optical power density is 10 µW/cm²)		*Power on projected pixel area*	*73.1 µW*
Target		*Reflected power of projected pixel area*	*51.2 µW*
Distance	*7.5 m*	*Effective diameter of objective*	*3.3 mm*
Reflectivity of target	*0.7*	***Power on pixel in fW***	***885***
Objective (CS-mount)		*Energy in pixel*	*11.1E-15 J*
Focal length	*4 mm*	*Energy of 1 photon*	*3.16E-19 J*
F/#	*1.2*	*Number of photons per pixel*	*35,000*
Transmission of lens:	*0.7*	***Number of electrons per pixel***	***22,800***
Transmission of filter:	*0.5*	*Sensitivity of output stage*	*3.6 µV/electr.*
Sensor		***Output voltage***	***82 mV***
Pixel size	*16 µm x 13 µm*	*#modulation cycles for generation of 1 electron*	*11*
Operating conditions		***Resulting distance accuracy***	***< 5 cm***
Integration time	*12.5 ms*		
Wavelength	*630 nm*		
Quantum efficiency	*0.65*		
Conversion capacitance	*40 fF*		
Amplification of source follower	*0.9*		
Modulation frequency	*20 MHz*		

Table 6.1 *Optical power budget for the 64-LED modulated light source.*

Phase homogeneity of the LEDs

The optical and electrical performance of the LEDs we use for the modulated light source has already been discussed above and in **Chapter 5** (c.f. **Figure 5.11**). In addition, for the distance measurement, it is important that there be no phase difference in the optical output of the LEDs. Such a phase difference could either be caused by electrical delays on the PCB that holds the LEDs or technological variations between the single LEDs. The next graph shows the measured phase of the single LEDs. In **Figure 6.12** we can see that the measured phase homogeneity of the LEDs is better than ± 0.5 ns. This is sufficient for a homogenous phase of the LED illumination in the far field.

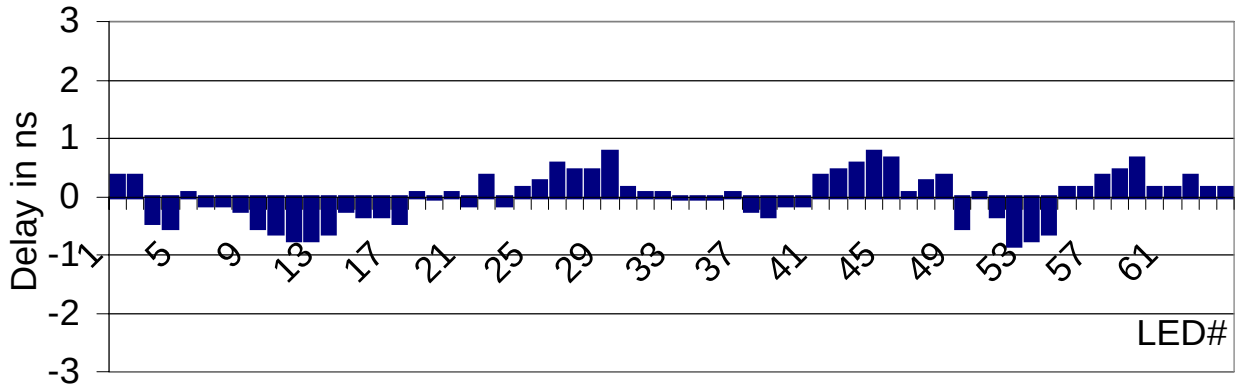

Figure 6.12 *Phase homogeneity of the LEDs used in the LED line arrangement for the TOF line camera.*

6.2.3 2D range measurement

Finally we present the results of range measurements performed with the TOF line range camera described above. For the first measurements, illustrated in **Figure 6.13**, we have used two different targets, a *black paperboard* and a *white sheet* of paper.

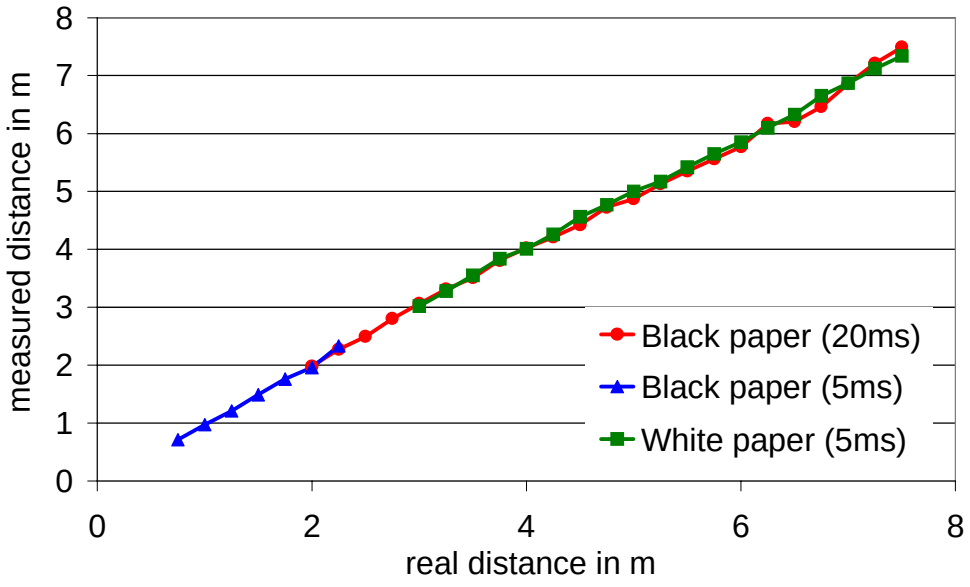

Figure 6.13 *Measurement results of TOF line camera (I). Measured distance of black paper and white paper at different integration times (5 ms and 20 ms).*

In **Figure 6.14** we present the measurement of a realistic indoor scene. The measured distance profile is taken with the 108-pixel line sensor, operated with 20 MHz modulation frequency (7.5 m distance range) and 50 ms integration time (20 Hz frame rate). By reducing the modulation frequency to 7.5 MHz, the distance range can be easily enlarged to 20 m.

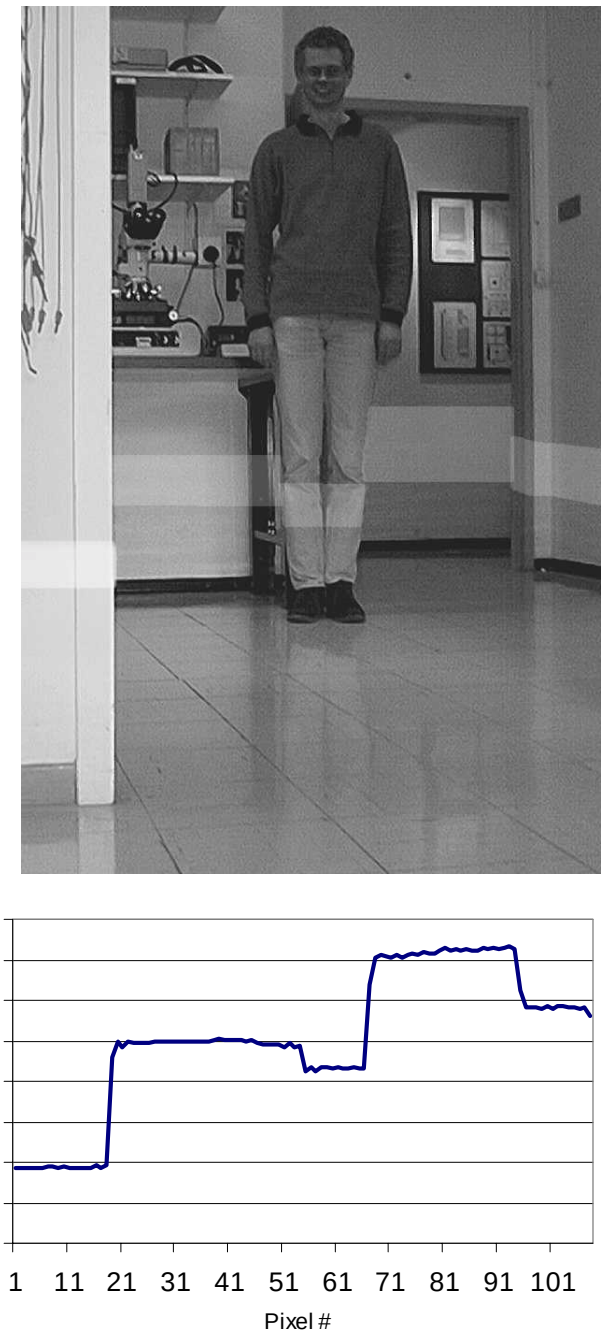

Figure 6.14 *Measurement results of TOF line camera (II). Distance profile of an indoor scene. Integration time: 50 ms (20 Hz frame rate), no averaging.*

6.3 3D range camera

In addition to the 1-tap pixel realization in a 108-pixel line sensor, we also implemented it in an array of 64 x 25 pixels. We describe the chip architecture, the camera realization and some measured 3D images in this section.

6.3.1 64 x 25 pixel lock-in image sensor

The 64 x 25 pixel TOF-imager was fabricated in ORBIT 2.0 µm CMOS/CCD technology using the American MOSIS prototyping service.

Chip layout and architecture

As for the realization of the line sensor, we used a TINY chip size (2 mm x 2 mm). The 1600 pixels can be randomly accessed by an address decoder; the reset is performed row-wise. The chip architecture and a micrograph of the chip are shown in **Figure 6.15**.

Electrical low-pass characteristic of the modulated photogates (RC string)

We have shown in **Section 6.2.1** that the serial connection of the CCD modulation gates results in an RC string that limits the maximum demodulation frequency, especially if the gates (i.e. the RC string) are connected only from one side. For the line sensor we could increase the electrical cut-off frequency by a factor of 30 by additionally connecting the CCD gates with metal wires at 3 points within the chain. This is not possible for the image sensor, which is introduced here, since the additional metal wires would drastically increase the pixel size and thus lower the optical fill factor. For the smaller number of pixels per line (64 instead of 108) the situation is, however, not as critical and the connection of the CCD gates from two sides results in a sufficiently fast time response. The SPICE simulation results are shown in **Figure 6.16**. The gate size of the modulation gates is 21 µm by 6 µm in this imager realization. This leads to a typical ohmic resistance of 75 Ω and a capacitance of 107 fF. The 3 dB cut-off frequency for the slowest gate is 55 MHz.

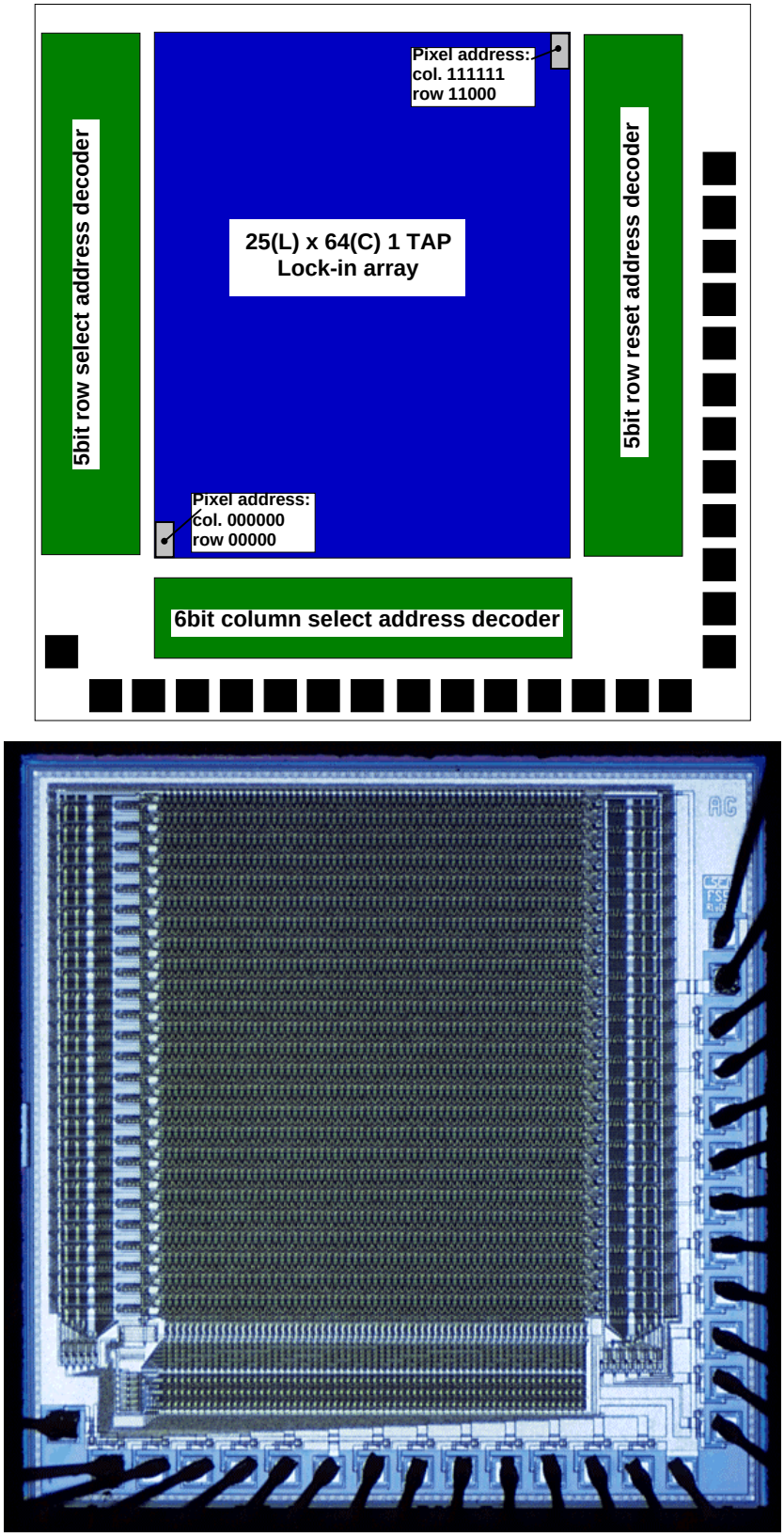

Figure 6.15 *TOF image detector: 64 x 25 one-tap pixel array accessed by a 6-bit column and a 5-bit row address decoder. Top: architectural overview, bottom: micrograph of the chip.*

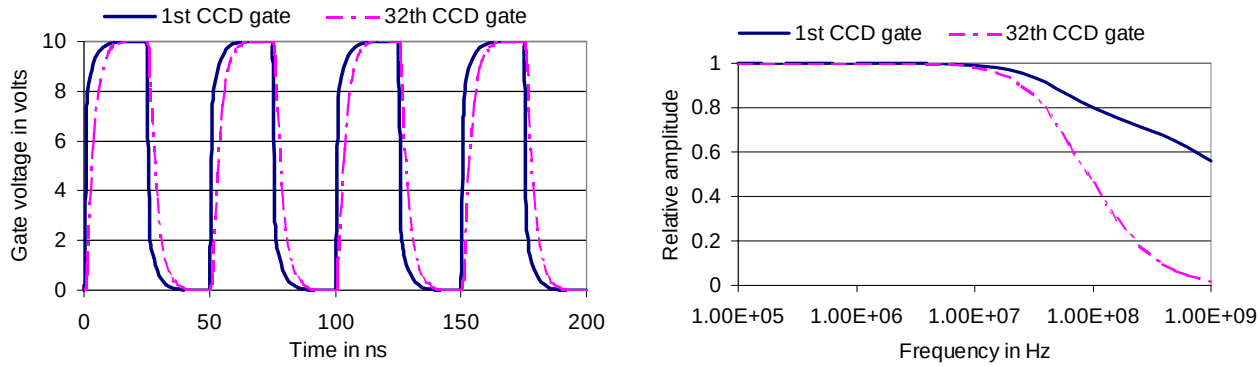

Figure 6.16 *Time response and amplitude spectrum of the modulation gates in the 64 x 25 pixels TOF-imager. The cut-off frequencies are, for the 1st and the last (64th) gate: 270 MHz and for the 32nd gate: 55 MHz.*

6.3.2 System architecture

The complete 3D camera system is shown in **Figure 6.17**. Again, system flexibility was an important factor in the camera design. The TOF-imager is controlled by the sequencer and driver boards introduced in **Section 6.1**; only the firmware had to be programmed anew for the sequencer.

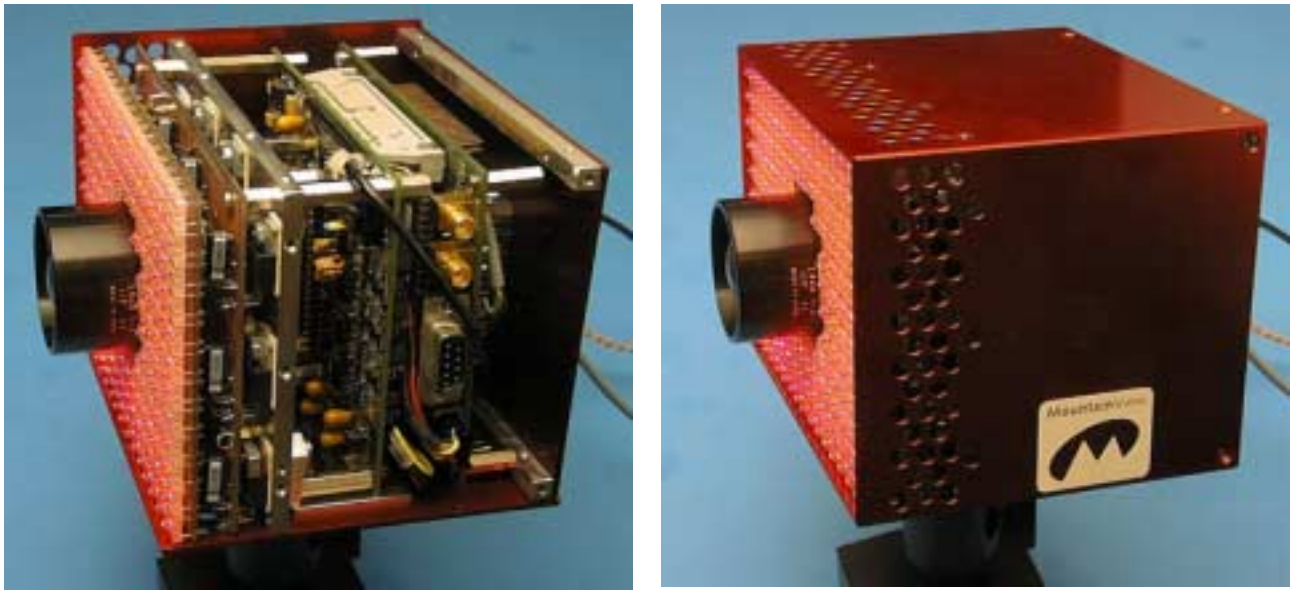

Figure 6.17 *Imaging time-of-flight range camera (3D). Left: open housing: from left to right: LED board, LED driver board, heat sink for LED drivers, camera driver board, sequencer board. Right: housing closed. (Size: 95 mm (H) x 125 mm (W) x 105 mm (D))*

In order to adapt the camera to different application needs, we have produced the LED module as a stacked 2 PCB- module, one carrying the driving electronics and the other one carrying the LEDs. So it is possible to easily change the LED type and thus the wavelength of the light source. **Figure 6.18** shows the 630 nm and an 820 nm LED module, each containing 160 LEDs.

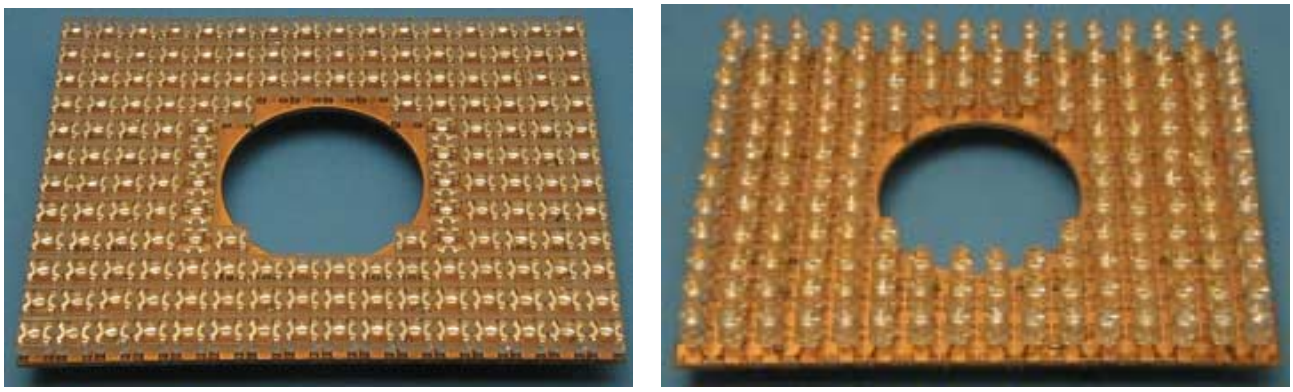

Figure 6.18 *LED modules for the 3D camera (160 LEDs). Left: 630 nm module (visible), right: 820 nm module (NIR, invisible). The 630 nm module offers a total optical power of 900 mW.*

The optical power of the HPWT-DH00 LEDs used for the 160-LED 630 nm module is, unfortunately, only about 5.5 mW (@ 50mA), rather than the 8.5 mW (@ 50mA) for the line sensor module (the distributor could only deliver LEDs of a lower power category). The total optical power of the 630 nm module is therefore about 900 mW.

Optical power budget

Since, in contrast to the line camera, we cannot increase the light intensity on the object by additional optics, in general we receive less light in each pixel than with the line camera. Therefore, we increase the integration time to 100 ms (4·25 ms, 10 Hz frame rate). With the 2.6 mm 1:1.0 CS-mount lens used, we can calculate the number of electrons received per pixel as a function of the target reflectivity and distance. This optical power budget is given in **Table 6.2**. The range resolution for a target at 7.5 m distance with a reflectivity of 0.7 is better than 9 cm.

Boundary conditions		***Calculation***	
Optical power of 160 LEDs	*900mW*	*Beam divergence at the target*	*7 m*
Beam divergence	*50°*	*Beam area at the target*	*38 m^2*
Target		*Projected pixel size on the target*	*180 mm x 40 mm*
Distance	*7.5 m*	*Projected size of photogates in the target*	*36 mm x 40 mm*
Reflectivity of target	*0.7*	*Power on projected photogate area*	*34 μW*
Objective (CS-mount)		*Reflected power of projected pixel area*	*24 μW*
Focal length	*2.6 mm*	*Effective diameter of objective*	*2.6 mm*
F/#	*1.0*	***Power on pixel in fW***	***260***
Transmission of lens:	*0.7*	*Energy in pixel*	*6.5E-15 J*
Transmission of filter:	*0.5*	*Energy of 1 photon*	*3.16E-19 J*
Sensor		*Number of photons per pixel*	*20,600*
Pixel size	*14.5 μm x 12.5 μm*	***Number of electrons per pixel***	***13,400***
Operating conditions		*Sensitivity of output stage*	*3.6 μV/electr.*
Integration time	*25 ms*	***Output voltage***	***48 mV***
Wavelength	*630 nm*		
Quantum efficiency	*0.65*	***Resulting distance accuracy***	***< 9 cm***
Conversion capacitance	*40 fF*		
Amplification of source follower	*0.9*		
Modulation frequency	*20 MHz*		

Table 6.2 *Optical power budget for 160-LED modulated light source.*

6.3.3 3D range measurement

Range measurements of 3D scenes are illustrated in **Figure 6.19 a** to **c**. **Figure 6.19 a** shows photographs of the scene taken with a high-resolution b/w camera, in order to give the reader a more detailed impression of the scene. In **Figure 6.19 b** we show the measured 3D data as a graphical representation, coded in both color and in the z-axis direction. In **Figure 6.19 c** we superimpose the 2D-b/w data of the observed scene, also acquired with our 3D TOF camera, on the 3D-grid, which results in a more physical impression of the scene.

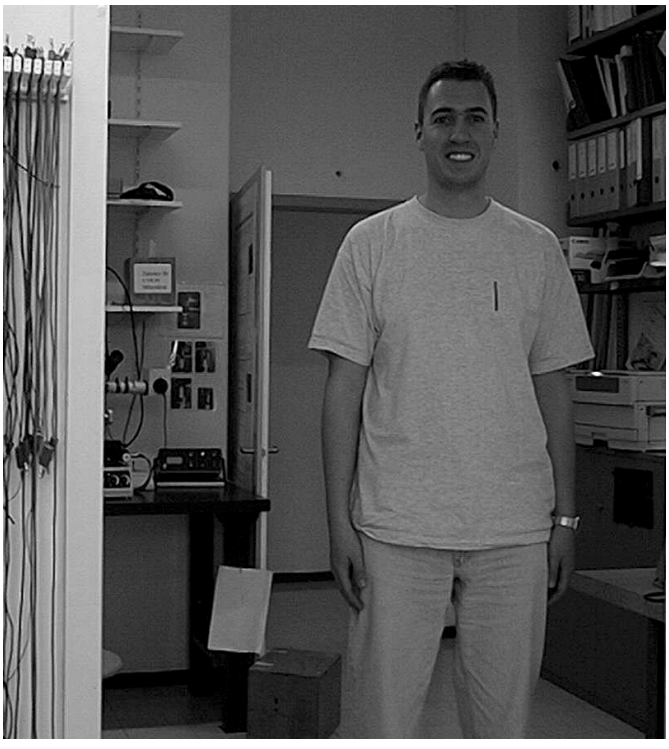

Figure 6.19 **a** *3D indoor scene: High-resolution b/w photograph. (Total integration time: 100 ms, 10 Hz frame rate.)*

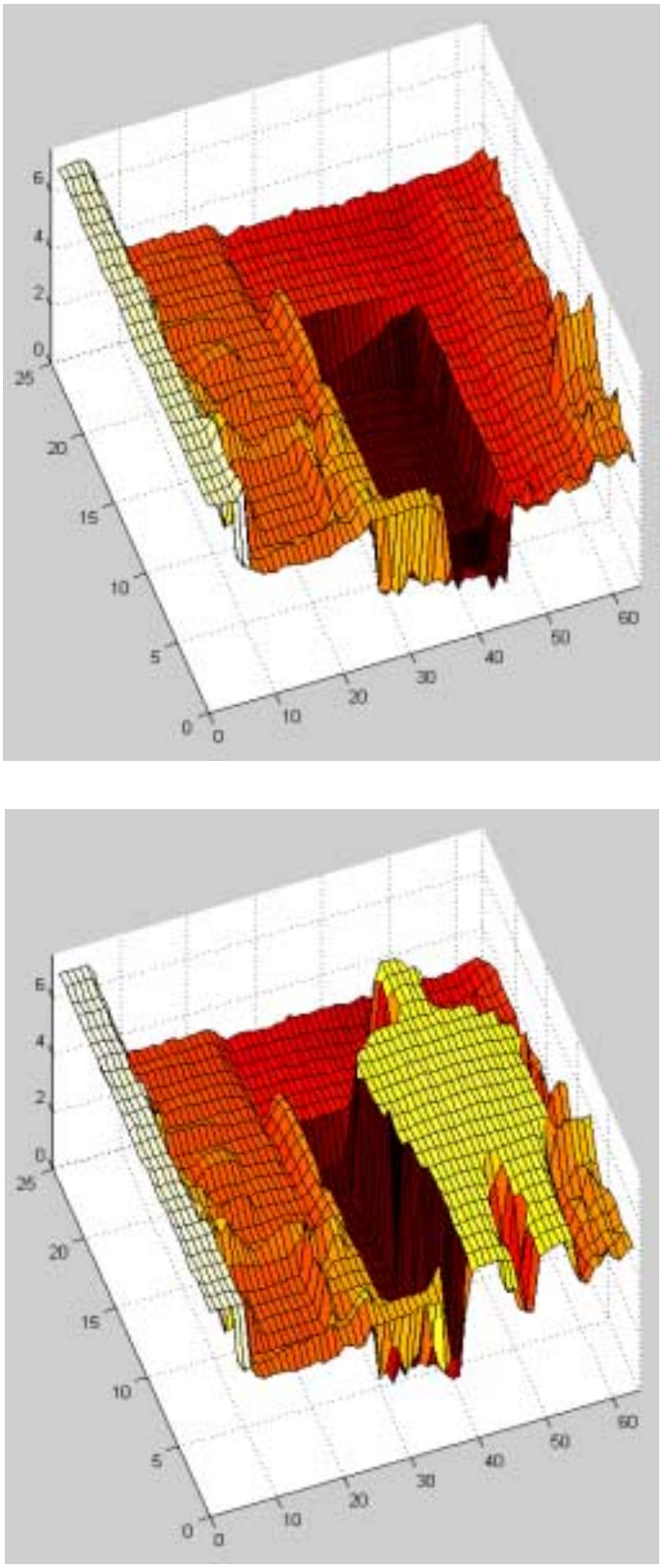

Figure 6.19 b *3D indoor scene: Measured 3D data. The distance information is coded both in the z-axis-direction and in color. (Total integration time: 100 ms, 10 Hz frame rate.)*

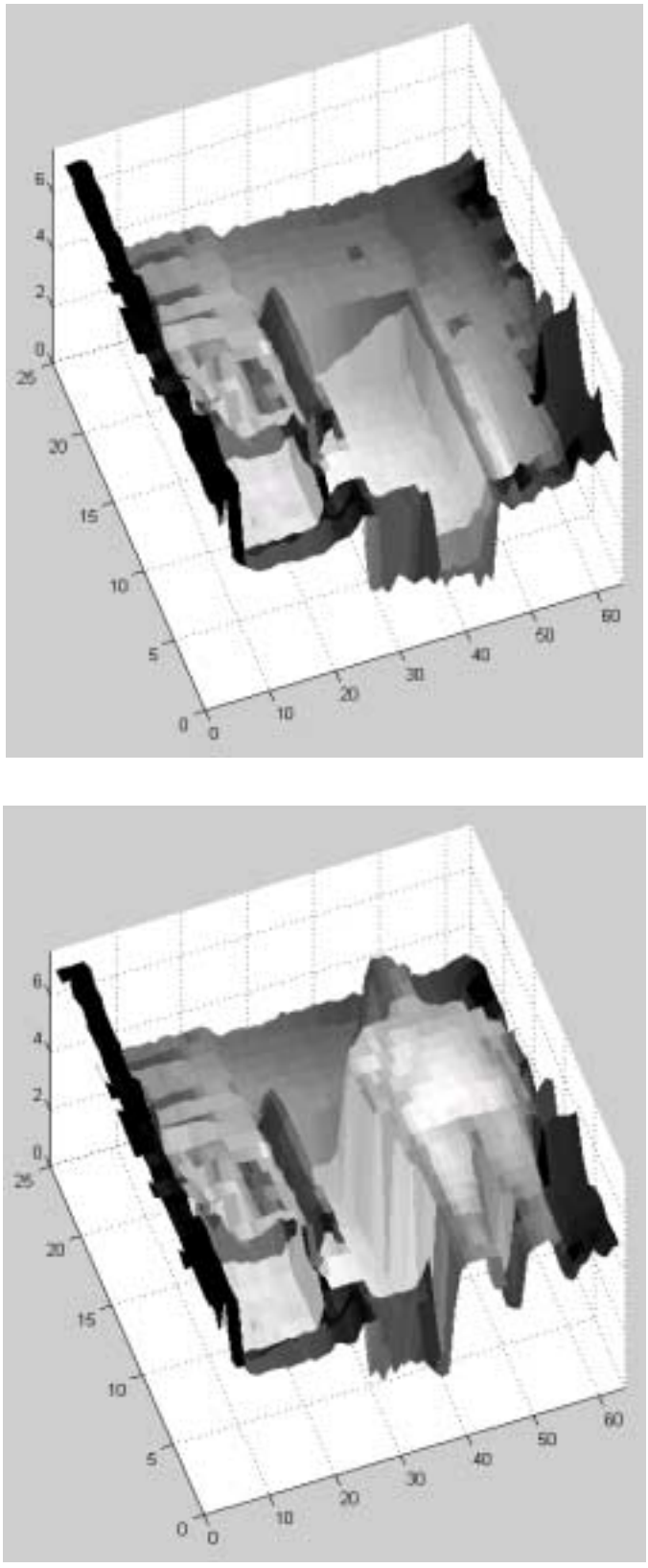

Figure 6.19 c *3D indoor scene: Measured 3D and 2D b/w data. The distance information is coded in the z-axis direction; the color of each pixel is the classical b/w intensity information, also measured with the TOF camera. (T_{int}: 100 ms, 10 Hz frame rate)*

Finally, **Figure 6.20** shows an 8-frame sequence of range images acquired with our 3D TOF camera. The integration time for the acquisition of these range images was 100 ms for each measurement (10 Hz frame rate).

[FIGURES ON NEXT TWO PAGES]

Figure 6.20 *Sequence of range images: A person approaching the 3D camera. The distance information is coded in both the z-direction and color (bright: close to the camera, dark: farther from the camera). The 2D b/w images on the left-hand side have been taken with the 3D camera simultaneously with the range images.*
(T_{int}: 100 ms, 10 Hz frame rate)

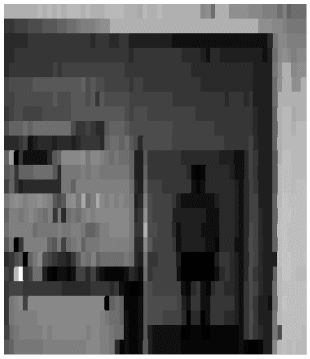

#1

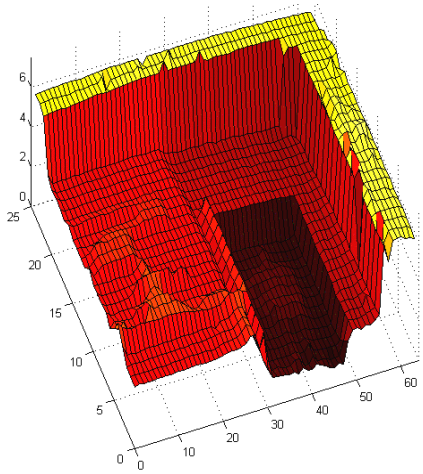

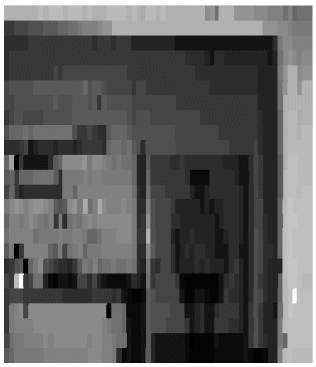

#2

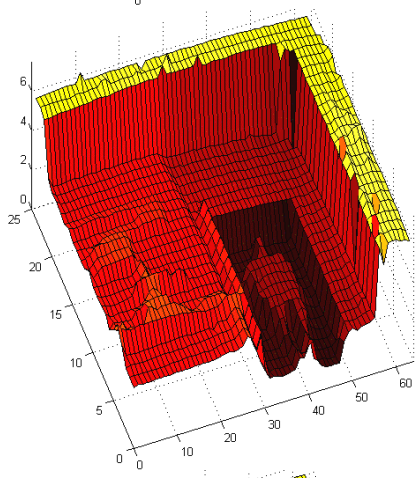

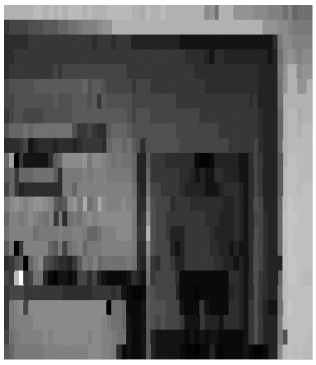

#3

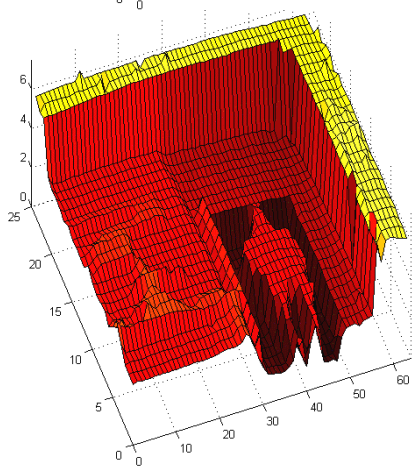

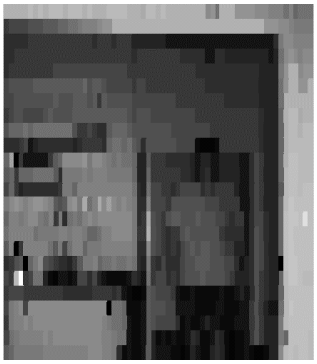

#4

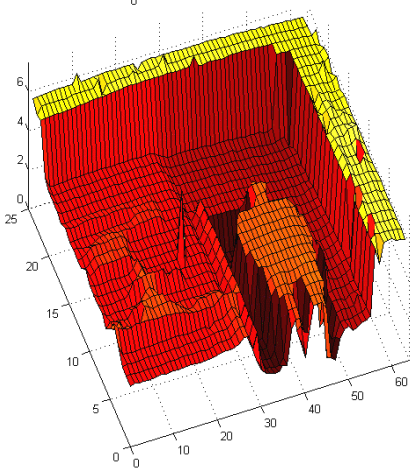

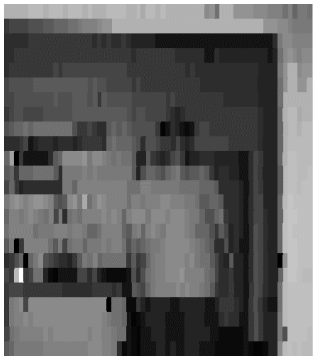

#5

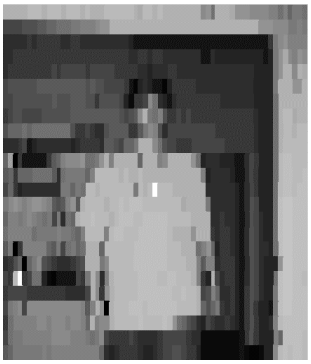

#6

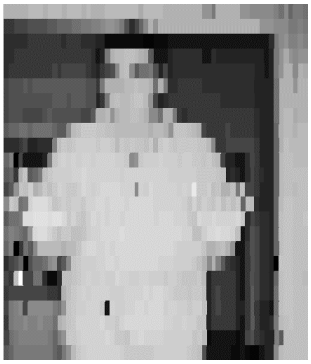

#7

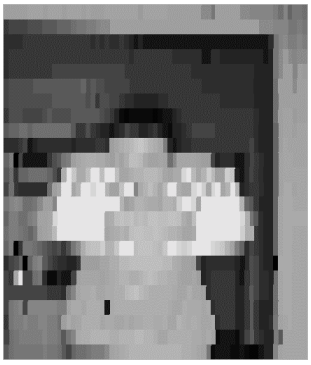

#8

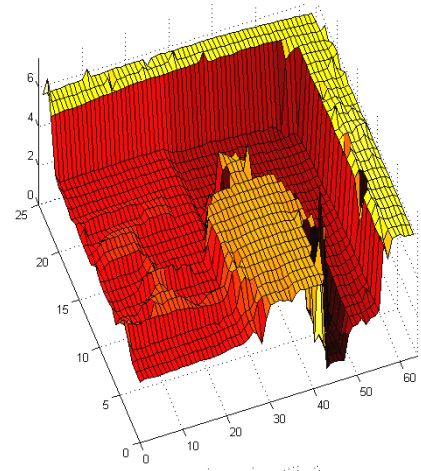
6
4
2
0
25
20
15
10
5
0
0
10
20
30
40
50
60

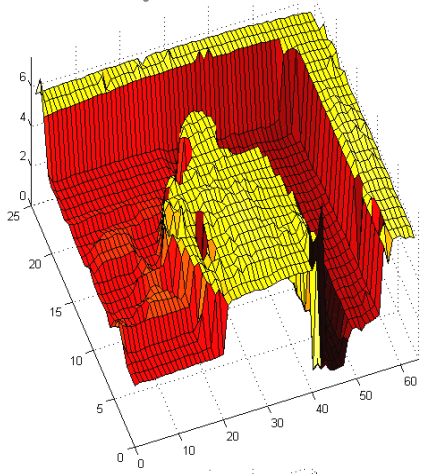
6
4
2
0
25
20
15
10
5
0
0
10
20
30
40
50
60

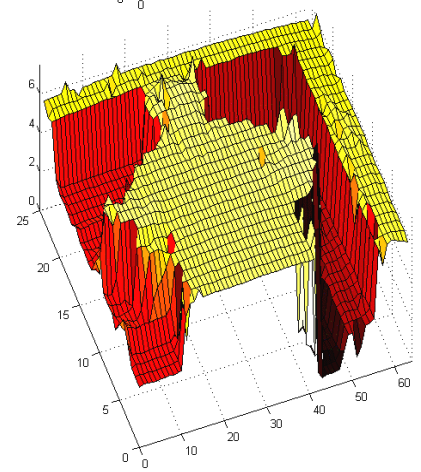
6
4
2
0
25
20
15
10
5
0
0
10
20
30
40
50
60

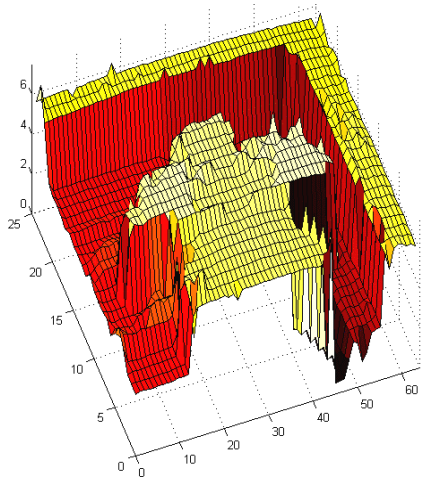
6
4
2
0
25
20
15
10
5
0
0
10
20
30
40
50
60

6.4 Discussion

With flexible implementations of a sequencer board and driving electronics suited for CMOS/CCD circuitry we have built two TOF range cameras. These are the world's first all-solid-state 2D and 3D time-of-flight cameras that are based on customized photoASICs. The arrangement of the 1-tap pixels in a line results in an RC string that limits the modulation frequency for the modulated photogates. The cut-off frequency can be increased by connecting the polysilicon strips from at least two sides. It is thus possible to operate the range cameras at a modulation frequency of 20 MHz, resulting in an unambiguous distance range of 7.5 meters. Over the full distance range we can measure non-cooperative targets with an accuracy of better than 10 centimeters. With the range measurements performed we could affirm the ranging accuracy predicted in our estimations in **Chapter 4.2**.

7. Summary and Perspective

In this thesis we have presented the world's first all-solid-state 3D time-of-flight range camera that is based on a customized photoASIC and does not require any mechanically moving parts. We achieve a distance resolution of a few centimeters over the range of several meters at a frame rate of 10 Hz for non-cooperative targets (reflectivity 0.7). The unambiguous distance range is 7.5 meters for 20 MHz modulation frequency and 20 meters for a modulation frequency of 7.5 MHz.

We have given an overview of the existing range measurement techniques and compared them to the time-of-flight method. Optical interferometry mainly targets measurements in the range of several centimeters, and is therefore not a real competitor in the 1-100 m range. The other popular ranging method, triangulation, either active or passive, suffers from shadowing effects and requires a large triangulation base and hence a large overall system size for good accuracy and distance range.

Furthermore, we have described and compared the classical CCD image sensors with CMOS APS imagers, which have gained more and more importance in recent years. One of the "secrets" of this CMOS APS boom is that they can be fabricated with standard technologies that are steadily being miniaturized and improved, driven by the computer industry. This makes it possible to implement more and more functionality within the sensor device and to realize more pixels on the same silicon area. From the existing range measurement techniques the time-of-flight method benefits most from this development in the semiconductor industry. While all range measurement systems will more or less decrease in size (note: triangulation will always require a large triangulation base for good accuracy), the TOF method will additionally gain in measurement resolution. This is mainly because the miniaturization in integrated circuits in general also leads to faster, lower noise circuits and therefore improves the time- and thus distance-resolution of TOF systems. For these reasons and in view of the additional advantages (no

shadowing problems, compact setup) we are convinced that time-of-flight is the 3D-measurement technique of the future.

To realize non-scanning 3D TOF cameras, an array of so-called demodulation pixels is required. Each of the pixels in this array must have the functionality to measure the arrival time of a modulated (optical) radiation field in addition to the intensity. The task of measuring the time of flight can be solved by synchronously sampling a periodically CW modulated optical signal. We have introduced such “sampling” demodulation pixels of different architectures. Our pixels have been implemented in a 2 μm CMOS/CCD technology. They make use of both the advantages of a CMOS-APS, such as random pixel access, and also the advantages of the CCD technique, which allows the addition of optically generated charge carriers, essentially free of noise, and their movement and distribution into defined storage areas in the semiconductor. We were able to show that, for a good homogenous performance of the pixels, the light sensitive area (photogate) should be accessed from only one (or two) site(s) since process inhomogeneities make it impossible to achieve homogenous sampling point sensitivity for a four side accessed photogate.

Especially since we use active illumination with the TOF method, the optical fill factor of the pixels is of essential importance. The 1-tap pixel that we implemented has an optical fill factor of 100% for the line sensor realization and 20% for the realization as an image sensor. That is already competitive with CMOS APS sensors. Additionally, the simple geometry of the light sensitive areas (lines of light sensitive areas, i.e. 100% fill factor in one dimension and 20% in the other dimension) makes it easy to realize and assemble highly efficient (cylindrical) microlenses. For these simple structures microlenses can drastically improve the optical fill factor (up to 100% for collimated light), so that, compared to our current setup, either the optical power or the integration time can be reduced by a factor of five. (For other photodetector arrays with asymmetrical photosites an efficient fill factor improvement by microlenses is often a problem).

We have extensively characterized and described the demodulation performance of the 1-tap pixel. For 20 MHz modulation frequency we measured a demodulation contrast of 40 % for a 630 nm modulated light source. With a simple model we could show that, even under DC conditions, the shutter efficiency of the pixel can never be better than 60 % to 70 %, since a fraction of light always travels directly

into the storage area. Additionally, the more sinusoidal rather than square shaped optical input signal at this frequency leads to an additional amplitude decrease so that the final operation limit in terms of modulation frequency is still not reached at 20 MHz. The reason why we did not further increase the modulation frequency was the limitation of the available control and driving electronics and also limitations of the light source we used. The measured time or phase accuracy strongly depends on the power of the modulated light and the integration time chosen for the signal acquisition. For an integration time of 12.5 ms and an optical power of 750 fW, the measured performance displays an accuracy of better than 250 picoseconds and 1.8 degrees respectively, resulting in a distance resolution of better than 4 cm. This is a surprising performance, because the above mentioned optical power implies that one electron is generated, statistically speaking, only every 13^{th} modulation period. This means that single electrons are moved, distributed and added in the pixel with excellent reliability. The measured performance shows excellent fit to the theoretical resolution predictions derived in Section 4.2. We are confident, therefore, that we fully understand the relevant physical processes and their influence on the distance resolution in any TOF ranging technique that relies on the demodulation of modulated wave fields.

Based on the 1-tap demodulation pixel we have built two range cameras: one TOF line camera (2D-range camera), working with the 108 pixel lock-in line sensor and one 3D camera based on the 64 x 25 pixel lock-in imager. The measured range accuracy is again in excellent agreement with our theoretical prediction. With the 3D camera we achieve a resolution of better than 10 cm for 100 ms integration time (10 Hz) at 7.5 meters distance for non-cooperative targets of 70% reflectivity. The range accuracy increases for shorter distances or longer integration times (more optical energy). The range accuracy of the line camera is even better, since the LED light can be focussed in one dimension, leading to an increase in optical power density on the target. For this line sensor application, however, the illumination setup and imaging optics can still be improved, since currently only about 5% of the optically illuminated area is imaged on the pixels.

The drawback of serial sampling point acquisition of our current pixel realization, that leads to measurement errors for quickly moving objects, can be overcome by a new pixel structure described in Section 5.3. This solves the homogeneity problem of accessing one light sensitive area within the pixel from four sides, as previously

suggested, by using two optically identical photosites per pixel, both accessed from two highly symmetrical sides. The “optical identity” can be achieved by a microlens array that equally distributes and focuses the incoming optical power per pixel to both photosites. With such a structure it will be possible to integrate all four sampling points in parallel.

In the near future it will be possible to fabricate CCD structures in sub-micron standard CMOS processes without any special CCD process option. This is because, for smaller technologies, the minimum gap between two transistor gates becomes so small that the potential barrier between these gates can be removed with relatively low gate voltages of a few volts. The possibility to change from a modified (non-standard) 2.0μm CMOS/CCD process, as we used for the pixels presented here, to a standard CMOS process brings several advantages: (1) The devices will become cheaper, (2) it will be possible for the first time to realize the complete bandwidth of CCD signal processing combined with additional on-chip functionality in a single process, and (3), it will be possible to realize smaller structures. This is an enormous advantage, because the diffusion-limited transfer time of charge carriers from one CCD gate to another increases with the square of the CCD gate’s length. With smaller technologies, shorter gates become possible, enabling a faster CCD transport. In particular, all of the pixels presented here will be realizable even with improved performance in such a technology. First results of such inter-poly-gap CCDs are presented in [CAR, FUR, HOP, KRA]. An interesting but more demanding alternative to the 2D-demodulation device introduced here would be the use of a sensitivity-modulated array of avalanche photodiodes. Such a device is introduced in [BIB]; however, as long as the observed problems with too high dark current and much too large excess noise factor are not solved, this approach remains impractical.

To summarize, we have shown that TOF is the range imaging technique of the future. We were able to demonstrate robust, compact range cameras (2D and 3D) with excellent performance that is only limited in a very predictable manner by ubiquitous quantum noise of the employed light. The ongoing miniaturization in microelectronics will lead to faster demodulation devices so that we can expect devices for demodulation frequencies beyond 100 MHz in the future. Also, it will be possible to realize additional functionality such as on-chip A/D conversion, distance

or phase calculation or even image processing tasks. This bright technological future of non-scanning TOF range cameras, combined with their photon noise limited performance and the absence of shadowing effects (from which all triangulation systems necessarily suffer), lead us to predict broad applications in safety, surveillance, inspection, production and autonomous navigation systems.

8. Appendix

8.1 Physical constants

Speed of light	c	$2.9979 \cdot 10^{8}$ m/s
Permeability of vacuum	μ_0	$1.2566 \cdot 10^{-6}$ H/m
Permittivity of free space	ε_0	$8.86 \cdot 10^{-12}$ F/m
Relative permittivity of SiO_2	ε_{ox}	3.9
Relative permittivity of Si	ε_{Si}	11.9
Electron charge	q	$1.6022 \cdot 10^{-19}$ C
Boltzmann constant	k	$1.3807 \cdot 10^{-23}$ J/K $8.6174 \cdot 10^{-5}$ eV/K
Electron rest mass	m_0	$9.1094 \cdot 10^{-31}$ kg
Proton rest mass	m_p	$1.6726 \cdot 10^{-27}$ kg
Planck constant	h	$6.6261 \cdot 10^{-34}$ J s $4.1357 \cdot 10^{-15}$ eV·s
Reduced Planck constant (h/2π)	$\hbar$	$1.0546 \cdot 10^{-34}$ J s $6.5821 \cdot 10^{-16}$ eV·s
Thermal potential at 300K (kT/q)	ϕ_T	0.025852 V
Electronvolt eV	eV	$1.6022 \cdot 10^{-19}$ J

8.2 Typical parameters of a 2 μm CMOS technology

Layer	Thickness / depth	Doping concentration	Sheet resistance
p substrate	-	$5 \cdot 10^{14}$ cm^{-3}	3000 Ω/square
APT implant (anti punch through)	-	$5 \cdot 10^{15}$ cm^{-3}	-
n+	0.3 μm	10^{20} cm^{-3}	30 Ω/square
p+	0.3 μm	10^{20} cm^{-3}	70 Ω/square
n-well	3.0 μm	$1.5 \cdot 10^{16}$ cm^{-3}	2500 Ω/sq.
Metal1	0.6 μm	-	0.06 Ω/sq.
Metal2	1.2 μm	-	0.03 Ω/sq.
Poly1	0.5 μm	-	20 Ω/square
Poly2	0.5 μm	-	25 Ω/square
Interpoly oxide	0.08 μm	-	-
Poly1 gate oxide	0.04 μm	-	-
Poly2 gate oxide	0.045 μm	-	-
Field oxide (poly to substrate)	0.6 μm	-	-
	Gate to oxide capacitances		
Poly1	$80 \cdot 10^{-5}$ pF/μm^2		
Poly2	$70 \cdot 10^{-5}$ pF/μm^2		

8.3 Conversion: LUMEN, WATT and CANDELA

Conversion of candela (cd) to watt (W)

$$\Phi_e[W] = I_v[cd] \cdot angle[sr] \cdot \frac{1}{V(\lambda_e)}$$

I_v Light intensity in candela

$V(\lambda_e)$ Spectral luminous intensity. Normalized to the human spectral daylight viewing sensitivity.

Φ_e Radiant flux in watt

Conversion of lumen (lm) to Watt (W)

$$\Phi_e[W] = \Phi_v[lm] \cdot \frac{1}{V(\lambda_e)}$$

Φ_v Luminous flux in lumen

Φ_e Radiant flux in watt

$V(\lambda_e)$ Spectral luminous intensity

Spectral luminous intensity V(λ) [RCA]

wavelength in nm	V(λ) normalized to 683 lm/W	wavelength in nm	V(λ) normalized to 683 lm/W
380	0.00004	550	0.995
390	0.00012	560	0.995
400	0.0004	570	0.952
410	0.0012	580	0.870
420	0.0040	590	0.757
430	0.0116	600	0.631
440	0.023	610	0.503
450	0.038	620	0.381
460	0.060	**630**	**0.265**
470	0.091	640	0.175
480	0.139	650	0.107
490	0.208	660	0.061
500	0.323	670	0.032
510	0.503	680	0.017
520	0.710	690	0.0082
530	0.862	700	0.0041
540	0.954		

8.4 Measurement conditions (MCD) for Chapter 5

MCD01:

Sequencer	*(Justin's sequencer + sequencer II)*
Quartz:	*16 MHz*
clock division factor:	*256 (CS0, CS1= 0, 1)*
sequencer clock:	*62.5 kHz*
word period:	*16 µs*
Camera setup	
Integration time:	*50ms*
#clock cycles for integration time	*3125 (3125*16µs=50ms)*
measured points:	*22*
integration time increment:	*2.4ms*
diffusing foil:	*folex film systems: folaproof Laserfilm/DM beidseitig matt, 90MY*
light source	*Schott KL1500 electronic (cold-light source)*
IF Filter:	*Coherent-Ealing, CWL: 633nm, HBW: 38nm, XT: 38%*
camera board:	*miniaturized board (Elantec drivers)*
lens:	*4mm, 1:1.2, CS mount*
Data acquisition:	*12 bit enhanced parallel port interface (CSEM product)*

MCD02:

LED: 630nm HPWT-DH00 not pulsed, Illumination with microscope

Power of LED:	6.7uW *(total behind ocular and 630nm Filter)*
Diameter of light spot (on chip):	19mm *(behind the filter)*
Area of light spot:	*19mm*19mm*pi/4*=284mm^2
→ Power-density on chip:	23.6 fW/µm^2
Size of photo gates:	144um^2
→ Power on photogate:	3.4pW
Integration time:	125ms
→ Energy on PG:	425fJ
Energy of 630nm photon:	3.16 E-19J
→ Number of incoming photons:	1'340'000 *(per pixel)*
QE at 630nm:	65%
→ Number of integrated electrons:	900'000 *(per pixel)*
Charge of integrated electrons:	1.44E-13C

→ Calculated output voltage swing:	3.25 V
Measured output voltage:	3.60 V

MCD03S:

Conditions SCCD

Illumination with microscope; LED pulsed at 1MHz (1:1 on/off ratio); 630nm IF-filter used; optical power measured behind the IF-filter

IF-Filter (COHERENT-EALING 42-7344):	*CWL: 633nm; HBW: 38nm; XT: 82%*		
LED:	*HPWT-DH00*	*LED average current*	*50mA*
Modulation frequency	*1MHz*	*Spot diameter:*	*22mm*
Total power of spot:	*6.0μW,*	*Spot area:*	*380·106μm2*
Wavelength:	*630nm*	*Size of photogates:*	*144μm2*
Integration time:	*125ms per Tap*	*Power on photogate:*	*2300 fW*
Energy of 630nm photon:	*3.16 E-19J*	*Energy on photogate:*	*288 fJ*
Quantum efficiency QE630nm:	*65%*	*#photons per photogate:*	*910'000*
Conversion capacitance:	*40fF*	*#electrons integrated per pixel:*	*590'000*
Amplification of SF stage:	*0.9*	*charge of #electrons int.*	*95 E-15 C*
output voltage swing (measured)	*2.3V*	*output voltage swing (theory)*	*2.15V*

Again, measured output voltage swing and theoretically calculated voltage swing are nearly the same.

MCD03B:

Conditions BCCD

Illumination with microscope; LED pulsed (average current: 50mA); 630nm IF-filter used; optical power measured behind the IF-filter

IF-Filter (COHERENT-EALING 42-7344):	*CWL: 633nm; HBW: 38nm; XT: 82%*		
LED:	*HPWT-DH00*	*Spot diameter:*	*17mm*
Total power of spot:	*1.4μW,*	*Spot area:*	*227·106μm2*
Wavelength:	*630nm*	*Size of photogates:*	*144μm2*
Integration time:	*125ms per Tap*	*Power on photogate:*	*888 fW*

MCD04S:

Conditions SCCD

LED	*630nm (HPWT-DH00), 50mA average*			
	Amplitude	C_1	C_2	Rise/fall time
PGL, PGR:	*8V*	*120pF*	*680pF*	*5ns*
IG	*10.7V*			
Integration time	*125ms per Tap*			

MCD04B:

Conditions BCCD

Illumination with microscope; LED pulsed (average current: 50mA); 630nm IF-filter used; optical power measured behind the IF-filter

IF-Filter (COHERENT-EALING 42-7344):	*CWL: 633nm; HBW: 38nm; XT: 82%*		
LED:	*HPWT-DH00*	*Spot diameter:*	*17mm*
Total power of spot:	*1.4µW,*	*Spot area:*	*227·10^{6}µm^2*
Wavelength:	*630nm*	*Size of photogates:*	*144µm^2*
Integration time:	*125ms per Tap*	*Power on photogate:*	*888 fW*

	Ampl.	*C1*	*C2*
PGL:	*8V*	*120pf*	*680pF*
PGR:	*8V*	*120pF*	*680pF*
PGM:	*3.5V*		
IG:	*10.7V*		

MCD05:

Integration time	*Measured optical power*	*Spot diameter*	*Spot area*
1.25ms	*5.5uW*	*2.4mm*	*4.5mm^2*
12.5ms	*5.5uW*	*10.3mm*	*83mm^2*
125ms	*5.5uW*	*26.5mm*	*552mm^2*

Output voltage swing for different optical input power conditions:

Quantum efficiency at 630nm:	*65%*
Gain of SF:	*0.9*
Conversion capacitance:	*40fF*

Integration time	Filter transm.	Power on photogate in W	#photons per photogate	#electrons per pixel	#electrons in T_{mod} (50ns)	#modulation cycles for gen. of 1 elec. per pixel	output voltage swing in mV
1.25ms	*100%*	*1.75E-10*	*6.93E+05*	*4.50E+05*	*18.0*	*0.06*	*1621*
	27%	*4.80E-11*	*1.90E+05*	*1.23E+05*	*4.9*	*0.2*	*444*
	8%	*1.44E-11*	*5.68E+04*	*3.69E+04*	*1.5*	*0.7*	*133*
	2%	*3.94E-12*	*1.56E+04*	*1.01E+04*	*0.4*	*2.5*	*36*
12.5ms	*100%*	*9.51E-12*	*3.76E+05*	*2.44E+05*	*0.978*	*1*	*880*
	27%	*2.60E-12*	*1.03E+05*	*6.70E+04*	*0.268*	*3.7*	*241*
	8%	*7.79E-13*	*3.08E+04*	*2.00E+04*	*0.080*	*12.5*	*72*
	2%	*2.14E-13*	*8.46E+03*	*5.50E+03*	*0.022*	*45*	*20*
125ms	*100%*	*1.44E-12*	*5.68E+05*	*3.69E+05*	*0.1477*	*7*	*1329*
	27%	*3.93E-13*	*1.56E+05*	*1.01E+05*	*0.0405*	*25*	*364*
	8%	*1.18E-13*	*4.66E+04*	*3.03E+04*	*0.0121*	*100*	*109*
	2%	*3.23E-14*	*1.28E+04*	*8.31E+03*	*0.0033*	*300*	*30*

LED: *630nm*

	Ampl.	*C_1*	*C_2*
PGL:	*8V*	*120pF*	*680pF*
PGR:	*10V*	*150pF*	*100nF*
PGM:	*6.5V*		
IG:	*10.7V*		

MCD06S:

Measurement conditions (SCCD)

Illumination with microscope; no IF-filter used; average LED current: 50mA

LEDs:	*4 different*	*Spot diameter:*	*22mm*
Wavelengths:	*470, 630, 740, 850nm*	*Spot area:*	*$380 \cdot 10^6 \mu m^2$*
Integration time:	*125ms per Tap*	*Size of photogates:*	*$144 \mu m^2$*
Total power of spot (meas. only for 630nm LED: HPWT-DH00):	*5.1µW @ 1kHz* *6.0µW @ 10kHz* *6.0µW @ 100kHz* *5.5µW @ 10MHz* *4.3µW @ 20MHz*	*Power on pixel (630nm LED):*	*1930fW @ 1kHz* *2270fW @ 10kHz* *2270fW @ 100kHz* *2080fW @ 10MHz* *1630fW @ 20MHz*
PGL	*8V*		
PGR	*10V*		
PGM	*6.5V*		

MCD06B:

Measurement conditions (BCCD)

Illumination with microscope; no IF-filter used; average LED current: 50mA

LEDs:	*4 different*	*Spot diameter:*	*17mm*
Wavelengths:	*470, 630, 740, 850nm*	*Spot area:*	*$227 \cdot 10^6 \mu m^2$*
Integration time:	*125ms per Tap*	*Size of photogates:*	*$144 \mu m^2$*
Total power of spot (meas. only for 630nm LED: HPWT-DH00):	*1.4µW @ 20MHz*	*Power on pixel (630nm LED):*	*888fW @ 20MHz*
PGL	*8V*		
PGR	*8V*		
PGM	*3.5V*		

MCD07:

Measurement conditions and distance accuracy achieved

Number of average runs:	*(1) No AVG*		
Control voltages:	*PGL*	*PGM*	*PGR*
	8V	*3.5V*	*8V*
		Standard deviation of error	
Average voltage swing:	*72 mV*	*in ns:*	*0.26 ns*
Optical power on the photogate:	*736 fW*	*in cm:*	*3.84 cm*
integration timer per Tap	*12.5ms*		
resulting frame rate	*20Hz*		
modulation frequency:	*20MHz*		

References

[AME] G. Amelio et al., “Experimental Verification of the Charge Coupled Device Concept”, *Bell Syst. Tech. Jour*., Vol. **49**, pp. 593-600, (1970).

[BEH] G. Beheim and K. Fritsch, “Range finding using frequency-modulated laser diode”, *Applied Optics*, Vol. **25**, pp. 1439-1442 (1986).

[BER] J. Beraldin et al., “Registered intensity and range imaging at 10 mega-samples per second”, *Optical engineering*, Vol. **31**, No. 1, pp. 88-94, (1992).

[BES] P. Besl, “Active Optical Range Imaging Sensors”, *Machine Vision and Applications*, Vol. **1**, pp. 127- 152, (1988).

[BEY] J. Beynon, et al., “Charge-coupled devices and their applications”, McGRAW-HILL Book Company, (1980).

[BIB] A. Biber, “Avalanche photodiode image sensing in standard silicon BiCMOS technology”, *Ph.D. Dissertation ETH Zurich*, Switzerland, No. **13544**, (2000).

[BLC] N. Blanc et al., “Digital low-power camera on a chip”, *Proc. International COST 254 Workshop on Intelligent Communication Technologies and Applications*, Neuchâtel, Switzerland, (1999).

[BLU] C. Blumer, “Characterization of a SCCD, a BCCD and a new Narrow-channel-BCCD line”, *Internship at CSEM Zurich*, (1999).

[BOU] S. Bourquin, “Low-coherence interferometry based on customized detector arrays”, *Ph.D. Dissertation EPFL-Lausanne*, Switzerland, No. **2171**, (2000).

[BOY] W. Boyle et al., “Charge coupled semiconductor devices”, *Bell Syst. Tech. Jour*., Vol. **49**, pp. 587-593, (1970).

[BRE] B. Breukmann, “Bildverarbeitung und optische Meßtechnik“, Franzis’, (1993).

[BRK] Brockhaus, “Naturwissenschaften und Technik”, Bd. **3**, ISBN 3-7653-0450-6, Mannheim, (1989).

[BRR] H. Breuer, “dtv-Atlas zur Physik, Tafeln und Texte”, Bd.**1**, 2.Auflage, ISBN 3-423-03226-x, (1990).

[CAR] J.E. Carnes et al., “Free Charge Transfer in Charge-Coupled Devices”, *IEEE Transactions on Electron Devices*, Vol. **19**, No.6, (1972).

[COR] S. Coren et al., “Sensation and Perception”, Fourth Edition, Harcourt Brace College Publishers (1994).

[CRE] K. Creath, “Phase-Measurement Interferometry Techniques”, *Progress in Optics,* Vol. **XXVI**, E. Wolf (Ed.), Elsevier, (1988).

[CS1] CSEM Zurich, Badenerstrasse 569, CH-8048 Zurich.

[DAS] Product brochure of Daimler-Benz Aerospace, “Laserkamera”, contact: wilfried.schroeder@ri.dasa.de.

[DEC] S. Decker et al., “A 256x256 CMOS imaging array with wide dynamic range pixels and column-parallel output”, *Proceedings of IEEE International Solid-State Circuits Conference*, (1998).

[DOR] R. G. Dorsch et al., “Laser triangulation: Fundamental uncertainty in distance measurement”, *Applied Optics*, Vol. **33**, pp. 1306-1314, (1994).

[ELA] Élantec Data Book, EL7202CS CCD driver, (1997).

[EMM] Product data sheet, “APSVGA- Low-power CMOS digital video camera”, EM Marin, (1999).

[EN2] K. Engelhardt, “Meßprinzipien, Eigenschaften und Limitierungen. Optische 3D-Meßtechnik”, *Technische Rundschau*, Issue **31**, pp. 44-51, (1993).

[ENG] K. Engelhardt, “Methoden und Systeme der optischen 3-D Messtechnik”, *XI. Internationaler Kurs für Ingenieurvermessung in Zürich*, Ferd. Dümmlers Verlag Bonn, (1992).

[FEM] http://www.femto.de

[FOS] E. Fossum, “Active Pixel Sensors: Are CCD’s Dinosaurs?”, *Proceedings of the SPIE*, Vol. **1900**, pp. 2-14, (1993).

[FUR] M. Furumiya et al., “A ½-inch 1.3N-Pixel Progressive Scan CCD Image Sensor Employing 0.25 mm Gap Single-Layer Poly-Si Electrodes" , *Proceedings of IEEE International Solid-State Circuits Conference*, San Francisco, (1999).

[HAM] Hamamatsu prospectus, “Image Intensifiers”, (1994).

[HAU] F. Hauser, “Internship at CSEM Zurich”, CSEM-internal report, (2000).

[HEC] E. Hecht, A.Zajac, “OPTICS”, Addison-Wesley, (1974).

[HEK] P. Heck, “Operation and characterization of a surface channel CCD-line”, *Diploma work* (Travail pratique de Diplôme), EPFL Lausanne/ CSEM Zurich, (1999).

[HOF] B. Hoffmann, “Einsteins Ideen”, Spektrum Akademischer Verlag, 1997; Translation of: “Relativity and Its Roots“, *Scientific American Books*, New York, (1983).

[HOP] C. R. Hoople et al., “Characteristics of Submicrometer Gaps in Buried-Channel CCD Structures”, *IEEE Transactions on electron devices*, Vol. **38**, No. 5, (1991).

[HOP] G. Hopkinson, et al. “Noise reduction techniques for CCD image sensors”, *J. Phys. E : Sci. Instrum.,* Vol. **15**, pp. 1214-1222, (1982).

[HP1] Hewlett Packard (now Agilent), “Super Flux LEDs, Technical Data”, Data sheet of HP SunPower Series, including *HPWT-DH00*, (1998).

[HP2] Hewlett Packard (now Agilent), “Super Flux LED, Categories and Labels”, Application Note **1149-7**, (1998).

[JE1] G. Jellison et al. “Optical functions of silicon at elevated temperatures”, *Journal of Applied Physics*, **76**, (1994).

[JE2] G. Jellison, “Optical functions of silicon determined by two-channel polarization modulation ellipsometry”, North-Holland Physics Publishing, *Optical Materials* **1**, pp. 41-47, (1992).

[KA2] H. A. Kappner, “Verfahren und Anordnung zur dreidimensionalen optischen Erfassung von Objekten”, *European Patent* No. **0 192 993 A1**, (1986).

[KAI] I. Kaisto, et al., “Optical range finder for 1.5m - 10m distances”, *Applied Optics*, Vol. **22**, No. 20, 3258-3264, (1983).

[KAP] H. Kappner, „Dreidimensionale sensorische Erfassung von Werkstücken“, *documentation of OPSIS GmbH*, Speyer, Germany, (1987).

[KOE] W. Koechner, “Optical Ranging System Employing a High Power Injection Laser Diode”, *IEEE Transactions on Aerospace and Electronic Systems*, Vol. **AES-4(1)**, pp. 81-91, (1968).

[KRA] J. Kramer, “Photo-ASICs: Integrated Optical Metrology Systems with Industrial CMOS Technology”, *Ph.D. Dissertation ETH Zurich*, Switzerland, No. **10186**, (1993).

[LA1] R. Lange et al., “Time-of-flight range imaging with a custom solid-state image sensor”, *Proceedings of the SPIE*, Vol. **3823**, pp. 180-191, Munich, (1999).

[LA2] R. Lange, et al, “Demodulation pixels in CCD and CMOS technologies for time-of-flight ranging”, *Proceedings of the SPIE*, Vol. **3965A**, pp. 177-188, San Jose, (2000).

[LA3] R. Lange, et al., “Seeing distances - A fast time-of-flight 3D camera”, *Sensor Review*, Vol. **20**, Issue 3, July 2000, to be published, (2000).

[LAX] S. Lauxtermann et al., “A high speed CMOS imager acquiring 5000 frames/sec”, *IEEE: IEDM Technical Digest*, pp. 875-878, Washington DC, (1999).

[LEI] http://www.leica.com/surv-sys/index.asp.

[MAZ] “Echtzeit-3D-Board zur Tiefenauswertung stereoskopischer Bilder”, *Prospectus of MAZ Mikroelektronik Anwendungszentrum Hamburg GmbH*, (1999).

[MOI] A. Moini, “Vision Chips or Seeing Silicon”, 3rd Rev*., Department of Electronics Engineering*, The University of Adelaide, Australia, (1997).

[MOR] I. Moring et al., “Acquisition of three-dimensional image data by a scanning laser rangefinder”, *Optical Engineering*, Vol. **28**, pp. 897-905, (1989).

[PAR] J. Parker et al., “Reflective tomography: images from range-resolved laser radar measurements”, *Applied Optics,* Vol. **27**, pp. 2642-2643, (1988).

[PHS] “Laser-Radar Imaging without Scanners”, *Photonics Spectra*, April 1994, pp. 28-30, (1994).

[POW] H. Powel et al., ”Charge-coupled device image sensors as a demodulator in a 2D-polarimeter with a piezoelastic modulator”, *Applied Optics*, Vol. **29**, No 8, pp. 1186-1190, (1990).

[PS1] P. Seitz, “Solid-State Image Sensing”, in *Handbook of Computer Vision and Applications*, B. Jähne, H. Haussecker and P. Geissler (Eds.), Academic Press, (1999).

[PS2] P. Seitz, “Image sensing with maximum sensitivity using industrial CMOS technology”, *Proceedings of the SPIE*, Vol. **3099**, Munich, (1997).

[RCA] RCA, “Electro-Optics Handbook”, Technical Series EOH-11, Commercial Engineering, *Harrison*, NJ 07029, (1974).

[RIG] Internet: http://www.riegl.co.at, (1998).

[RIX] M. Rioux, “Laser range finder based on synchronized scanners”, *Applied Optics*, Vol. **23**, No 21, pp. 3837-3844, (1984).

[SAL] B. Saleh, M. Teich, “Fundamentals of Photonics”, ISBN 0-471-83965-5, John Wiley & Sons, (1991).

[SC1] R. Schwarte, “Principles of 3-D Imaging Techniques”, in *Handbook of Computer Vision and Applications*, B. Jähne, H. Haussecker and P. Geissler (Eds.), Academic Press, (1999).

[SC2] R. Schwarte et al., “Pseudo- noise (PN)- laserradar without scanner for extremely fast 3D-imaging and navigation”, *MIOP ’97*, Stuttgart, (1997).

[SC3] R. Schwarte et al., “A new active 3D-Vision system based on rf-modulation interferometry of incoherent light”, Photonics East-Intelligent Systems and Advanced Manufacturing, *Proceedings of the SPIE*, Vol. **2588**, Philadelphia, (1995).

[SEQ] C. Séquin, et al., “Charge Transfer Devices“, Academic Press, (1975).

[SLO] J. Szydlo, et al., “Air-turbine driven optical low-coherence reflectometry at 28.6 kHz scan repetition rate”, *Optics communications*, **154**, pp. 1-4, (1998).

[SP1] T. Spirig et al., “The lock-in CCD – Two-dimensional synchronous detection of light”, *IEEE Journal of quantum electronics*, Vol. **31**, No. 9, pp. 1705-1708, (1995).

[SP2] T. Spirig et al., “The multitap lock-in CCD with offset subtraction*”, IEEE Transactions on electron devices*, Vol. **44**, No. 10, pp. 1643-1647, (1997).

[SP3] T. Spirig, P. Seitz, “Vorrichtung und Verfahren zur Detektion und Demodulation eines intensitätsmodulierten Strahlungsfeldes”, *German Patent* No. **DE 44 40 613 C 1**, (1996).

[SP4] T. Spirig, “Smart CCD/CMOS Based Image Sensors with Programmable, Real-time, Temporal and Spatial Convolution Capabilities for Applications in Machine Vision and Optical Metrology”, *Ph.D. Dissertation ETH Zurich*, Switzerland, No. **11993**, (1997).

[STR] T. Strand, “Optical three-dimensional sensing for machine vision”, *SPIE’s Optical Engineering*, Vol. **24** (1), pp. 33-40, (1985).

[SUT] D. Sutter et al., “self-starting 6.5fs pulses from a Ti:sapphire laser using a semiconductor saturable absorber and double-chirped mirrors*”, IEEE Journal of Selected Topics in Quantum Electronics* , Vol. **4**, pp. 169-178, (1998).

[SZ1] S. Sze, “Semiconductor Devices, Physics and Technology”, 1st edition, *John Wiley & Sons*, (1985).

[SZ2] S. Sze, “Physics of semiconductor devices”, 2nd edition, *John Wiley & Sons*, (1981).

[TEU] A. Theuwissen, “Solid-State Imaging with Charge-Coupled Devices“, *Kluwer Academic Publishers*, (1995).

[TIE] U. Tietze, C. Schenk, “Halbleiter- Schaltungstechnik”, 10th edition, *Springer-Verlag*, (1993).

[TOR] J. R. A. Torrea et al., “Matching photometric-stereo images”, *J. Opt. Soc. Am. A*, Vol. **15**, pp. 2966-2975, (1998).

[VIZ] O. Vietze, “Active pixel image sensors with application specific performance based on standard silicon CMOS processes”, *Ph.D. Dissertation ETH Zurich*, Switzerland, No. **12038**, (1997).

[VOG] T. Vogelsong et al., “Scientific/industrial camera-on-a-chip using Active Column Sensor ™ CMOS technology”, *Proceedings of the SPIE*, Vol. **3965A**, San Jose CA, (2000).

[WON] H. Wong, “Technology and device scaling considerations for CMOS imagers“, *IEEE Transactions on Electron Devices*, Vol. **43**, No. 12, (1996).

[XU] Z. Xu, “Investigation of 3D-Imaging Systems Based on Modulated Light and Optical RF-Interferometry (ORFI) - ZESS-Forschungsberichte”, *Shaker Verlag Aachen*, ISBN 3-8265-6736-6, (1999).

[ZIM] E. Zimmermann et al., “Stabilized three-wavelength source calibrated by electronic means for high-accuracy absolute distance measurements”, *Optics Letters,* Vol. **21**, pp. 531-533, (1996).

Acknowledgments

This work has been carried out in the Image Sensing Group of the PSI (Paul Scherrer Institut), which later became part of CSEM (Centre Suisse d'Electronique et de Microtechnique SA) in Zurich, Switzerland. I would like to thank the section head of this group, *Prof. Peter Seitz* for his supervision and guidance of this work during the last three years. He gave many fruitful inputs for this work and my publications. Especially he taught me how to be efficient in my work.

Also I would like to thank *Prof. Rudolf Schwarte* for agreeing to be my Ph.D. advisor and for leading me into the world of Photonics.

Furthermore, I must not forget to thank *Dr. Alice Biber* for introducing me to CMOS IC design and for her permanent practical and mental support of my work. We had many interesting discussions about technical problems and other things in life. She always knew the right questions to ask. Additionally, Alice reviewed nearly every English sentence I produced during my work.

I owe thanks to my officemate *Dr. Nicolas Blanc*, who always had an open ear to my problems and provided me with coffee and other fruitful inputs.

I gratefully acknowledge the invaluable help of *Peter Metzler* in all kinds of analog electronic problems. For digital electronics and CCD drivers I could profit from the profound experience of *Dr. Peter Schwider*. For assisting me in "C" programming and English language problems, and for discussing the latest sports events I thank *Graham Lang*.

I thank my friends *Thomas Ammer*, *Dr. Gerd Blau*, *Vincenzo Monterosso* (thanks for extending my horizons at the rock concert in Hallenstadion), *Dr. Stephane Bourquin* and *Philipp Zeller* for their social and technical support.

It is a pleasure to express my thanks also to all other members of the Image Sensing Group, who contributed to this work in one way or the other: *Dr. Kai Engelhardt*, *Dr. Stefan Lauxtermann*, *Dr. Roger Dangel*, *Martin Wäny*, *Georg Israel*, *Dr. Michel Willemin*, *Gerben Boer* and not to forget *Ernst Meier*.

I do not want to forget to thank my family, who were always interested in my work and my life. My *parents*, who made possible my complete education, and my brother *Christoph* and my sister *Kathrin*, who also were always there for me, when I needed them. Most important of all, my thanks go to my wife *Anja* for her love, support and patience over the last years.

In case I should have forgotten anyone, I beg for generous forgiveness.

The work was partly funded by the Swiss Priority Program OPTIQUE II, whom we thank for this support.

Publication list

1. R. Lange, P. Seitz, “Solid-state time-of-flight range camera”, *IEEE Journal of Quantum Electronics*, submitted for publication, (2000).
2. R. Lange, P. Seitz, “Seeing distances - A fast time-of-flight 3D camera”, *Sensor Review*, Vol. **20**, No. 3, July 2000, pp. 212-217, MCB University Press, ISSN 0260-2288, (2000).
3. R. Lange, P. Seitz, “Demodulation pixels in CCD and CMOS technologies for time-of-flight ranging”, *Proceedings of the SPIE*, Vol. **3965A**, pp. 177-188, San Jose CA, (2000).
4. R. Lange, P. Seitz, “Real-time range camera based on a novel imager with demodulation pixels”, *SPIE’s International Technical Group Newsletter*, Vol. **10**, No. 2, Bellingham, (1999).
5. R. Lange, P. Seitz, R. Schwarte, “Time-of-flight Entfernungskamera in CMOS/CCD- Technik mit pixelintegrierten optischen Lock-in-Verstärkern”, *Berichtsband **70** zur Fachtagung Optische Formerfassung 1999*, pp. 271-280, VDI-VDE, Stuttgart, (1999).
6. R. Lange, P. Seitz, A. Biber, R. Schwarte, “Time-of-flight range imaging with a custom solid-state image sensor”, *Proceedings of the SPIE*, Vol. **3823**, pp. 180-191, Munich, (1999).
7. R. Lange, P. Seitz, “Solid-State Time-of-Flight Distance Measurement System Based on Novel Lock-in Sensors”, *Proceeding of IWOM99*, The International Workshop on Optical Metrology (CD), Liverpool John Moores University, School of Engineering, (2000).
8. H. Heinol, R. Schwarte, Z. Xu, H. Neuhaus, R. Lange, “First Experimental results of a New 3D-Vision System Based on RF-Modulation Interferometry”, *Kongreßband OPTO96- Optische Sensorik Meßtechnik Elektronik*, AMA Fachverband für Sensorik, pp. 67-72, Leipzig, (1996).
9. Z. Xu, R. Schwarte, H. Heinol, R. Lange, J. Li, “Simulation of a 3D-color vision system based on synthetic non-linear modulation”, *Proceedings of the SPIE*, Vol. **2904**, pp. 361-369, Boston MA, (1996).

Patent pending

R. Lange, P. Seitz, “Device and method for spatially resolved photodetection and demodulation of modulated electromagnetic waves”, (2000).

b/w image

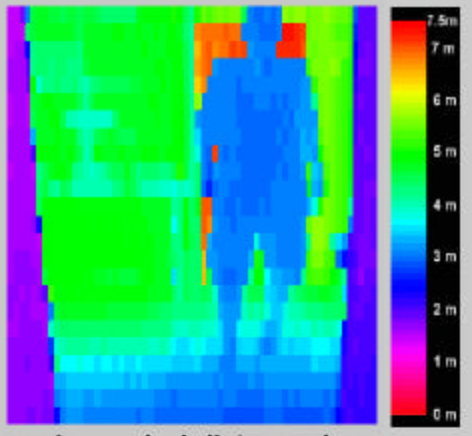

color-coded distance image

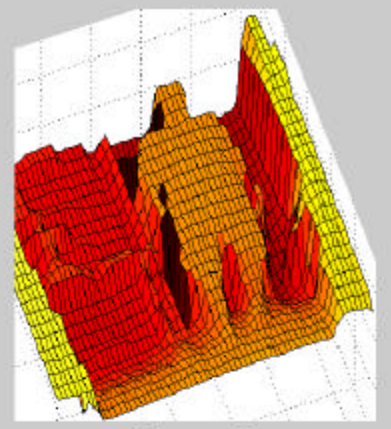

3D mesh

In this work the theory and practice of range cameras based on the time-of-flight principle are developed. As a key result the world's first imaging all-solid-state 2D and 3D time-of-flight range cameras without moving parts are realized. The cameras are based on customized image sensors, arrays of so-called demodulation pixels, which allow the measurement in each pixel of the local background illumination level, as well as the amplitude and the arrival time (phase) of a modulated optical wave field. The high timing resolution obtained, a few hundred picoseconds, leads directly to a distance resolution of a few centimeters over a measurement range of up to 20 m. With the single exception of the image sensors, only commercially available electronic components are used to build the 3D cameras.

The measured performance of the range cameras developed is mainly limited by photon noise, in excellent agreement with theoretical predictions. It is concluded that this time-of-flight range camera technology will find many applications in the fields of machine vision, automated navigation, safety and surveillance.

b/w image

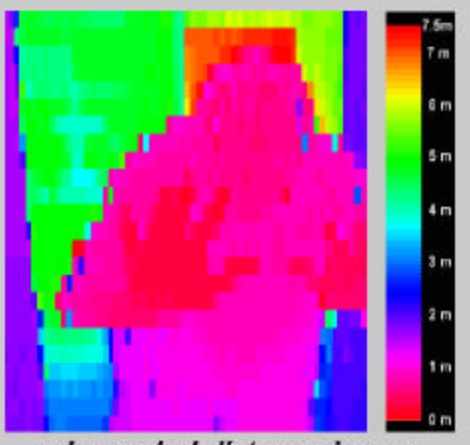

color-coded distance image

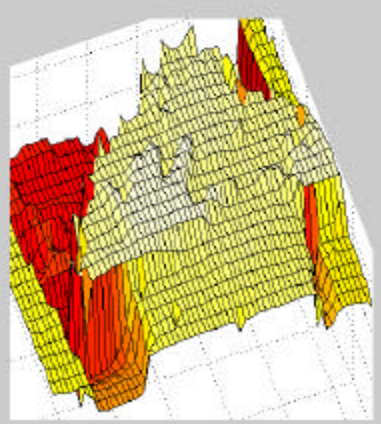

3D mesh